Dissertation

submitted to the

Combined Faculty of Mathematics, Engineering and Natural Sciences

of

Heidelberg University, Germany

for the degree of

Doctor of Natural Sciences

Put forward by

Tom Wickenhäuser

born in Cologne, Germany

Oral examination: November 5, 2025

Investigations on Organic, Inorganic and Hybrid Materials for Lithium-Ion Batteries

Referees: Prof. Dr. Rüdiger Klingeler
Prof. Dr. Joachim Spatz

Abstract

This work investigates potential cathode and anode materials for lithium-ion batteries with respect to their physical and electrochemical properties. The focus lies on novel triphenylamine-based polymers (FTN-Pol) as cathode materials, as well as photo-enhanced charging using the spinel $LiMn_2O_4$ as cathode. Additionally, the suitability of hybrid organic–inorganic perovskites (HOIPs), particularly $MAPbBr_3$, as anode materials is studied. Physical characterization is conducted using X-ray diffraction and scanning electron microscopy, while electrochemical properties are assessed via cyclic voltammetry, galvanostatic cycling, and chronoamperometry. Electrochemical analysis of the FTN-Pol system demonstrates that N-heterotriangulenes provide a redox-active and electrochemically stable backbone for polymeric cathodes. The rigid spirocyclic structure promotes high redox site accessibility while minimizing side reactions. While FTN-Pol exhibit limited specific capacity due to the high molecular weight of the redox unit, it achieves 87 % utilization of its theoretical capacity, a Coulombic efficiency of 99.6 %, and stable long-term cycling performance. Studies on the $LiMn_2O_4$ spinel reveal that light exposure enhances electrochemical performance by increasing charge extraction and accelerating reaction kinetics. Controlled experiments confirm that these effects are primarily attributable to photonic interactions with the electronic structure of the material, such as improved charge carrier mobility, rather than solely to thermal effects. The investigation of HOIP-based anodes indicates current limitations in terms of chemical stability, electrolyte compatibility, and long-term cycling durability. Nevertheless, under controlled conditions, redox activity and photoinduced effects can be observed, suggesting potential for niche applications or further research.

Zusammenfassung

In der vorliegenden Arbeit werden potenzielle Kathoden- und Anodenmaterialien für Lithium-Ionen-Batterien hinsichtlich ihrer physikalischen und elektrochemischen Eigenschaften untersucht. Im Fokus stehen neuartige, triphenylaminbasierte Polymere (FTN-Pol) als Kathodenmaterialien sowie das photobeschleunigte Laden mit dem Spinell $LiMn_2O_4$ als Kathode. Darüber hinaus wird die Eignung hybrider organisch-anorganischer Perowskite (HOIPs), insbesondere $MAPbBr_3$, als Anodenmaterialien analysiert. Die physikalische Charakterisierung erfolgt mittels Röntgendiffraktometrie und Rasterelektronenmikroskopie, während elektrochemische Eigenschaften durch zyklische Voltammetrie, galvanostatisches Zyklieren und Chronoamperometrie untersucht werden. Die elektrochemische Analyse des FTN-Pol-Systems zeigt, dass N-Heterotriangulene ein elektrochemisch stabiles und redoxaktives Rückgrat für polymere Kathoden darstellen. Die starre spirozyklische Struktur begünstigt eine hohe Redoxstellenzugänglichkeit bei gleichzeitig geringen Nebenreaktionen. Trotz der durch die hohe Molekülmasse limitierten spezifischen Kapazität erreicht FTN-Pol eine Kapazitätsauslastung von 87 %, eine coulombische Effizienz von 99,6 % und stabile Langzeitzyklen. Die Untersuchungen am $LiMn_2O_4$-Spinell zeigen, dass Lichtbestrahlung die elektrochemische Leistungsfähigkeit durch erhöhte Ladungsentnahme und beschleunigte Reaktionskinetik verbessert. Kontrollierte Experimente belegen, dass diese Effekte primär auf photonische Wechselwirkungen mit der elektronischen Struktur, etwa eine erhöhte Ladungsträgermobilität, und nicht ausschließlich auf thermische Einflüsse zurückzuführen sind. Für die untersuchten HOIPs deuten die Ergebnisse auf derzeit bestehende Einschränkungen hinsichtlich chemischer Stabilität, Elektrolytkompatibilität und Zyklenfestigkeit im Langzeiteinsatz hin. Unter kontrollierten Bedingungen lassen sich jedoch Redoxaktivität und photoinduzierte Effekte beobachten, was auf Potenzial für spezifische Anwendungen oder weiterführende Studien schließen lässt.

List of Partial Publications

Publication that is presented in the main part of the thesis at hand:

- A. Jocic, **T. Wickenhäuser**, S. Lindenthal, W. Zhang, J. Zaumseil, R. Schröder, R. Klingeler, M. Kivala *"Redox-active, photoluminescent porous polymers based on spirofluorene-bridged N-heterotriangulenes and their feasibility as organic cathode materials"*, Chemical Science (2024)
  DOI: 10.1039/D4SC04276J

Further publications resulting from the thesis project

- L. Ueberricke, F. Mildner, Y. Wu, E. Thauer, **T. Wickenhäuser**, R. Klingeler, M. Mastalerz et al. *"Redox-active, porous pyrene tetraone dendritic polymers as cathode materials for lithium-ion batteries"*, Materials Advances (2023)
  DOI: 10.1039/D2MA01039A

- P. Kollenz, C. Herrle, L. Göhringer, **T. Wickenhäuser**, W. Pernice, R. Klingeler, F. Deschler *"Excited State Reservoir Computing using Hybrid Perovskite Electrochemically-Gated Luminescent Cells"*, heiDOC (2025)
  DOI: 10.11588/heidok.00035906

Contents

1 Introduction **1**

2 Theoretical Background and Experimental Methods **7**

2.1 Working Principle of Lithium Ion Batteries 7

2.2 Physical Characterization Techniques 11

2.2.1 X-Ray Diffraction 11

2.2.2 Scanning Electron Microscopy 12

2.3 Electrochemical Studies 13

2.3.1 Theoretical Bachground 13

2.3.2 Cyclic Voltammetry 15

2.3.3 Chronoamperometry 16

2.3.4 Galvanostatic Cycling 17

2.3.5 Electrochemical Impedance Spectroscopy 19

2.4 Electrochemical Setup 21

2.4.1 Electrode Preparation 21

2.4.2 Battery Cell Setup 23

2.4.3 Electrolytes 27

2.4.4 Light source 29

2.4.5 Carbon Black Reference Measurement 29

3 Triphenylamine-Based Cathode Material **33**

3.1 Organic Cathode Materials: State of the Art 33

3.1.1 Conjugated Polymers 34

3.1.2 Non-Conjugated Redox-active Polymers 36

3.1.3 Triphenylamin-based Cathode Material 37

3.2 Spirofluorene Bridged N-heterotriangulenes Polymer 42

3.2.1 Physical Characterization 42

3.2.2 Electrochemical Investigations 43

3.2.3 Conclusions 55

3.3 Sulfur-Chain Functionalization of FTN-Pol: Electrochemical Impact and Limitations . . . 57
3.3.1 Motivation for Sulfur Chain Integration into FTN-Pol . . . 57
3.3.2 Background on Sulfur in Lithium Battery Systems . . . 57
3.3.3 Electrochemical Reference Measurement of Sulfur-Based Electrodes 58
3.3.4 Electrochemical Characterization . . . 60
3.3.5 Electrochemical Impact of Sulfur Chain Integration into FTN-Pol . 67
3.4 Electrochemical Effects of Terthiophene Functionalization in FTN-Based Redox Polymers . . . 69
3.4.1 Electrochemical Behavior of FTN-Pol Functionalized with Terthiophene (3T) . . . 70
3.4.2 Comparison with Bare FTN-Pol: Influence of Terthiophene Incorporation . . . 72
3.5 Conclusion and Outlook . . . 73

4 Decoupling Photothermal Effects in Photo-Enhanced $LiMn_2O_4$ Battery 75
4.1 Inorganic Cathode Materials: State of the Art . . . 75
4.1.1 Tranistion Metal Oxides . . . 75
4.1.2 Manganese-Based Oxides . . . 76
4.1.3 $LiMn_2O_4$ Spinel . . . 77
4.2 Synthesis . . . 79
4.3 Electrochemical Characterization . . . 79
4.3.1 Electrochemical Baseline Behavior of $LiMn_2O_4$ Electrodes . . . 79
4.3.2 Reference Study: Photo-Induced Effects in $LiMn_2O_4$ (Lee et al.) . . 80
4.3.3 Light and Heat Effects on Cycling . . . 83
4.3.4 Impact of Illuminated Area on the Electrochemical Response of $LiMn_2O_4$ Electrodes . . . 87
4.3.5 Time-Dependent Electrochemical Response of $LiMn_2O_4$ Under Photo-Accelerated Conditions . . . 89
4.3.6 Comparison . . . 91
4.4 Conclusions . . . 94

5 Hybrid Organic Inorganic Perovskite Anode Material 97
5.1 Hybrid Organic Inorganic Battery Material: State of the Art . . . 98
5.1.1 Hybrid Organic Inorganic Perovskites . . . 98
5.2 Synthesis of Hybrid Organic–Inorganic Perovskites . . . 104
5.2.1 $MAPbBr_3$ . . . 105

5.2.2 $EBAPbI_3$ . . . 105
5.2.3 $CsMnBr_3$ . . . 105
5.2.4 $EBA_4Bi_2Br_{10}$ . . . 105
5.3 Physical Characterization . . . 106
5.4 Electrochemical Characterization . . . 107
5.4.1 Reaction Mechanisms in $MAPbBr_3$ . . . 107
5.4.2 Limited Voltage Range Studies . . . 113
5.4.3 Electrolyte Studies . . . 119
5.4.4 Perovskite Variations . . . 127
5.4.5 External Effects . . . 138
5.5 Conclusions and Overview . . . 146

6 Summary and Conclusion **149**

Bibliography **155**

1 Introduction

Global energy demand has been steadily increasing, with global primary energy consumption growing at an average rate of approximately 2 % annually, except in 2020 due to the peak of the COVID-19 pandemic [1]. Currently, 81.5 % of the world's primary energy supply still originates from fossil fuels [1], whose combustion releases significant amounts of carbon dioxide (CO_2) into the atmosphere. The long-term trend in atmospheric CO_2 concentration, visualized in the Keeling Curve (Figure 1.1), shows a relatively stable concentration around 265 ppm for much of the last 10,000 years, with a modest increase to approximately 275 ppm until around 1800. However, since the onset of the Industrial Revolution, anthropogenic emissions have driven CO_2 concentrations to unprecedented levels, reaching 427 ppm as of 2024 [2, 3].

While natural fluctuations in CO_2 levels, ranging between 180 ppm and 300 ppm, have occurred over the past 800,000 years, the sharp increase in recent centuries is undeniably human-induced [2]. According to the 2023 IPCC report, neither atmospheric CO_2 concentrations nor net global greenhouse gas (GHG) emissions are expected to decline significantly in the coming years [5]. Elevated GHG concentrations contribute to the greenhouse effect [6], wherein CO_2 absorbs infrared radiation emitted by the Earth's surface, preventing heat loss to space and thereby warming the planet [7]. Furthermore, increased CO_2 uptake by oceans leads to acidification, which lowers pH levels and calcium carbonate saturation, adversely affecting marine ecosystems [8]. This climatic shift is evidenced by the increase in global surface temperatures from 13.67 °C in 1924 to 15.19 °C in 2024 [9], resulting in severe environmental impacts such as glacial melting and sea-level rise [10, 11], more frequent extreme weather events [5, 12], loss of biodiversity [13, 14], and growing numbers of environmental refugees [15]. Mitigating these drastic outcomes necessitates a rapid reduction in anthropogenic GHG emissions, particularly CO_2, by transitioning to renewable energy (RE) sources like hydropower, solar, and wind [16]. These technologies are among the most effective and scalable strategies for addressing both climate change and the growing global energy demand [17, 18]. As of 2024, RE accounts for approximately 15 % of global energy production, with hydropower contributing 6 % [1]. Due to economies of scale and technological advances, the market costs of solar photovoltaics have

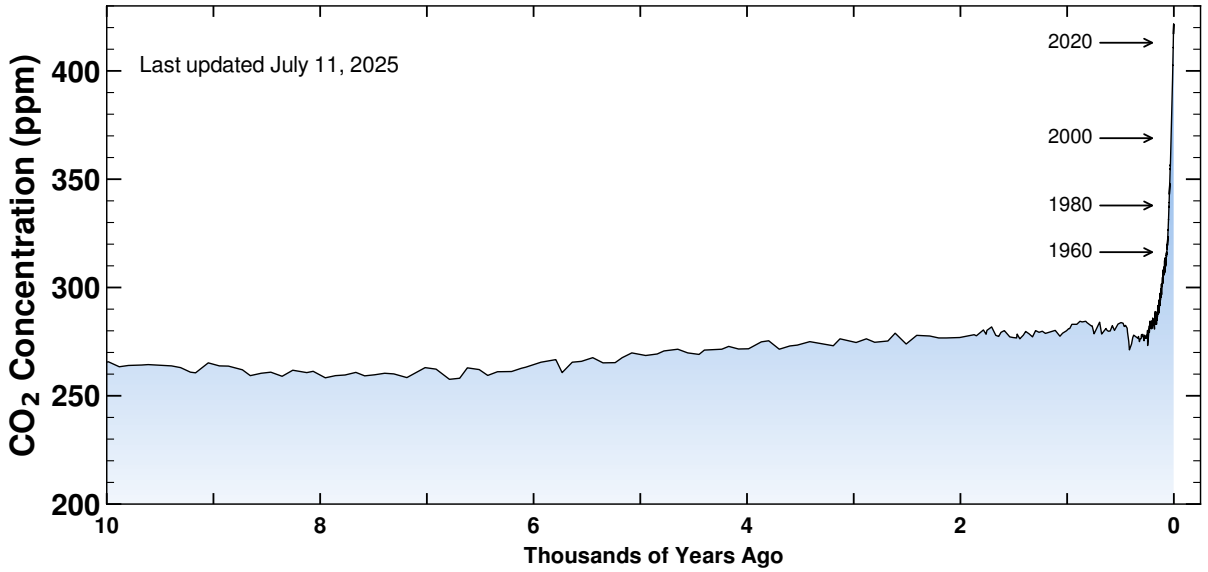


Figure 1.1: The Keeling Curve: Atmospheric CO_2 concentration over the past 10,000 years. Reproduced from the Keeling Curve archives [4].

fallen from 600 $ to 70 $ per megawatt-hour (MW h), while onshore and offshore wind energy costs have decreased from 150 $ and 140 $ to 60 $ and 80 $ per MW h, respectively, between 2000 and 2020 [5]. For comparison, fossil fuel-derived electricity typically costs between 80 $ and 150 $ per MW h [5]. Despite these advantages, integrating RE into the electrical grid poses two key challenges: (1) Instability and intermittency - since RE output is weather-dependent, it introduces variability that can compromise grid stability [19], and (2) Grid accommodation - as exemplified by the "duck curve", increased solar output may cause midday overgeneration and steep ramping needs during morning and evening hours, leading to energy restriction and reduced overall efficiency [20, 21].

A promising solution to these challenges is the deployment of efficient energy storage systems (ESS), which can store excess RE generated during low-demand periods and release it during peak demand [22, 23]. The efficient storage and utilization of renewable energy thus forms the central motivation of this thesis.

A Brief Summary of the History of Lithium Ion Batteries

The development of batteries has a rich history, beginning in the late 18th century with pioneering discoveries in electrochemistry. Luigi Galvani's experiments at the University of Bologna and Alessandro Volta's subsequent invention of the voltaic pile at the University of Pavia marked the inception of the electrochemical cell [24]. Volta's discovery laid the foundation for electrochemical energy storage, making batteries widely known to human-

ity. The progress continued through the 19th century; in 1866, Georges-Lionel Leclanché introduced a practical primary battery using a zinc anode and a manganese dioxide-carbon cathode immersed in an aqueous ammonium chloride solution [25]. This “Leclanché cell” became the forerunner to modern dry cells. Shortly before, in 1859, Gaston Planté developed the first rechargeable lead–acid battery, an innovation that remains relevant today in applications like automotive starter batteries. Later, in 1901, Swedish engineer Waldmar Jungner invented the nickel–cadmium (NiCd) rechargeable battery, another milestone in secondary battery technology [26]. These foundational works in electrochemical energy storage highlighted both the potential and limitations of early batteries. Zinc- and lead-based systems were relatively low in energy density, prompting researchers to explore alternative materials. It was intuitive to consider lithium, being the lightest metal with the highest electrochemical potential, as a promising candidate to increase energy density dramatically [26]. Research into lithium-based batteries began during the mid-20th century. Initial efforts focused on primary lithium batteries, but the quest for a stable and safe rechargeable lithium system became a central challenge. In the 1960s and 1970s, early studies demonstrated the promise of lithium in battery chemistry. Selis et al. [27] and Casey et al. [28] examined the behavior of lithium in electrochemical cells, including its effects on battery energy at elevated temperatures. In 1978, a key milestone was achieved when M.S. Whittingham introduced the concept of lithium intercalation into transition metal dichalcogenides, particularly titanium disulfide (TiS_2), leading to the first prototype lithium-ion battery with a TiS_2 cathode and lithium metal anode [29]. While Whittingham’s system demonstrated electrochemical reversibility, its use of metallic lithium posed severe safety risks. Lithium’s high reactivity with both air and electrolyte caused formation of a passivating layer known as the solid electrolyte interface (SEI). While partially protective, irregularities in the SEI could lead to lithium dendrite formation, short circuits, and even fires or explosions [30, 31]. These hazards were tragically demonstrated in early devices like the MOLICEL, which resulted in serious incidents including battery fires [32]. To address safety issues, researchers sought safer electrode materials.

In 1980, John B. Goodenough identified lithium cobalt oxide ($LiCoO_2$) as a cathode material with a layered structure analogous to TiS_2 but with superior stability in ambient conditions [33]. Around the same time, graphite was investigated as a potential intercalation anode. The so-called "rocking-chair" battery concept, where lithium ions shuttle between intercalating cathode and anode materials during charge and discharge, was proposed and experimentally validated throughout the 1980s. Significant contributions came from Besenhard, Yazami and Touzain [34, 35], who demonstrated lithium intercalation into graphite and evaluated its reversibility using solid polymer electrolytes.

One of the most essential development came in 1985 when Akira Yoshino built a prototype LIB using $LiCoO_2$ as the cathode, polyacetylene (later replaced by more stable carbonaceous materials) as the anode, and a non-aqueous electrolyte. Yoshino's design eliminated reactive metallic lithium, dramatically improving battery safety. His LIB passed critical safety tests, including collision tests, without igniting, unlike earlier lithium-metal-based designs [36]. In 1991, Sony commercialized Yoshino's design, ushering in the modern era of lithium-ion batteries. The initial LIBs featured graphite anodes, $LiCoO_2$ cathodes, and liquid electrolytes. Subsequent safety concerns, especially involving dendritic lithium growth and thermal runaway, led to further refinements [37]. These included the development of polymer electrolytes and replacement of $LiCoO_2$ with safer, lower-cost cathodes such as lithium iron phosphate ($LiFePO_4$, or LFP), now dominat in many applications. In 2000 Shirakawa, Alan J. Heeger and Alan G. MacDiarmid were the recipients of the prestigious Nobel Prize in Chemistry "for the discovery and development of conductive polymers" [38] and in 2019 the Nobel Prize in Chemistry was awarded to John B. Goodenough, M. Stanley Whittingham and Akira Yoshino "for their contributions to the development of the lithium-ion battery" [39].

Today, LIBs are the backbone of portable electronics, electric vehicles, and grid-scale energy storage. Their high energy density, cycle life, and declining production costs have made them indispensable in modern energy infrastructure. Nevertheless, ongoing challenges, such as resource shortage, safety at high capacities, and environmental concerns, continue to drive research toward next-generation battery technologies. Understanding the evolution from early electrochemical cells to today's LIBs not only contextualizes their significance but also motivates continued innovation in electrochemical energy storage.

To develop more powerful lithium-ion batteries, understanding the interplay between storage mechanisms, transport processes as well as their relationship to the electrode morphology and structure is essential. This thesis investigates novel organic, inorganic and hybrid substances as anode and cathode materials in LIBs. The focus here is on the electrochemical properties of the materials. Furthermore, the influence of light on batteries is being investigated, similar to the idea of a photobattery - battery that uses light to either increase the energy storage performance or to be charged solely with light.

The following chapters explore the development and characterization of advanced electrode materials for lithium-based energy storage systems, with a particular focus on organic, inorganic, and hybrid materials. Chapter 2 outlines the theoretical foundations and experimental methods employed, including physical and electrochemical characterization techniques. Chapter 3 investigates triphenylamine-based redox polymers and their

structural modifications to enhance electrochemical performance. Chapter 4 examines photothermal effects in $LiMn_2O_4$-based cathodes under illuminated conditions, aiming to decouple light-induced contributions from thermal effects. Chapter 5 shifts to hybrid organic–inorganic perovskites as emerging anode materials, analyzing their synthesis, reaction mechanisms, and electrochemical behavior. The work concludes with a comprehensive summary Chapter 6 of the findings and an outlook on future research directions in battery material development.

2 Theoretical Background and Experimental Methods

2.1 Working Principle of Lithium Ion Batteries

In lithium-ion batteries, chemical energy is converted into electrical energy through redox (reduction–oxidation) reactions. Throughout this energy conversion process, one chemical species undergoes oxidation, releasing electrons that are conducted through an external circuit to a second redox-active species, which is subsequently reduced. This fundamental mechanism forms the basis of electrochemical energy storage. The galvanic cell is one of the most well-known electrochemical systems. In such a configuration, two electrode materials with different redox potentials are immersed in separate electrolyte solutions, which are connected by a porous separator that permits ionic transport while preventing the direct mixing of the electrolytes. The general structural design and operational principle are similar across all electrochemical cells. These cells are typically composed of three main components: the anode, the cathode, and the electrolyte. The electrolyte serves to transport ions between the electrodes and is essential for maintaining electrical neutrality within the cells. As such, high ionic conductivity of the electrolyte is crucial to ensure efficient operation. In contrast, significant electronic conductivity within the electrolyte is undesirable, as it would facilitate internal short-circuiting, thereby compromising cells efficiency and safety. The output voltage of an electrochemical cell is determined by the redox potential difference between the electrodes and typically ranges from 1 to 3 V, rarely exceeding 5 V. Electrochemical cells are broadly classified as either primary or secondary, depending on the reversibility of the redox reactions involved. Primary cells are designed for single-use applications and are not rechargeable, as their electrochemical reactions are thermodynamically or kinetically irreversible. As a consequence, these cells must be disposed after the stored chemical energy has been fully converted. The lack of constraints on reversibility allows for a wider range of materials and typically results in higher energy densities in primary cells compared to secondary ones. In contrast, secondary cells are designed to be rechargeable and require that the redox reactions at both electrodes be chemically reversible. During the charging process, an external electrical

current is applied to drive the redox reactions in the opposite direction, thereby restoring the electrodes to their original charged states. The ability of a secondary cell to undergo repeated charge–discharge cycles depends on the reversibility of the redox reactions and the structural stability of the electrode materials. High-performance secondary batteries can typically endure thousands of such cycles. A more detailed description of the fundamentals of electrochemical cells and their classification can be found in [40–42].

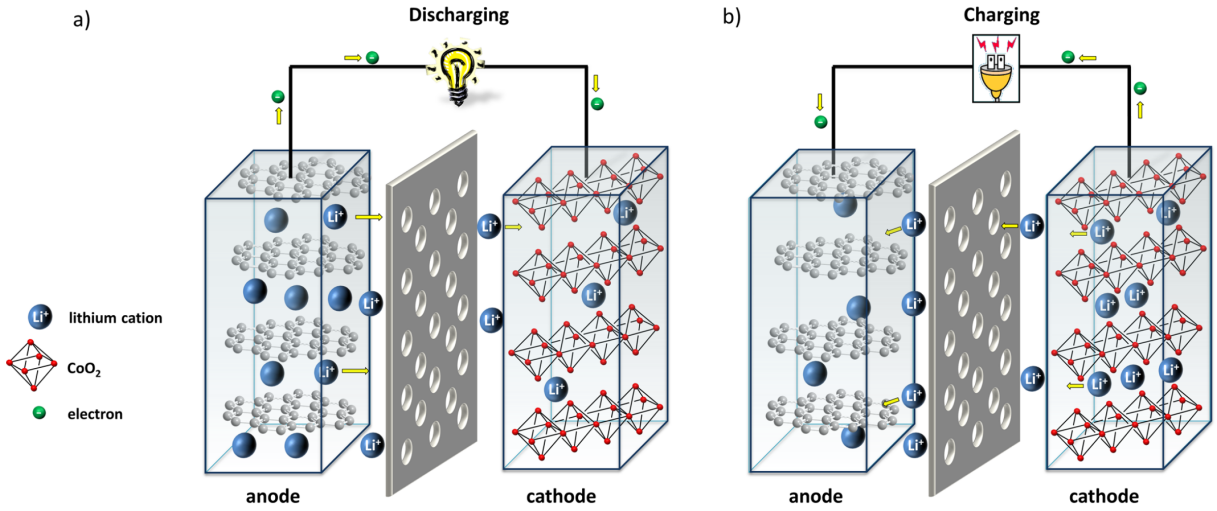


Figure 2.1: Schematic illustration of the working principle of a lithium-ion battery based on a $Li_{1-x}CoO_2{}^{x-}$ cathode and a graphite anode. **(a)** Discharge process: lithium atoms in the graphite anode are oxidized to Li^+, releasing electrons that travel through the external circuit to the cathode, where they are consumed in the reduction of $CoO_2{}^{1-}$. Simultaneously, Li^+ ions migrate through the electrolyte to the cathode, ensuring charge balance. **(b)** Charge process: application of an external voltage reverses the redox reactions, reducing Li^+ ions at the graphite anode and oxidizing the cathode material, effectively reintercalating lithium into the anode. Adapted from Muench et al. [42].

Among secondary batteries, lithium-ion systems have become dominant due to their high energy density and reversible redox chemistry. Figure 2.1 illustrates the fundamental processes occurring during the operation of a lithium-ion battery comprising a graphite anode and a layered lithium metal oxide cathode, specifically $Li_{1-x}CoO_2x-$. Both electrodes are immersed in an electrolyte containing lithium salts (e.g. $LiPF_6$), enabling ionic conductivity. Under open-circuit conditions, each electrode establishes an electrochemical equilibrium with the electrolyte, resulting in the accumulation of surface charges and the development of the cells potential. Upon connecting the electrodes via an external circuit, the potential difference between them provides the driving force for electron flow from the graphite anode to the $CoO_2{}^-$ cathode. At the same time, lithium atoms intercalated within the graphite structure are oxidized to Li^+ ions, which migrate through the electrolyte toward the cathode. The arriving Li^+ ions are then inserted into the layered

structure of the CoO_2^- cathode material while the electrons are consumed in the reduction of Co^{4+} to Co^{3+}, completing the redox cycle. In an idealized cell system, the rate-limiting step for battery performance is often the ionic mobility within the electrolyte. Therefore, minimizing the resistance of the electrolyte is a key consideration in battery design. During the charging process, as shown in Figure 2.1b), an external current is applied in the opposite direction, driving the reduction/intercalation of Li^+ into the graphite anode and the oxidation of the cathode material, thereby restoring the initial lithium distribution. The use of intercalation materials such as graphite has been a major advancement in lithium-ion battery technology, as it prevents the deposition of metallic lithium and mitigates the formation of dendritic structures that could lead to internal short-circuits. The immobilization of lithium within the graphite lattice thus enhances both the safety and cyclability of the battery. For comprehensive discussions of the working principles of lithium-ion batteries, the reader is referred to [30, 37, 42].

The development of advanced electrode materials remains a central objective in contemporary battery research. Since the commercial introduction of the first lithium-ion battery by Sony in 1991, graphite has become the standard anode material, while transition metal oxides, particularly those with layered or rock-salt structures, have dominated as cathode materials [43]. These materials enable lithium storage through highly reversible intercalation reactions (Figure 2.2 a)), wherein Li^+ ions diffuse into interstitial sites of the host crystal lattice. Ideally, this process induces only minor expansion of the lattice and avoids significant structural degradation, thereby preserving the crystallographic integrity of the host material.

While intercalation reactions in conventional cathode materials offer excellent reversibility, their theoretical capacity is typically limited by the maximum number of Li^+ ions that can be reversibly inserted per formular unit, which is often close to one Li^+ but depends on the material system [45]. To meet the increasing energy density demands of applications such as electric vehicles, where driving range remains a critical metric, alternative lithium storage mechanisms are being actively pursued. In this context, conversion and alloying-type reactions (Figure 2.2 b), c)) have garnered significant attention due to their potential to accommodate multiple Li^+ ions per formula unit, resulting in markedly higher gravimetric and volumetric energy densities. Alloying mechanisms involve the formation of intermetallic compounds between lithium and low-mass elements such as Mg, Al, Si, Ge, Sn, Ag, and Zn [46–48]. Conversely, conversion reactions occur in transition metal compounds of general formula MX (M = Fe, Co, Ni, etc.; X = O, N, F, S, P), wherein the metal species is fully reduced and, in the case of oxides, Li_2O is concurrently formed [49]. This mechanism was first reported by Poizot et al.in 2000 for transition metal oxides

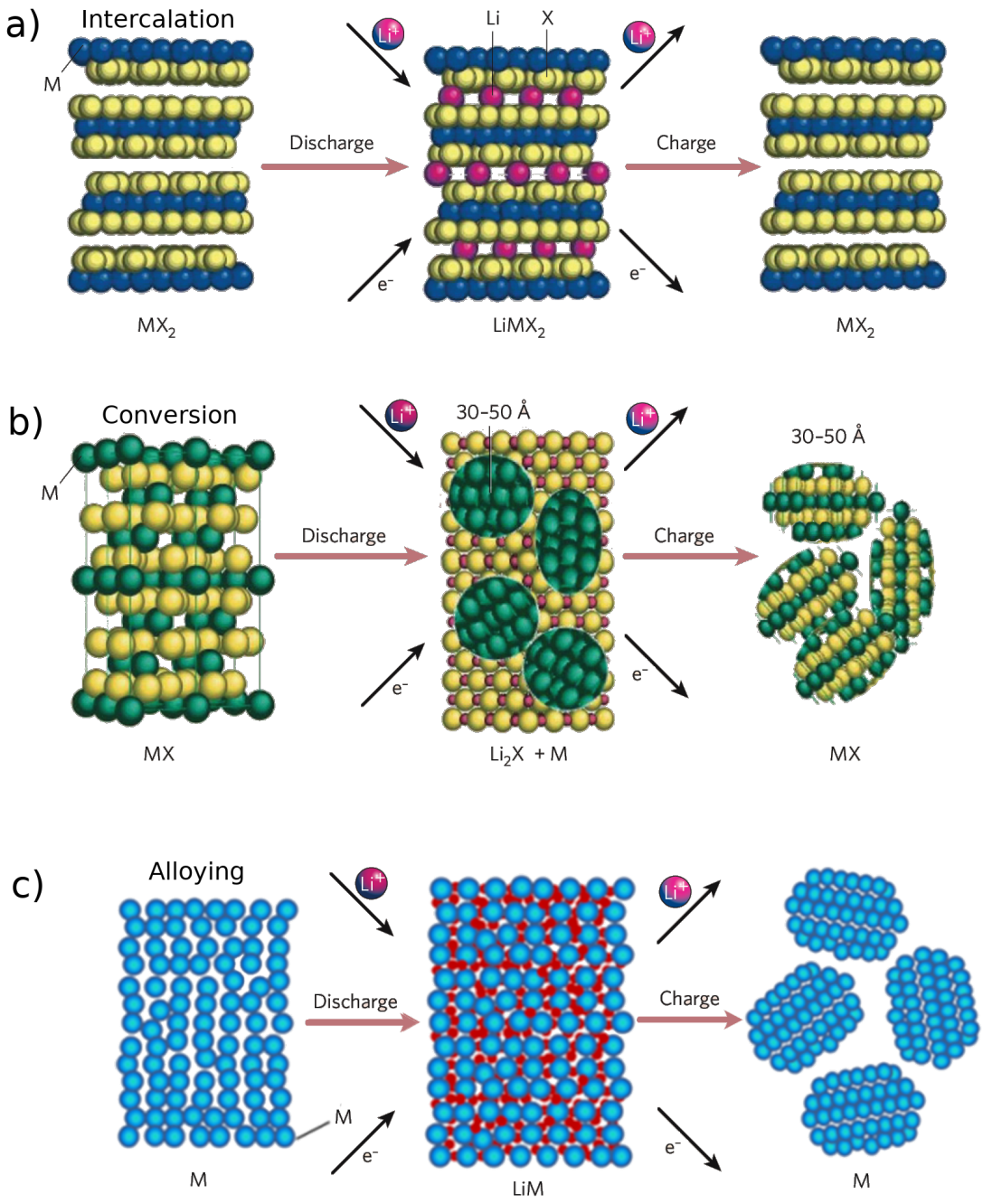


Figure 2.2: Schematic illustration of the three principal lithium storage mechanisms in electrode materials: **a)** Intercalation — Lithium ions are reversibly inserted into the host crystal lattice without significant structural changes, typically enabling one Li^+ ion per formula unit. **b)** Conversion — Lithium reacts with transition metal compounds, leading to the complete reduction of the metal and formation of Li_2O; this mechanism offers higher capacity but involves major structural transformations. **c)** Alloying — Lithium forms intermetallic compounds with low-mass elements such as Si or Sn, providing high specific capacities at the expense of substantial volume changes and mechanical stress. Adapted from [44, 45].

[50]. The reversibility of the conversion reaction is critically dependent on the morphology of the resulting metal nanoparticles, which must be sufficiently small and catalytically active to facilitate the decomposition of Li_2O [51]. Although both alloying and conversion reactions enable higher capacities compared to traditional intercalation, they are accompanied by substantial structural and volumetric changes. These mechanical stresses can cause pulverization of the electrode material, leading to the formation of electrochemically inactive regions and consequent capacity fading [51].

2.2 Physical Characterization Techniques

In order to investigate the electrochemical performance of novel battery materials, prior physical characterization is essential. The physical properties of the materials investigated in this thesis were characterized using methods of X-ray diffraction (Section 2.2.1) and scanning electron microscopy (Section 2.2.2). Their theoretical principles and experimental implementation are described below.

2.2.1 X-Ray Diffraction

All of the diffraction measurements presented in this study were performed by Ilse Glass using a Bruker D8 ADVANCE ECO diffractometer equipped with copper K_α radiation ($\lambda(K_{\alpha_1}) = 0.154\,06\,\text{nm}$, $\lambda(K_{\alpha_2}) = 0.154\,44\,\text{nm}$) at the Institute of Geosciences, Heidelberg University. Sample preparation was carried out in a two-step process: the powdered material was manually dispersed in isopropanol using a mortar to ensure a homogeneous distribution, which is essential for obtaining reproducible and representative diffraction patterns. The resulting suspension was then uniformly applied to a silicon sample holder. Data acquisition was conducted in continuous scanning mode, with the diffracted intensity recorded as a function of the scattering angle (typically at a step size of $2\,\theta = 0.02°$). The primary objective of the data analysis was phase identification and assignment of crystalline components in the samples. For this purpose, the observed Bragg reflections were compared against reference patterns from the Inorganic Crystal Structure Database [52]. The lower limit of quantification (LOQ) in laboratory-based powder XRD is inherently sample-dependent and influenced by factors such as peak overlap, preferred orientation of crystallites, and the presence of amorphous phases. Nevertheless, a commonly accepted guideline suggests a LOQ of $\approx 1\text{-}5\,\text{wt}\%$ [53–55]. Similarly, the visibility of nanocrystalline domains in diffractograms depends on these factors, with the lower limit of detection for crystallite size generally accepted to be in the range of $2\text{-}4\,\text{nm}$ [53, 56, 57].

2.2.2 Scanning Electron Microscopy

Scanning electron microscopy (SEM) is a crucial technique for investigating the morphology and surface topography of solid specimens. Unlike a transmission electron microscope, SEM analysis does not require the sample to be electron-transparent [58]. In SEM, the sample surface is raster-scanned with a finely focused, high-energy electron beam (typically ranging from 100 V to 100 kV) [59]. These electrons are generated under high vacuum conditions via thermionic or field emission, then accelerated by an applied voltage and focused using electromagnetic lenses [60]. Upon interaction with the sample surface, the primary electron beam induces the emission of both secondary electrons (SEs) and backscattered electrons (BSEs). The number and spatial distribution of these emitted electrons depend on the local surface structure and chemical composition of the sample. SEs are low-energy electrons (a few eV) emitted due to inelastic scattering events, primarily from within a few nanometers of the sample surface. They are particularly sensitive to surface features, making them well-suited for topographic and morphological characterization [61].

In contrast, BSEs result from elastic scattering processes and retain a higher fraction of their initial energy, allowing them to originate from deeper regions of the sample. The BSE yield is strongly dependent on the atomic number (Z) of the constituent elements, thereby providing compositional contrast in the resulting images [62]. The emitted electrons are detected by specific detectors (SE and BSE), and the image is generated by mapping the signal intensity as a function of the beam position. While SEM is applicable to a broad range of sample types, its spatial resolution (typically ≤ 1 nm) is lower than that of TEM, which can reach resolutions ≤ 0.1 nm [59].

In this study, SEM analyses were performed using a Zeiss SEM (LEO 1530) and a JEOL SEM (JSM-7610F), both equipped with BSE and energy-dispersive X-ray spectroscopy (EDS) detectors. All measurements were carried out at the Institute for Physical Chemistry of the Heidelberg University. The primary aim was to investigate the morphology and particle size distribution of powdered electrode materials. Sample preparation involved attaching a layer of self-adhesive conductive carbon tape (Plano) to the respective SEM specimen holder. A small quantity of the powder was dispersed onto the tape using tweezers. Excess, non-adherent particles were removed by gentle mechanical tapping followed by a light stream of compressed air. For samples with low electrical conductivity, a conductive gold coating of ≈ 10 nm thickness was applied using a Blazers sputtering device (Union SCD 004), operated at 25 mA for 25 s. This conductive layer mitigates charging effects and improves image quality by enhancing the emission and collection of SEs and BSEs [58].

2.3 Electrochemical Studies

A concise overview of the fundamental principles of electrochemistry is presented below. Furthermore, the electrochemical characterization techniques employed in this study namely cyclic voltammetry (CV), galvanostatic cycling (GCPL), and electrochemical impedance spectroscopy (EIS) are systematically described.

2.3.1 Theoretical Bachground

Electrochemistry primarily addresses the principles governing the conversion between electrical and chemical energy. For comprehensive explanations, the reader is referred to standard textbooks [63–65]. The following concise summary of battery-related fundamentals is derived from these sources.

A secondary battery operates based on the reversible conversion of chemical energy into electrical energy. Its basic architecture comprises one or more galvanic cells. Each galvanic cell consists of two electronically conductive electrodes, physically divided by a separator that allows ionic but not electronic conduction. These electrodes are immersed in an ionically conductive medium, the electrolyte. Ion transport within the electrolyte between the electrodes completes the internal circuit, while the external circuit enables the performance of electrical work. Energy conversion occurs primarily through redox reactions:

$$\mathrm{Ox} + z \cdot \mathrm{e}^- \underset{\text{Oxidation}}{\overset{\text{Reduction}}{\rightleftharpoons}} \mathrm{Red}. \tag{2.1}$$

In electrochemical systems, Ox and Red denote the oxidized and reduced forms of a chemical species, respectively. The parameter z represents the number of electrons transferred during the redox reaction and is referred to as the equivalence number. According to conventional terminology in electrochemistry, during battery discharge, the electrode at which oxidation occurs is defined as the anode, whereas the electrode where reduction takes place is referred to as the cathode. The fundamental thermodynamic expression governing a reversible electrochemical transformation is given by:

$$\Delta G = \Delta H - T\Delta S. \tag{2.2}$$

In this context, ΔG denotes the change in Gibbs free energy, representing the maximum reversible work obtainable from a chemical reaction under constant temperature and pressure. ΔH corresponds to the enthalpy change, which reflects the energy released or

absorbed during the reaction. ΔS signifies the change in entropy, and T is the absolute temperature. The term $T\Delta S$ corresponds to the thermal energy, i.e., heat generated as a result of the electrochemical transformation of the reactants. The Gibbs free energy change, ΔG, associated with a chemical reaction is directly related to the electrical work that can be obtained from the reaction when it occurs in an electrochemical cell, as described by the following equation:

$$\Delta G = -zFE. \tag{2.3}$$

In this equation, z represents the number of electrons transferred per mole of reactant, F is the Faraday constant, and E denotes the cell potential associated with the specific redox reaction. The cell voltage for a given redox couple is determined by the corresponding electrochemical potentials. The total quantity of electrical charge produced (zF) depends on the amount of reactive material available.

In practical systems, not all species, meaning the different types of ions, molecules, or atoms present in the solution, actively participate in the reaction. Therefore, the concept of activity (a) is more appropriate than concentration for accurately describing electrochemical processes. Activity refers to the effective concentration of reactive species, that is, the portion of species per unit volume that is thermodynamically active in the reaction. At equilibrium, ΔG as a function of the activity of the reacting species is expressed by the following relationship:

$$\Delta G = \Delta G_0 + RT \ln\left(\frac{a_{Red}}{a_{Ox}}\right), \tag{2.4}$$

where ΔG_0 denotes the standard Gibbs free energy change, and R represents the universal gas constant. When combined with the earlier relationship between Gibbs free energy and the electrochemical potential (formular 2.3), this leads to the formulation of the Nernst equation. It relates the actual cell potential E to the standard electrode potential E^0 under non-standard conditions.

$$E = E^0 + \frac{RT}{zF} \cdot \ln(\frac{a_{Red}}{a_{Ox}}). \tag{2.5}$$

The open-circuit voltage (OCV, also known as the electromotive force, EMF) of a galvanic cell is determined by the difference in electrochemical potentials between the cathode and the anode:

$$\phi_{cell} = \phi_{anode} - \phi_{cathode}. \tag{2.6}$$

2.3.2 Cyclic Voltammetry

Cyclic voltammetry (CV) is one of the most widely employed electrochemical techniques due to its ability to provide comprehensive insights into redox processes [66]. During the measurement, an external potential is applied to the working electrode relative to a reference electrode, here, a lithium metal electrode (see Figure 2.3 a)). The measurement begins at an initial potential E_1, is linearly swept to a reversal potential E_2, and then returned to E_1, forming a triangular potential waveform. This sequence corresponds to one cycle, although typically multiple cycles are recorded to observe the evolution of the electrochemical behavior. In the context of this work, a typical scan rate v of $0.1\,\mathrm{mV\,s^{-1}}$ is used. The resulting current is continuously recorded and can be visualized as a function of time (see Figure 2.3 b)).

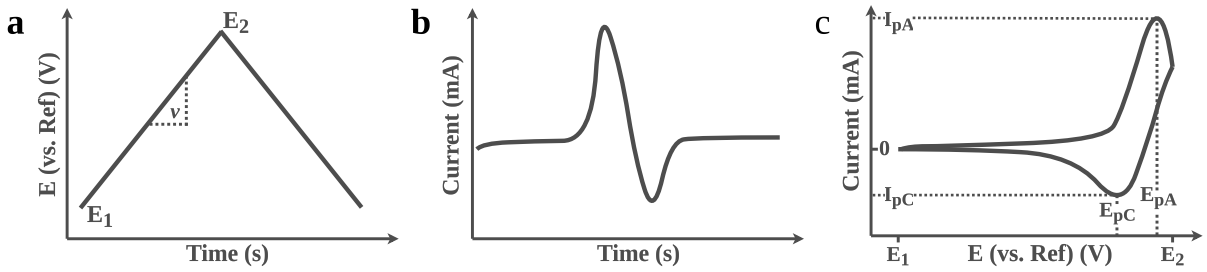


Figure 2.3: Schematic representation of a standard cyclic voltammetry (CV) experiment. **a)** Application of a linearly swept potential in a triangular waveform between E_1 and E_2 at a defined scan rate v. **b)** Resulting current response as a function of time. **c)** The corresponding cyclic voltammogram, indicating the anodic (E_{pA}) and cathodic (E_{pC}) peak potentials. Adapted from [67].

The graphical representation of current as a function of applied potential constitutes the cyclic voltammogram (Figure 2.3 c)). In accordance with IUPAC convention, this work adopts the sign convention in which anodic (oxidation) currents (I_{pA}) are represented as positive, while cathodic (reduction) currents (I_{pC}) are shown as negative [68]. Characteristic peaks observed in a CV correspond to electrochemically active redox processes. The potentials at which these peaks occur, denoted E_{pA} (anodic peak potential) and E_{pC} (cathodic peak potential) can be compared with literature values to identify the underlying redox reactions. Furthermore, the peak shape and width at half maximum provide insight into the kinetics of the redox process and the degree of crystallinity of the electrode

material [63, 69]. CV can also be employed to isolate and analyze individual electrochemical processes, provided that the redox peaks are sufficiently separated. By selectively adjusting the potential window to encompass specific reactions, additional processes can be introduced and analyzed sequentially. A more detailed introduction to the technique can be found in [66].

Another important parameter in electrochemical analysis is the overpotential, η, commonly defined in cyclic voltammetry as the difference between the anodic and cathodic peak potentials, $\eta = E_{pA} - E_{pC}$. This quantity reflects the kinetic barriers that must be overcome for the electrochemical reaction to proceed, including charge transfer resistance and mass transport limitations. Elevated overpotentials typically indicate poor electron transfer or hindered diffusion of reactants, which can degrade reaction efficiency. As such, overpotential analysis provides critical insight into the mechanistic and transport properties of electrode processes, supporting the development and optimization of high-performance electrochemical systems [63].

2.3.3 Chronoamperometry

Chronoamperometry (CA) is a powerful electrochemical technique widely employed in the characterization of lithium-ion batteries (LIBs). It involves applying a sudden potential step that shifts the system away from its OCV, thereby perturbing the electrochemical equilibrium. The resulting current response is recorded as a function of time, providing insight into charge transfer kinetics, ion diffusion, and electrode stability [70]. These parameters are critical for evaluating the performance and reliability of LIB materials.

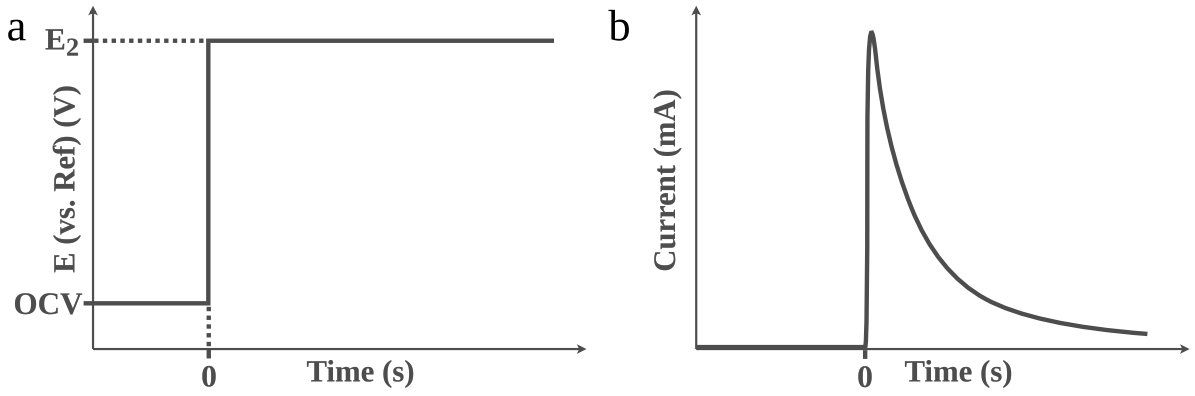


Figure 2.4: Schematic representation of a standard chronoamperometry (CA) experiment. **a)** Application of a potential step between OCV and E_2. **b)** Resulting current response as a function of time.

At the beginning of a typical CA experiment, the working electrode is at its equilibrium potential (OCV), as illustrated in Figure 2.4 a). At time t = 0, the potential is instantaneously stepped to a defined level E_2. This sudden change induces a transient current, which is continuously recorded, as shown in Figure 2.4 b). The resulting current-time (I - t) profile often follows the Cottrell equation for diffusion-limited systems:

$$I(t) = \frac{zFAc\sqrt{D}}{\sqrt{\pi t}}, \tag{2.7}$$

where z is the number of electrons, F is the Faraday constant, A is the electrode area, c the analyte concentration, and D is the diffusion coefficient [71]. Deviations from this behavior may indicate kinetic limitations, surface reactions, or other transport phenomena within the electrode or electrolyte [63].

2.3.4 Galvanostatic Cycling

The classical method for analyzing the charge–discharge behavior of electrode materials is galvanostatic cycling. In this technique, a constant current is applied during both the charging and discharging phases, and the resulting change in cell voltage over time is recorded producing what is known as a potential profile or voltage curve. The magnitude of the applied current is often referred to as the cycling rate or current density. In this study, galvanostatic cycling with potential limitation (GCPL) is employed to prevent deep discharge and overcharge, thereby preserving the integrity of the electrode materials.

GCPL measurements provide rich insights into the electrochemical behavior of the system. First, the shape of the voltage profile can reveal the nature of the electrochemical processes. For instance, in systems governed by Nernstian behavior, plateaus appear in the potential curve at voltages close to the equilibrium potential of the redox couple. These plateaus are analogous to the peak features observed in cyclic voltammograms.

Second, the total charge transferred during cycling, obtained by integrating the current over time, allows quantitative assessment of the extent of electrochemical reactions and the lithium content in the electrode material. This value is commonly expressed as the specific capacity (C_{spec}), which reflects the amount of charge per unit mass of active material. For a constant current I applied over a time interval t, the specific capacity is calculated via:

$$C_{spec} = \frac{1}{m} \int_0^t I(t)\, dt. \tag{2.8}$$

The theoretical, material-specific capacity of an electrode material can be calculated using Faraday's law, which relates the quantity of charge to the amount of substance undergoing electrochemical transformation:

$$C_{theo} = \frac{z \cdot F}{M_W}. \tag{2.9}$$

This calculation incorporates the molar mass (M_W) of the active material and the Faraday constant (F). In practical measurements, both the current and the resulting capacity are normalized to the mass of the electrochemically active components of the electrode.

For anode materials, which are typically cycled within a voltage range of 0.01 to 3.00 V, the total electrochemically active mass includes not only the active material itself but also the conductive carbon black additive. This additive exhibits electrochemical activity in the 0 to 1.5 V range, as demonstrated by a reference measurement shown in Figure 2.4.5. Therefore, the current is reported as current density in units of $\mathrm{mA\,g^{-1}}$, and the resulting capacity is expressed as specific capacity in $\mathrm{mA\,h\,g^{-1}}$.

In contrast, within the operational voltage range of cathode materials (usually 1.5 to 4.5 V), conductive carbon black does not participate in redox processes and can thus be excluded from capacity calculations (see Figure 2.4.5). For cathode materials, the cycling rate is often reported using C-rates, where a C/x rate indicates the current required to fully charge or discharge the theoretical capacity of the material in x hours. In these cases, the reported capacity refers exclusively to the mass of the active material and is again expressed in $\mathrm{mA\,h\,g^{-1}}$.

An important parameter used to evaluate the reversibility of electrochemical processes is the coulomb efficiency (CE). It is defined as the ratio of the charge extracted during discharge to the charge input during charge, and is mathematically expressed as follows [72]:

$$CE = \left(\frac{Q_{discharge}}{Q_{charge}} \right) \times 100\%, \tag{2.10}$$

where $Q_{discharge}$ and Q_{charge} represent the discharged and charged capacities, usually expressed in $\mathrm{mA\,h\,g^{-1}}$, respectively. A CE close to 100 % indicates highly reversible electrochemical reactions with minimal parasitic or side reactions.

Another critical indicator of battery material performance is cycling stability, which quantifies the retention of capacity over repeated charge–discharge cycles. It reflects the long-

term durability of the material and its resistance to degradation [22, 73]. The combined assessment of specific capacity and cycle stability constitutes the overall electrochemical performance, a central metric for evaluating the viability and potential of electrode materials in practical energy storage applications.

2.3.5 Electrochemical Impedance Spectroscopy

Electrochemical Impedance Spectroscopy (EIS) is a powerful, non-destructive technique widely used to investigate the kinetic processes and interfacial properties of electrochemical systems [74]. The method involves the application of a small-amplitude sinusoidal voltage perturbation in potentiostatic mode (PEIS), typically of the form:

$$U(t) = U_0 \sin(\omega t), \tag{2.11}$$

where U_0 is the voltage amplitude and ω is the angular frequency. The system's response is recorded as a sinusoidal current:

$$I(t) = I_0 \sin(\omega t + \phi), \tag{2.12}$$

where I_0 is the current amplitude and ϕ is the phase shift between voltage and current.

For the impedance measurement to yield meaningful and physically interpretable results, three fundamental conditions must be satisfied:

1. Linearity: The system must respond linearly to the perturbation. Although electrochemical systems are inherently non-linear, linearity can be approximated by using a sufficiently small excitation amplitude, commonly around 10 mV which keeps the system within a pseudolinear regime.

2. Causality: The system's output (current) must be fully determined by the input (voltage), implying no influence from future inputs.

3. Stationarity (Stability): The system must remain time-invariant during the measurement. It should maintain a stable baseline state until perturbed, and must be capable of returning to this state after the perturbation has ceased.

Under these conditions, the EIS technique enables the extraction of information related to charge transfer resistance, double-layer capacitance, diffusion processes, and other electrochemical parameters [75]. Under the aforementioned boundary conditions, the frequency-

dependent impedance (also referred to as AC resistance) of an electrochemical system can be calculated using Ohm's law in the frequency domain [76]:

$$Z(\omega) = \frac{\mathcal{F}\{U(t)\}}{\mathcal{F}\{I(t)\}}, \tag{2.13}$$

where $\mathcal{F}\{U(t)\}$ and $\mathcal{F}\{I(t)\}$ denote the Fourier transforms of the applied voltage and the resulting current, respectively. This procedure is repeated across a broad frequency spectrum typically from a few (Hz) up to (MHz) to obtain a comprehensive impedance spectrum. The wide frequency range enables the selective excitation of processes with varying characteristic time constants, thereby allowing a detailed analysis of different electrochemical phenomena within the cell. The resulting impedance data are commonly represented in a Nyquist plot, where the imaginary part of the impedance (Im(Z)) is plotted against the real part (Re(Z)). This representation facilitates the deconvolution of overlapping electrochemical processes by associating them with their respective time constants. Specifically, high-frequency (fast) processes appear on the left side of the plot (low Re(Z)), while low-frequency (slow) processes manifest toward the right (high Re(Z)), as illustrated in Figure 2.5 a).

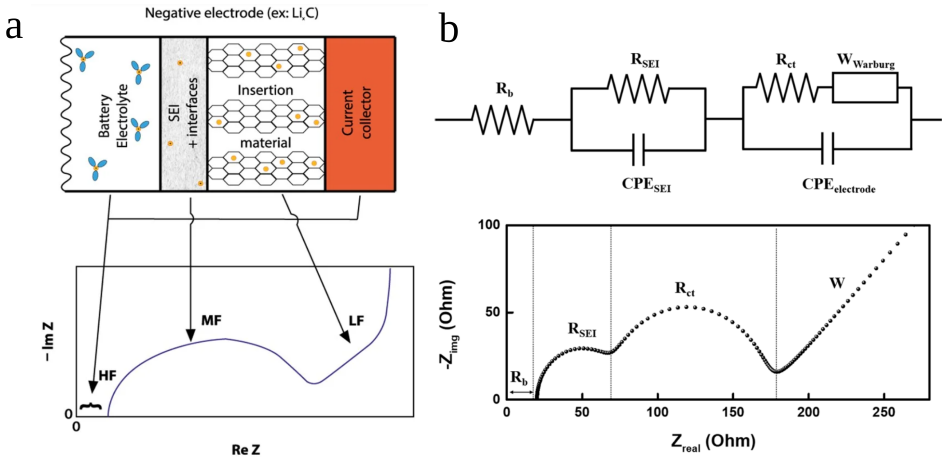


Figure 2.5: a) Schematic depiction of a representative electrochemical impedance spectrum (EIS) for a battery material in the Nyquist plot format, adapted from [77]. **b)** Illustration of an equivalent electrical circuit model commonly used to simulate the impedance response of battery materials, along with the corresponding Nyquist plot of the simulated impedance spectrum, adapted from [78].

The acquired impedance spectra are typically interpreted using equivalent circuit models (see Figure 2.5 b), in which the electrochemical behavior of the system is represented by a combination of resistive, capacitive, and, in some cases, inductive elements. These circuit elements are used to simulate various physical and interfacial processes occurring within

the electrochemical cell. For a comprehensive discussion of impedance modeling and interpretation, the reader is referred to [76], which also forms the basis for the methodological approach adopted in this work.

In the present study, Potentiostatic Electrochemical Impedance Spectroscopy (PEIS) was performed using a small perturbation amplitude of 10 mV, applied over a frequency range spanning from 200 kHz to 1 mHz. To ensure measurement reproducibility and a well-defined electrochemical state, each cell was allowed to equilibrate at its OCV for several hours prior to the impedance measurement. Additionally, a second PEIS measurement was conducted post-analysis to verify system stability and repeatability.

2.4 Electrochemical Setup

All electrochemical measurements were conducted using a multi-channel VMP3 [79], a VSP potentiostat/galvanostat [80], and a Battery Cycler System (BCS) [81], all manufactured by BioLogic GmbH. The VMP3 system offers two operational modes for performing Electrochemical Impedance Spectroscopy (EIS). Both the VMP3 and VSP instruments are equipped with three terminals for potential sensing and two terminals for current application, enabling accurate control and measurement of electrochemical responses. The experiments were controlled using EC-Lab software [82], also provided by BioLogic, which allows for the customization of all electrochemical techniques applied in this study, including cyclic voltammetry (CV), chronoamperometry (CA), galvanostatic cycling with potential limitation (GCPL), and EIS. Once configured, the software performs measurements autonomously according to the predefined protocols. To ensure electrochemical equilibrium prior to measurement, a 12-hour open-circuit voltage (OCV) stabilization period was implemented before each experiment. All measurements were carried out in a controlled laboratory environment maintained at a temperature of $25 \pm 1\,^{\circ}\mathrm{C}$, with the VSP, VMP3, and BCS systems set in the same thermally regulated space.

2.4.1 Electrode Preparation

In this study, electrodes were prepared using distinct protocols tailored to the requirements of anode and cathode materials. While the general procedure for EIS measurements closely followed the respective preparation methods for each electrode type, the diameter of the current collectors was uniformly adjusted to 18 mm to ensure consistency across EIS experiments. The reproducibility and reliability of the electrochemical data are strongly

influenced by the quality of the electrodes, which in turn depends on several critical parameters: weighing accuracy, homogeneity of the electrode slurry during mixing, uniformity in coating onto the current collectors, and mass loading consistency. Given that these steps were conducted manually, precise control over these variables was inherently limited. Based on repeated trials and comparative measurements, the typical electrochemical measurement uncertainty due to electrode preparation variability was estimated to lie between 5 % and 10 %, which is within the expected range for laboratory-scale experiments of this nature.

Cathode Material

The fabrication of cathode electrodes was performed in accordance with the group's established internal standard protocol [83]. Initially, the active material (AM), conductive carbon black (CB; Super C65, Timcal), and polyvinylidene fluoride (PVDF; Solvay Plastics) binder were accurately weighed in a mass ratio of 50:40:10 wt% (AM:CB:PVDF). In the first step, PVDF was dissolved in N-methyl-2-pyrrolidone (NMP) under continuous stirring using a magnetic stirrer and stir bar. Subsequently, the carbon black and active material were added to the solution, and the resulting dispersion was stirred for an additional 24 h to ensure homogeneity. To adjust the viscosity of the slurry and enhance its adhesion properties, partial evaporation of NMP was carried out in a vacuum drying oven (65 °C, 12 mbar). Once an appropriate consistency was achieved, the slurry was applied manually using a spatula onto a aluminum mesh current collector ($\varnothing = 10$ mm for CV and GCPL measurements; $\varnothing = 18$ mm for PEIS), with the following specifications: wire diameter = 0.1 mm, open area = 27 %, and thickness = 0.25 mm. The coated electrodes were dried in a vacuum oven for 24 h, followed by mechanical compression using a hydraulic press at 10 MPa to improve electrode density and adhesion. Finally, the electrodes subjected to an additional drying step before being transferred into an argon-filled glovebox ($O_2 < 1$ ppm, $H_2O < 1$ ppm) for subsequent electrochemical cell assembly.

Anode Material

Anode fabrication was performed exclusively under argon atmosphere in a glovebox ($O_2 < 1$ ppm, $H_2O < 1$ ppm) to prevent degradation of the air-sensitive hybrid organic inorganic perovskite materials. The preparation protocol was adapted based on methodologies similar to [83]. The active material (AM), Super C65 carbon black (CB; Super C65, Timcal), and polyvinylidene fluoride (PVDF; Solvay Plastics) binder were weighed in a mass ratio of 60:30:10 wt% (AM:CB:PVDF). These components were dispersed in N-

methyl-2-pyrrolidone (NMP) and mixed for 2 h using a Fisherbrand Model 120 high-shear disperser, ensuring a uniform and well-integrated slurry. Following mixing, the NMP was evaporated under vacuum conditions until a paste-like consistency was achieved. The resulting slurry was then manually applied using a spatula onto mesh-type copper current collectors with a diameter of $\varnothing = 10\,\text{mm}$ (for CV and GCPL measurements) or $\varnothing = 18\,\text{mm}$ (for PEIS). For light-induced measurements a light translucient carbon tape (Sigracet 39 AA, 280 µm thickness and 80 % porosity) punch out with a diameter of $\varnothing = 10\,\text{mm}$ was used. The copper mesh used had a wire diameter of 0.115 mm, an open area of 30.3 %, and thickness of 0.25 mm. The coated electrodes were initially dried overnight under vacuum, then mechanically compacted using a hydraulic press (TMAX battery press), and finally subjected to a second drying step. All steps, including weighing, mixing, coating, and pressing, were carried out within the inert atmosphere of the glovebox to preserve the chemical integrity of the anode materials.

2.4.2 Battery Cell Setup

In the following section, the various battery cell configurations employed in this work are described. The majority of the electrochemical measurements were performed using standard CR2032-type coin cells. For light-induced electrochemical measurements, two types of optically accessible cell designs were utilized: the ECC-Opto-10 cell from EL-Cell [84] and a custom-designed windowed coin cell fabricated by KIT Campus Transfer GmbH [85]. Additionally, for PEIS, the PAT cell system from EL-Cell [86] was employed due to its superior electrode alignment and reference electrode placement, allowing for high-resolution impedance measurements.

Coin Cell

For most of the electrochemical measurements, including GCPL and CV, CR2032-type coin cells (with a diameter of $\varnothing = 20\,\text{mm}$, height $= 3.2\,\text{mm}$) were assembled, as schematically illustrated in Figure 2.6. These types of cells are the most commonly used format in battery research due to their convenience and reliability [42]. The cell housing consists of a stainless steel (SS316) negative case with an integrated Teflon seal and a stainless steel (SS316) positive case, which together form an airtight enclosure upon crimping. A stainless steel spring, placed inside the negative case, applies uniform mechanical pressure to ensure stable electrical contact across all internal components. Positioned on the spring is a stainless steel (SS316) spacer, serving as the current collector for the counter electrode. A lithium metal disk (with a diameter of $\varnothing = 10\,\text{mm}$, (TMAX Battery Equipments), purity

$>99.9\,\%$) is placed atop this spacer and serves as the counter/reference electrode. Next, two layers of separator (Whatman GF/D, with a diameter of $\varnothing = 16\,\mathrm{mm}$) are added, each saturated with $65\,\mu\mathrm{L}$ of the electrolyte solution (see relevant Section 2.4.3 for electrolyte composition). The final internal component is the working electrode, consisting of a net-like current collector (Al, Cu or Carbon tape with a diameter of $\varnothing = 10\,\mathrm{mm}$) coated with the active cathode or anode material. The assembled components are hermetically sealed using a coin cell crimper to complete the button cell fabrication. For further procedural details and assembly techniques, refer to the standard protocol outlined in [87].

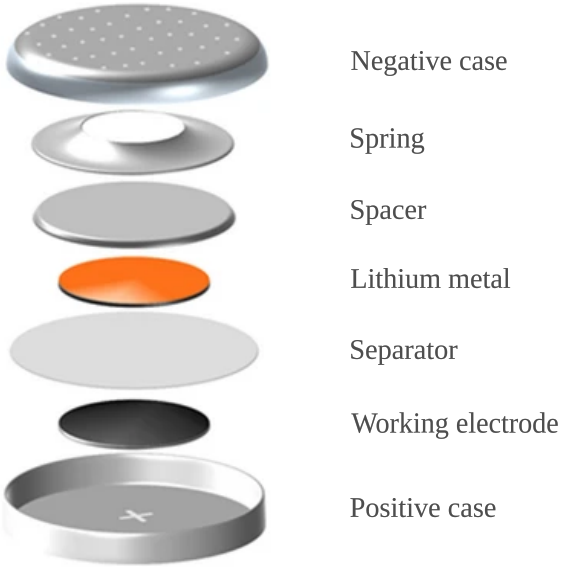


Figure 2.6: Schematic representation of a typical coin cell and its components, adapted from [88].

ECC-Opto-10

Light-induced electrochemical measurements were conducted using the ECC-Opto-10 optical electrochemical cell (EL-Cell, [84]) configured in a face-to-face setup. A schematic representation of the cell assembly is presented in Figure 2.7. The cell is structurally enclosed by a stainless steel lid featuring a transparent sapphire glass window (with a diameter of $\varnothing = 22\,\mathrm{mm}$, 3 mm thickness; component 1) and a stainless steel cell base (component 12). To ensure airtight sealing, a polyethylene (PE) window seal (component 2) is positioned beneath the window. Below this, a stainless steel contact disk with a hole (with a diameter of $\varnothing = 4\,\mathrm{mm}$; component 3) allows for directed illumination of the underlying components. The working electrode under investigation (with a diameter of $\varnothing = 10\,\mathrm{mm}$; component 4) is placed directly beneath the contact disk, followed by a separator layer (Whatman GF/D, with a diameter of $\varnothing = 10\,\mathrm{mm}$; component 5) and the lithium metal

reference electrode (component 6). The lower part of the assembly includes the piston (component 7), a stainless steel contact ring (component 8), the inner sleeve (component 9), the window thrust ring (component 10), and the window flange (component 11), all contributing to mechanical stability and electrical contact.

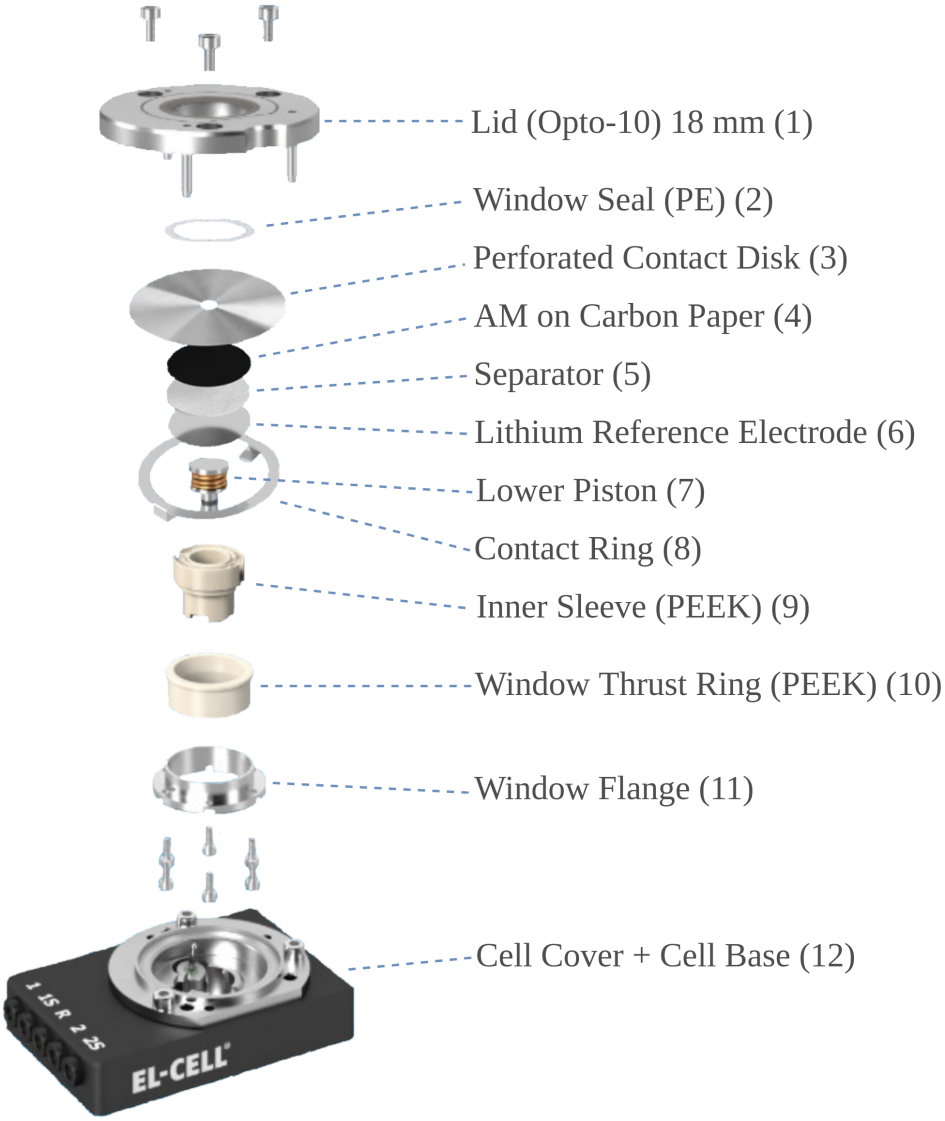


Figure 2.7: Schematic representation of the ECC-Opto-10 cell (EL-Cell) utilized for light-induced electrochemical measurements, highlighting its key components, adapted from [84].

Windowed Coin Cell

For light-induced test measurements, custom designed coin cells were fabricated by KIT Campus Transfer GmbH to enable light irradiation onto the electrode of the cell [85]. The

structural design was identical to the standard CR2032-type coin cell described previously (see Figure 2.6), with the exception of a $\varnothing = 5\,\mathrm{mm}$ hole drilled into the stainless steel cell cap. This aperture allowed for controlled illumination of the electrode area. To maintain the cell's airtightness and ensure proper sealing, the hole was subsequently EPOXY-sealed with Kapton window. A photograph of the modified windowed coin cell is shown in Figure 2.8.



Figure 2.8: Photograph of a coin cell with an optical window, adapted from KIT Campus Transfer GmbH [85].

PAT Cell

Electrochemical impedance spectroscopy (EIS) measurements were conducted using a PAT (pouch-type analytical test) cell from EL-Cell, schematically depicted in Figure 2.9. The cell architecture comprises a two-part stainless steel housing (components 1 and 9), polyethylene sealing elements (2), and upper and lower stainless steel plungers (3 and 8). The configuration includes a lithium metal counter electrode (with a diameter of $\varnothing = 18\,\mathrm{mm}$, component 4), the working electrode (with a diameter of $\varnothing = 18\,\mathrm{mm}$, component 7), and the PAT core (component 6), which serves as the electrochemical interface. At the core of the assembly is the PAT core module, illustrated on the right in Figure 2.9. This module features an outer retaining ring with a circular inner shoulder (with a diameter of $\varnothing = 21.6\,\mathrm{mm}$) designed to accommodate both the reed contact and the lithium reference electrode. The separator (with a diameter of $\varnothing = 21.6\,\mathrm{mm}$) is placed atop this assembly and secured by an inner clamping ring, ensuring precise electrode alignment. This design offers a symmetric alignment of the working and counter electrodes and positions the reference electrode in close proximity to the working electrode, thereby minimizing

measurement artifacts. This spatial configuration significantly enhances the data quality and reproducibility of impedance measurements. For a detailed analysis of the influence of cell geometry on impedance spectra and associated effects, refer to [89].

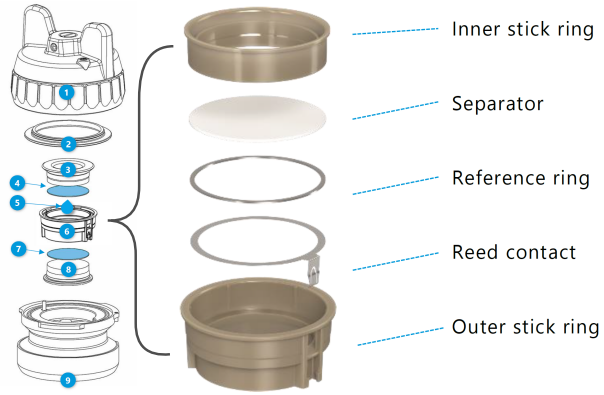


Figure 2.9: Schematic representation of a PAT (pouch-type analytical test) cell and its components, adapted from [90].

2.4.3 Electrolytes

This section provides an overview of the physical and chemical properties and considerations related to the electrolytes used in this study. Understanding these properties is essential because the electrolyte significantly influences battery performance, safety, and longevity [41]. In lithium-ion batteries, the electrolyte facilitates the transport of lithium ions between the electrodes. An ideal electrolyte must exhibit high ionic conductivity to support efficient ion transport while maintaining negligible electronic conductivity to prevent internal short circuits. Furthermore, suitable electrolytes are characterized by chemical and thermal stability, minimal reactivity with solvents and other cell components (e.g., current collectors, separators), and good salt dissociation behavior to ensure a high concentration of free charge carriers.

Currently, lithium hexafluorophosphate ($LiPF_6$) is the most widely used lithium salt in commercial lithium-ion battery electrolytes. Although $LiPF_6$ does not exhibit peak performance in any single property, it offers a balanced compromise across key criteria, including ionic conductivity, stability, and solubility. In contrast, other lithium salts often exhibit trade-offs: improvements in one property tend to result in compromises in others. A notable advantage of $LiPF_6$ is its ability to form a passivating layer on aluminum current collectors, thereby preventing further corrosion or degradation [91]. However, $LiPF_6$ is highly sensitive to moisture. Even trace amounts of water lead to its decomposition, producing hydrofluoric acid (HF), which is corrosive and detrimental to cell performance [92].

The presence of water also significantly decreases thermal stability: under inert conditions, decomposition begins at approximately 100 °C.

As an alternative, this work also investigated lithium bis(trifluoromethylsulfonyl)imide (LiTFSI). Compared to $LiPF_6$, LiTFSI exhibits superior thermal and chemical stability, as well as higher ionic conductivity [93]. A key limitation of LiTFSI is its corrosive effect on aluminum current collectors, a common component in lithium-ion batteries [94]. Studies have shown that in 1 M LiTFSI-based electrolytes, aluminum corrosion initiates around 4.6 V vs. Li/Li^+, leading to pitting and degradation of the current collector. This corrosion is exacerbated by the $TFSI^-$ anion, which can form soluble $Al(TFSI)_3$ complexes, undermining the protective oxide layer on aluminum [95, 96].

To prepare the electrolyte, lithium salts are dissolved in organic solvents. In this work, the solvents used were ethylene carbonate (EC), dimethyl carbonate (DMC), 1,2-dimethoxyethane (DME), and 1,3-dioxolane (DOL), which were mixed in a 1:1 volume ratio. It is important that at least one of the solvents has a high dielectric constant to ensure sufficient dissociation of the lithium salts. Additionally, good solvents must be both chemically and thermally stable, particularly inert toward other cell components. Stability against oxidation is a key factor in improving the safety of lithium-ion batteries. Furthermore, low viscosity facilitates faster transport of lithium ions within the electrolyte system [30, 91]. Carbonate-based solvents such as EC, PC, and DEC are well-known for their high dielectric constants, which enable efficient salt dissociation, but they also exhibit relatively high viscosities, which can impede ion mobility [30, 91]. In contrast, ether-based solvent mixtures, particularly DOL and DME in combination with the salt LiTFSI, have shown excellent performance in forming stable passivation layers (solid electrolyte interphase, SEI) on the electrodes, especially in lithium-metal and lithium-sulfur battery systems [97].

To investigate the effects of lithium insertion into a material, a stable interface between the material and the electrolyte is essential [91, 98]. Previous approaches, particularly those adapted from battery technologies, have commonly employed conventional liquid electrolytes composed of lithium salts dissolved in organic aprotic solvents [40, 91]. However, such polar solvents can degrade specific materials such as hybrid organic inorganic perovskites at the electrolyte interface. Increasing the electrolyte concentration to high molarities (≈ 5 M) has been shown to mitigate this issue to some extent, enabling broader electrochemical measurements [99]. Nonetheless, for detailed and accurate analysis of these specific materials, a more inherently stable interface is required. Therefore, a polymer-based solid-state electrolyte, comprising LiTFSI in polyethylene oxide (PEO), is employed.

The polyethylene oxide (PEO) was first dried under vacuum at 80 °C, while the LiTFSI salt which was used was stored in an argon filled glovebox. Subsequently, 1.26 g of PEO, 816 mg of LiTFSI, and 11 mL of acetonitrile were combined under an argon atmosphere glovebox ($O_2 < 1$ ppm, $H_2O < 1$ ppm) and stirred for 24 h at 400 rpm using a magnetic stirrer resulting in 2.54 M LiTFSI in PEO. To eliminate air bubbles, the solution was degassed by transferring it in an open container through the small antechamber of the argon glovebox three times. The degassed solution was then cast onto a parafilm sheet using a doctor blade coater from TMAX Battery Equipments at room temperature, with a set film thickness of 400 µm. The resulting film was dried on a hotplate at 70 °C for minimum 48 h under argon atmosphere. This synthesis protocol is adapted from reference [100].

2.4.4 Light source

For the light-induced battery setup LMO and $MAPbBr_3$ composite electrodes were prepared similar to the coin cell configuration. However in this setup carbon paper (Sigracet 39 AA) was used as a light-transparent current collector. The ECC-OPTO-10-cell (EL-Cell) is equipped with a sapphire glass window (with a diameter of $\varnothing = 22$ mm, 3 mm thickness) and was arranged in a face-to-face electrode configuration (see 2.4.2). In contrast to the coin cell preparation only a single layer of separator was used along with a correspondingly smaller volume (50 µL) of electrolyte. A high power tunable xenon lamp (TLS120XeLamp) was utilized as the light source, positioned at a distance of (25 mm) perpendicular to the cell window ensuring that the illuminated region of the electrode was fully exposed to the light. Additionally both a UV filter (Edmund N-WG320) and an IR filter (Edmund EDSP800) were applied to minimize unwanted heating. Measurements were conducted at an energy density of $\approx 100\,\mathrm{mW\,cm^{-2}}$ across a wavelength range of 320 – 800 nm. The temperature of the cell was monitored using an IR thermometer (Fluke 62 MAX [101]), directed at the window of the cell and validated by a reference measurement. Upon activation of the light source the temperature inside the cell increased by 6 °C.

2.4.5 Carbon Black Reference Measurement

An essential component of the working electrode is conductive carbon black (CB), which is commonly incorporated into the composite alongside the active material to enhance the overall electronic conductivity [102]. This improved conductivity facilitates efficient charge transport, thereby ensuring that a maximal number of electrochemically active sites are electrically accessible. In addition to its conductive function, CB is also capable of

lithium-ion intercalation, thereby contributing to the overall specific capacity observed in galvanostatic charge–discharge profiles (GCPLs) as well as to the redox activity in cyclic voltammetry (CV) measurements, typically within the potential window of 0 V to 1.5 V.

To accurately distinguish the electrochemical features attributable to CB from those of the active material in subsequent measurements, a reference measurement of CB was conducted. For this purpose, working electrodes were prepared with a mass ratio of 90:10 wt% CB to polyvinylidene fluoride (PVDF), and cast onto copper current collectors (refer to Section 2.4.1 for fabrication details). These electrodes were assembled into coin cells for electrochemical characterization.

Figure 2.10 a) presents the CV results for these reference CB electrodes. The figure displays the first, second, fifth, and tenth (dis)charge scans, depicted in black, red, blue, and green, respectively, recorded at a scan rate of $0.1\,\mathrm{mV\,s^{-1}}$. During the first discharge (black curve), two distinct reduction peaks are observed at 0.2 V and 0.01 V, denoted as R_{SEI} and R_{CB2}, respectively. In the subsequent charge scan, oxidation peaks appear at 0.2 V (O_{CB2}) and 0.96 V (O_{CB1}). In the second, fifth and tenth discharge scans (red, blue and green curves), the peak at R_{CB2} persists, and a the reduction feature emerges at 0.87 V (R_{CB1}). The corresponding charge scans retain the same oxidation features observed during the initial cycle. The disappearance of the R_{SEI} peak after the first cycle indicates an irreversible process, attributed to the formation of the solid electrolyte interphase (SEI) layer [103]. The remaining peaks, identified as redox pairs R_{CB1}/O_{CB1} and R_{CB2}/O_{CB2}, are ascribed to the reversible intercalation and deintercalation of Li^+ ions into the carbon black matrix [104].

Figure 2.10 b) displays the results of a GCPL measurement, showing the evolution of specific capacity over the first 200 charge/discharge cycles at a current density of $100\,\mathrm{mA\,g^{-1}}$. The initial discharge capacity of $438\,\mathrm{mA\,h\,g^{-1}}$ rapidly decreases following the first cycle and stabilizes at approximately $230\,\mathrm{mA\,h\,g^{-1}}$. Interestingly, a gradual increase in capacity is observed with extended cycling, rising from approximately $230\,\mathrm{mA\,h\,g^{-1}}$ at cycle 10 to around $280\,\mathrm{mA\,h\,g^{-1}}$ by cycle 200. The gradual increase in specific capacity can be attributed to two primary mechanisms. First, progressive electrolyte wetting likely contributes to this behavior, as the porous CB structure may not be fully infiltrated by the electrolyte during initial cycles. Over time, improved penetration enables more uniform ionic access to internal surfaces, thereby activating previously electrochemically inactive regions [105, 106]. Second, electrochemical activation of the carbon matrix may occur, wherein repeated cycling induces structural rearrangements or exposes new lithium storage sites within the disordered or amorphous domains of CB [107]. Together, these effects

enhance the electrochemical utilization of CB and contribute to the observed increase in reversible capacity.

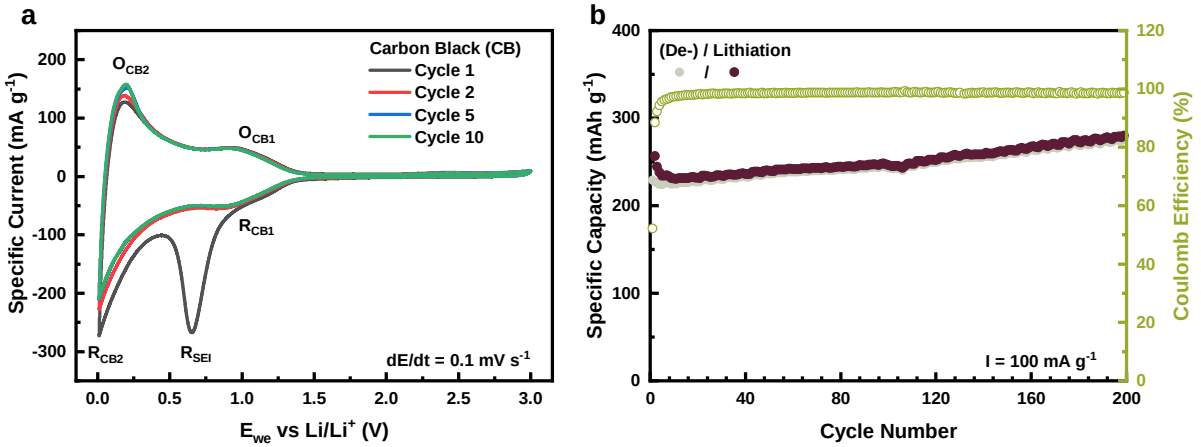


Figure 2.10: Cyclic voltammetry (CV) and galvanostatic charge–discharge (GCPL) measurements of carbon black (CB). **a)** CV curves recorded at a scan rate of $0.1\,\mathrm{mV\,s^{-1}}$ for cycles 1, 2, 5, and 10, shown in black, red, blue, and green, respectively. Distinct reduction and oxidation peaks are labeled R and O. **b)** Specific charge and discharge capacities obtained from GCPL measurements at a constant current of $100\,\mathrm{mA\,g^{-1}}$ within a voltage window of 0.01 V to 3.00 V.

3 Triphenylamine-Based Cathode Material

Triphenylamine (TPA)-based cathode materials have gained considerable attention in the development of organic lithium-ion batteries (LIBs) due to their high electrochemical tunability and redox-active nitrogen center. Their structural versatility allows for diverse functionalization, enabling the design of materials with enhanced stability and conductivity. Within this context, TPA derivatives have emerged as promising candidates for high-performance organic cathodes. A detailed connection of TPA-based materials to the broader field of organic electrode research is discussed in the following Section. Building upon this framework, this chapter investigates a spirofluorene-bridged N-heterotriangulene polymer (FTN-Pol), designed to combine the electronic benefits of TPA with a robust conjugated polymer backbone.

3.1 Organic Cathode Materials: State of the Art

The increasing global energy demand presents significant challenges for efficient energy storage, particularly in mobile applications. Although Li-ion batteries with inorganic active materials are widely used for their high power density, they lack flexibility, safety, and environmental sustainability [42]. To meet evolving requirements, alternative solutions based on abundant, non-toxic, and renewable materials, such as organic polymers, are being explored. These polymers benefit from the vast variety of redox-active organic compounds that enable reversible energy storage through simple redox reactions. Unlike intercalation-based inorganic materials, organic polymers offer fast charge/discharge rates and long cycle life [108]. Their redox properties can be tailored by chemical modification, allowing for customizable battery voltages and the development of both cathode and anode materials. Additionally, the flexibility of polymer films and the scalability of polymer manufacturing techniques could make them ideal for modern, flexible electronics [109].

Although most redox-active polymers are still derived from fossil fuels, research into renewable synthesis routes is progressing [110]. Historically, interest in organic batteries began with the discovery of conductive conjugated polymers in 1977 [111], leading to early commercial attempts with materials like polypyrrole and polyaniline [112]. However,

these systems suffered from issues like variable voltage due to the dependence on doping levels, resulting in poor charging behavior and short lifespans [113]. Modern approaches aim to resolve these challenges using polymers with isolated redox-active units on insulating backbones, which provide stable voltages and improved cycle life while retaining the environmental and structural advantages of organic materials [108]. For a material to be used in batteries, it must undergo a reversible redox reaction. Organic compounds offer structural diversity and tunable redox properties, enabling higher capacities and adjustable voltages, though synthesis complexity and cost must be balanced. A key challenge is solubility into the electrolyte, which can cause self-discharge. This can be mitigated by embedding redox-active units into polymers. Organic materials are classified as p-type, n-type, or b-type, based on their redox behavior.They can serve as either cathodes or anodes depending on potential. n-type materials, when neutral, are meant to receive electrons and become negatively charged (n^-) during the redox process, while p-type materials, when neutral, are meant to release electrons and become positively charged (p^+) during the redox process. Their redox mechanisms differ significantly from inorganic materials, with kinetics and performance varying based on molecular structure and reaction type.

3.1.1 Conjugated Polymers

Conjugated polymers have been studied for battery applications since the 1980s due to their intrinsic conductivity and π-conjugated structures, which enable charge delocalization [114]. These polymers feature alternating single and double bonds along their backbone, allowing electrons to move more freely and thus providing semiconducting or conducting properties that are advantageous for energy storage. Their electrical conductivity is highly dependent on the doping level that modulates the charge carrier density within the polymer backbone. However, practical limitations such as sloping voltage profiles, restricted doping capacities, and structural degradation at high charge densities hinder their broader application [108, 115, 116]. Despite early commercial failures, research continues due to their potential in flexible, lightweight, and high-power devices like supercapacitors and paper-based batteries [117].

Poly(pyrrole) (PPy)

Poly(pyrrole) (PPy) is among the most investigated conjugated polymers for use in electrochemical energy storage systems. Traditionally used as a cathode material, PPy has also demonstrated functionality as an anode, depending on cell configuration [118]. Innovative applications include a “paper-based” battery architecture, where PPy is deposited

on cellulose nanofibers to yield a flexible electrode capable of both battery and supercapacitor behavior [117]. In aqueous Li-ion systems, PPy has achieved improved cycling stability and moderate capacities as anode ($47\,\mathrm{mA\,h\,g^{-1}}$) at an average operating voltage of 0.85 V [119, 120]. Free-standing PPy films further enhance mechanical stability and enable stretchable devices for biomedical use. While some PPy composites are better suited for supercapacitors, significant gains in battery performance have been realized by doping with redox-active species such as $Fe(CN)_6{}^{4-}$, leading to improved capacity and rate capability [121]. Covalent anchoring of ferrocene to the PPy backbone also flattens discharge profiles and more than triples the specific capacity [122].

Poly(thiophene) (PT)

Poly(thiophene) (PT) and its derivatives represent a classes of conducting polymers investigated for battery electrodes, with reports dating back to 1983 [123]. Substituted thiophenes have shown promising electrochemical performance, achieving capacities up to $95\,\mathrm{mA\,h\,g^{-1}}$ when used as anodes [124]. More recently, a solvent-free synthesis method utilizing $FeCl_3$ has yielded capacities as high as $400\,\mathrm{mA\,h\,g^{-1}}$ through the formation of thioether cations [125]. Efforts to enhance functionality through the incorporation of redox-active moieties, specific functional groups or parts of a molecule responsible for its chemical reactivity, like TEMPO have had mixed results; while the redox capacity is increased, oxidative degradation of the thiophene backbone can reduce long-term performance [126]. Block copolymers of PT with polyethylene oxide (PEO) offer a complementary approach, enabling the design of ionically and electronically conductive solid polymer electrolytes for potential next-generation solid-state batteries [127].

Poly(aniline) (PANI)

Poly(aniline) (PANI) holds historical significance as one of the first polymers explored for battery applications as investigations already started in the late 1960s [128]. Its redox chemistry is pH-dependent and governed by proton-coupled electron transfer with only the emeraldine salt form being conductive. Modifications to the PANI structure have aimed to enhance capacity and stability. For example, a quinone-functionalized derivative achieved a capacity of $120\,\mathrm{mA\,h\,g^{-1}}$ with good cycling retention [129]. Sulfur-based modifications have produced high initial capacities, up to $980\,\mathrm{mA\,h\,g^{-1}}$, but suffer from rapid degradation [130]. Copolymerization with disulfide or ferrocene units has improved redox diversity and cycling stability. PANI complexes with polyacids, such as poly(2-acrylamido-2-methyl-1-propanesulfonic acid) (PAAMPSA), have demonstrated excellent stability at high voltages

and improved cycling behavior [131, 132]. Additionally, fused-ring derivatives and PANI-derived nitrogen-doped carbons, produced via pyrolysis, have expanded the material's potential, offering high initial capacities, though often at the cost of reversibility [133, 134].

3.1.2 Non-Conjugated Redox-active Polymers

Due to the inherent limitations of conjugated polymers, such as sloping redox potentials and a restricted number of redox-active sites (see in Section 3.1.1), research has increasingly turned toward non-conjugated redox-active polymers over the past decade. These materials typically consist of an insulating polymer backbone functionalized with electroactive groups, which have well-defined redox potentials due to the localized nature of the redox events. In addition to stable organic radicals, various classical electrochemically active moieties have been explored. As these polymers offer tunable redox behavior and structural diversity, they represent a promising alternative to conventional inorganic electrodes [112].

Carbonyl Compounds

Carbonyl-based cathode materials are a prospective class for rechargeable batteries due to their reversible redox activity centered on carbonyl (C=O) groups. These materials include quinones, polyimides, and other aromatic carbonyl compounds that can undergo two-electron redox reactions, providing high theoretical capacities. For example, poly(anthraquinonylsulfide) shows a reversible redox reaction at 2.33 V vs. Li/Li^+, has good cycling stability and specific capacity of $185\,mA\,h\,g^{-1}$ at $50\,mA\,g^{-1}$ [135]. A crosslinked porous polyimide cathode material tested in lithium metal half-cells delivered a high discharge capacity of $160\,mA\,h\,g^{-1}$ at $30\,mA\,g^{-1}$ and retained 77 % of its capacity after 2000 cycles at $150\,mA\,g^{-1}$. [136] Similar to conductive polymers like polyaniline (PANI), polythiophene (PT), and polypyrrole (PPy), carbonyl polymers can be chemically modified to improve conductivity and stability. However, challenges such as poor intrinsic conductivity and dissolution in electrolytes remain. Strategies like copolymerization, grafting onto conductive backbones, and incorporating carbon nanomaterials help address these issues [137, 138]. Quinones are a good option for cathode materials due to high theoretical capacities, redox tunability, and structural versatility. Polyimides offer stability and reversibility but generally lower voltages as well as partial utilization of their redox capacity.

Organosulfur Compounds

Sulfur, abundantly available and largely produced as a waste product from fossil fuel processing, has gained attention as a component in battery electrodes due to its favorable redox chemistry, accessibility, and environmental advantages (small environmental footprint)[139]. While organosulfur molecules suffer from poor stability and solubility, polymer-bound organosulfur compounds offer improved performance [140, 141]. Among these, disulfides and thioethers are the main classes studied. Disulfide polymers store charge via reversible two-electron oxidation of disulfide bonds, however early examples suffered from low cycling stability due to inefficient bond rebonding [142, 143]. Zhang et al. [107] introduced thioether-based polymers as a new class of electroactive materials for batteries. Examples include poly(2-phenyl-1,3-dithiolane) and poly[1,4-di(1,3-dithiolan-2-yl)benzene], which store energy through reversible oxidation to thioether dications.

3.1.3 Triphenylamin-based Cathode Material

In addition to carbonyl- and sulfur-based redox-active materials, various other non-conjugated polymers with functional groups such as triphenylamine (TPA) have also been explored for their charge storage capabilities. Poly(triphenylamine) (PTPA) and its derivatives have emerged as promising redox-active materials for battery electrodes. Yang et al. [144] first demonstrated the use of a highly cross-linked PTPA prepared via oxidative polymerization with ferric chloride $FeCl_3$. This polymer forms porous particles that allow effective ion transfer and electrolyte penetration. It exhibits good conductivity (≈ 1.0 S cm^{-1} when doped) and operates at an average discharge voltage of 3.8 V with a capacity of 91 mA h g^{-1}. After 1000 cycles at a high rate (20C), the material retains 92 % of its original capacity. However, it suffers from a relatively high self-discharge rate of 10 % over two weeks. To improve performance, researchers explored poly[tris(thienylphenyl)amine] derivatives, which feature one thiophene bridge per phenyl ring. These polymers have a similar voltage range 4.2 V to 3.5 V and benefit from dual redox activity: triphenylamine and thiophene moieties contribute capacities of 94 mA h g^{-1} and 35 mA h g^{-1}, respectively. These are reflected in two distinct discharge plateaus and yield 91 % capacity retention after 50 cycles [145]. A more recent development includes poly(4-cyano triphenylamine), which incorporates electron-withdrawing cyano groups to raise the redox potential. This polymer achieves a discharge potential of 3.9 V and a capacity of 80 mA h g^{-1} at 40 mA g^{-1}, maintaining 74 % capacity even when the charge/discharge rate is increased tenfold. Cycling stability also remains high with only minor degradation [146].

Despite the promising charge/discharge performance of PTPA, its electrochemical characterization revealed relatively broad redox half-waves. This behavior can be attributed to the ortho- and para-directing effects of the central nitrogen atom in the TPA moiety, which leads to the formation of a structurally heterogeneous polymer during oxidative polymerization. Such structural inhomogeneity adversely affects the redox properties of the material [144]. To address this issue, various ortho-bridging groups, such as carbonyl, dimethylmethylene, or ether linkages, have been introduced into the TPA framework [147–149]. These modifications enforce planarity in the otherwise propeller-shaped TPA structure, yielding a class of compounds known as N-heterotriangulenes (N-HTAs). The planar configuration of N-HTAs enables enhanced delocalization of spin and charge across the π-conjugated system, stabilizing the nitrogen-centered radical cations [150]. In 2021, Wang et al. [151] reported the first cathode active polymer derived from carbonyl-bridged TPAs, designated TN-(CO)-Pol. This material was synthesized via a carbonyl-based condensation polymerization facilitated by Lawesson's reagent. The incorporation of rigid carbonyl units resulted in a two-dimensional (2D) polymer with a layered nanosheet morphology. TN-(CO)-Pol exhibited a specific capacity of $340\,\mathrm{mA\,h\,g^{-1}}$ and maintained 95 % of its capacity over 200 cycles. In parallel, Müllen [152] and co-workers synthesized a dimethylmethylene-bridged N-HTA polymer (TN-(Me)-Pol) via Yamamoto coupling. This polymer showed an amorphous morphology and excellent air stability, supporting its application as a robust p-type semiconductor in organic field-effect transistors (OFETs). However, TN-(Me)-Pol was not suitable as a cathode material, due to its solubility in common organic solvents and the presence of poorly defined and partially irreversible redox processes. To date, no additional studies have been reported on the application of N-HTA-based polymers as cathode materials in lithium-ion batteries.

FTN-Pol

Kivala and colleagues recently introduced a novel class of N-heterotriangulenes (N-HTAs) featuring sterically encumbered C(sp^3)-based spirofluorene bridging units, termed FTNs. An Overview of reported redox-active polymers derived from triphenylamine (TPA) and FTN-Pol, which is investigated in this thesis can be seen in Figure 3.1. The combination of steric shielding and conformational restriction around the nitrogen center in these structures significantly stabilizes the corresponding radical cations, which were successfully isolated and structurally confirmed via X-ray crystallography [153]. Furthermore, the high conformational rigidity of the FTN framework induces unique aggregation behavior, resulting in diverse morphologies accompanied by substantial variations in photophysical properties [154].

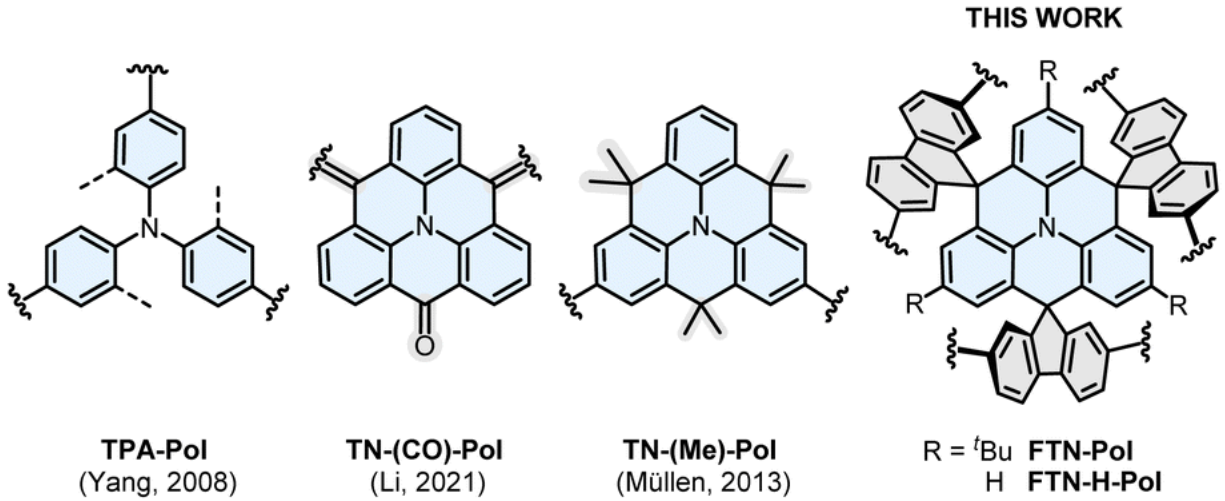


Figure 3.1: Summary of reported redox-active polymers based on triphenylamine (TPA) and nitrogen-centered heterotriangulenes (N-HTAs), including molecular fragments of the spiro-bridged N-HTA-based polymer FTN-Pol synthesized by Kivala and colleagues, which is studied in this thesis. Adapted from [155].

The monomers FTN-Br_6 and FTN-H-Br_6 were synthesized via a multistep route involving lithium–bromine exchange, cyclization, and selective dealkylation, yielding up to 90 % for key steps. Subsequent Yamamoto polymerization afforded the insoluble polymers FTN-Pol and FTN-H-Pol in 58 % and 55 % yield, respectively, which were purified by Soxhlet extraction and are stable in common organic solvents. More details can be found in Jocic et al. [155].

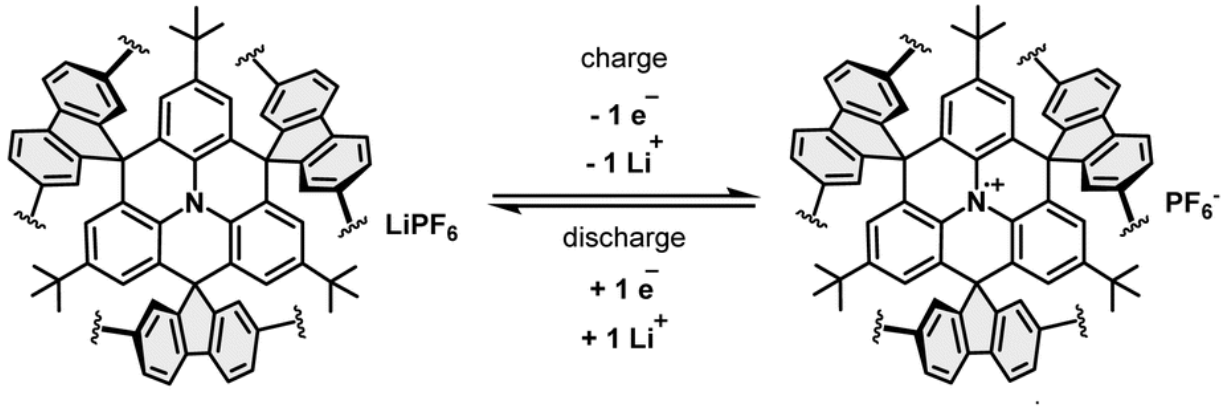


Figure 3.2: Schematic representation of the proposed redox reaction mechanism of FTN-Pol in lithium ion half-cell with electrolyte $LiPF_6$ solution. The mechanism is proposed based on initial cyclic voltammetry (CV) measurements in solution. Adapted from [155].

Figure 3.2 illustrates the proposed electrochemical redox mechanism of FTN-Pol during cycling as a cathode material in lithium-ion batteries. Each monomer unit of FTN-Pol contains a nitrogen-centered redox-active site capable of undergoing a one-electron oxidation. Upon oxidation, the resulting positively charged polymer is stabilized by PF_6^-

counterions from the electrolyte. During the subsequent reduction, lithium ions migrate toward the PF_6^- anions to restore charge neutrality. This single redox process theoretically corresponds to a specific charge capacity of $29.97\,\mathrm{mA\,h\,g^{-1}}$, assuming one electron is transferred per N-HTA unit ($z = 1$).

FTN-Pol + Sulfur

Another FTN derivative examined in this study consists of FTN moieties linked by sulfur chains composed of approximately ten sulfur atoms (corresponding to 15 sulfur atoms per formula unit). This molecular design aims to introduce additional redox-active centers to enhance the inherently low theoretical capacity of approximately $30\,\mathrm{mA\,h\,g^{-1}}$. The polymer is synthesized such that individual FTN monomers are interconnected via sulfur linkages at the R substitution sites.

Lithium–sulfur (Li–S) batteries have attracted considerable attention as promising candidates for next-generation energy storage systems, primarily due to their high theoretical energy density of approximately $2500\,\mathrm{Wh\ kg^{-1}}$. This high energy density arises from the substantial specific capacities of both the sulfur cathode ($1672\,\mathrm{mA\,h\,g^{-1}}$) and the lithium-metal anode ($3860\,\mathrm{mA\,h\,g^{-1}}$) [156]. In addition to their electrochemical advantages, sulfur is naturally abundant, cost-effective, and environmentally friendly. Compared to lithium–air batteries, which face fundamental limitations and low practical energy densities, Li–S batteries are regarded as more viable for practical application [157]. During discharge, Li^+ ions are released from the lithium-metal anode and migrate through the electrolyte toward the sulfur cathode, while electrons travel through the external circuit. This electrochemical process results in the formation of lithium sulfide (Li_2) as the final discharge product at the cathode [158] (see Fig. 3.3). Nonetheless, several critical challenges impede their commercialization. These include the intrinsically low electronic and ionic conductivities of sulfur and its discharge product (Li_2S), the dissolution and migration of intermediate lithium polysulfides leading to material loss and poor coulomb efficiency, and the degradation of the lithium-metal anode due to surface passivation and the formation of an unstable solid electrolyte interphase (SEI) [159]. Addressing these issues is mandatory for enabling the long-term stability and practical deployment of Li–S battery systems. To address some of the aforementioned challenges, the sulfur chains were incorporated into a polymer matrix. Based on the Equation 2.3, and using a molar mass of $M_W(S) = 481.0\,\mathrm{g\,mol^{-1}}$ and $M_W(\text{FTN-Pol}) = 894.2\,\mathrm{g\,mol^{-1}}$, with redox site quantities of $z(S) = 30$ and $z(\text{FTN-Pol}) = 1$, the resulting composite polymer is expected to exhibit a theoretical capacity of approximately $604\,\mathrm{mA\,h\,g^{-1}}$.

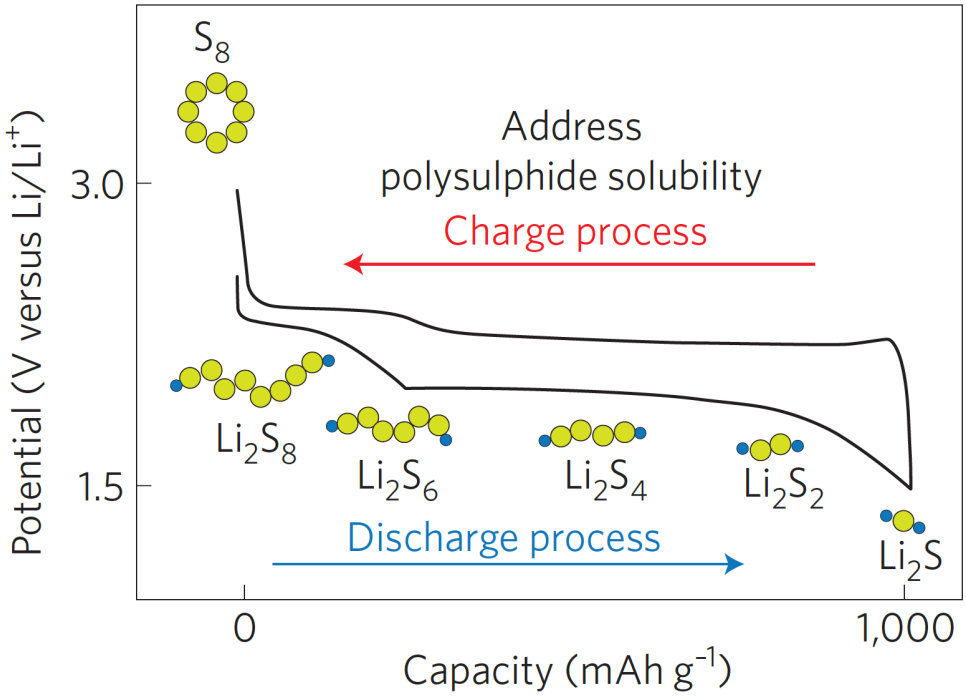


Figure 3.3: Measured potential curves for Li-S-batteries and schematic representation of the proposed charge/discharge reaction mechanism of sulfur in lithium ion half-cell. Adapted from [160].

FTN-Pol + Terthiophene

Another idea was to embed the sulfur atoms in a more rigid structure before linking them to the FTN-Pol. For this purpose, terthiophene ($[C_4H_3S]_2C_4H_2S$) was chosen which added 3 sulfur oxidation centers. Similar to the sulfur chains, this molecule is also centered at the R-site between the FTN monomers similar to the aforementioned sulfur chains. The reaction mechanism would be expected to be similar to the sulfur chains and its theoretical capacity is $345\,\mathrm{mA\,h\,g^{-1}}$ with $M_W(\text{Terthiophene}) = 372.4\,\mathrm{g\,mol^{-1}}$ and $M_W(\text{FTN-Pol}) = 894.2\,\mathrm{g\,mol^{-1}}$, with redox site quantities of $z(\text{Terthiophene}) = 13.5$ and $z(\text{FTN-Pol}) = 1$.

3.2 Spirofluorene Bridged N-heterotriangulenes Polymer

The following chapter has been partially published in [155].

3.2.1 Physical Characterization

The following physical characterization data were obtained by A. Jocic. They are presented here to support the interpretation of the samples investigated in this thesis; a detailed discussion can be found in [155].

The influence of polymerization on the photoluminescence (PL) properties of FTN-based systems was investigated by A. Jocic using emission spectroscopy, with comparison to the molecularly dissolved model compound FTN. FTN exhibits a sharp emission at 377 nm (3.29 eV) with a shoulder at 368 nm and a spectral tail extending to 500 nm. In contrast, FTN-Pol, when dispersed in tetrahydrofuran (THF), displays a bathochromically shifted and significantly broadened emission centered at 490 nm (2.53 eV), extending to 750 nm. Solvent-dependent emission studies reveal broad dual-emission features (≈ 430 nm and ≈ 500 nm) across various solvents, with increased solvent polarity inducing red-shifts. Photoluminescence quantum yields (PLQYs) range from 0.01 to 0.03, consistent with that of FTN ($\Phi = 0.04$), with lower PLQYs generally observed in more polar solvents.

Further characterization by A. Jocic included compositional analysis via elemental combustion, which confirms the chemical identity of FTN-Pol and FTN-H-Pol. ToF-SIMS analysis rules out residual nickel content. PXRD data indicate that both polymers are amorphous. Raman and FT-IR spectroscopy confirm the complete consumption of bromofunctional groups, evidenced by the absence of characteristic C–Br stretching vibrations ($\approx 1058 - 1060\,\mathrm{cm}^{-1}$) and the presence of C–H fluorenyl modes ($\approx 1020\,\mathrm{cm}^{-1}$), aligning with dehalogenated model compounds. Thermogravimetric analysis demonstrates high thermal stability, with decomposition onsets at $\approx 500\,^{\circ}\mathrm{C}$ for FTN-Pol and $\approx 700\,^{\circ}\mathrm{C}$ for FTN-H-Pol. Minor weight losses below 400 °C are attributed to desorption of moisture and gases, while mass loss between $400 - 600\,^{\circ}\mathrm{C}$ likely corresponds to cleavage of tert-butyl side groups.

Morphological and porosity data provided by A. Jocic further describe the structure of the polymers. SEM analysis reveals amorphous globular particles with coralloid surfaces forming larger agglomerates. Nitrogen sorption measurements at 77 K show type I isotherms with hysteresis, indicating microporous networks undergoing elastic deforma-

tion. BET surface areas are high, with FTN-Pol and FTN-H-Pol exhibiting values of 690 and 682 $m^2 g^{-1}$, respectively. NL-DFT analysis shows that FTN-Pol contains micropores (0.70 nm) and mesopores (0.84 nm and 1.21 nm). FTN-H-Pol features slightly larger and more broadly distributed pores (0.78 – 3.08 nm), which is attributed to the absence of tert-butyl substituents in the monomer. These bulky groups enhance solubility, direct polymerization, and protect reactive positions on the N-HTA core. Owing to the superior structural definition and synthetic control of FTN-Pol, subsequent electrochemical investigations are focused on this polymer.

3.2.2 Electrochemical Investigations

In the following section, the electrochemical properties of the FTN-based polymer are systematically investigated. Cyclic voltammetry was employed to explain the redox mechanism and investigate the polymer's behavior over an extended voltage window. Additionally, the effect of electrode composition on electrochemical performance is evaluated by varying the proportion of conductive carbon black across different voltage regimes. To monitor the development and progression of redox processes, the CV voltage window was incrementally expanded, and the corresponding voltammograms were recorded.

Long-term galvanostatic cycling experiments were performed to evaluate the cycling stability of the material within both narrow and extended voltage ranges, comprising 400 and 100 cycles, respectively. Particular attention was given to the determination of the half-wave redox potential ($E_{1/2}$) and the associated overpotential (η). Finally, rate capability tests were conducted to further correlate electrochemical kinetics with redox potential and overpotential behavior[1].

Reaction Mechanism Investigation

Figure 3.2 illustrates the proposed redox mechanism operative in FTN-Pol when employed as a cathode material in lithium-ion batteries [155]. Each monomeric unit of FTN-Pol contains a redox-active nitrogen center within the N-hetero-triangulene (N-HTA) core, which undergoes a reversible one-electron redox process during electrochemical cycling. Upon oxidation, the nitrogen center transitions from a neutral amine (N^0) to a radical cation state (N^+), resulting in the formation of a delocalized, positively charged polymeric backbone. This oxidized state is electrostatically stabilized by PF_6^- anions present in the

[1] Electrochemical data in this work are subject to an estimated uncertainty of 5 – 10 %, primarily due to manual electrode preparation (weighing accuracy, slurry homogeneity, and mass loading), as explained in Section 2.4.1.

electrolyte, which serve as counterions to maintain charge neutrality within the system. During the subsequent reduction process, the nitrogen-centered radical cation is reduced back to its neutral state (N^0) via the uptake of one electron per monomer unit. At the same time, lithium cations (Li^+) from the electrolyte migrate toward the associated PF_6^- anions to restore local charge balance, completing the redox cycle. This electrochemical transformation is thus localized at the nitrogen site, which acts as the primary redox-active center. Based on this one-electron redox process ($z = 1$) per N-HTA unit, the theoretical specific charge capacity of FTN-Pol is calculated to be $29.97\,\mathrm{mA\,h\,g^{-1}}$. This value reflects the capacity contribution derived exclusively from the reversible oxidation and reduction of the nitrogen centers within the polymer network.

The distinct electrochemical behavior of the FTN monomer, particularly its narrow and well-defined oxidation to a stabilized nitrogen-centered radical cation [155], motivated the investigation of FTN-Pol as a potential cathode material for lithium-ion batteries. Composite electrodes were prepared by combining FTN-Pol (50 wt%) with carbon black (CB, 40 wt%) as the conductive additive and polyvinylidene fluoride (PVdF, 10 wt%) as the binder (for detailed electrode preparation procedures, see 2.4.1). Notably, CB exhibits no redox activity within the investigated voltage window, as confirmed by control experiments (see 2.4.5). Electrochemical characterization was performed using a standard coin-cell configuration. The electrolyte consisted of 1 M $LiPF_6$ in a 1:1 (v/v) mixture of ethylene carbonate (EC) and dimethyl carbonate (DMC), with metallic lithium employed as both counter and reference electrode (for details, see 2.4.2).

The CVs depicted in Figure 3.4 illustrate the electrochemical behavior of FTN-Pol-based composite electrodes in different voltage ranges and over multiple cycles. In Figure 3.4 a), CVs recorded between 2.5 V and 4.0 V vs. Li/Li^+ at a scan rate of $0.1\,\mathrm{mV\,s^{-1}}$ reveal a distinct oxidation peak (O) at $3.85\,\mathrm{V} \pm 0.01\,\mathrm{V}$ and a corresponding reduction peak (R) at $3.78\,\mathrm{V} \pm 0.01\,\mathrm{V}$. Resulting in a redox potential ($E_{1/2}$) of $3.82\,\mathrm{V} \pm 0.02\,\mathrm{V}$ with an overpotential (η) of $0.07\,\mathrm{V} \pm 0.02\,\mathrm{V}$ (The errors were estimated from the graphs). Additionally, a shoulder-like feature emerges around 4.0 V. While the first cycle (black trace) shows the highest peak intensity, a notable decrease in current is observed in the second cycle (red trace). However, subsequent cycles (5th and 10th, shown in blue and green, respectively) exhibit only minor decline in current, indicating a stabilization of electrochemical activity. The sharp and symmetric nature of the redox peaks demonstrates that the electrochemical characteristics of the monomeric FTN unit are retained in the polymeric structure. Furthermore, the minimal decline in current beyond the second cycle suggests that the architecture of FTN-Pol effectively mitigates typical degradation pathways of organic electrode materials, such as dissolution into the electrolyte.

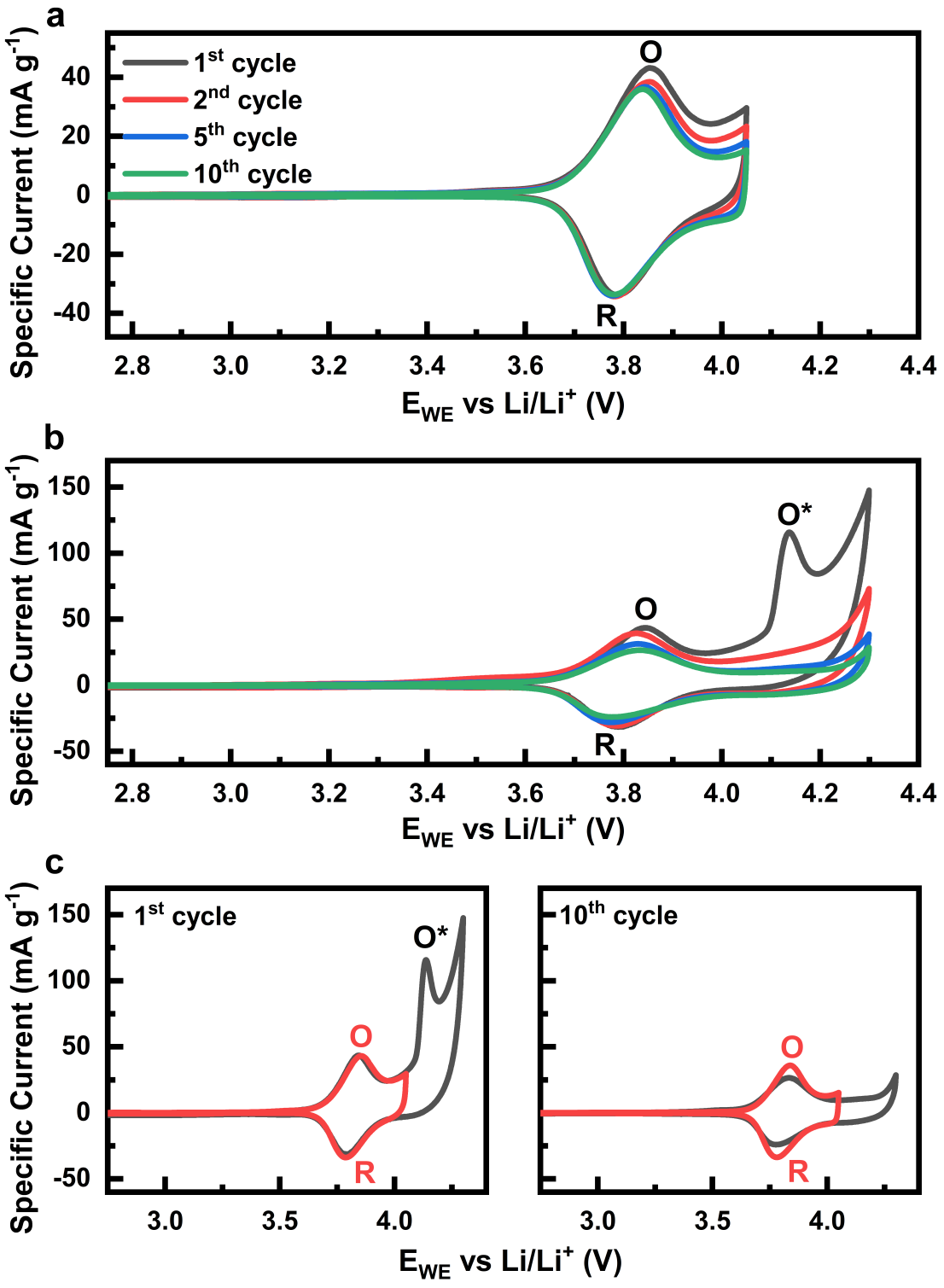


Figure 3.4: CVs of FTN-Pol-based composite electrodes (50 wt%) recorded in 1 M $LiPF_6$ in EC/DMC (1:1 v/v) at a scan rate of 0.1 mV s^{-1}. Specific currents are normalized to the mass of FTN-Pol. **a)** CV in the voltage range of 2.5 – 4.0 V vs. Li/Li^+. **b)** CV in the extended voltage range of 2.5 – 4.3 V vs. Li/Li^+. **c)** Comparison of the first cycle in both voltage ranges. **d)** Comparison of the 10th cycle in both voltage ranges. [155]

Figure 3.4 b) shows data with the voltage range extended to 4.3 V which enables the elucidation of the origin of the shoulder-like feature. This extended CV reveals the appearance of an additional oxidation peak (O*) at 4.15 V in the first cycle. However, this feature lacks a corresponding reduction peak and disappears entirely in the second cycle, indicating that O* corresponds to an irreversible oxidation process. Importantly, the inclusion of this higher voltage regime appears to accelerate the fading of the primary redox couple O/R.

Figure 3.4 c) and d) show a direct comparison between the narrow and extended voltage windows in the first and tenth cycles, respectively. In the first cycle (c)), the oxidation and reduction peaks of the primary redox couple overlap in both regimes, confirming the reversibility of the main redox process. However, the shoulder around 4.0 V becomes more pronounced in the extended voltage window, confirming its association with the onset of the additional oxidation event O*. In the tenth cycle (d)), the extended CV reveals a significant decrease in the intensity of both O and R, along with the complete disappearance of O*, compared to the narrower voltage range. These findings further confirm that the inclusion of the irreversible O* process adversely affects the long-term stability of the primary redox activity in FTN-Pol.

Changing Carbon Black Content in the Electrodes

To gain deeper insight into the electrochemical behavior of FTN-Pol, the content of conductive carbon black (CB) within the composite electrodes was systematically increased. Enhancing the CB fraction improves the overall electrical conductivity of the electrode, which can facilitate access to previously inactive or kinetically hindered redox centers. This modification is anticipated to enhance charge transport throughout the electrode matrix, thereby potentially improving the overall electrochemical performance of the material [42].

Figure 3.5 presents a comparative study of the CV profiles of FTN-Pol-based composite electrodes with varying CB content, highlighting the influence of electrode composition on the electrochemical behavior. In Figure 3.5 a), the CV of an electrode composed of FTN-Pol:CB:PVDF in a 50:40:10 wt% ratio shows a well-defined and symmetric redox couple. The oxidation peak appears at $3.85\,\mathrm{V} \pm 0.01\,\mathrm{V}$ and the reduction peak at $3.78\,\mathrm{V} \pm 0.01\,\mathrm{V}$ vs. $\mathrm{Li/Li^+}$, resulting in a redox potential $\mathrm{E_{1/2}}$ of $3.82\,\mathrm{V} \pm 0.02\,\mathrm{V}$ and an overpotential η of $0.07\,\mathrm{V} \pm 0.02\,\mathrm{V}$. The measured current shows only a slight decrease after the second cycle, indicating good stability and minimal degradation over multiple cycles. Figure 3.5 b) displays the CVs of a modified electrode with increased CB content (FTN-Pol:CB:PVDF in a 30:60:10 ratio). Here, the redox couple remains centered around $3.82\,\mathrm{V} \pm 0.03\,\mathrm{V}$

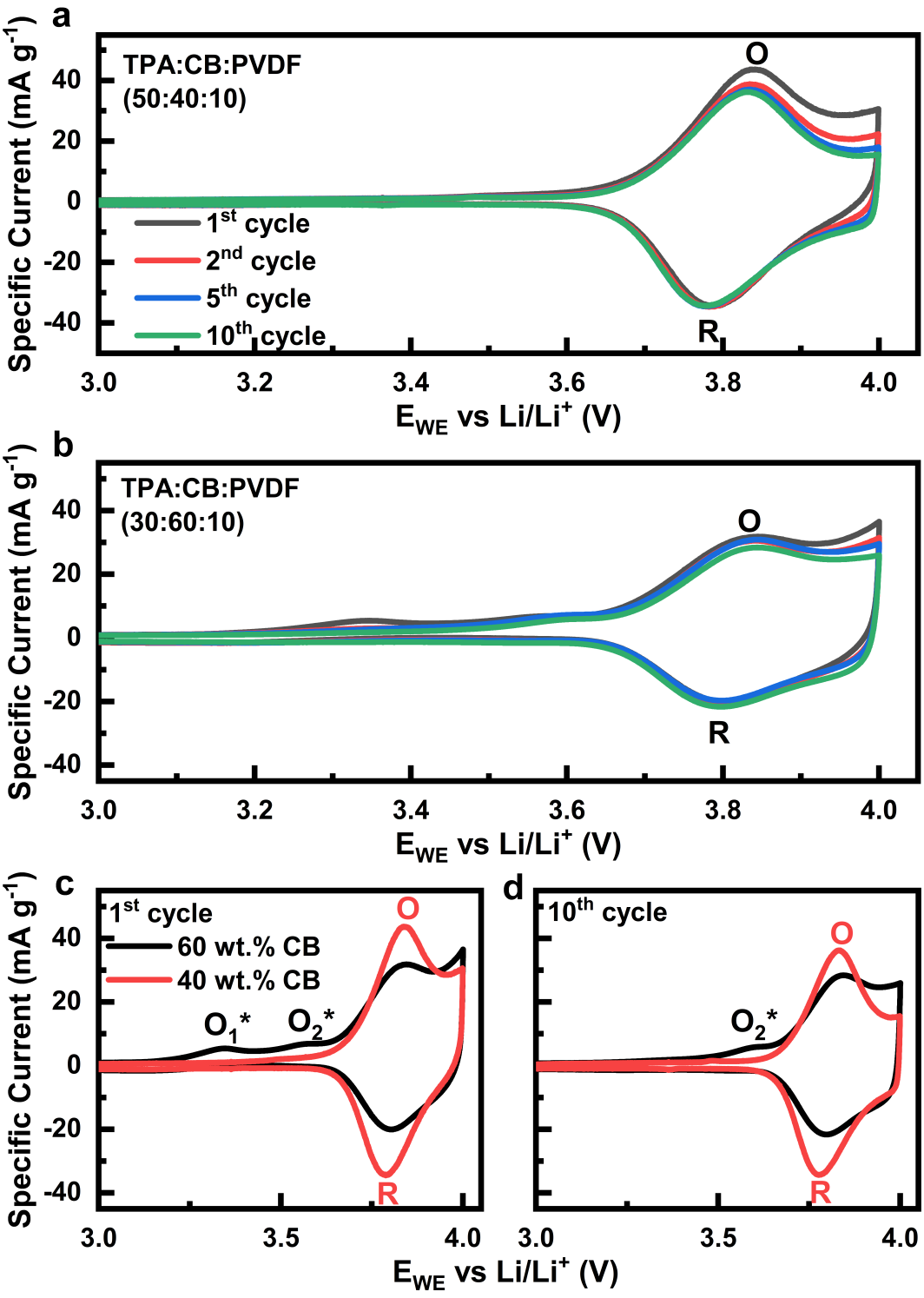


Figure 3.5: CVs of FTN-Pol-based composite electrodes recorded in 1 M $LiPF_6$ in EC/DMC (1:1 v/v) at a scan rate of 0.1 mV s^{-1} in a voltage range of 2.5 - 4.0 V vs. Li/Li^+. Specific currents are normalized to the mass of FTN-Pol. **a)**, **b)** CV of electrodes composed of FTN-Pol:CB:PVDF (50:40:10), (30:60:10). **c)**, **d)** Comparison of the first, 10th cycle with both electrode compositions. [155]

with slightly reduced overpotential ($0.04\,V \pm 0.03\,V$), suggesting similarly efficient electron transfer. However, two additional oxidation features emerge: an irreversible peak O_1* at 3.34 V and a reversible peak O_2* at 3.64 V, both lacking corresponding reduction peaks. The shoulder-like feature around 4.0 V observed in the previous composition also persists. Notably, the current remains nearly unchanged from cycle 1 to cycle 5, but shows a more pronounced decline from cycle 5 to 10, indicating evolving interfacial or structural changes with prolonged cycling in the higher CB matrix. Figure 3.5 c), d) offer a direct comparison between the two electrode compositions in the first and tenth cycles, respectively. The electrode with 60 wt% CB exhibits broader and smaller redox peaks compared to the 40 wt% CB composition, consistent with the Randles–Ševčík equation which correlates smaller and broader peaks with diminished diffusion kinetics. However, this is not reflected in the overpotential values, which remain comparable between both systems. Importantly, the higher CB content introduces additional redox features (O_1* and O_2*) not attributable to CB itself, possibly hinting at polymer-CB interfacial effects. Moreover, the enhanced CB environment leads to a more gradual decline in current over 10 cycles, which could suggest improved structural integrity and suppressed dissolution of FTN-Pol in the electrolyte, ultimately promoting redox stability during extended cycling.

Detailed Investigation of Changing Potential Windows

The electrochemical behavior of FTN-Pol changes significantly depending on the applied potential window, affecting both the reversibility and the appearance of redox features, as shown in Section 3.2.2. To systematically evaluate the influence of the upper voltage limit, a stepwise CV protocol was employed, wherein the upper cutoff voltage was incrementally increased by 0.1 V after every three cycles. This approach enables a precise assessment of how gradual changes in the potential window affect the redox behavior and stability of FTN-Pol.

In Figure 3.6 a) a CV where the upper voltage limit was gradually increased in 0.1 V increments after every three cycles, ranging from 2.5 V - 4.0 V (red curve) to 2.5 - 4.5 V vs. Li/Li^+ (magenta curve), using a 30 wt% FTN-Pol composite in 1 M $LiPF_6$ in EC:DMC (1:1 v/v) at a scan rate of $0.1\,mV\,s^{-1}$ is shown. Initially, the primary redox couple (O/R) appears clearly, with the oxidation peak (O) centered at $3.85\,V \pm 0.02\,V$ and the reduction peak (R) at $3.81\,V \pm 0.02\,V$, yielding a redox potential ($E_{1/2}$) of $3.83\,V \pm 0.03\,V$ and a overpotential (η) of $0.04\,V \pm 0.03\,V$. These values are consistent with previous measurements. However, as the upper voltage limit is extended, both the oxidation and reduction peaks progressively diminish, nearly vanishing after 16 cycles. No sign of an O_1* feature appears,

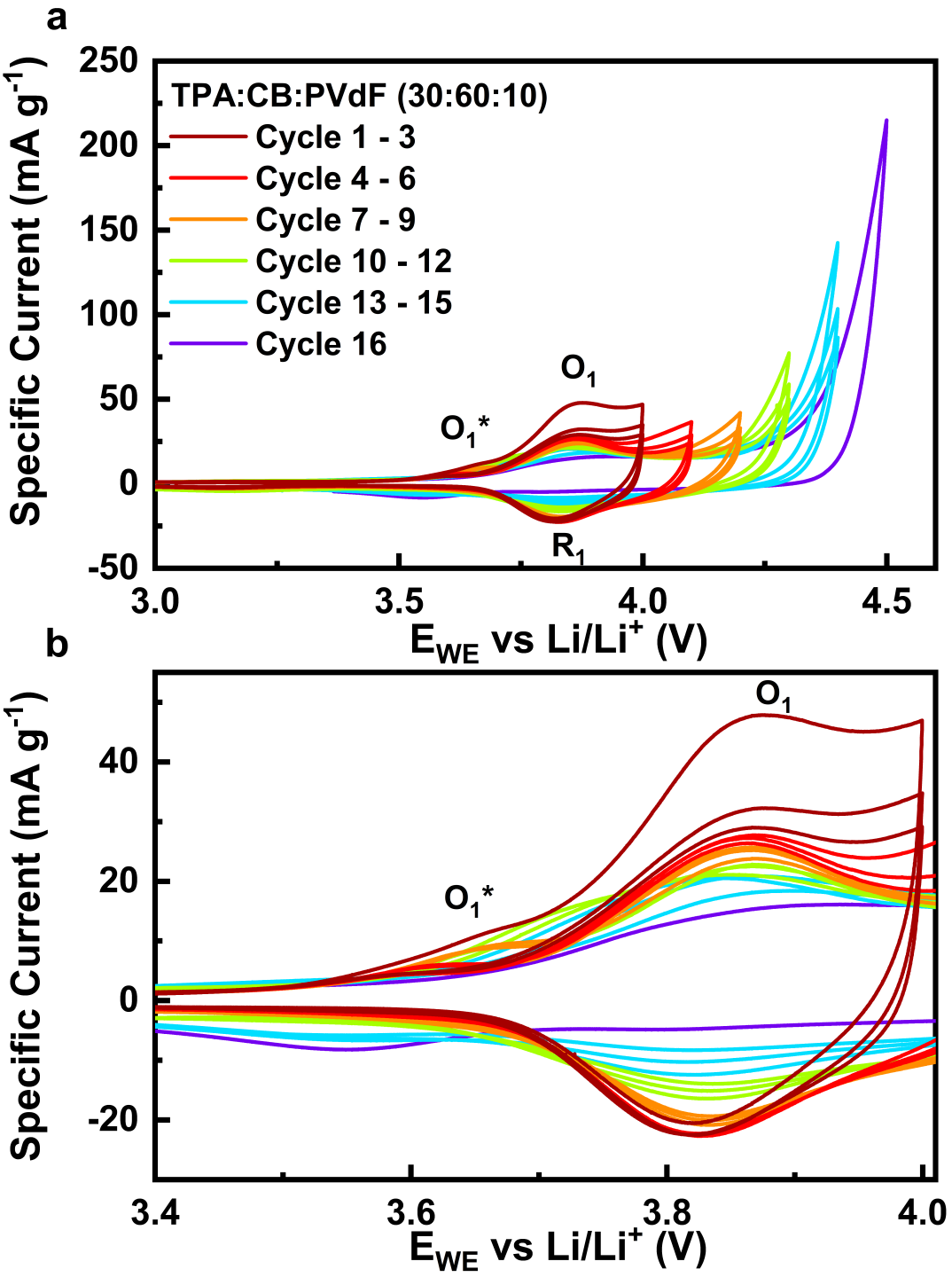


Figure 3.6: Stepwise CV to show the impact of changing potential window on electrochemical properties of FTN-Pol. **a)** CV of FTN-Pol based composite electrodes (30 wt%) recorded in 1 M $LiPF_6$ in EC:DMC (1:1 v/v) at a scan rate of 0.1 mV s^{-1} in the voltage range of 2.5 - 4.0 V vs. Li/Li^+ (red) stepwise increasing the upper voltage limit by 0.1 V every 3 cycles up to 2.5 - 4.5 V vs. Li/Li^+ (magenta). **b)** Zoom in of a) to highlight the evolution of redox reactions during stepwise CV. [155]

but the secondary oxidation peak O_2* emerges, similar to 3.5. A magnified view of the redox evolution is provided in Figure 3.6 b), allowing a closer look on these changes. The oxidation signal rapidly weakens after the first cycle, while the reduction peak remains more stable only until around the sixth cycle before it begins to fade too. Notably, after the 15th cycle, the reduction peak undergoes a sudden potential shift (magenta curve), signalizing significant alteration or degradation of the redox-active species. The O_2* feature, initially visible in the first cycle, is strongly suppressed in the subsequent scan, but then reappears with increasing intensity and a gradual shift, eventually overlapping with the main oxidation peak O after cycle 13. This merging behavior suggests that O_2* may evolve into or interfere with the primary redox process under extended voltage limits. Ultimately, by the time the upper limit reaches 4.4 V, signs of sudden changes in redox peaks and therefor irreversible degradation are evident, emphasizing that 2.5 V - 4.0 V is an optimal operating window to preserve the electrochemical integrity of FTN-Pol.

Cycling Stability Investigations

Long-term galvanostatic charge/discharge cycling was performed on the FTN-Pol composite electrode at a current density of 100 mA g^{-1} (approximately 3 C), within a voltage window of 2.5 - 4.0 V vs. Li/Li^+ (Figure 3.7 a), b)). The initial charge capacity of 26 mA h g^{-1} , corresponding to approximately 87 % of the theoretical capacity, gradually decreased during the first 20 cycles, stabilizing at 21 mA h g^{-1} . This corresponds to a capacity retention of 81 %. As shown in Figure 3.7 a), the charge/discharge voltage profiles exhibit near completly overlap up to 3.95 V, and only negligible deviations are observed beyond the 20th cycle across the entire voltage range. The Coulombic efficiency (CE) of the FTN-Pol electrode progressively increases during the initial cycling period, reaching a value above 97 % after 25 cycles and stabilizing after roughly 100 cycles at 99.6 %, indicating a highly reversible redox process centered at the nitrogen site (Figure 3.7 c)). The electrochemical performance of FTN-Pol is governed not only by the redox activity of the nitrogen-containing heterotriangulene (N-HTA) units but is also significantly influenced by the polymer's microporous architecture. The high surface area and uniform pore size distribution enhance lithium-ion storage capacity and diffusion kinetics, thereby improving specific capacity and cycling stability [161]. The microporous structure facilitates effective electrode–electrolyte interaction, increasing the number of accessible redox-active sites [31]. Additionally, the interconnected porosity supports efficient ion transport within the polymer matrix, contributing to improved rate capability and reduced charge-transfer resistance [162]. Structural robustness, submitted by the rigid spiro-linked framework of FTN-Pol, further supports its long-term electrochemical stability [163].

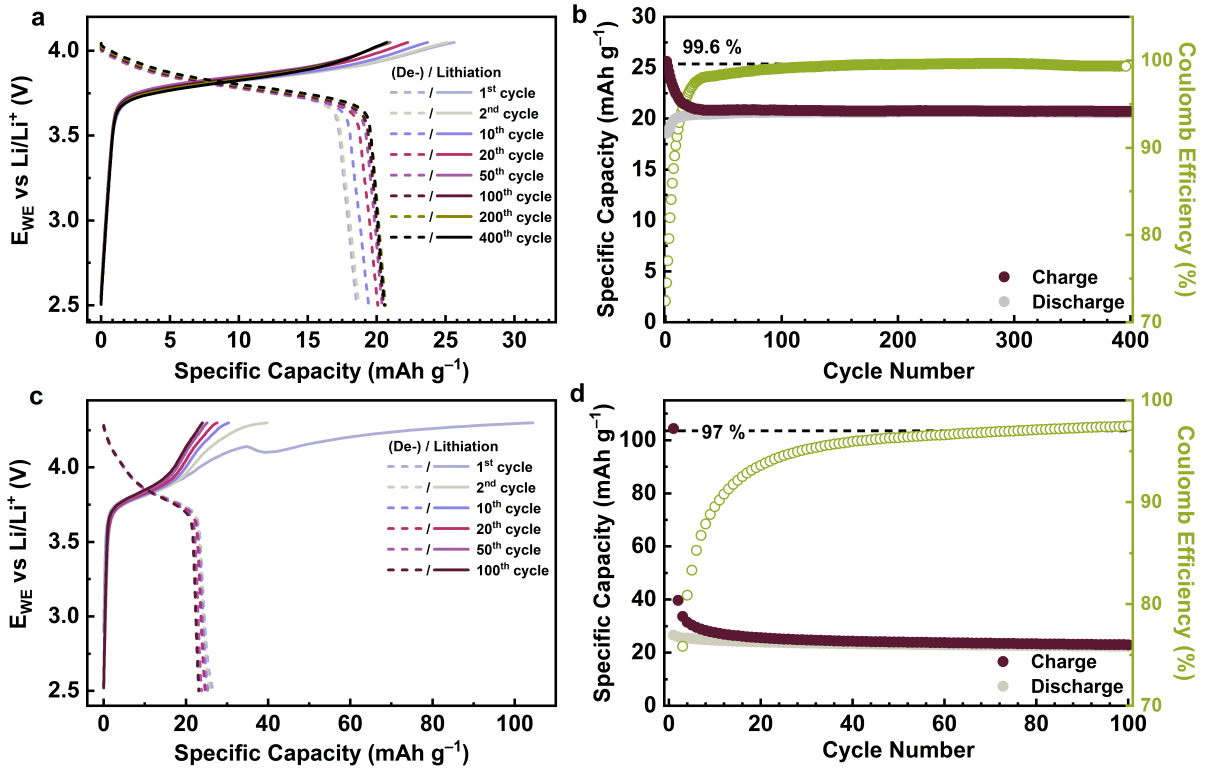


Figure 3.7: a), c) Galvanostatic charge–discharge voltage profiles of selected cycles recorded at a current density of 100 mA g^{-1} (approximately 3 C) within the voltage ranges of 2.5 - 4.0 V vs. Li/Li^+ **a)** and 2.5 - 4.3 V vs. Li/Li^+ c). **b), d)** Long-term cycling performance of FTN and FTN-Pol electrodes at 100 mA g^{-1} over 400 cycles b) and 100 cycles d), respectively. Capacities are normalized with respect to the mass of active material (FTN-Pol), and the contribution of carbon black (CB) has been subtracted. [155]

To evaluate the influence of the oxidative side process O*, galvanostatic cycling was also conducted in an extended voltage window of 2.5 - 4.3 V vs. Li/Li^+ (Figure 3.7 c), d)). In this regime, the electrode exhibits a significantly higher initial charge capacity of 105 mA h g^{-1}, followed by a sharp decline to 40 mA h g^{-1} in the second cycle. Subsequent cycles show a more gradual capacity fading, eventually stabilizing at approximately 25 mA h g^{-1} by cycle 100. The pronounced capacity loss between the first and second cycles emphasizes the irreversible nature of the O* process, as previously discussed. The CE in the extended voltage window gradually improves, reaching 97 % after 75 cycles, which further confirms the irreversible character of redox reactions occurring between 4.0 - 4.3 V vs. Li/Li^+ (Figure 3.7 d)). These observations suggest that the long-term reversible capacity is primarily governed by the O/R process. The slightly elevated capacity observed in the extended voltage window relative to the 4.0 V cut-off condition is attributed to the reactions in the 4.0 V to 4.3 V range.

Redoxpotential and Overpotential Studied in Different Potential Windows

To further investigate the influence of varying upper voltage limits on the redox behavior of the FTN-Pol composite electrode, the evolution of the redox potential ($E_{1/2}$) and the overpotential (η) was analyzed in both a reduced and an extended potential window.

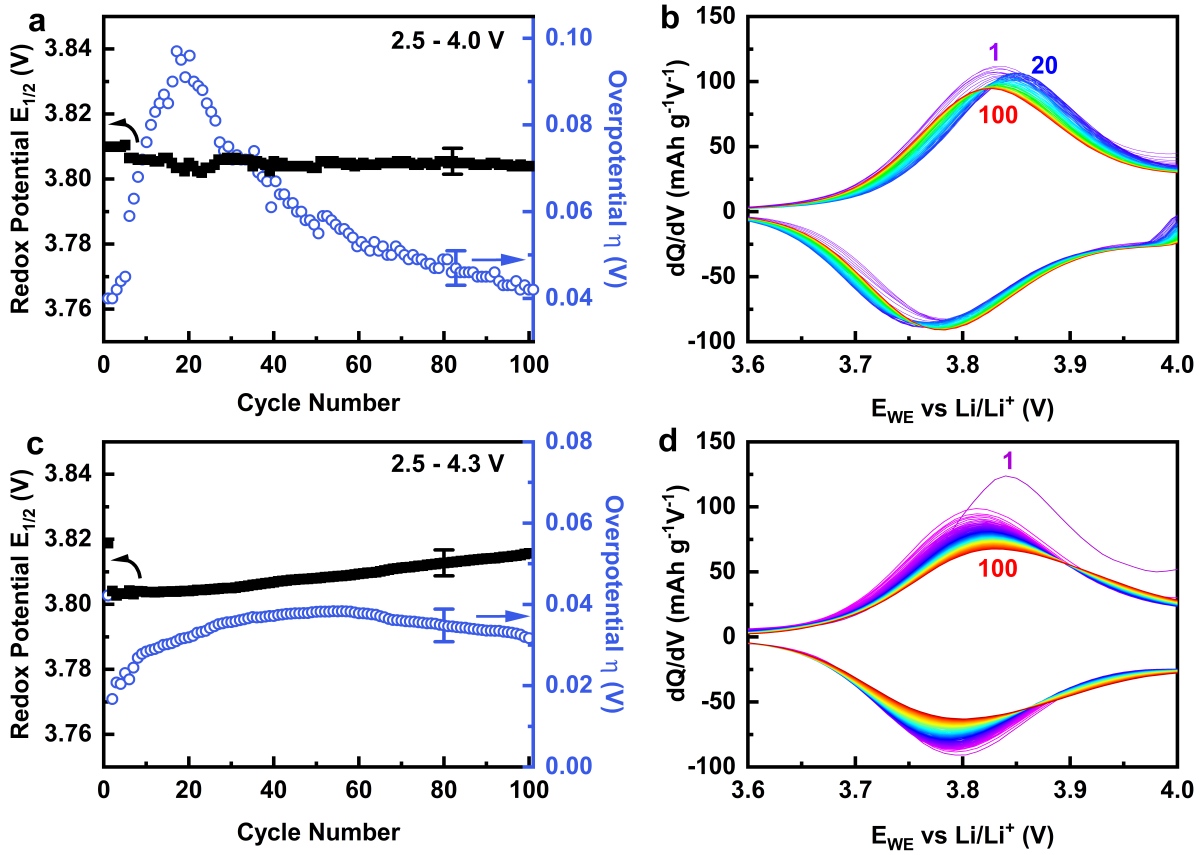


Figure 3.8: Electrochemical analysis of FTN-Pol electrodes cycled at 100 mA g^{-1} (approximately 3 C) in different potential windows. **a)** Evolution of the redox potential ($E_{1/2}$) and overpotential (η) over 100 cycles, derived from differential analysis of galvanostatic charge/discharge profiles in the reduced potential window of 2.5 - 4.0 V vs. Li/Li^+. **b)** Corresponding dQ/dV plots illustrating the stability of redox peaks over 100 cycles. **c)** Evolution of $E_{1/2}$ and η over 100 cycles in the extended potential window of 2.5 - 4.3 V vs. Li/Li^+. **d)** dQ/dV curves demonstrating progressive degradation and redox peak instability under extended voltage conditions. [155]

Figure 3.8 illustrates the electrochemical response of FTN-Pol electrodes cycled at 100 mA g^{-1} (approximately 3 C) in the two voltage regimes, with particular emphasis on the redox stability observed within the reduced potential window (2.5 - 4.0 V vs. Li/Li^+) and the redox potential shifts that emerge in the extended window (2.5 - 4.3 V vs. Li/Li^+).

In the reduced potential window (Figure 3.8 a)), the evolution of $E_{1/2}$, calculated as the mean of the oxidation (O) and reduction (R) peak potentials, and the overpotential

($\eta = V_O - V_R$) are shown over 100 cycles. These values were extracted from differential capacity plots (dQ/dV) (Figure 3.8 b)) obtained from galvanostatic charge/discharge profiles recorded between 2.5 - 4.0 V vs. Li/Li^+ (Figure 3.7 a)). The redox potential remains highly stable throughout the 100 cycles, averaging $3.807\,V \pm 0.005\,V$ vs. Li/Li^+. The error was estimated from the dQ/dV. In contrast, the overpotential exhibits a non-monotonic trend: it initially increases from $0.040\,V \pm 0.005\,V$ to a maximum of $0.097\,V \pm 0.005\,V$ vs. Li/Li^+ within the first 20 cycles, followed by a gradual, exponential decrease back to $0.040\,V \pm 0.005\,V$ vs. Li/Li^+ by cycle 100. This behavior indicates a stable redox reaction mechanism and suggests the robustness of the polymer backbone, although changes in diffusive kinetics or interfacial resistance may occur during early cycling. Figure 3.8 b) shows the corresponding dQ/dV curves, derived from the galvanostatic profiles in Figure 3.7 a). A slight positive shift in the oxidation peak and a corresponding negative shift in the reduction peak are observed during the first 20 cycles. However, both peak positions and intensities stabilize significantly after 60 cycles, further confirming the long-term electrochemical stability of the redox process in this potential range.

In contrast, cycling in the extended potential window (2.5 - 4.3 V vs. Li/Li^+) leads to different behavior, as presented in Figs. 3.8 c), d). The redox potential ($E_{1/2}$) and overpotential (η) were extracted using the same method as described above, based on differential analysis of galvanostatic profiles (Figure 3.8 d)). Unlike the stable response in the reduced window, the redox potential in the extended window shows a notable shift over time. After a rapid drop from $3.819\,V \pm 0.005\,V$ to $3.803\,V \pm 0.005\,V$ vs. Li/Li^+ between the first and second cycles, it gradually increases over the following 98 cycles, reaching $3.816\,V \pm 0.005\,V$ vs. Li/Li^+ by cycle 100. This continuous upward shift in redox potential may reflect structural rearrangements or irreversible side reactions within the polymer matrix, further implicating the O* process (active between 4.0 V - 4.3 V) is responsible for the poor Coulombic efficiency observed for the extended voltage range. The overpotential in the extended window also exhibits a dynamic profile: it starts at $0.0167\,V \pm 0.005\,V$, increases steadily to a maximum of $0.383\,V \pm 0.005\,V$ at cycle 55, and then slightly declines to $0.317\,V \pm 0.005\,V$ vs. Li/Li^+ by cycle 100. These shifts suggest increased polarization and redox process destabilization at elevated voltages. The corresponding dQ/dV curves in Figure 3.8 d), derived from the charge/discharge profiles shown in Figure 3.7 c), further highlight the instability of the redox peaks. Over the course of 100 cycles, the oxidation and reduction peaks become increasingly broadened and asymmetric, indicating the progressive degradation of the redox process under extended voltage operation.

Rate-Performance

Figure 3.9 illustrates the electrochemical performance of FTN-Pol electrodes cycled at a reduced current density of 10 mA g^{-1} (approximately C/3), emphasizing redox stability and rate capability.

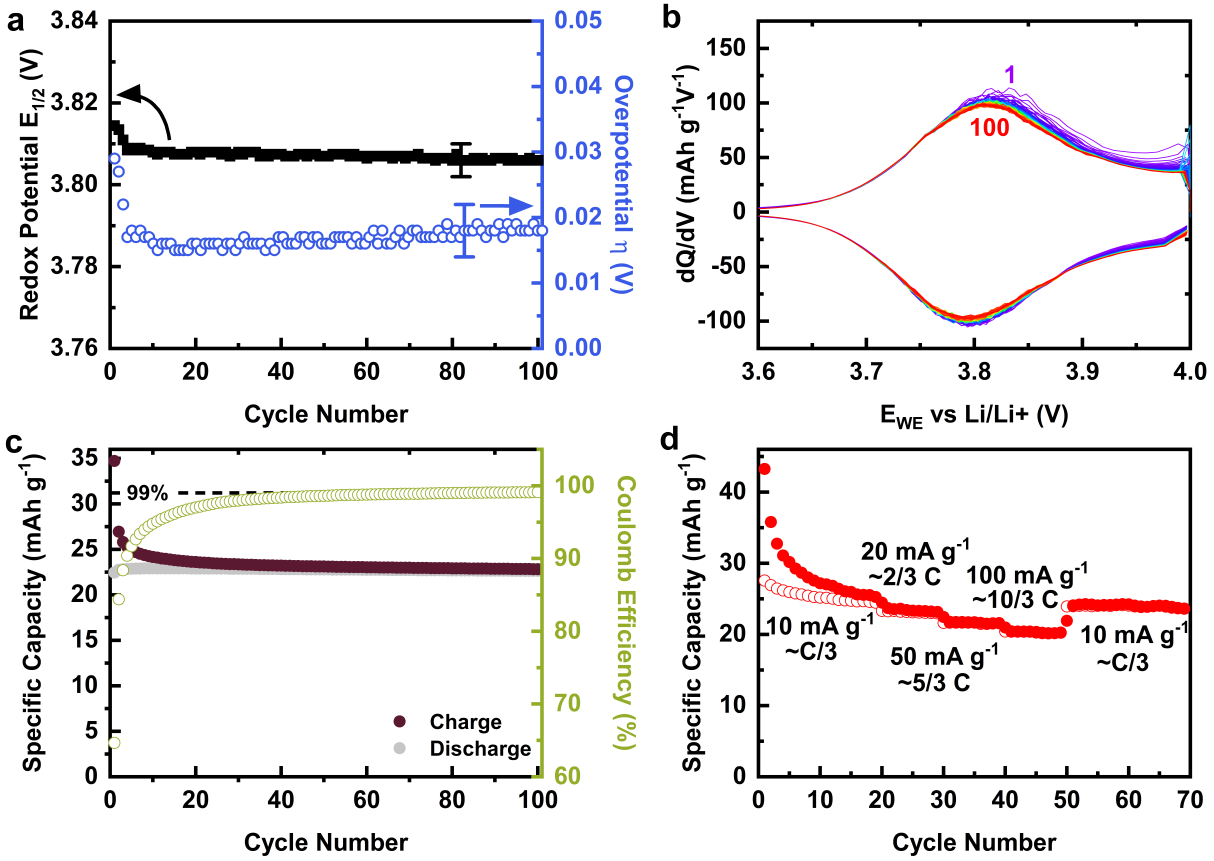


Figure 3.9: Electrochemical performance of FTN-Pol electrodes cycled at a reduced current density of 10 mA g^{-1}. **a)** Evolution of the redox potential ($E_{1/2}$) and overpotential (η) over 100 cycles, derived from differential analysis of galvanostatic charge/discharge profiles. **b)** Selected dQ/dV curves obtained from charge/discharge measurements in the voltage range of 2.5 V to 4.0 V vs. Li/Li^+, illustrating redox peak stability over 100 cycles. **c)** Specific capacity as a function of cycle number at 10 mA g^{-1}, with values normalized to the mass of the active material (FTN-Pol). **d)** Rate capability test showing the reversible capacity at various current rates (≈C/3, 2/3 C, 5/3 C, and 10/3 C), highlighting the robustness and reversibility of the FTN-Pol electrode under varying charge/discharge conditions. [155]

The evolution of the redox potential ($E_{1/2}$) (black), determined as the mean of the oxidation O and reduction R peak potentials, along with the overpotential (η) (blue), is presented in Figure 3.9 a). These potentials were extracted from the differential plots (dQ/dV) of galvanostatic charge/discharge profiles obtained within the voltage range of 2.5 - 4.0 V vs. Li/Li^+ (Figure 3.9 b)). The redox potential remains highly stable over 100

cycles at $3.807\,\mathrm{V} \pm 0.005\,\mathrm{V}$ vs. $\mathrm{Li/Li^+}$. After a rapid decline within the initial 10 cycles, the overpotential stabilizes at $0.017\,\mathrm{V} \pm 0.005\,\mathrm{V}$ vs. $\mathrm{Li/Li^+}$, indicating minimal kinetic polarization and suggesting a robust and reversible redox process under low-rate cycling conditions. This behavior demonstrates improved stability in comparison to higher current density cycling ($\approx 3\,\mathrm{C}$, see Figure 3.8 a)). The dQ/dV profiles in Figure 3.9 b) further confirm the electrochemical stability of FTN-Pol. Beyond a slight decrease in redox peak intensity following the third cycle, both peak positions and amplitudes remain essentially unchanged over extended cycling. The minimal initial loss likely reflects a relatively minor contribution from parasitic reactions near 4.0 V, in contrast to the more pronounced side reactions observed under higher current densities (Figure 3.8). The sustained symmetry between anodic and cathodic peaks beyond the 20th cycle further supports the conclusion that the redox processes remain fully reversible throughout prolonged cycling. These observations also suggest that typical degradation pathways in organic electrode materials, such as dissolution of active species into the electrolyte, are effectively suppressed in FTN-Pol due to its molecular design [164].

Long-term cycling data at $10\,\mathrm{mA\,g^{-1}}$ (Figure 3.9 c)) reveal an initial charge capacity of $35\,\mathrm{mA\,h\,g^{-1}}$, which stabilizes at $24\,\mathrm{mA\,h\,g^{-1}}$ after 20 cycles, corresponding to 80 % of the theoretical capacity. In line with observations at higher rates, the Coulombic efficiency (CE) increases steadily during the initial cycles and reaches a plateau at 99.1 % by cycle 100. Notably, this steady-state CE is achieved more rapidly at C/3 than at 3 C, further indicating that the reduced current density limits the impact of side reactions affecting early-cycle CE (Figure 3.7 b)). The rate performance of FTN-Pol is presented in Figure 3.9 d). The electrode was initially cycled at $10\,\mathrm{mA\,g^{-1}}$ for 20 cycles, during which the charge capacity decreased from 43 to $25\,\mathrm{mA\,h\,g^{-1}}$ (corresponding to 83 % of the theoretical value). Subsequent increases in current density to $\approx 2/3\,\mathrm{C}$, $\approx 5/3\,\mathrm{C}$, and $\approx 10/3\,\mathrm{C}$ yield reversible capacities of 23, 22, and $21\,\mathrm{mA\,h\,g^{-1}}$, respectively. Upon returning to $\approx \mathrm{C}/3$ (cycle 50), the specific capacity recovers to $24\,\mathrm{mA\,h\,g^{-1}}$, demonstrating excellent rate capability and reversibility of the FTN-Pol composite electrode. The primary variation in capacity is observed within the first 20 cycles and is strongly dependent on current density, a phenomenon attributed to transient side reactions, which are more pronounced at higher rates.

3.2.3 Conclusions

FTN-Pol represents the first cathode material based on nitrogen-centered hetero-triangulene analogues (N-HTA), in which the redox activity at the nitrogen center has been systemat-

ically investigated under electrochemical cycling conditions. The incorporation of a rigid spirocyclic architecture provides a well-defined microporous framework, enabling the design of a redox-active polymer with both high CE and excellent long-term cycling stability. Previous studies on structurally related triphenylamine-based polymers, such as TPA-Pol, have demonstrated that enhanced microporosity correlates with improved electrochemical performance due to increased accessible surface area (see Table 3.1). In comparison, FTN-Pol operates within a similar redox potential range ($\approx 3.8\,\mathrm{V}$ vs. $\mathrm{Li/Li^+}$), but exhibits a narrower and more defined cyclic voltammogram. This observation suggests enhanced stabilization of the nitrogen-centered oxidation state through the extended π-conjugation of the N-HTA system. While FTN-Pol possesses a lower specific capacity than TPA-Pol, attributable to the higher molecular weight of its spiro-bridged redox-active units, it nonetheless achieves 87 % of its theoretical capacity, exceeding the 81 % attained by TPA-Pol. Furthermore, FTN-Pol demonstrates robust cycling performance, reaching a CE of 99.6 % after 400 cycles, which is comparable to the 99.3 % CE of TPA-Pol after 1000 cycles. The rate capability of FTN-Pol is also competitive. As the current density increases from 50 to $100\,\mathrm{mA\,g^{-1}}$, the specific capacity decreases only slightly from 21.68 to $20.35\,\mathrm{mA\,h\,g^{-1}}$. In comparison, TPA-Pol exhibits a capacity drop from 77.11 to $69.96\,\mathrm{mA\,h\,g^{-1}}$ under identical conditions (see Table 3.1). These results confirm that FTN-Pol is a promising candidate for high-performance organic cathode materials, offering stable and reversible redox behavior coupled with structural robustness and high electrochemical efficiency.

	$\mathbf{C_{theo}}$ $\mathbf{mA\,h\,g^{-1}}$	$\mathbf{E_{1/2}}$ **(V)**	$\mathbf{C_{@10}}$ $\mathbf{mA\,h\,g^{-1}}$	**CE** (%) **(C-rate)**	**Porosity** $\mathbf{(m^2\,g^{-1})}$	**Reference**
TPA-Pol	111	3.80	91	99.4 (20 C)	n.a.	[144]
SP-TPA	109	3.60	93	99.0 (1 C)	66	[165]
YP-TPA	109	3.60	105	99.0 (1 C)	544	[165]
OP-TPA	109	3.60	73	99.0 (1 C)	1557	[165]
PBDAPA	154	3.73	133	n.a.	130	[166]
PTDAPTz	109	3.80	75	n.a.	930	[167]
FTN-Pol	30	3.81	22	99.6 (3 C)	690	This work

Table 3.1: Comparative summary of electrochemical performance parameters for FTN-Pol and previously reported triphenylamine (TPA)-based polymers employed as cathode materials [155].

3.3 Sulfur-Chain Functionalization of FTN-Pol: Electrochemical Impact and Limitations

3.3.1 Motivation for Sulfur Chain Integration into FTN-Pol

Jocic et al. [155] introduces a strategy adressing the limited theoretical capacity of FTN-Pol, leveraging additional redox-active moieties into the polymeric framework. Specifically, sulfur chains were covalently integrated between FTN monomers to form a three-dimensional redox-active network. In this modified structure, each FTN monomer connects to three other FTN units via sulfur linkages composed of approximately ten sulfur atoms. These sulfur bridges serve as structural connectors and introduce a high density of redox-active centers into the polymer backbone. By leveraging the high theoretical capacity of sulfur-based redox chemistry, this approach improves the capacity of the resulting composite polymer, while preserving the favorable electronic properties and structural integrity of the original FTN-Pol material.

3.3.2 Background on Sulfur in Lithium Battery Systems

Lithium–sulfur (Li–S) batteries have emerged as a promising next-generation energy storage technology, primarily due to their high theoretical energy density of $\approx 2500\,\mathrm{W\,h\,kg^{-1}}$. This originates from the large specific capacities of elemental sulfur ($1672\,\mathrm{mA\,h\,g^{-1}}$) and lithium metal ($3860\,\mathrm{mA\,h\,g^{-1}}$) [156]. Sulfur is also attractive from a practical standpoint due to its abundance, low cost, and environmental compatibility. During discharge, lithium ions from the anode react with sulfur at the cathode, ultimately forming lithium sulfide (Li_2S). However, the system is hindered by several critical challenges, including the low intrinsic conductivity of sulfur and its discharge products, the dissolution and migration of intermediate lithium polysulfides (the polysulfide shuttle), and the degradation of the lithium-metal anode due to unstable SEI formation. Section 3.1.3 contains a more detailed description.

Incorporating sulfur into the polymeric framework attempts to mitigate those limitations by immobilising the sulfur species, suppressing polysulfide dissolution, and enhance the structural integrity of the cathode. In this work, sulfur chains were covalently bound within the FTN-Pol backbone to achieve these objectives. A theoretical estimate of the sulfur-functionalized polymer capacity reaches $604\,\mathrm{mA\,g^{-1}}$. The calculation (see Formular 2.9) assumes a molecular weight of $481.0\,\mathrm{g\,mol^{-1}}$ for sulfur and $894.2\,\mathrm{g\,mol^{-1}}$ for the FTN-Pol backbone, with roughly 15 redox-active sulfur atoms each with ($z = 2$) and one FTN

redox site per formula unit. This value represents a significant improvement over the original FTN-Pol and illustrates the potential of sulfur incorporation as an effective route to enhance the energy storage performance of organic cathode materials.

3.3.3 Electrochemical Reference Measurement of Sulfur-Based Electrodes

Measurements on conventional sulfur electrodes serve as a reference study for the sulfur-functionalized FTN polymer. Figure 3.10 shows the electrochemical characterization of the conventional reference electrodes composed of elemental sulfur, carbon black (CB), and polyvinylidene fluoride (PVDF) in a 50:40:10 weight ratio, and assembled similarly to FTN-based electrodes. However, the electrolyte used for these studies was 1 M lithium bis(trifluoromethanesulfonyl)imide (LiTFSI) dissolved in a 1:1 (v/v) mixture of 1,3-dioxolane (DOL) and dimethoxyethane (DME), which is more commonly applied in Li–S battery literature [168–170], rather than the 1 M $LiPF_6$ carbonate-based electrolyte used for FTN-Pol.

CV was performed at a scan rate of 0.1 mV s^{-1} over a potential window of 3.0 V to 1.5 V vs. Li/Li^+ for five cycles and can be seen in Figure 3.10 a). The open-circuit voltage (OCV) prior to cycling was measured at 2.35 V, which is in reasonable agreement with literature values around 2.55 V [158]. The CV profiles exhibit two characteristic cathodic peaks: the first (R_1), at 2.22 V, corresponds to the reduction of elemental sulfur (S_8) to higher-order lithium polysulfides (Li_2S_x, $4 < x < 5$), while the second (R_2), at 1.97 V, is associated with further reduction of these intermediates to insoluble lower-order polysulfides such as Li_2S_2 and Li_2S. On the anodic sweep (O_{1+2}), a broad oxidation peak centered around 2.49 V reflects the reversible conversion of Li_2S/Li_2S_2 back to elemental sulfur. Notably, cycle 1 to 5 show highly overlapping peak shapes and positions, indicating stable and reproducible redox behavior of the sulfur-based system under the selected conditions.

GCPL measurements (Figure 3.10 b)) were also conducted using the same sulfur:CB:PVDF electrode configuration and electrolyte composition. Cells were cycled at a current density of 50 mA g^{-1}, which approximates a C/16 rate, within the voltage range of 3.0 V to 1.5 V vs. Li/Li^+. The measured OCV of 2.34 V aligns well with the CV results. The discharge curve reveals two distinct voltage. plateaus: the first (R_1) at 2.32 V, corresponding to the S_8 to Li_2S_x conversion and contributing approximately 150 mA h g^{-1}, and the second (R_2) at 2.14 V, associated with the reduction to Li_2S and contributing about 800 mA h g^{-1}. This yields an overall discharge capacity of 968 mA h g^{-1}. Two corresponding plateaus appear

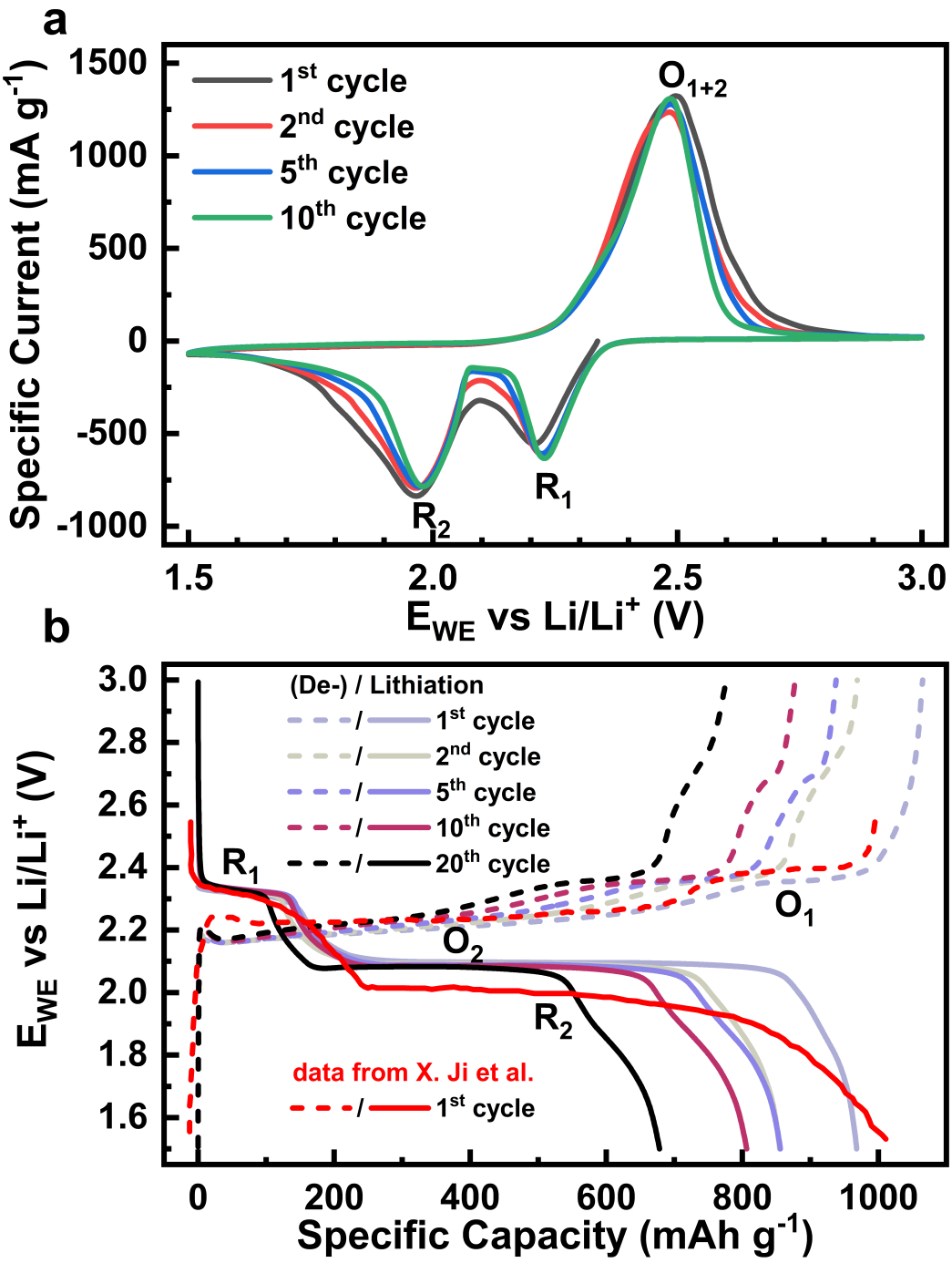


Figure 3.10: Electrochemical characterization of a conventional sulfur:CB:PVDF composite electrode (50:40:10 wt%) in a Li–S battery configuration using 1 M LiTFSI in DOL:DME (1:1 v/v) as electrolyte. **a)** CV profiles recorded over 10 cycles at a scan rate of 0.1 mV s^{-1} between 3.0 - 1.5 V vs. Li/Li^+, showing two characteristic cathodic peaks (R_1, R_2) and a broad anodic peak (O_{1+2}) associated with sulfur redox reactions. **b)** GCPL profiles measured at 50 mA g^{-1} (C/16), highlighting the typical discharge plateaus at 2.32 V and 2.14 V and charge plateaus at 2.19 V and 2.36 V, corresponding to the stepwise reduction and oxidation of elemental sulfur. For comparison, reference profiles from Ji et al. [158] are included to contextualize the electrochemical behavior.

during the charging process: the first (O_1) at 2.19 V, contributing 800 mA h g^{-1}, and the second (O_2) at 2.36 V, contributing 200 mA h g^{-1}, resulting in a total charge capacity of 1065 mA h g^{-1}. This is in agreement with the aforementioned CV results, except for the potential position of the reduction and oxidation reactions. This deviation is likely due to the selected scan rate, which influences ion diffusion kinetics and thus the overpotential, leading to a drift between the positions of the redox peaks.

These results are compared with literature data from Ji et al. [158], in which sulfur:CB:PVDF (80:10:10) electrodes were cycled in 1 M $LiPF_6$ dissolved in tetra(ethylene glycol) dimethyl ether (TEGDME) at 170 mA g^{-1} (C/10). An OCV of 2.54 V was reported, along with similar voltage plateaus at 2.32 V (R_1) and 2.24 V (R_1) during discharge, yielding a comparable capacity of 1000 mA h g^{-1}. The corresponding charge process was shown to exhibit plateaus at 2.24 V (O_1) and 2.40 V (O_2), contributing to a total of 995 mA h g^{-1}. The good agreement between our measurements and the literature values validates the electrochemical activity of sulfur under our conditions and provides a reliable reference framework for interpreting the behavior of sulfur within the FTN-Pol-S composite. Only the shift of 0.1 V in the second reduction plateau (R_2) between literature and our reference measurement remains unexplained.

3.3.4 Electrochemical Characterization

Reaction Mechanism Investigation

To explore the proposed synergistic redox behavior and reaction mechanisms of the newly developed sulfur-functionalized FTN polymer, composite electrodes were prepared using the composition FTN-Pol+S:CB:PVDF in a 50:40:10 weight ratio, as described in Section 2.4.1. This represents the first investigation of the combined electrochemical activity of the FTN-Pol backbone and covalently bound sulfur chains.

In Figure 3.11 a) cyclic voltammograms, performed on the FTN-Pol+S composite electrodes in 1 M $LiPF_6$ dissolved in a 1:1 (v/v) mixture of ethylene carbonate (EC) and dimethyl carbonate (DMC) are presented. The scan rate was set to 0.1 mV s^{-1} over a potential range of 4.0 V to 1.5 V vs. Li/Li^+) for five cycles. The OCV of 3.00 V closely matches that observed for FTN-Pol without sulfur chains, indicating that the equilibrium potential is dominated by the FTN-Pol redox center. A pronounced and reversible oxidation peak (O_1) was observed at 4.00 V, which corresponds to the oxidation of the FTN-Pol backbone. However, in comparison to the unmodified FTN-Pol ($O_1 \approx 3.85$ V), the peak is both shifted and broadened (see Figure 3.2). This shift and broadening may result

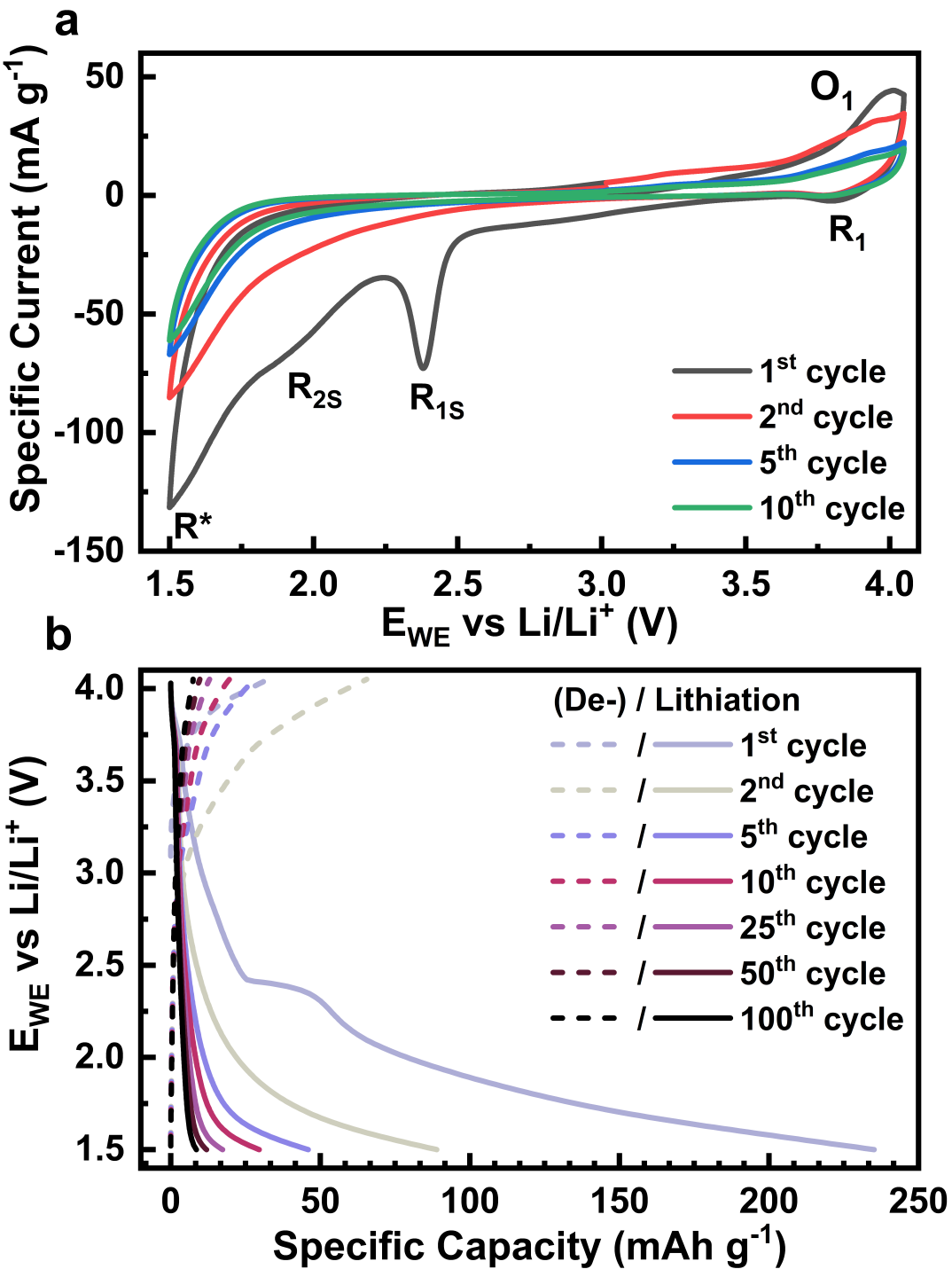


Figure 3.11: Electrochemical characterization of the sulfur-functionalized FTN-Pol composite electrode (FTN-Pol+S:CB:PVDF = 50:40:10 wt%) in 1 M $LiPF_6$ in EC:DMC (1:1 v/v). **a)** CV over 10 cycles at 0.1 mV s^{-1} between 4.0 V and 1.5 V vs. Li/Li^+, showing a dominant oxidation peak at 4.00 V (O_1) attributed to the FTN-Pol backbone. Additional reduction peaks related to sulfur redox activity appear at 2.38 V (R_{S1}) and ≈ 2.00 V (R_{S2}), with an undefined feature (R*) at ≈ 1.5 V. The pronounced redox asymmetry and lack of sulfur oxidation peaks suggest poor reversibility and possible polysulfide dissolution. **b)** GCPL profile recorded at 100 mA g^{-1}, confirming the asymmetric behavior with observable discharge plateaus at 2.39 V (R_{S1}) and a broad low-voltage region below 2.25 V encompassing R_{S2} and R*. Rapid capacity fading over five cycles further supports the occurrence of polysulfide shuttle effects and instability of the sulfur–polymer composite system.

from kinetic limitations caused by the presence of sulfur. Sulfur possesses intrinsically poor electronic conductivity ($\approx 5 \times 10^{-30}\,\mathrm{S\,cm^{-1}}$) [171], which impedes efficient electron transport through the polymer matrix. The corresponding reduction peak (R_1) at 3.79 V, expected to close the redox couple with O_1, is almost absent, suggesting significant redox asymmetry. This could be due to poor charge-transfer kinetics, partial electrode passivation, or the dominance of parasitic side reactions. The resulting redox potential is centered around 3.90 V with an overpotential of 0.2 V. These values are notably shifted compared to pure FTN-Pol. The increased overpotential, approximately three times higher than in the original system, further supports the hypothesis of electron transport hindrance within the modified polymer structure. Additionally, two reduction features attributed to sulfur redox activity were observed: R_{1S} at 2.38 V and R_{2S} around 2.00 V. These peaks seem to be approximately consistent with reference/literature values for sulfur conversion reactions, where R_{1S} corresponds to the reduction of S_8 to higher-order polysulfides (Li_2S_x, $4 < x < 5$) [158]. However, both features are irreversible. An additional low-potential feature (R*) was detected at $\approx$ 1.5 V, which rapidly decreases over the first five cycles, and cannot be clearly assigned to known sulfur or FTN-related redox processes. Reductive decomposition of DOL and DME, which leads to SEI formation, typically begins between $\approx$ 0.6 V and 1.3 V vs. Li/Li^+. Therefore, it is unlikely that this process is responsible for R* [172]. Notably, no sulfur oxidation peaks (O_{S1+2}) are observed during the first cycle, despite their expected appearance around 2.5 V as seen in Figure 3.10 a). Instead, only a very weak oxidation signal appears near 3.3 V. This suggests that poor kinetics may delay the sulfur oxidation process by nearly 1 V. The absence of O_{S1+2} in the first cycle is consistent with the lack of a prior corresponding sulfur reduction process. Nevertheless, even in later cycles, the oxidation peak remains minimal and disappears by approximately the fourth cycle, indicating limited reversibility or active material loss. The poor reversibility of R_{1S}, R_{2S}, and R* may indicate substantial sulfur dissolution into the electrolyte and the onset of polysulfide shuttle effects, phenomena well-documented in lithium–sulfur systems [158, 160]. Although the material was originally designed to suppress sulfur dissolution, as discussed in the introduction, these findings suggest that the mitigation strategy may not have been fully effective.

In Figure 3.11 b) GCPL measurements were carried out under similar conditions. Electrodes were cycled at a current density of $100\,\mathrm{mA\,g^{-1}}$ (approximating a C/6 rate) between 4.0 V and 1.5 V using 1 M $LiPF_6$ in EC:DMC (1:1, v/v) as the electrolyte. The initial OCV of 3.09 V agrees well with the CV findings. A distinct oxidation plateau (O_1) at 3.99 V results in a specific capacity of $66\,\mathrm{mA\,h\,g^{-1}}$. The corresponding reduction plateau (R_1) is only faintly observable, confirming the asymmetric redox behavior also observed

in the CV. Further discharge reveals a reduction plateau at 2.39 V (R_{1S}), contributing approximately 30 mA h g^{-1}, although this process is again irreversible. Below 2.25 V, a broad and undifferentiated plateau extended down to 1.5 V, encompassing contributions from both R_{2S} and R*, and amounting to 180 mA h g^{-1}. The total initial discharge capacity thus reached 235 mA h g^{-1}. However, this capacity shows poor reversibility: it declines to 89 mA h g^{-1} in the second cycle and further to 46 mA h g^{-1} by the fifth cycle. This substantial fading supports the hypothesis of polysulfide dissolution and shuttle mechanisms, as described by Bruce et al. (2011) and Ji et al. (2009) [158, 160].

Despite the incorporation of sulfur chains into the FTN-Pol backbone, the electrochemical measurements reveale significant challenges associated with the irreversibility of sulfur redox reactions. In particular, the rapid capacity fading and the appearance of poorly defined reduction features indicate that it was not possible to effectively immobilize the sulfur species, suppress polysulfide dissolution, or maintain the structural integrity of the cathode. These phenomena are consistent with known shuttle effects commonly observed in lithium–sulfur systems. To address these issues and potentially stabilize the redox behavior of sulfur within the polymer matrix, modifications to the electrolyte composition were explored as a next step.

Electrolyte Variation

The electrochemical performance, stability, and reaction pathways of redox-active polymer systems are strongly affected by the electrolyte composition, especially in systems incorporating sulfur-containing moieties [173–175]. Parameters such as electrolyte salt and solvent properties affect not only ion transport and redox kinetics but also the solubility of intermediate species and the severity of parasitic effects like the polysulfide shuttle. To systematically investigate these effects, two alternative electrolyte systems, 1 M LiTFSI in DOL:DME (1:1, v/v) and 1 M $LiClO_4$ in EC:DMC (1:1, v/v), are evaluated and directly compared to the baseline electrolyte of 1 M $LiPF_6$ in EC:DMC (1:1, v/v). These variations were selected to probe differences in salt dissociation strength, solvent polarity, and known interactions with sulfur species (e.g., shuttle suppression or promotion). This comparison aims to identify electrolyte formulations that enhance the electrochemical reversibility and stability of FTN-Pol systems with integrated sulfur chains, thereby guiding future optimization strategies for energy storage devices.

In Figure 3.12, GCPL measurements and their corresponding derivatives (dQ/dV) are shown which was obtained under conditions similar to those described in Figure 3.11 b). Electrodes were cycled between 4.0 V and 1.5 V at a current density of 100 mA g^{-1}. Data

from Figure 3.12 b) are consistent with the previously reported data (Figure 3.11 b), serving as a reliable basis for comparison. Its derivative plot is shown in Figure 3.12 a). The electrochemical profile in $LiPF_6$/EC:DMC exhibits features closely resembling those observed in cyclic voltammogram (Figure 3.11 a), including an OCV near 3.0 V and a distinct, reversible oxidation peak (O_1) at 4.00 V, corresponding to the oxidation of the FTN-Pol. This peak is both shifted and broadened relative to the single FTN-Pol reference system, indicating altered redox kinetics or electronic interactions likely introduced by the presence of sulfur chains. The associated reduction peak (R_1), observed at 3.80 V, is suppressed, resulting in a redox potential ($E_{1/2}$) of 3.90 V and an overpotential (η) of 0.20 V, both significantly deviating from the sulfur-free system. Additional irreversible reduction events are identified at lower potentials, namely R_{S1} at 2.38 V and R_{S2} around 2.00 V. These are consistent with multi-electron sulfur conversion reactions (e.g., $S_8 \rightarrow Li_2S_x$). However, all redox features decay steadily, with capacity retention falling to $\approx 13\,\%$ after 10 cycles and only 3 % after 400 cycles, underscoring the significant challenges posed by polysulfide dissolution and shuttle effects in $LiPF_6$-based systems [158, 160].

In Figures 3.12 c) and d), galvanostatic charge–discharge measurements and their derivatives are presented for the FTN-Pol + sulfur electrodes cycled in 1 M LiTFSI in DOL:DME (1:1, v/v). The OCV of the system is observed at 2.87 V, slightly lower than that in $LiPF_6$-based electrolyte, indicating a shift in the equilibrium potential possibly due to altered interfacial interactions or solvation effects. A distinct oxidation peak (O_1) appears at 3.96 V, corresponding to FTN-Pol oxidation, which is less broadened and more sharply defined than in $LiPF_6$, indicating more favorable redox kinetics in this electrolyte. The corresponding reduction peak (R_1) at 3.87 V is broad and of low intensity, decays rapidly within the first five cycles, but stabilizing at a very low level up to 400 cycles. Compared to $LiPF_6$, this behavior indicates similar underlying redox asymmetry, but with a faster initial decay likely due to enhanced sulfur dissolution in DOL:DME. The resulting redox potential ($E_{1/2}$) is 3.92 V, with a reduced overpotential of 0.09 V, pointing to improved charge-transfer kinetics in this solvent system. At lower potentials, multiple closely spaced and partially overlapping reduction peaks, collectively denoted R_{S1}, appear at 2.43 V, 2.28 V, and 2.19 V. These are attributed to sulfur conversion reactions and are initially pronounced but decay within the first five cycles, thereafter remaining relatively low but stable up to 400 cycles. Notably, in contrast to $LiPF_6$, a corresponding oxidation peak (O_{S1}) is clearly observed. In the first cycle, O_{S1} appears as a broad feature centered around 2.4 V, becoming significantly sharper and more defined in the second cycle at 2.37 V, but with broad high-voltage shoulders. Due to artifacts in the derivative at 2.3 V, certain data points were excluded for clarity. These artifacts can result from the

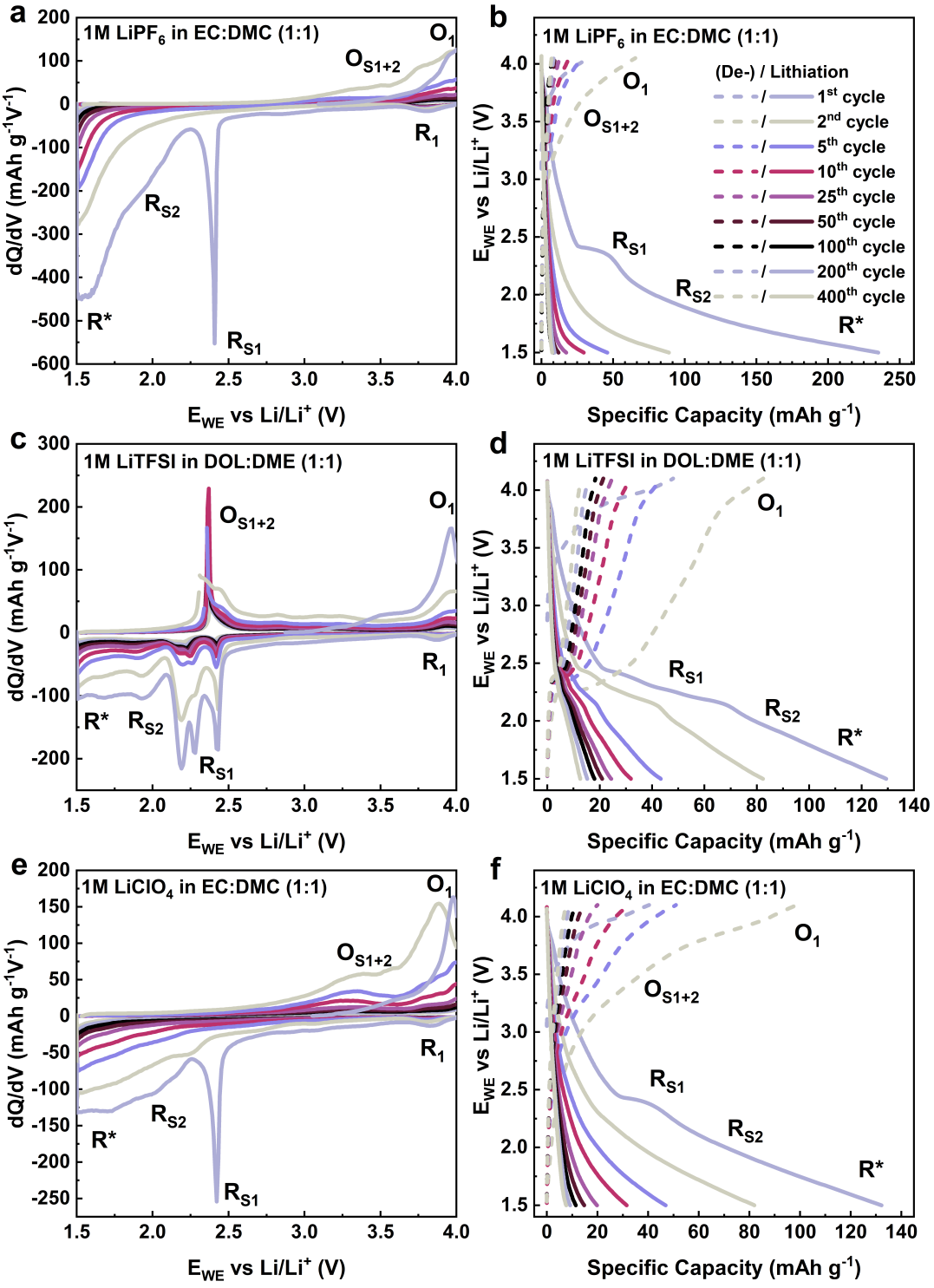


Figure 3.12: Electrochemical performance of FTN-Pol+S electrodes in different electrolyte systems. GCPL profiles (left column) and corresponding differential capacity plots (right column) recorded at 100 mA g^{-1} between 4.0 V and 1.5 V over 400 cycles for: **a)** ,**b)** 1 M LiPF6 in EC:DMC (1:1, v/v), **c)**, **d)** 1 M LiTFSI in DOL:DME (1:1, v/v), and **e)**, **f)** 1 M $LiClO_4$ in EC:DMC (1:1, v/v). Redox features corresponding to FTN-Pol (O_1/R_1) and sulfur (O_S/R_S) are labeled. All systems show partial reversibility of sulfur redox processes, with varying degrees of peak resolution, redox asymmetry, and capacity fading. Capacity retention is highest in the LiTFSI system during early cycles, though long-term stability remains limited in all cases due to polysulfide dissolution and shuttle effects.

axis transformation applied to the GCPL potential plateau plot, where specific capacity was plotted on the x-axis and the working electrode potential (E_{WE}) on the y-axis. This change can lead to situations where the curve no longer represents a proper mathematical function, specifically, when multiple E_{WE} values correspond to a single specific capacity. In such cases, the derivative with respect to E_{WE} is not defined. To avoid misleading features in the derived data, particularly around 2.3 V, the affected data points were excluded from the plot. A exact correspondence between O_{S1} and the individual R_{S1} components remains ambiguous, but their reversible nature suggests partially improved sulfur redox activity in this electrolyte. An additional broad reduction feature appears near 1.94 V, possibly denoted R_{S2}, and extends to 1.5 V (R*), indicative of deeper sulfur reduction processes. In terms of capacity (Figure 3.12 d)), the FTN-Pol oxidation (O_1) contributes approximately 50 mA h g^{-1}, while its corresponding reduction (R_1) accounts for only 4 mA h g^{-1}. The RS1 process, occurring between 2.47 V and 2.14 V, contributes approximately 50 mA h g^{-1}. An additional 50 mA h g^{-1} arises from RS2/R (extending down to 1.5 V), resulting in a total initial discharge capacity of 129 mA h g^{-1}. The oxidation peak OS_1 yields approximately 33 mA h g^{-1}, supporting partial reversibility of the sulfur redox processes. However, all redox features exhibit a rapid decay, retaining only $\approx 25\,\%$ of the initial capacity after 10 cycles and $\approx 10\,\%$ after 400 cycles, reflecting significant long-term capacity fading, likely driven by continuous sulfur loss and shuttle effects in the DOL:DME-based electrolyte.

Figures 3.12 e) and f) present galvanostatic charge–discharge profiles and corresponding derivatives for FTN-Pol + sulfur electrodes cycled in 1 M $LiClO_4$ in EC:DMC (1:1, v/v). The OCV is measured at 3.05 V, nearly identical to that observed for the $LiPF_6$ system, suggesting a similar initial electrochemical equilibrium. In the first cycle, a pronounced and reversible oxidation peak (O_1) appears at 3.98 V, corresponding to the oxidation of FTN-Pol. While initially well-defined, the O_1 peak exhibits a rapid shift to 3.87 V in the second cycle and subsequently moves beyond the measurement window (> 4.0 V), consistent with redox peak evolution due to structural or kinetic changes in the electrode–electrolyte interface. The typical fading behavior observed in previous systems is also evident here. The corresponding reduction peak (R_1) at 3.83 V is present but minimal, with poor symmetry relative to O_1. This pronounced redox asymmetry suggests hindered charge-transfer kinetics or possible passivation processes that impede full reversibility of the FTN redox couple. The resulting average redox potential (E1/2) is 3.91 V, with an overpotential (η) of 0.15 V, both closely matching those of the $LiPF_6$-based system. At lower potentials, a sulfur-associated reduction peak (R_{S1}) emerges at 2.42 V, followed by R_{S2} near 2.00 V and an additional unassigned feature (R*) at 1.5 V, all of which are irreversible and rapidly decay within the first five cycles. The peak positions agree well with both literature and the

$LiPF_6$ reference system, reinforcing their assignment to sulfur conversion reactions. However, the lack of reversibility again points to sulfur dissolution and shuttle effects, which degrade performance over cycling [158, 160]. Notably, no sulfur oxidation peaks (O_{S1+2}) appear in the first cycle, where signals around 2.5 V would be expected based on reference sulfur data (Figure 3.10 a)). Instead, a weak and broad oxidation feature is visible at approximately 3.3 V, suggesting that poor kinetics or altered sulfur redox pathways may shift oxidation processes by nearly 1 V. This behavior closely mirrors the $LiPF_6$ system and is consistent with the absence of a preceding sulfur reduction reaction. Even in subsequent cycles, the sulfur oxidation signal remains weak and disappears entirely by the fifth cycle, indicating poor reversibility and likely active material loss over time. Capacity-wise (Figure 3.12 f), the FTN-Pol oxidation process (O_1) delivers approximately 40 mA h g^{-1}, while its associated reduction (R_1) contributes only 3 mA h g^{-1}. R_{S1} centered at 2.4 V contributes 20 mA h g^{-1}, and R_{S2} along with R* (down to 1.5 V) account for an additional 50 mA h g^{-1}. A weak oxidation feature O_{S1} appears around 3.4 V, contributing approximately 35 mA h g^{-1}. The total initial specific discharge capacity amounts to 132 mA h g^{-1}. However, all redox features decay steadily, with capacity retention falling to approximately 24 % after 10 cycles and only 6 % after 400 cycles, underscoring the significant challenges posed by polysulfide dissolution and shuttle effects in $LiClO_4$-based systems.

3.3.5 Electrochemical Impact of Sulfur Chain Integration into FTN-Pol

In the following, the key electrochemical behaviors observed across different electrolyte systems are summarized, and the interactions between the polymeric and sulfur redox centers, along with their dependence on electrolyte composition, are highlighted.

Retention of FTN-Pol Redox Activity

Across all electrolyte systems, the characteristic oxidation peak (O_1) of FTN-Pol remains a dominant and recurring feature, appearing between 3.96 V and 4.00 V vs. Li/Li^+. This confirms that the oxidation of the conjugated polymer backbone remains electrochemically accessible despite the presence of sulfur. The corresponding reduction process (R_1), however, is significantly suppressed or nearly absent, resulting in large redox asymmetries and overpotentials ranging from 0.09 V (LiTFSI) to 0.2 V ($LiPF_6$). These deviations from ideal reversibility may be attributed to kinetic hindrances, charge trapping, or partial electrode passivation upon cycling.

Sulfur Redox Contributions and Reversibility

The presence of sulfur is further reflected in reduction processes observed between ≈2.0 and 2.4 V vs. Li/Li^+, associated with the stepwise conversion of elemental sulfur (S_8) to Li_2S via polysulfides (Li_2S_x, with x typically between 4 and 5). However, the reversibility and persistence of these redox signals vary considerably across the electrolytes:

In $LiPF_6$ (EC:DMC): Sulfur reduction peaks (R_{S1}, R_{S2}) are observed but are largely irreversible. The sulfur oxidation process (O_{S1+2}), expected near 2.5 V, is delayed and appears weakly at ≈3.3 V. These features fade within the first 5–10 cycles, suggesting poor kinetics and significant sulfur loss due to dissolution and polysulfide shuttling.

In LiTFSI (DOL:DME): The redox behavior of sulfur is notably more pronounced. A composite sulfur oxidation peak (O_{S1+2}) emerges at ≈2.37 - 2.43 V during the early cycles, indicating more favorable redox kinetics in this ether-based electrolyte. Multiple sharp and reversible reduction peaks (R_{S1}) within this range contribute meaningfully to the total capacity. However, these decay rapidly within the first 5 cycles before reaching a stable but low-intensity plateau up to 400 cycles.

In $LiClO_4$ (EC:DMC): Sulfur redox features resemble those in $LiPF_6$, with minimal oxidation activity and mostly irreversible reduction peaks. Pronounced O_{S1+2} signals are absent within the expected voltage window. Only weak sulfur oxidation (O_{S1+2}) occurs at ≈3.4 V, further indicating poor sulfur oxidation and limited reversibility.

Electrolyte-Dependent Capacities and Stability

The total initial specific capacities vary significantly among the electrolytes:

$$1\,\text{M } LiPF_6 \text{ (EC:DMC)}: \approx 235\,\text{mA h g}^{-1}$$

$$1\,\text{M LiTFSI (DOL:DME)}: \approx 129\,\text{mA h g}^{-1}$$

$$1\,\text{M } LiClO_4 \text{ (EC:DMC)}: \approx 132\,\text{mA h g}^{-1}$$

While $LiPF_6$ enables the highest initial capacity, the resulting poor performance indicates sulfur oxidation kinetics and severe capacity fading, attributed to parasitic reactions and polysulfide dissolution. When using LiTFSI-electrolyte the electrodes show lower capacity but better-defined and more reversible sulfur redox features in the early cycles, pointing to its potential for future optimization. $LiClO_4$ displays intermediate performance, with behavior largely similar to $LiPF_6$ but no advantage in sulfur redox activity. All systems demonstrate a steep decline in capacity within the first 10 cycles, stabilizing at

approximately 3 – 10 % of the initial capacity after 400 cycles. This highlights the general challenge of sulfur integration in polymer systems: while additional redox-active centers can enhance capacity, their long-term contribution is limited by solubility issues and interfacial instability.

Summary and Outlook

The observations support that sulfur chain integration introduces additional redox activity but also introduces significant complexity. The electrolyte plays a critical role in dictating the accessibility, reversibility, and stability of sulfur redox reactions. Among the tested systems, batteries with LiTFSI in DOL:DME show the most promising behavior with regard to sulfur utilization, albeit at the cost of lower initial capacity. Future efforts could focus on mitigating sulfur loss through physical confinement strategies or solid-electrolyte interphases, as well as exploring hybrid electrolytes that balance kinetic accessibility with redox stability.

3.4 Electrochemical Effects of Terthiophene Functionalization in FTN-Based Redox Polymers

To improve the energy storage capacity of FTN-Pol, it is essential to introduce additional redox-active units without compromising electronic conductivity or cycling stability. While FTN-Pol exhibits high redox potential and excellent reversibility, its relatively low specific capacity limits practical application. One strategy to address this is the incorporation of conjugated, redox-active thiophene derivatives, such as terthiophene (3T), which are known for their electrochemical activity and π-conjugated backbone, potentially enhancing both charge delocalization and faradaic contribution [124–126]. Integrating 3T units into the FTN-Pol framework aimes to (i) increase the total number of redox-active sites, (ii) extend the operational voltage window, and (iii) assess the trade-off between capacity enhancement and long-term stability. Moreover, sulfur-containing conjugated moieties such as 3T offer a platform to study sulfur redox chemistry and associated irreversible processes within polymeric hosts. The following section explores how introducing of 3T alters the electrochemical behavior of FTN-Pol, with particular focus on redox kinetics, capacity evolution, and cycling durability.

3.4.1 Electrochemical Behavior of FTN-Pol Functionalized with Terthiophene (3T)

To explore the redox mechanism and electrochemical contributions of terthiophene (3T) integrated into the FTN-Pol backbone, composite electrodes were fabricated with a FTN-Pol+3T:CB:PVDF weight ratio of wt% 50:40:10, as described in Section 2.4.1. This subsection presents the first detailed study on the synergistic electrochemical behavior of 3T-functionalized FTN-Pol as a cathode material in lithium-ion batteries.

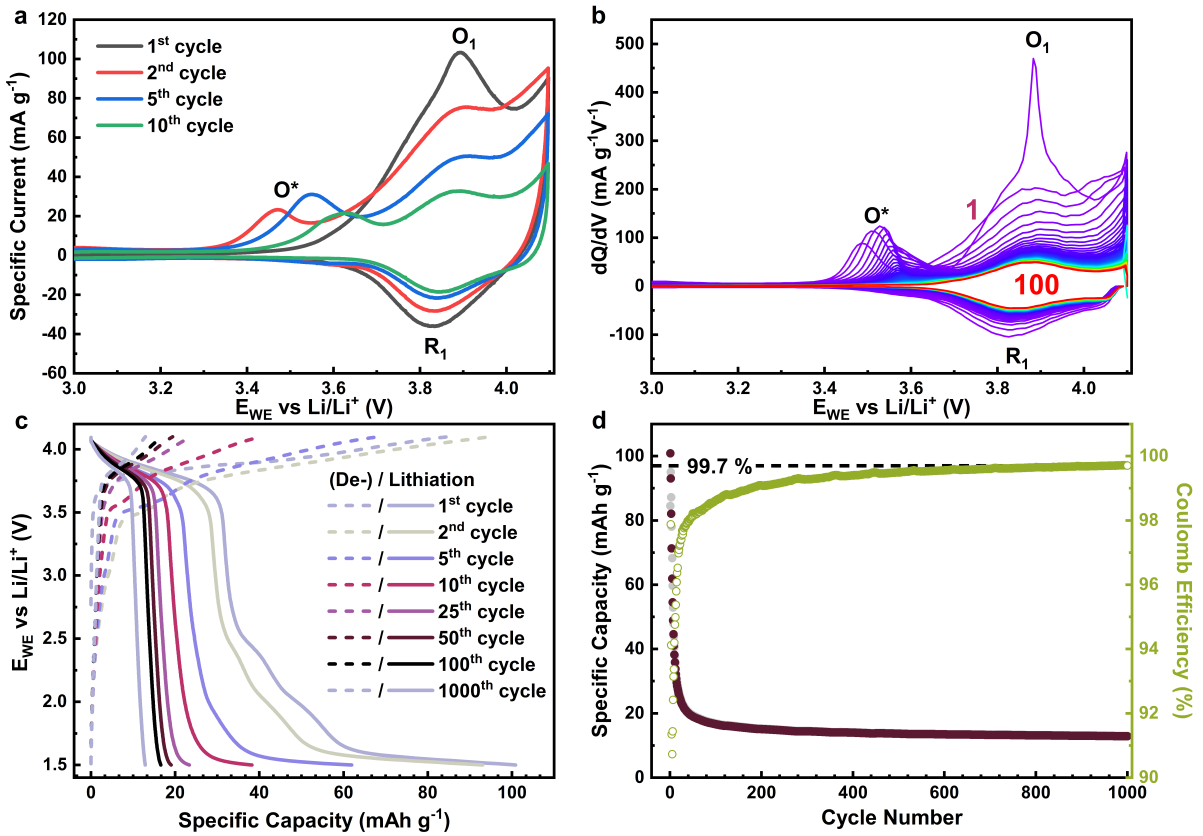


Figure 3.13: Electrochemical characterization of the FTN-Pol+3T composite electrode in a lithium-ion battery configuration. **a)** CV over ten cycles at a scan rate of 0.1 mV s^{-1} between 3.0 V and 4.1 V vs. Li/Li^+ reveals redox peaks associated with FTN oxidation (O_1) and a newly emerging oxidation feature (O*) ascribed to terthiophene units. **b)** Differential capacity plots (dQ/dV) derived from galvanostatic cycling at 100 mA g^{-1} highlight a comparable redox profile with reversible FTN activity and transient terthiophene-related oxidation. **c)** GCPL profiles display initial multi-step capacity contributions from both FTN and 3T, including low-voltage discharge features attributed to sulfur reduction. **d)** Cycling performance and Coulombic efficiency over 1000 cycles show an initial specific capacity of 101 mA h g^{-1} with a marked decline in the first 50 cycles, stabilizing at 12.9 mA h g^{-1} beyond 600 cycles, accompanied by a high Coulombic efficiency exceeding 99.7 %.

Cyclic voltammetry was conducted in 1 M $LiPF_6$ dissolved in a 1:1 (v/v) mixture of EC and DMC, as shown in Figure 3.13 a). The scan rate was $0.1\,mV\,s^{-1}$ within a voltage window of 3.0 - 4.1 V vs. Li/Li^+ over ten consecutive cycles. The OCV prior to the first scan was measured at 2.79 V.

The initial anodic sweep shows a pronounced oxidation peak (O_1) at 3.89 V, consistent with the oxidation of the FTN-Pol framework. This peak exhibits a strong intensity decay over subsequent cycles. It is accompanied by a shoulder-like feature, similar to those observed for bare FTN-Pol, confirming its origin within the polymer rather than the 3T moieties. On the cathodic side, a reduction peak (R_1) emerges at 3.83 V, which exhibits a lower intensity than its oxidative counterpart and a more gradual decay. These redox peaks yields a redox potential ($E_{1/2}$) of 3.86 V and an overpotential (η) of 0.06 V, indicative of moderate reversibility for the FTN-Pol system. Interestingly, from the second cycle onward, a new oxidation feature (O*) develops at 3.47 V, with no corresponding reduction peak. This asymmetry suggests an irreversible oxidation process, likely associated with sulfur atoms in the 3T units, possibly irreversible stabilized through PF_6^- coordination or other side reactions. As cycling progressed, O* shifts to higher voltages, evolving from 3.46 V (cycle 2) to 3.63 V (cycle 10), with its amplitude initially increasing before diminishing, suggesting a transient redox process likely tied to 3T's contribution.

To further investigate the redox mechanisms, differential capacity plots (dQ/dV) extracted from galvanostatic charge–discharge profiles conducted between 3.0 V and 4.1 V at $100\,mA\,g^{-1}$ (approximately 1 C rate) are shown in Figure 3.13 b). The dQ/dV traces mirrors the CV results, with an initial OCV of 2.77 V. The dominant oxidation and reduction peaks (O_1/R_1) is observed at 3.88 V and 3.84 V, respectively, yielding a slightly improved overpotential ($\eta = 0.04$ V), which indicates enhanced kinetics under constant current operation. The O* feature, as in CV, was detected beginning at 3.48 V in early cycles, with a peak shift and growth through cycle 10, after which the amplitude steadily declined. By cycle 25, the O* peak was no longer visible, indicating a loss of electrochemical activity possibly due to degradation or irreversible transformation of the 3T units.

Figure 3.13 c) presents the charge–discharge curves recorded between 1.5 and 4.1 V at $100\,mA\,g^{-1}$ over 1000 cycles. The initial OCV was 2.75 V. The first charge process exhibits a plateau near 3.9 V, delivering approximately $85\,mA\,h\,g^{-1}$, aligning well with the O_1 peak in CV. During discharge, a plateau at ≈ 3.7 V corresponding to $\approx 31\,mA\,h\,g^{-1}$ (R_1), while a deeper discharge down to 1.5 V reveals additional plateaus. Between 2.5 V and 1.9 V, a minor shoulder disappears after the fifth cycle, possibly linked to the reduction of sulfur species forming intermediate lithium polysulfides (Li_2S_x), akin to RS_1

and RS_2 processes. A more pronounced reduction plateau (R*) extending to 1.5 V contributes $\approx 40\,\mathrm{mA\,h\,g^{-1}}$, bringing the initial discharge capacity close to $100\,\mathrm{mA\,h\,g^{-1}}$. Upon charging, no corresponding low-voltage oxidation (i.e., OS_1) emerges. However, a modest oxidation plateau at $\approx 3.6\,\mathrm{V}$, likely associated with 3T oxidation, delivers $\approx 15\,\mathrm{mA\,h\,g^{-1}}$. Overall, every capacity contribution decays evenly, dropping to 28 % of the initial value after 10 cycles and only 13 % after 1000 cycles.

Figure 3.13 d) shows the long-term cycling performance and Coulombic efficiency of FTN-Pol+3T at $100\,\mathrm{mA\,g^{-1}}$. The initial specific capacity reaches $101\,\mathrm{mA\,h\,g^{-1}}$, representing 87 % of the theoretical capacity. A sharp capacity loss occurs in the first 50 cycles, stabilizing at $19.2\,\mathrm{mA\,h\,g^{-1}}$ (17 %). Beyond 600 cycles, the capacity stabilizes at $12.9\,\mathrm{mA\,h\,g^{-1}}$ (13 %) and remains at this level through the 1000th cycle. Despite the significant capacity fade, the Coulombic efficiency rapidly stabilizes, reaching 99.7 % after 600 cycles. This suggests high reversibility of the remaining redox-active sites and minimal parasitic reactions, highlighting the electrochemical robustness of the FTN-Pol framework even after partial degradation of the 3T components.

3.4.2 Comparison with Bare FTN-Pol: Influence of Terthiophene Incorporation

The electrochemical analysis of FTN-Pol functionalized with terthiophene (3T) reveals distinct modifications in redox behavior and cycling performance compared to bare FTN-Pol, as previously studied. Both measurements display a characteristic high-voltage redox couple associated with the FTN moieties, with oxidation peaks (O_1) observed at ≈ 3.88 - 3.89 V and reduction peaks (R_1) near 3.83 - 3.84 V vs. Li/Li^+. The composite retains the average redox potential $E_{1/2} \approx 3.86\,\mathrm{V}$) and exhibits a low overpotential ($\eta = 0.04$ - 0.06 V), indicating that the incorporation of 3T does not impede the intrinsic redox activity of the FTN units. However, the presence of 3T introduces new and irreversible redox processes. In FTN-Pol+3T, an additional oxidative feature (O*) appears at $\approx 3.47\,\mathrm{V}$ from the second cycle onward, which is absent in the bare FTN-Pol. This peak progressively shifts toward higher potentials over early cycles, ultimately disappearing by cycle 25. Partial oxidation of the sulfur atoms in the 3T moieties likely causes this behavior, possibly followed by irreversible side reactions or passivation (e.g., PF_6^- complexation). The absence of a corresponding reduction peak reinforces the hypothesis that 3T undergoes non-reversible oxidation processes. Capacity-wise, FTN-Pol+3T delivers a notably higher initial specific capacity of $101\,\mathrm{mA\,h\,g^{-1}}$, compared to the typical $26\,\mathrm{mA\,h\,g^{-1}}$ reported for bare FTN-Pol. The capacity gain is attributed to additional faradaic contributions from the terthiophene

groups, particularly the low-voltage reduction process (R*) extending to 1.5 V. However, this enhancement is short-lived, with significant capacity decay occurring within the first 50 cycles, dropping to 19.2 mA h g^{-1} and further stabilizing at only 12.9 mA h g^{-1} after 1000 cycles. In contrast, bare FTN-Pol typically demonstrates a more stable capacity retention profile, albeit at lower initial values, highlighting a trade-off between initial energy density and cycling stability introduced by 3T functionalization. Notably, the Coulombic efficiency (CE) of FTN-Pol+3T stabilizes at 99.7 % beyond 600 cycles, matching the high reversibility reported for FTN-Pol alone. This suggests that while 3T enhances initial capacity, it may undergo irreversible transformations, leaving behind a redox-stable FTN backbone that governs the long-term cycling behavior.

In summary, terthiophene incorporation into FTN-Pol enables temporary capacity enhancement through additional redox-active sites, but also introduces irreversible processes that limit long-term stability. These findings provide insight into the structure–performance relationship of redox-active polymer composites and underline the need for further molecular tuning to stabilize 3T-derived contributions.

3.5 Conclusion and Outlook

The development and electrochemical evaluation of nitrogen-centered triphenylamine analogues (N-HTAs) as redox-active units show that structural modifications to FTN-Pol and its derivatives significantly affect their electrochemical performance. The findings collectively underscore the tunability and trade-offs inherent in the molecular design of triphenylamine-based cathode materials. The base system, FTN-Pol, demonstrates that N-HTAs can serve as stable and efficient redox-active backbones in polymeric cathodes. The rigid spirocyclic structure provides a defined microporous network that promotes redox accessibility while suppressing side reactions, as evidenced by the high Coulombic efficiency (99.6 %) and long-term cycling stability. Although its specific capacity is modest due to the higher molecular weight of the redox unit, FTN-Pol achieves a utilization rate of 87 % of its theoretical capacity, outperforming some conventional triphenylamine-based systems in this respect. These results confirm the value of rigid, conjugated architectures for enabling stable charge transport and redox reversibility in organic cathode materials. Building on this foundation, the integration of sulfur chains into FTN-Pol was investigated as a strategy to enhance capacity by adding complementary redox-active centers. The data reveal that sulfur incorporation does indeed introduce additional redox features, particularly in the voltage range of 2.0 – 2.4 V vs. Li/Li^+. However, the performance

strongly depends on the electrolyte system used. Ether-based electrolytes (1 M LiTFSI in DOL:DME) supports more reversible sulfur redox processes compared to carbonate-based systems ($LiPF_6$, $LiClO_4$ in EC:DMC), which suffered from rapid capacity fading and poor reversibility due to polysulfide dissolution and shuttling. Even in the best case, sulfur contributions were short-lived, with only $\approx 3-10\,\%$ of the initial capacity retained after 400 cycles. These results highlight the challenges of combining sulfur chemistry with redox polymers, including interfacial instability and the need for improved sulfur confinement strategies. In a complementary approach, terthiophene (3T) functionalization of FTN-Pol aimed to enhance initial capacity through π-conjugated sulfur-containing moieties. The resulting FTN-Pol+3T composite exhibited a significant increase in initial capacity ($101\,\mathrm{mA\,h\,g^{-1}}$), stemming from additional faradaic contributions at low voltages. However, this benefit was counterbalanced by pronounced capacity fading within the first 50 cycles, attributed to irreversible oxidation processes involving the 3T units. Despite this decay, the long-term Coulombic efficiency remained high (99.7 %), indicating that the redox activity ultimately reverted to the stable FTN backbone. The findings illustrate a fundamental limitation: while capacity can be enhanced through molecular augmentation, long-term electrochemical stability often suffers due to irreversible side reactions or structural degradation.

In conclusion, the studies presented in this chapter illustrate the potential and complexity of molecular engineering in triphenylamine-derived cathode materials. The core FTN-Pol platform provides a stable, redox-efficient scaffold, while functionalization strategies such as sulfur chain addition or 3T incorporation offer increased energy density, but at the cost of reversibility and long-term stability. These results emphasize the importance of balancing capacity, kinetics, and durability through thoughtful structural design.

Future work should prioritize the stabilization of additional redox-active groups, especially sulfur-based and thiophene-based moieties, through advanced confinement techniques (e.g., covalent binding, nanoencapsulation, or network formation) and interface engineering. Hybrid electrolytes or solid-state systems may mitigate polysulfide dissolution and improve redox selectivity. Moreover, extending the concept of N-centered redox units to other rigid, π-conjugated frameworks could unlock new design principles for next-generation organic cathodes with tunable redox properties, high voltage windows, and improved energy densities. Ultimately, the continued refinement of such molecular architectures will be essential for the realization of sustainable and high-performance organic lithium-ion batteries.

4 Decoupling Photothermal Effects in Photo-Enhanced $LiMn_2O_4$ Battery

Recent studies have demonstrated that $LiMn_2O_4$ (LMO) electrodes exhibit enhanced electrochemical performance under illumination, a phenomenon attributed to photo-induced charge carrier dynamics [176]. However, light exposure also may cause local heating, making it challenging to disentangle the contributions of photonic and thermal effects. In this thesis, the influence of light and temperature on the electrochemical behavior of LMO is systematically studied by decoupling these two factors through controlled experiments.

4.1 Inorganic Cathode Materials: State of the Art

4.1.1 Tranistion Metal Oxides

Transition metal oxides are among the most widely studied cathode materials for lithium-ion batteries due to their high energy density, structural versatility, and ability to reversibly intercalate lithium ions. These compounds, typically involving metals such as cobalt, nickel, manganese, and vanadium, exhibit diverse electrochemical properties that can be tuned through doping and structural modification. As the demand for higher-performance and more sustainable energy storage grows, transition metal oxides continue to play a critical role in advancing next-generation lithium-ion battery technologies.

$LiCoO_2$

Among the widely studied transition metal oxide cathode materials, lithium cobalt oxide ($LiCoO_2$) was one of the earliest introduced and remains a foundational material in lithium-ion batteries (LIBs). $LiCoO_2$ offers a high energy density and a theoretical specific capacity of approximately $274\,\mathrm{mA\,h\,g^{-1}}$. However, it suffers from thermal instability at elevated voltages, limiting its long-term safety and reliability in high-energy applications [177]. An alternative to $LiCoO_2$ for next-generation LIBs is lithium nickel oxide ($LiNiO_2$). Although it only gained significant attention in the past two decades, $LiNiO_2$ provides a higher

practical capacity of around 200 mA h g^{-1}. One mayor drawback is that its synthesis poses considerable challenges, particularly due to lithium volatilization during high-temperature calcination, which hinders the formation of stoichiometric $LiNiO_2$. The material was originally designed by Dyer in 1954 [178] and later extensively investigated in the 1990s by Dahn et al. as a potential replacement for $LiCoO_2$ [179, 180]. Nickel's lower cost and greater abundance relative to cobalt make $LiNiO_2$ economically advantageous. It is also isostructural to $LiCoO_2$, enabling facile lithium intercalation [178]. Despite these benefits, $LiNiO_2$ suffers from poor thermal stability and limited cycle life [181].

Vanadium Oxides

Another significant class of cathode materials includes vanadium oxides (V_xO_y), which have been extensively explored for LIB applications. For instance, vanadium oxide (V_6O_{13}) doped with aluminum or iron has shown improved electrochemical performance, achieving an initial specific discharge capacity of 427 mA h g^{-1} [182]. Similarly, doping V_6O_{13} with aluminum and sodium led to enhancements in both cycling stability and discharge capacity [183]. Vanadium pentoxide (V_2O_5) is regarded as one of the most promising vanadium-based cathode materials for a variety of battery chemistries, including LIBs, sodium-ion batteries (SIBs), and magnesium-ion batteries (MgIBs). It is valued for its low cost, inherent safety, high lithium-ion storage capacity, and natural abundance [97]. For example, rod-like V_2O_5 structures have demonstrated specific capacities of 255 mA h g^{-1} [184]. Furthermore, copper-doped V_2O_5 exhibited increased cell volume and oxygen vacancies in the crystal lattice, resulting in an enhanced discharge capacity of 293 mA h g^{-1}, compared to 236 mA h g^{-1} for the undoped counterpart [185]. In another approach, the incorporation of graphene with monolayer V_2O_5 has been proposed as a promising cathode configuration, offering superior cycling stability and electrical conductivity [186]. Additionally, $Li_{1+x}V_3O_8$ has gained attention as an advanced vanadium-based cathode material. This compound is known for its excellent safety characteristics, high theoretical capacity and low environmental impact, making it a strong candidate for sustainable LIB technologies [187].

4.1.2 Manganese-Based Oxides

The second major class of cathode materials for LIBs is represented by the family of manganese-based oxides, commonly denoted as $Li_xMn_yO_z$. Extensive research has been conducted on various compositions within this group due to their promising electrochemical performance.

Li_2MnO_3

Carbon-coated lithium manganese oxide (Li_2MnO_3) has demonstrated excellent rate capability and a high discharge capacity of approximately 280 mA h g^{-1} at a current density of 10 mA g^{-1} [188]. Furthermore, hollow-structured composites of xLi_2MnO_3 · (1-x)$LiNiO_2$ ($x = 0.3$ - 0.7) have been investigated, exhibiting a stable discharge capacity around 210 mA h g^{-1} [189]. $LiNi_{0.5}Mn_{1.5}O_4$, a high-voltage spinel compound, has emerged as another promising cathode material due to its high power and energy density. When modified with 0.5 wt% Al_2O_3, the resulting material exhibited improved Li^+ diffusion coefficients, as well as enhanced cycling stability and rate performance [190]. Co-doping of $Li_{1.2}Ni_{0.2}MnO_2$ with Al and B also resulted in superior cycling performance, with a discharge capacity of 120 mA h g^{-1} at 5 C and a capacity retention of 89 % after 100 cycles at 1 C [191]. Another variant, $Li_{1.2}Mn_{0.6}Ni_{0.2}O_2$, delivered an initial discharge capacity of 266 mA h g^{-1} at 20 mA g^{-1} and maintained approximately 220 mA h g^{-1} after 50 cycles at 50 mA g^{-1} [192]. Sun et al. synthesized $LiNi_{0.5}Mn_{1.5}O_4$ using MnO_2, leading to exposure of 111 crystal facets and suppressed Mn dissolution. The resulting material displayed high tolerance to ultrafast lithium-ion insertion/extraction, retaining 85 % of the maximum capacity (92 % initial) after 1500 cycles at 30 C, with an average coulomb efficiency of 97 % [193]. Similarly, $LiMn_{1.8}Ni_{0.2}O_4$ synthesized from MnOOH exhibited higher phase purity and a discharge capacity of 122 mA h g^{-1}, with over 80 % capacity retention at 5 C [194].

$LiNiMnCoO_2$, NMC

Lithium nickel cobalt manganese oxides ($LiNiMnCoO_2$, NMC) form another notable class of cathode materials. $LiNi_{0.5}Mn_{0.3}Co_{0.2}O_2$ synthesized through a polymer-assisted chemical solution process exhibited an initial capacity of 189 mA h g^{-1} at 0.05 C [195]. A gradient-structured version of the same composition, prepared via co-precipitation, achieved over 90 % capacity retention after 100 cycles at 5 C, with excellent thermal stability [184].

4.1.3 $LiMn_2O_4$ Spinel

Another widely studied composition, Lithium manganese oxide $LiMn_2O_4$ (LMO), is noted for its favorable cyclic stability, capacity retention, and cost-effective synthesis. Lithium manganese oxide ($LiMn_2O_4$), which crystallizes in a spinel structure belonging to the Fd3m space group, has been widely recognized as a promising cathode material for LIBs, primarily due to the natural abundance of manganese and its environmental friendliness [196]. As illustrated in Figure 4.1, the crystal structure of spinel $LiMn_2O_4$ features Li^+

ions located at the tetrahedral 8a sites, while Mn^{3+}/Mn^{4+} ions occupy the octahedral 16d sites within a cubic close-packed arrangement of O^{2-} anions [197]. The Li^+ ions at the 8a sites migrate through a three-dimensional (3D) diffusion network during lithiation and delithiation processes [198] according to:

$$LiMn_2O_4 \rightarrow Li_{(1-x)}Mn_2O_4 + xLi^+ + xe^- \qquad (0 < x < 1) \tag{4.1}$$

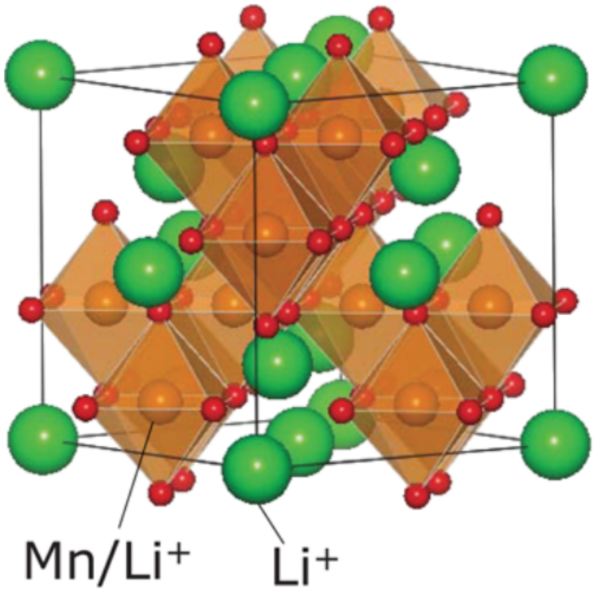


Figure 4.1: Schematic illustration of the spinel crystal structure of $LiMn_2O_4$, highlighting the arrangement of lithium ions (green), manganese ions (orange), and oxygen atoms (red) within the three-dimensional lattice framework that contributes to its electrochemical properties. Adapted from [199].

Reported initial and reversible discharge capacities were $115\,mA\,h\,g^{-1}$ and $105\,mA\,h\,g^{-1}$, respectively, at a rate of 0.1 C [200]. Additionally, Al-doped $LiMn_2O_4$ has been explored for its enhanced electrochemical stability. Increasing the aluminum content led to reductions in particle size and lattice parameters, improving life-cycle performance. Specifically, a doping level of 16 % yielded a specific capacity of $101\,mA\,h\,g^{-1}$ at 0.5 C and a capacity retention of 94 % [201].

4.2 Synthesis

Polycrystalline $LiMn_2O_4$ was synthesized using a conventional solid-state reaction route by Yuan[1], with synthesis conditions adapted from several established protocols reported in the literature [202–204]. A more detailed description of the synthesis procedure can be found in reference [205]. Stoichiometric quantities of Li_2CO_3 (99 %, Sigma-Aldrich) and Mn_2CO_3 (99.9 %, Sigma-Aldrich) were thoroughly homogenized using an agate mortar to ensure uniform distribution of the precursors. The mixed powders were subjected to a multi-step thermal treatment under ambient air with continuous air flow. An initial calcination was conducted at 500 °C for 1 h, followed by an additional 2 h treatment, with intermediate manual grinding to enhance reactivity and phase development. Subsequently, a final high-temperature calcination step was carried out at 800 °C for 48 h, intended to promote the crystallization of the spinel structure and eliminate any remaining carbonate species. The sintering parameters were critically optimized to avoid the formation of secondary phases. The phase purity and crystallographic integrity of the synthesized $LiMn_2O_4$ are confirmed in the work by Yuan [205].

4.3 Electrochemical Characterization

4.3.1 Electrochemical Baseline Behavior of $LiMn_2O_4$ Electrodes

The electrochemical behavior of $LiMn_2O_4$ (LMO) was studied using cyclic voltammetry (CV) and galvanostatic charge–discharge (GCPL) techniques in lithium-ion half-cells. Composite working electrodes were prepared by mixing LMO (75 wt%), carbon black (CB, 15 wt%), and polyvinylidene fluoride (PVDF, 10 wt%) as binder (see Methods 2.4.1). Electrochemical measurements were carried out using CR2032-type coin cells with lithium metal as the reference electrode and 1 M $LiPF_6$ in ethylene carbonate/dimethyl carbonate (EC/DMC, 1:1 vol. %) as electrolyte[2].

CV scans were recorded in the potential window of 3.4 – 4.5 V vs Li/Li^+ at a scan rate of 0.1 mV s^{-1} (Figure 4.2 a). The voltammograms exhibit two prominent oxidation peaks at 4.09 V (O_1) and 4.20 V (O_2), along with corresponding reduction peaks at 3.93 V (R_1) and 4.05 V (R_2), which are characteristic of the spinel LMO structure [197]. These features correspond to the stepwise intercalation/deintercalation of Li^+ ions into and out of the

[1] Kirchhoff Institute for Physics, Heidelberg University

[2] Electrochemical data in this work are subject to an estimated uncertainty of 5 – 10 %, primarily due to manual electrode preparation (weighing accuracy, slurry homogeneity, and mass loading), as explained in Section 2.4.1.

tetrahedral 8a sites within the spinel lattice [206, 207]. A shoulder at 3.85 V observed during the first reduction cycle (R_1) disappears in subsequent scans, likely due to the irreversible reduction of minor impurities. The redox peak positions remain largely stable over 10 cycles, with only a slight decrease in the intensity of peak O_1, suggesting a high degree of reversibility. The average redox potentials, calculated as the mean of the respective oxidation and reduction peaks, are $E_{1/2}(1) = 4.01 \pm 0.03$ V and $E_{1/2}(2) = 4.12 \pm 0.03$ V. The corresponding overpotentials, $\eta_1 = 0.08 \pm 0.03$ V and $\eta_2 = 0.07 \pm 0.03$ V, were determined according to the definitions provided by Bard and Faulkner [63], with peak fitting used to estimate standard deviations.

Complementary GCPL cycling was performed at a current density of 100 mA g^{-1} ($\approx 2/3$ C-rate) within the same voltage window (Figure 4.2 b). The initial charge capacity was 112 mA h g^{-1}, corresponding to 76 % of the theoretical capacity, and decreased to 82 mA h g^{-1} by the 100th cycle. In the first cycle, peak O_1 accounted for approximately 56 % of the capacity, decreasing to 45 % by the fifth cycle and then stabilizing, consistent with CV observations. Further insight into redox processes was gained through derivative analysis of the charge/discharge profiles (Figure 4.2 c), yielding refined redox potentials of $E_{1/2}(1) = 4.01 \pm 0.01$ V and $E_{1/2}(2) = 4.13 \pm 0.01$ V, with associated overpotentials $\eta_1 = 0.03 \pm 0.01$ V and $\eta_2 = 0.03 \pm 0.01$ V. While redox potentials from CV and GCPL are in agreement with each other, the higher overpotentials in CV are attributed to its scan rate–dependent kinetic nature [208, 209]. An anomaly in the O_1 peak during the first GCPL cycle suggests an irreversible process limited to the initial charge, and is therefore not discussed further. These results indicate the consistency of the synthesized LMO's electrochemical behavior with previously reported characteristics in the literature [176, 210, 211].

4.3.2 Reference Study: Photo-Induced Effects in $LiMn_2O_4$ (Lee et al.)

In a recent study, Lee et al. demonstrated that photo-illumination can significantly accelerate the charging kinetics of lithium-ion batteries utilizing spinel $LiMn_2O_4$ (LMO) as the cathode material [176]. Their findings suggest that light exposure under constant voltage conditions enhances the current response. However, their experimental design presents challenges in decoupling the effects of light-induced charge excitation from photothermal contributions.

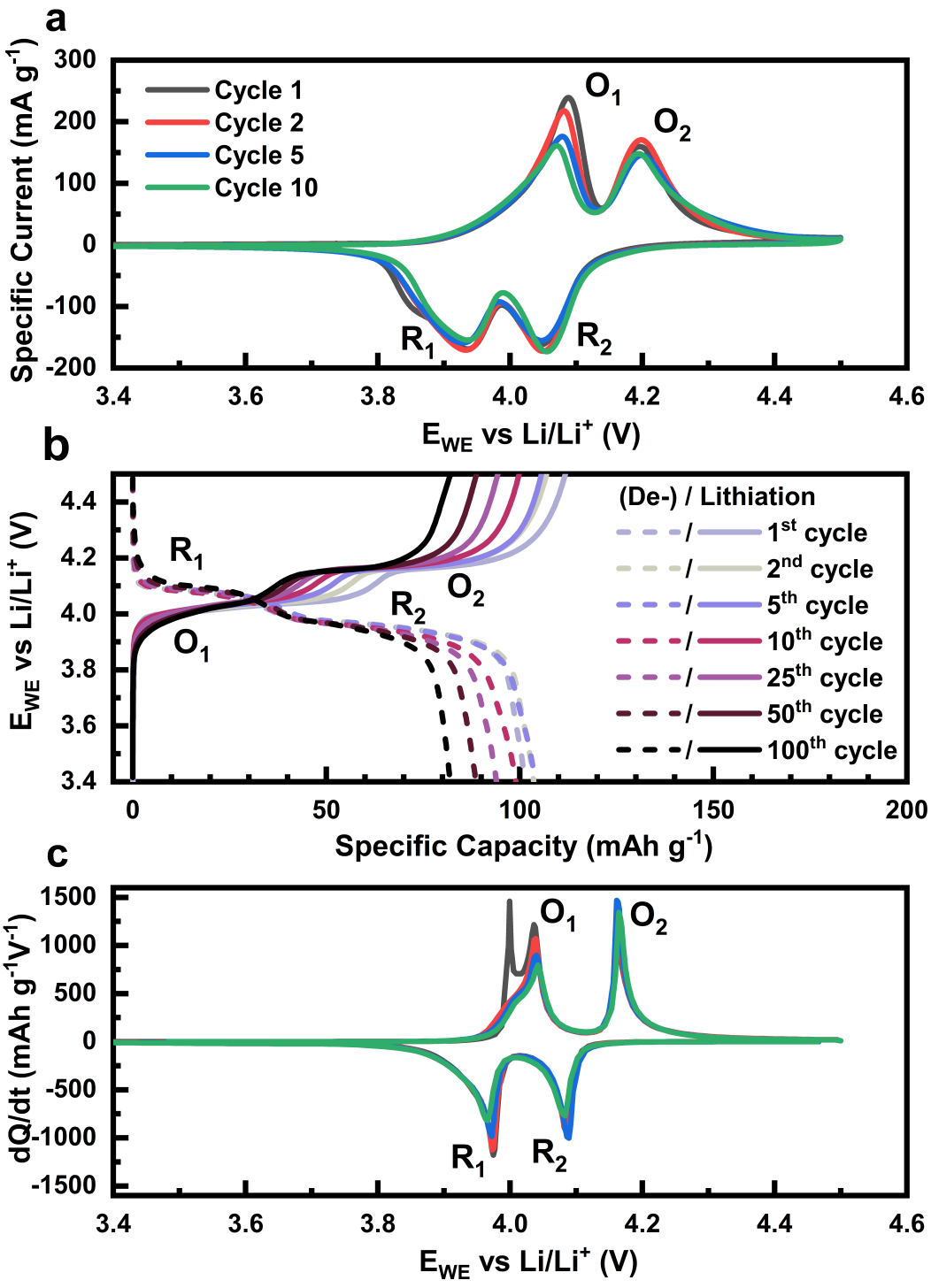


Figure 4.2: a) CV of LMO based composite electrodes (75 wt%) with 1 M $LiPF_6$ and a scan rate of 0.1 mV s^{-1} in the voltage range of 3.4 - 4.5 V. **b)** Galvanostatic charge and discharge profiles of selected cycles with a current density of 100 mA g^{-1} ($\approx$ 2/3 C-rate). **c)** Selected derivatives of galvanostatic charge/discharge measurements with a current density of 100 mA g^{-1} ($\approx$ 2/3 C-rate) in the voltage range of 3.4 - 4.5 V.

Electrochemical measurements were performed under both dark and illuminated conditions using a 300 W Xenon arc lamp (Atlas Specialty Lighting) with an IR filter to minimize unwanted heating. The spectral range of the light source spanned 300 - 1100 nm, with less than 5 % of its energy in the UV region. Despite IR filtering, a modest temperature increase of $\approx 7\,^{\circ}\mathrm{C}$ was observed at 1 SUN intensity ($100\,\mathrm{mW\,cm^{-2}}$), measured via an IR thermometer. To evaluate thermal effects separately, control experiments were conducted by heating the open cell to elevated temperatures in the absence of light. The observed increase in charging current under these conditions was significantly smaller than under illumination, indicating a non-negligible but limited role of temperature in enhancing electrochemical performance. CA measurements were carried out by applying a constant voltage of 4.07 V versus Li/Li^+ using a Gamry potentiostat and a Solartron SI1260 analyzer. The LMO electrodes contained 20 - 25 mg of active material. Additional galvanostatic cycling experiments were conducted between 3.2 and 4.4 V at varying C-rates (2 C to C/10).

Figure 4.3 summarizes the primary results from Lee et al. In the chronoamperometry (CA) experiment, a constant voltage of 4.07 V was applied, and the current was recorded over 22 minutes. Under dark conditions, the cell delivered a total charge of 2.21 C ($26.1\,\mathrm{mA\,h\,g^{-1}}$), corresponding to approximately 42 % of the theoretical capacity. In contrast, illumination under the same conditions resulted in a significantly higher charge of 4.36 C ($52\,\mathrm{mA\,h\,g^{-1}}$), reaching $\approx 92\,\%$ of the practical capacity.

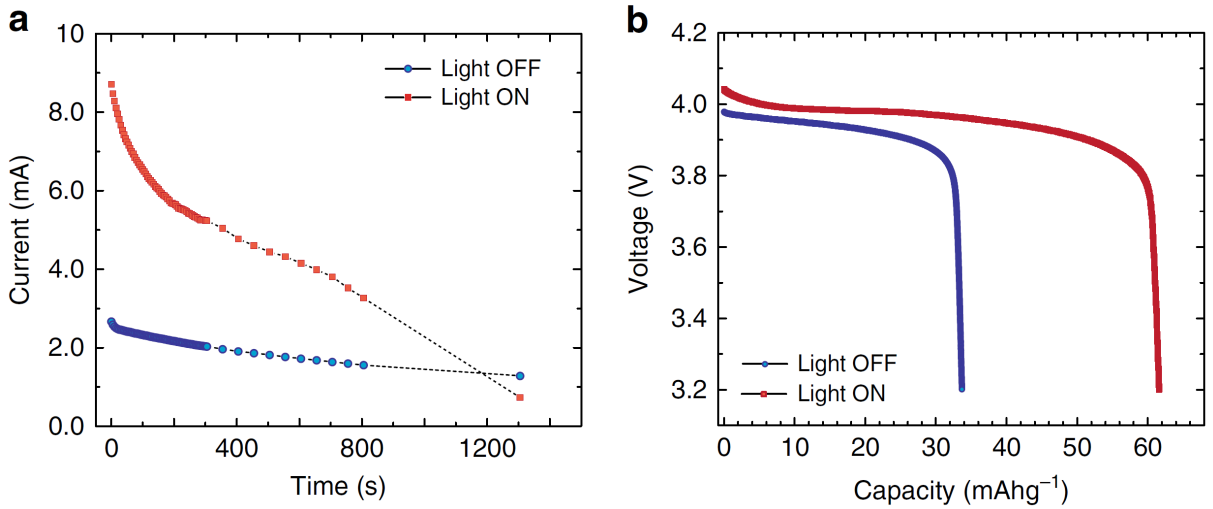


Figure 4.3: Photo-enhanced electrochemical performance of $LiMn_2O_4$ under illumination (adapted from Lee et al. [176]). **a)** Chronoamperometric response at a constant voltage of 4.07 V comparing "light-on" and "light-off" conditions. Illumination leads to a significantly higher current and integrated charge passed, indicating enhanced Li^+ deintercalation. **b)** Galvanostatic discharge following the constant-voltage hold shows greater capacity in the light-charged state, confirming the increased lithium extraction. The combined results support a photo-induced acceleration of the charging process in LMO cathodes.

Follow-up galvanostatic discharge confirmed that the lithium extracted during light-assisted charging was reinserted during discharge. The enhancement in charge rate under illumination was reported to range from a factor of 1.7 to 3.4, depending on the device. Importantly, Raman and UV-Vis spectroscopy confirmed the structural and chemical stability of the electrodes and electrolyte under light exposure. Lee et al. attributed the enhanced performance to photo-induced electronic excitation of Mn^{3+} ions in the LMO lattice. Upon illumination, Mn^{3+} undergoes photo-oxidation to Mn^{4+}, releasing electrons that facilitate faster Li^+ deintercalation. This process is supported by EPR spectroscopy, which showed an increased presence of Mn^{4+} species under illumination.

$$Mn^{3+} \xrightarrow{h\nu} [Mn^{3+}]^* \approx Mn^{4+}(\text{hole}) + e^-(\text{electron}) \tag{4.2}$$

Additionally, a surface-mediated disproportionation reaction of Mn^{3+} may occur under illumination:

$$2Mn^{3+} \xrightarrow{h\nu} 2[Mn^{3+}]^* \approx Mn^{4+} + Mn^{2+} \tag{4.3}$$

The study by Lee et al. provides evidence for photo-assisted enhancement of Li^+ extraction in $LiMn_2O_4$ via electronic excitation mechanisms. Nonetheless, due to partial heating and the absence of direct temperature control within the cell interior, a complete decoupling of photothermal and photochemical contributions remains unresolved. These findings form a valuable benchmark for the present work, which aims to investigate and isolate these effects in a controlled manner.

4.3.3 Light and Heat Effects on Cycling

To investigate the individual contributions of light and temperature to the electrochemical behavior of LMO, experiments were conducted based on the setup by Lee et al. [176], using a windowed ECC-Opto-10 cell with a xenon light source (see Section 2.4.2, 2.4.4). Figure 4.4 a) displays chronoamperometric (CA) measurements where LMO composite electrodes were subjected to four conditions: illumination at ambient temperature (cyan), and non-illuminated measurements at 25 °C (black), 30 °C (magenta), and 40 °C (red). A constant potential of 4.07 V vs Li/Li^+ was applied for 22 minutes, targeting completion of the first oxidation reaction O_1 (see Figure 4.2), representing $\approx 50\,\%$ state of charge. In all conditions, the current decreases over time as lithium ions are extracted and Mn centers oxidize. At 25 °C (black) without illumination, the current quickly drops within the first

2 min and then stabilizes around 0.6 mA g^{-1}, indicating incomplete progression of O_1. A similar trend is observed at 30 °C (magenta), where the current plateaus at 0.8 mA g^{-1} after ≈ 5 min. At 40 °C (red), the current declines more steeply after 20 min, suggesting more advanced oxidation. Under illumination (cyan), the cell initially exhibits a higher current, which drops rapidly before stabilizing at ≈ 1.7 mA g^{-1} and then decreases further, approaching zero, indicating near-complete oxidation within the 22-minute period.

Subsequent discharge measurements at 10 mA g^{-1}(C/15) following the CA experiments (Figure 4.4 b) show expected reduction plateaus near 4.0 V. However, the 25 °C non-illuminated sample deviates, displaying a lower plateau around 3.9 V, suggesting that full oxidation is not achieved. These findings align with Figure 4.5, where kinetic factors such as temperature and light shift the potential required to complete oxidation, and hence, the applied 4.07 V is insufficient in cooler, dark conditions (black). Compared to the ≈ 58 mA h g^{-1} expected capacity at 4.07 V (Figure 4.2), the illuminated sample reaches 45 mA h g^{-1} (78 %), while the dark conditions yields 38 mA h g^{-1} (40 °C), 22 mA h g^{-1} (30 °C), and just 9 mA h g^{-1} (25 °C). To confirm thermal effects, Figure 4.4 c) shows temperature recordings during the CA experiments. Measurements were taken every minute using an IR thermometer aimed at the cell window. The light-off measurements alignes well with their set temperatures, while illumination (cyan) causes a rise from 25 °C to ≈ 30 °C within 7 min. A reference test (orange), conducted with the windowed cell open and illuminated for 22 min, confirms this temperature stabilization around 30 °C. These results indicate that even when temperatures are matched through controlled conditions, illumination still significantly accelerates oxidation kinetics, doubling the amount of charge converted during the CA duration. This supports the findings of Lee et al. [176], yet also emphasizes the importance of carefully selecting the applied potential, as slight kinetic shifts can prevent full access to the oxidation range.

Figure 4.5 a) presents GCPL curves over the full voltage range (3.4 – 4.4 V) at 30 mA g^{-1} (C/5) for the first cycle. The redox activity under illumination at 30 °C (cyan) is compared with dark conditions at 25 °C (black), 30 °C (magenta), and 40 °C (red). All conditions show the characteristic two-step redox behavior, achieving ≈ 135 mA h g^{-1} (91 % of theoretical capacity). However, the O_1 oxidation plateau in the 25 °C dark case lies almost entirely above 4.07 V, explaining the incomplete oxidation observed in the prior CA experiment. To clarify these shifts, Figure 4.5 b) shows derivative curves, revealing consistent redox features across all measurements, but with shifts depending on temperature and illumination. Figure 4.5 c) summarizes the redox potentials ($E_{1/2}$), determined by Gaussian fitting of the derivative peaks. No significant shift in $E_{1/2}$ is observed across conditions: $E_{1/2}(1) = 4.006 \pm 0.004$ V and $E_{1/2}(2) = 4.128 \pm 0.002$ V.

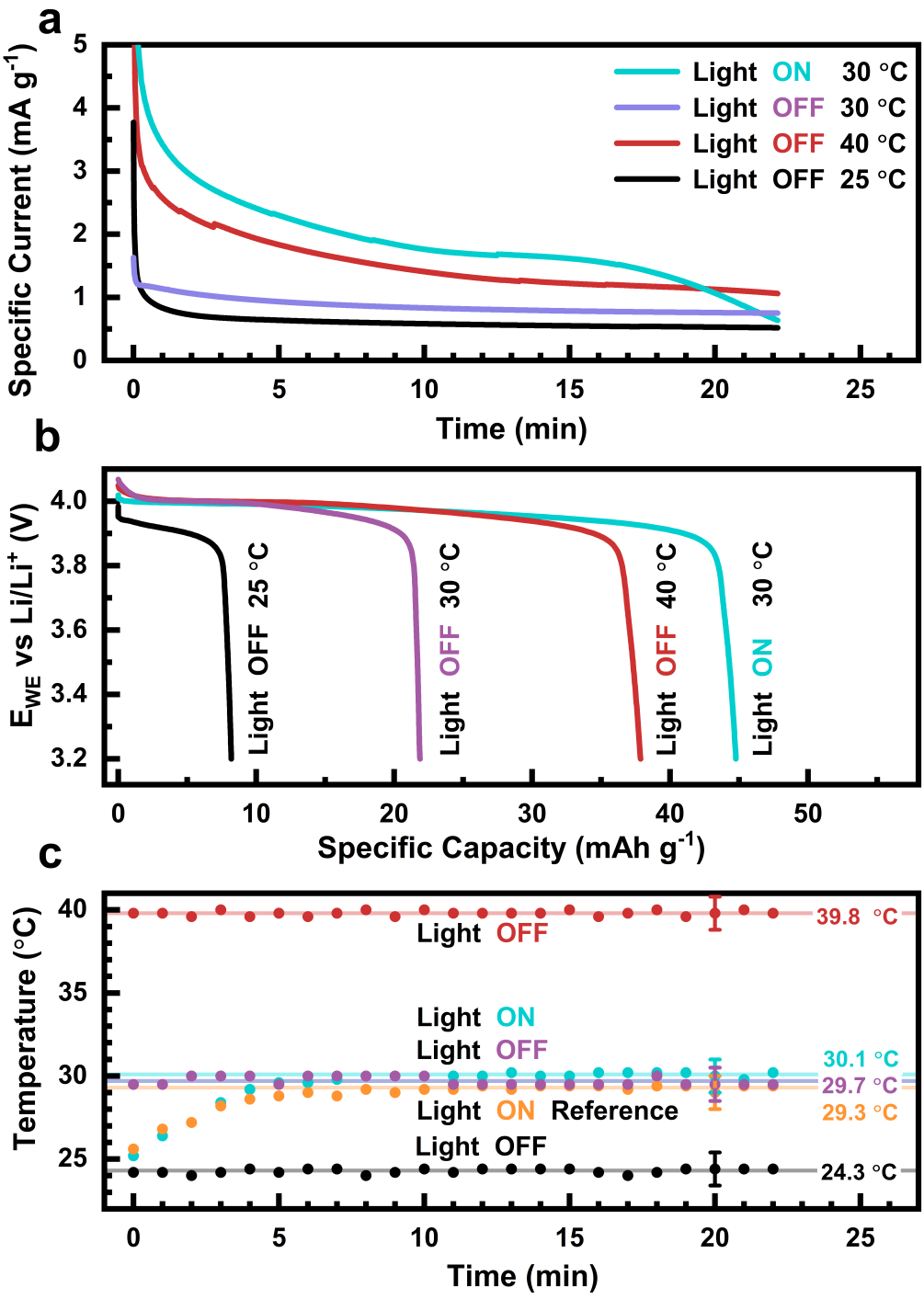


Figure 4.4: Electrochemical performances and temperature measurements of LMO composite electrodes for light ON at 30 °C (cyan) and light OFF at 25 °C (black), 30 °C (magenta), 40 °C (red). **a)** Chronoamperometry measurements holding 4.07 V vs. Li/Li^+ for 22 min according to [176]. **b)** Discharge curves at constant currents of 10 mA g^{-1} (C/15) right after chronoamperometry measurements without illumination. **c)** Temperature recordings during chronoamperometry measurements and a reference measurement (orange).

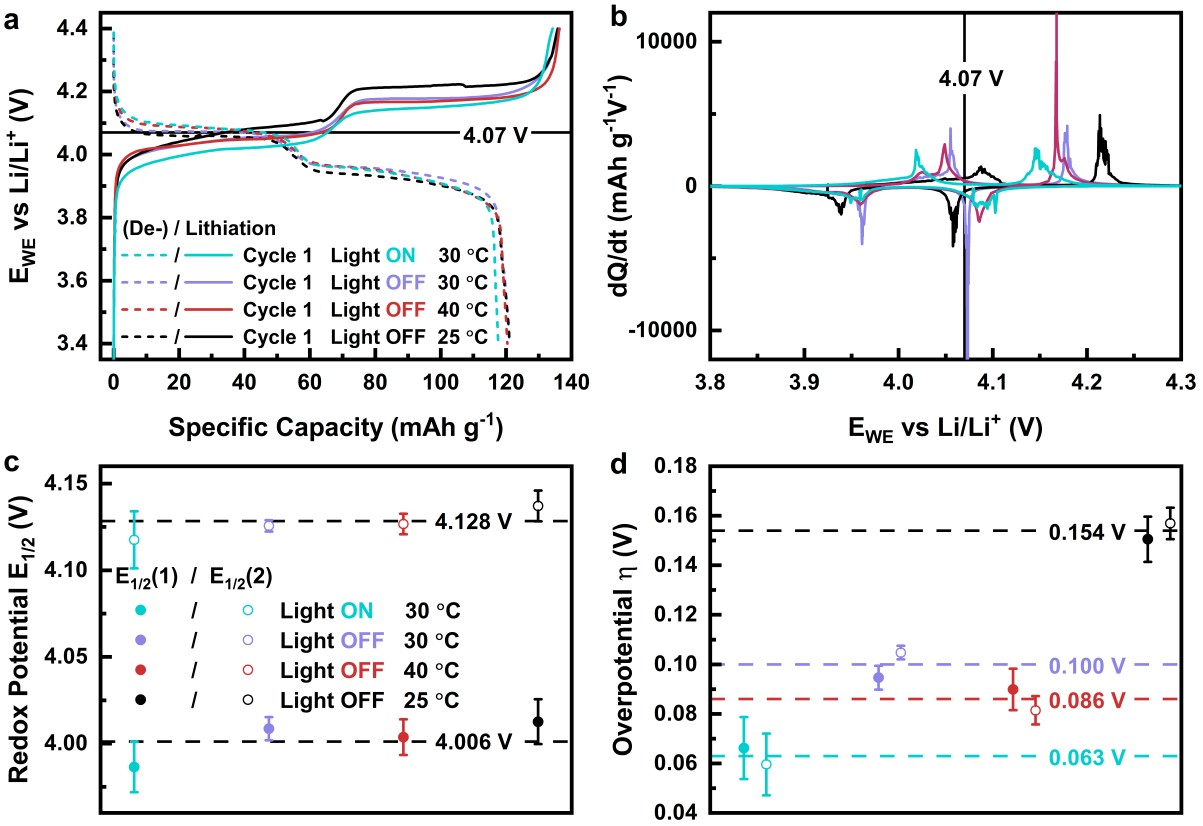


Figure 4.5: a) Galvanostatic charge/discharge potential profiles of LMO composite electrodes for light ON at 30 °C (cyan) and light OFF at 25 °C (black), 30 °C (magenta), 40 °C (red) measured in a voltage range of 3.4 - 4.4 V at a constant current of 30 mA g^{-1} (C/5) for the first cycle. **b)** Derivatives of galvanostatic charge/discharge measurements with a current density of 30 mA g^{-1} (C/5) in the voltage range of 3.4 - 4.4 V. **c)** Redoxpotential $E_{1/2}$ and **d)** Overpotential η read from the derivatives.

However, Figure 4.5 d) shows the overpotentials (η), which do vary considerably. At 25 °C in the dark (black), $\eta = 0.154 \pm 0.009$ V. With increasing temperature, overpotentials drop: $\eta = 0.100 \pm 0.005$ V (30 °C, magenta), $\eta = 0.086 \pm 0.009$ V (40 °C, red). Illumination at 30 °C (cyan) further reduces η to 0.063 ± 0.010 V. These findings demonstrate that while redox potentials remain stable, the overpotentials and therefore kinetic barriers are significantly reduced by both heat and light. This is consistent with enhanced ionic conductivity and reaction kinetics at elevated temperatures [208, 212–214]. Additionally, comparing the 30 °C dark and illuminated conditions reveals a ≈ 40 % reduction in overpotential due to light, even at constant temperature. This supports the mechanism proposed by Lee et al. [176], in which light promotes Mn^{3+} photoexcitation to Mn^{4+} (hole generation), with electrons migrating via polaron hopping toward the current collector under applied bias, thus accelerating the oxidation reaction.

4.3.4 Impact of Illuminated Area on the Electrochemical Response of $LiMn_2O_4$ Electrodes

While previous experiments, both in this thesis and by Lee et al., established that light enhances the electrochemical performance of $LiMn_2O_4$ (LMO) electrodes, the extent to which this effect depends on the illuminated surface area remains unclear. Since the generation of photo-induced charge carriers is inherently a surface-mediated process, the effective area exposed to light may directly influence the degree of performance enhancement. In this section, we explore the relationship between illuminated electrode area and the electrochemical response by systematically varying the illuminated area while maintaining consistent environmental and electrochemical conditions. These experiments provide insight into the spatial dynamics of photo-acceleration and help assess the scalability and practical integration of light-enhanced LMO cathodes in battery systems.

To investigate how the size of the illuminated region influences the photo-acceleration of LMO electrodes, CA and subsequent discharge measurements were performed under three controlled conditions at a constant temperature of 30 °C: (i) without illumination (magenta), (ii) with partial illumination of 3.14 mm^2 (green), and (iii) with full illumination of 12.57 mm^2 (cyan). The illumination area was varied by using a smaller perforated contact disk hole diameter of $\varnothing = 2$ mm instead of $\varnothing = 4$ mm in the ECC-Opto-10 cell while keeping all other parameters constant. Figure 4.4 a) displays the CA responses under these three configurations over a 22-minute period, during which a constant potential of 4.07 V vs Li/Li^+ was applied. Under dark conditions (magenta), the current quickly declined within the first 2 min and stabilized around 0.8 $mA\,g^{-1}$, indicating that the oxidation process O_1 did not reach completion, consistent with previously reported behavior. In contrast, both illuminated conditions exhibited initially higher currents followed by a rapid decline and eventual stabilization. The sample illuminated over 12.57 mm^2 (cyan) reached a steady-state current of 1.7 $mA\,g^{-1}$ before decreasing toward zero, suggesting near-complete oxidation of Mn centers during the CA period. When the illumination area was reduced to 3.14 mm^2 (green), a similar current profile was observed, albeit with a slower decline, and a plateau of 1.0 $mA\,g^{-1}$ before the terminal drop, indicating slower reaction kinetics and incomplete charge transfer relative to the larger area. Following CA, constant-current discharge (C/15) measurements were conducted (Figure 4.4 b). All conditions showed the expected reduction plateau near 4.0 V, corresponding to the R_1 redox couple. The specific capacity of the illuminated sample with the larger area (cyan) reached 45 $mA\,h\,g^{-1}$ (78 % of the theoretical 58 $mA\,h\,g^{-1}$ expected at 4.07 V), while the smaller illuminated area (green) yielded only 30 $mA\,h\,g^{-1}$ (52 %). The dark condition at

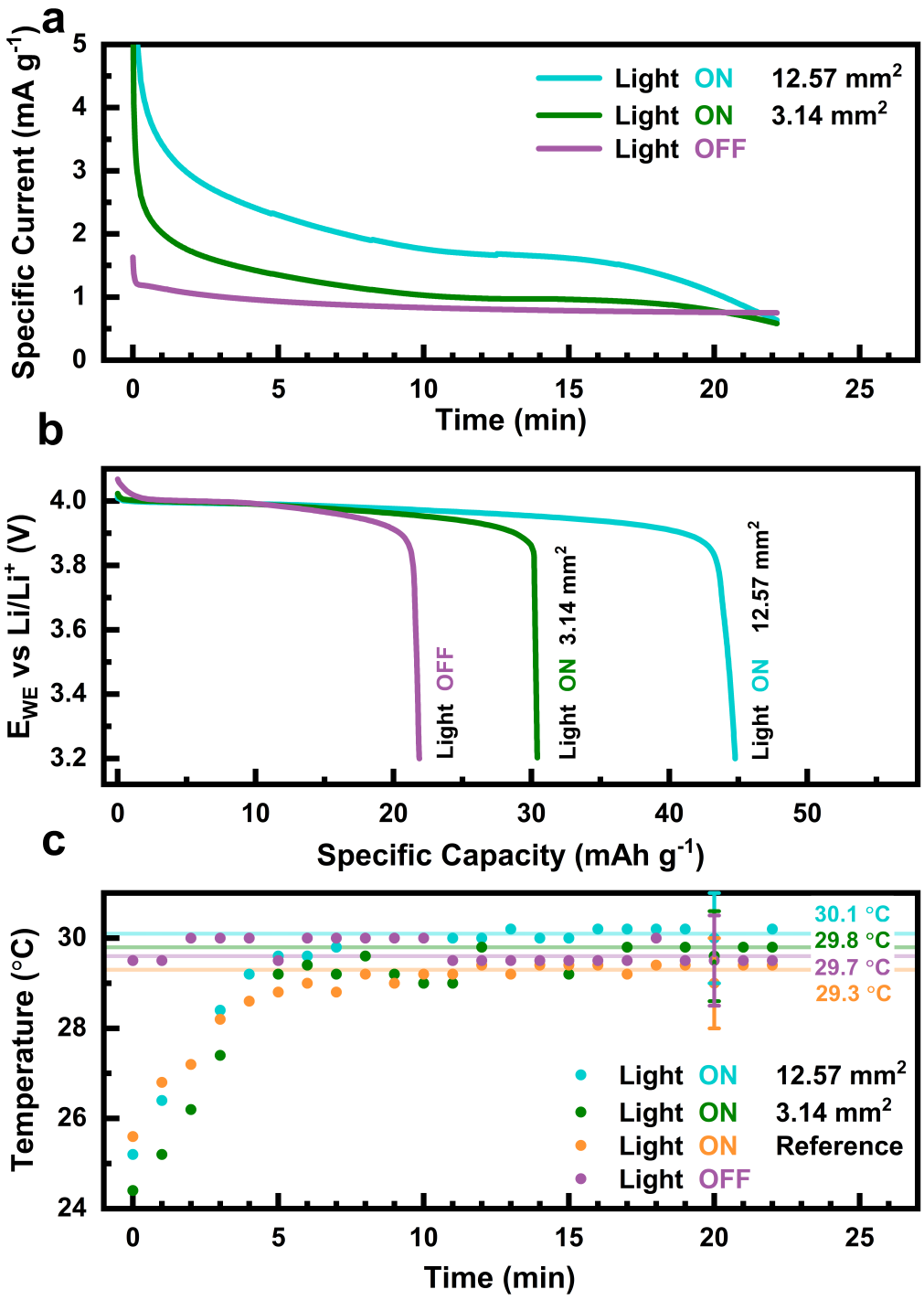


Figure 4.6: Electrochemical performance and temperature measurements of LMO composite electrodes under varied illuminated areas at 30 °C: light OFF (magenta), light ON with 3.14 mm^2 (green), and light ON with 12.57 mm^2 (cyan). **a)** Chronoamperometry measurements at a constant potential of 4.07 V vs Li/Li$^+$ for 22 min following the protocol in [176]. **b)** Discharge curves at a constant current of 10 mA g^{-1} (C/15) measured immediately after chronoamperometry, performed in the dark. **c)** Temperature recordings during chronoamperometry, taken every minute using an IR thermometer directed at the cell window.

30 °C (magenta) achieved just 22 mA h g^{-1} (38 %), reinforcing that both light exposure and illuminated area play significant roles in enhancing electrochemical performance.

To isolate photonic effects from thermal contributions, temperature recordings were performed concurrently during the CA experiments and are shown in Figure 4.4 c). These were acquired at one-minute intervals using an IR thermometer pointed at the cell window. Dark condition measurements remained stable at 30 °C as expected. Under illumination (both green and cyan), the cell temperature rose from 25 °C to approximately 30 °C within the first 7 minutes, after which it stabilized. A reference test (yellow), conducted with the cell window fully opened during 22 minutes of illumination, confirmed this thermal behavior, validating that both illuminated conditions reached and sustained 30 °C during measurement.

Collectively, these results suggest that while both temperature and illumination independently enhance oxidation kinetics in LMO cathodes, the extent of the illuminated surface significantly impacts charge conversion. Larger illuminated areas accelerate reaction rates more effectively, likely by generating a higher density of photo-induced carriers over a wider active zone.

4.3.5 Time-Dependent Electrochemical Response of $LiMn_2O_4$ Under Photo-Accelerated Conditions

To investigate the time-dependent behavior of the electrochemical performance in LMO cathodes under photo-accelerated conditions, CA and galvanostatic GCPL measurements were conducted under both illuminated and non-illuminated conditions for varying durations. The key question addressed here is whether extending the CA duration leads to convergence in electrochemical performance between illuminated and dark conditions, isolating the influence of photonic stimulation from purely thermal effects.

Figure 4.7 a) displays CA results at a constant potential of 4.07 V vs Li/Li^+ for LMO electrodes. Two 22-min experiments were performed: one under illumination (cyan) and one in the dark (magenta), replicating prior work [176]. Additionally, a prolonged dark reference measurement (gray) was conducted for 70 min, allowing the current to decay fully to ≈ 0 mA g^{-1}, thus serving as a benchmark for complete electrochemical saturation. Both the illuminated and short-duration dark measurements yielded comparable current profiles, consistent with earlier observations (see Figure 4.4 a). In contrast, the extended 70-min CA experiment in the dark showed a distinct plateau at approximately 1.05 mA g^{-1}, which remained stable for the first 55 min before declining to 0 mA g^{-1} within the final

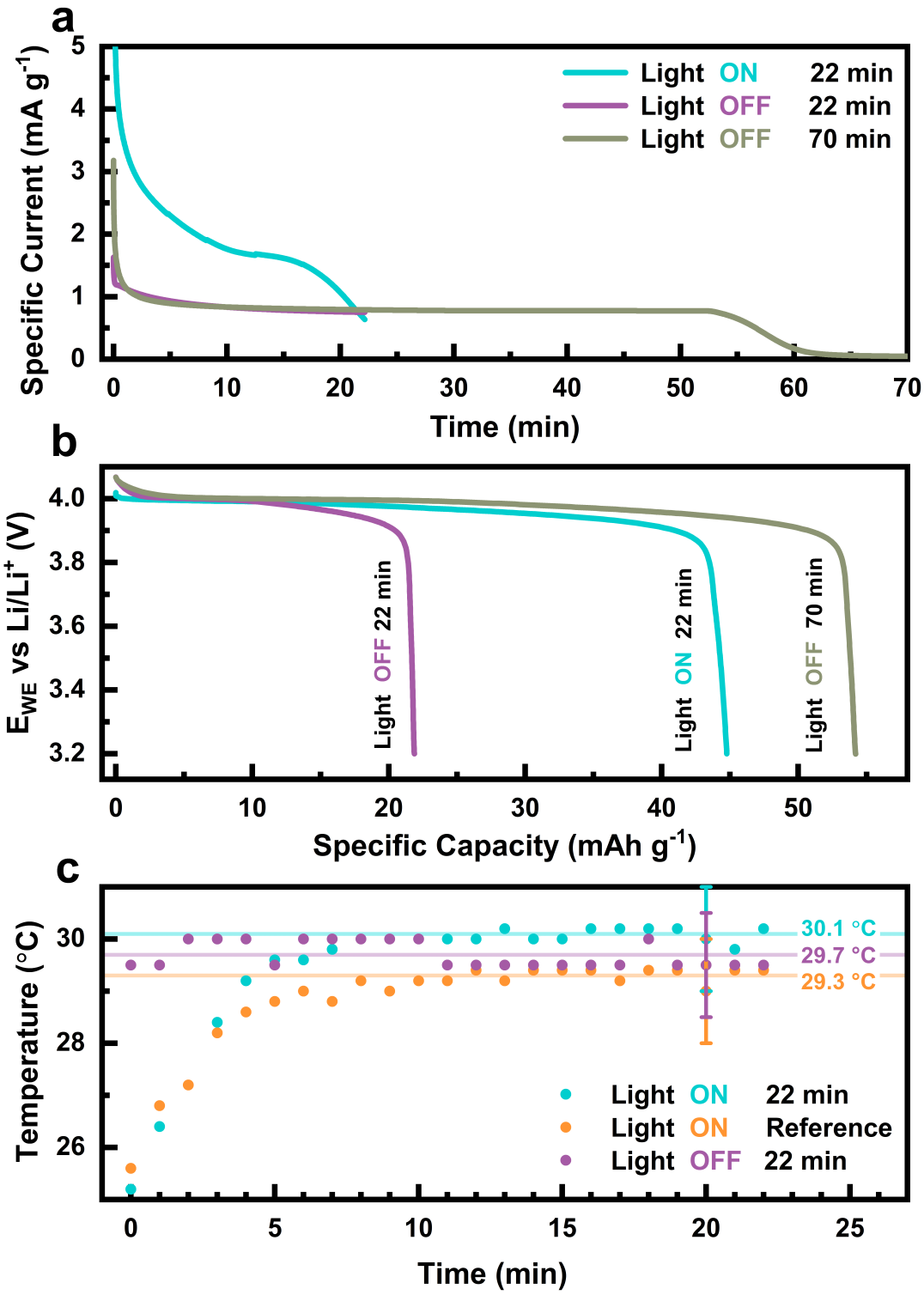


Figure 4.7: Electrochemical performances and temperature measurements of LMO composite electrodes for light ON (cyan), light OFF (magenta) for 22 min and light OFF (gray) for 70 min. **a)** Chronoamperometry measurements holding 4.07 V vs. Li/Li^+ for 22 min according to [176] and for reference 70 min. **b)** Discharge curves at constant currents of 10 mA g^{-1} (C/15) right after chronoamperometry measurements without illumination. **c)** Temperature recordings during chronoamperometry measurements.

10 min. This confirms that a significantly longer CA duration in the absence of light is required to reach a comparable level of charge transfer as achieved in shorter photo-assisted experiments.

Subsequent GCPL measurements were conducted without illumination at a constant current of $10\,\mathrm{mA\,g^{-1}}$ (C/15 rate), immediately following the CA experiments (Figure 4.7 b). As in the CA measurements, the 22-min light ON (cyan) and light OFF (magenta) protocols led to specific capacities of $45\,\mathrm{mA\,h\,g^{-1}}$ and $22\,\mathrm{mA\,h\,g^{-1}}$, respectively, again aligning well with previous data (Figure 4.4 b). Notably, the extended 70-min CA (gray) resulted in a significantly higher capacity of $54\,\mathrm{mA\,h\,g^{-1}}$, representing approximately 93 % of the theoretical capacity for this material. This supports the hypothesis that sufficient time under dark conditions enables the system to achieve an electrochemical state similar to that attained through short-term illumination, thereby separating time-dependent ionic and electronic processes from photo-induced acceleration. Temperature evolution during the CA experiments is shown in Figure 4.7 c). The thermal profiles closely resemble those observed in previous area variation studies (Figure 4.6), confirming consistent heating behavior across different illumination and timing protocols. This indicates that while light contributes to localized heating, the decoupling of thermal and photonic contributions requires careful time-resolved analysis, as demonstrated in this study.

4.3.6 Comparison

To ensure a meaningful comparison between this work and the study by Lee et al.[176], the experimental conditions were closely aligned. Both studies utilized a Xenon light source with an intensity of approximately $100\,\mathrm{mW\,cm^{-2}}$. While Lee et al. employed a coin cell configuration with a Kapton window, this thesis utilized an ECC-Opto-10 cell equipped with a sapphire glass window. Electrode compositions were similar in terms of active material, carbon, and binder ratios (75:5:20), though Lee et al. used self-standing electrodes with an active mass loading of 20 - 25 mg, whereas light-translucent graphite tape–based electrodes with a significantly lower mass loading of 2 - 3 mg were used in this study. Electrolyte formulations differed slightly: Lee et al. used 1.2 M $LiPF_6$ in EC:EMC (70:30), while 1 M $LiPF_6$ in EC:DMC (50:50) was used here. In both cases, CA was performed at 4.07 V, corresponding to an approximate 50 % state of charge, for a duration of 22 min. Illumination during CA leads to a temperature increase of approximately + 7 °C in Lee et al.'s study and + 5 °C in the present work. The expected specific capacities at 4.07 V, determined via prior GCPL measurements, are $65\,\mathrm{mA\,h\,g^{-1}}$ and $56\,\mathrm{mA\,h\,g^{-1}}$ for Lee et al. and this work, respectively.

	T °C	**Power** mW cm^{-2}	**t** min	**C_{CA}** (mA h g^{-1})	**C_{GCPL}** (mA h g^{-1})	**Plateau** (V)	**$C_{exp.}$** (mA h g^{-1})
	25[a]	-	22	8.0	8.2	3.92	58
Light	30[b]	-	22	19.1	21.9	3.97	58
OFF	40[c]	-	22	34.4	37.9	4.00	58
	30[d]	-	70	50.2	54.2	3.98	58
Lee et al.	23[e]	-	22	26.1	34.0	3.93	65
Light	30[f]	100	22	42.4	44.8	3.99	58
ON	30[g]	25	22	25.7	30.4	3.98	58
Lee et al.	30[h]	100	22	52.0	62.0	3.97	65

Table 4.1: Comparison of electrochemical capacities obtained from chronoamperometry (CA) and galvanostatic cycling (GCPL) under dark and illuminated conditions at different temperatures, as reported in this thesis and by Lee et al. [176]. CA capacities reflect delithiation only and are consistently lower than GCPL capacities (lithiation). Illumination improves capacity and reduces overpotentials in both studies, as evident from redox plateau shifts. Differences at 25 °C are attributed to kinetic limitations affecting oxidation efficiency. [a]black, [b]magenta, [c]red, [d]gray, [e]blue, [f]cyan, [g]green, [h]red – color references used in figures.

A detailed comparison between the results of this thesis and those reported by Lee et al. [176] under various light and temperature conditions is summarized in Table 4.1. Capacities from CA were obtained by integrating the current response during a constant-voltage hold and reflect the extent of lithium extraction (delithiation) at the selected potential of 4.07 V. As expected, all capacities derived from CA are lower than their corresponding GCPL values, due to the unidirectional nature of the delithiation process and the effectively infinite lithium reservoir present in the counter electrode. This imbalance leads to more lithium insertion during prior GCPL lithiation than can be extracted during CA, reducing apparent capacity in the latter. Both this study and that of Lee et al. observe a notable enhancement in delithiation capacity under illumination, accompanied by a moderate temperature rise of approximately 5 °C and 7 °C, respectively. At 25 °C in the dark, this work yield substantially lower capacities (8.0 mA h g^{-1} from CA; 8.2 mA h g^{-1} from GCPL) compared to Lee et al. (26.1 mA h g^{-1} from CA; 34.0 mA h g^{-1} from GCPL). These differences are not due to active mass loading, as capacities are normalized to active material mass. Rather, the lower room-temperature performance may result from kinetic limitations at the selected potential, as confirmed by GCPL and derivative analysis in Figure 4.5. Specifically, at 25 °C in the dark, the O_1 plateau shifts to above 4.07 V, leading to incomplete oxidation during CA and hence reduced capacity. This highlights the importance of selecting an appropriate hold voltage in constant-voltage experiments, especially when reaction kinetics are sluggish.

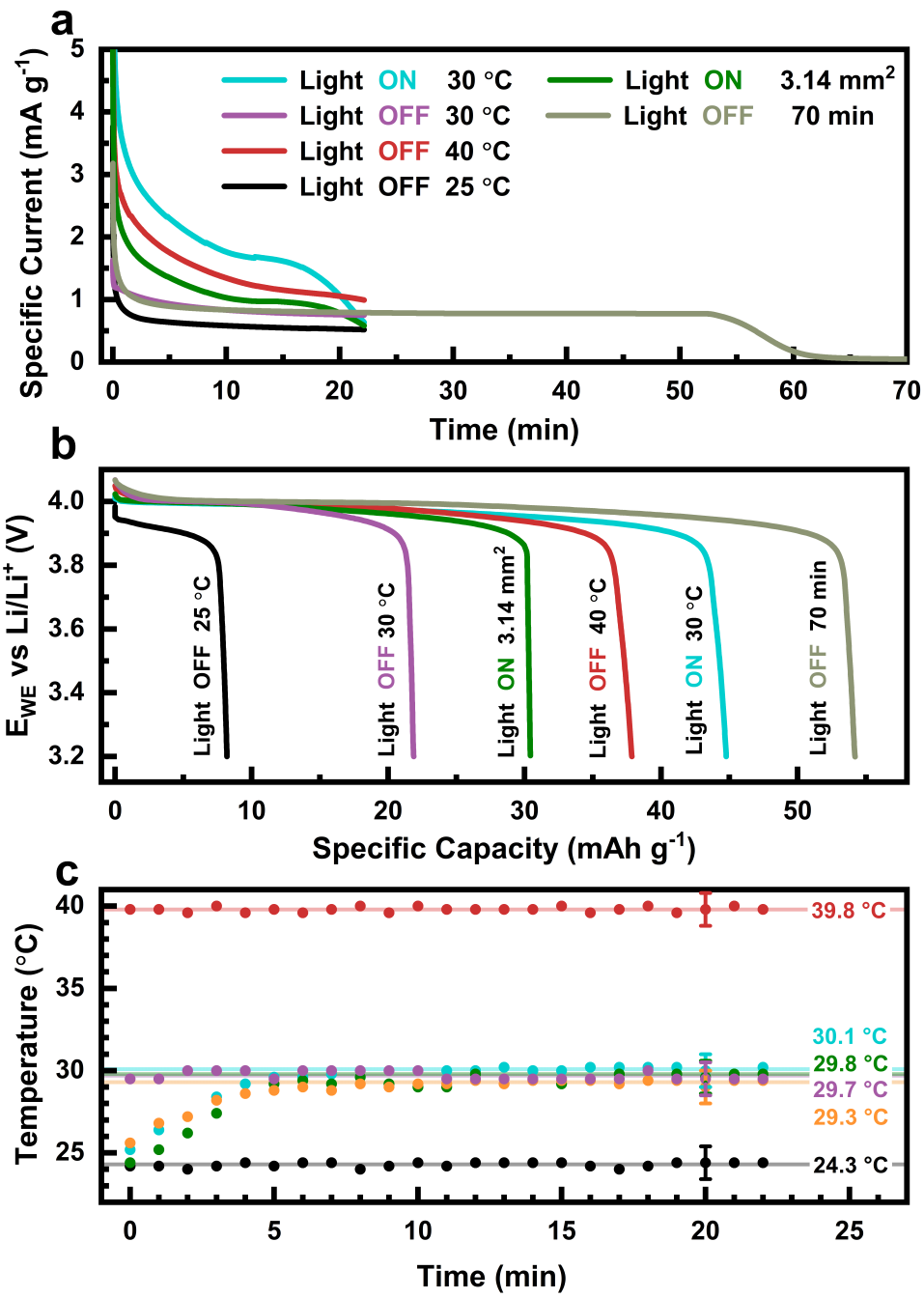


Figure 4.8: Summary of electrochemical performances and temperature measurements of LMO composite electrodes for light ON at 30 °C (cyan), 3.14 mm^2 (green) and light OFF at 25 °C (black), 30 °C (magenta), 40 °C (red) and for 70 min (gray). **a)** Chronoamperometry measurements holding 4.07 V vs. Li/Li^+ for 22 min according to [176]. **b)** Discharge curves at constant currents of 10 mA g^{-1} (C/15) right after chronoamperometry measurements without illumination. **c)** Temperature recordings during chronoamperometry measurements and a reference measurement (orange).

Upon illumination at 30 °C, the capacity improves significantly in both studies. In this thesis, capacities reach 42.4 mA h g^{-1} (CA) and 44.8 mA h g^{-1} (GCPL), while Lee et al. reported 52.0 mA h g^{-1} (CA) and 62.0 mA h g^{-1} (GCPL), respectively. These enhancements are further reflected in the shift of the O_1 redox plateau toward lower potentials under illuminated conditions, ≈ 3.92 to 3.99 V in this work and ≈ 3.93 to 3.98 V in Lee et al., indicating reduced overpotentials and facilitated reaction kinetics. Overall, the experimental trends are in strong agreement, except for the significantly lower capacities observed at 25 °C under dark conditions in this study, which can be attributed to the kinetic limitations discussed above. This underlines the necessity of carefully matching the electrochemical protocol to the intrinsic electrode kinetics when performing photoelectrochemical studies.

4.4 Conclusions

The photo-enhanced electrochemical behavior of $LiMn_2O_4$ (LMO) electrodes has gathered significant interest for its potential in improving lithium-ion battery performance through light-assisted processes. Across both the chronoamperometric and galvanostatic investigations, it seems evident that illumination contributes to measurable enhancements in reaction kinetics and capacity delivery. However, these improvements are not solely attributable to photonic effects; thermal contributions from localized heating complicate the interpretation of photo-response. By methodically decoupling light and heat through controlled chronoamperometric and galvanostatic experiments, this study confirms that light exposure increases the rate of Li^+ extraction beyond what can be accounted for by thermal enhancement alone. Even at equivalent temperatures (≈ 30 °C), illuminated cells deliver nearly double the charge during fixed-voltage oxidation periods compared to their non-illuminated counterparts. This supports the hypothesis that light interacts with the LMO electronic structure, likely by promoting charge carrier delocalization or suppressing recombination, thereby reducing interfacial resistances and facilitating faster redox reactions.

Furthermore, the spatial illumination studies previously discussed demonstrate that the degree of photo-enhancement scales with the illuminated area, suggesting that photo-induced charge transport is at least partially localized and surface-mediated. These findings collectively indicate that while thermal effects are non-negligible and can enhance kinetics, true photochemical contributions are distinct and significant when light is adequately controlled and matched to the material's absorption properties.

This study also examines how $LiMn_2O_4$ (LMO) cathodes behave electrochemically over time under both illuminated and non-illuminated conditions. Chronoamperometry (CA) and galvanostatic charge/discharge (GCPL) measurements reveal that short-term illumination (22 min) significantly accelerates the electrochemical response, achieving charge transfer levels that require much longer times (70 min) in the dark. The longer dark CA test ultimately matches the illuminated result, suggesting that photo-acceleration primarily reduces the time needed to reach a similar electrochemical state. Temperature data show consistent heating patterns, highlighting the need to distinguish between photonic and thermal effects in such experiments. A detailed comparison with the benchmark study by Lee et al. (2019) further validates the findings of this work. Both studies employ comparable illumination conditions (100 $mW\,cm^{-2}$ xenon light) and observe substantial increases in delithiation capacity under light exposure, accompanied by moderate thermal heating ($\approx$ 5 - 7 °C). Capacities measured at 25 °C under dark conditions are significantly lower in this study (8.0 $mA\,h\,g^{-1}$ from CA; 8.2 $mA\,h\,g^{-1}$ from GCPL) compared to those reported by Lee et al. (26.1 $mA\,h\,g^{-1}$ from CA; 34.0 $mA\,h\,g^{-1}$ from GCPL). These discrepancies cannot be explained by differences in active mass loading, as all capacities are normalized to the mass of active material. Rather, the lower capacity observed at room temperature in this study appears to stem from kinetic limitations specific to the applied potential. As demonstrated by the GCPL and derivative analysis in Figure 4.5, the O_1 oxidation plateau at 25 °C under dark conditions shifts to potentials above 4.07 V, resulting in incomplete delithiation during chronoamperometric measurements and consequently reduced extracted capacity. These results confirm the key observation reported by Lee et al., namely, that illumination produces a measurable enhancement in the electrochemical response of LMO electrodes. However, the underlying mechanism proposed by Lee et al., involving Mn^{3+} photoexcitation and enhanced polaronic conduction, remains plausible but unconfirmed. Instead, it emphasizes that a rigorous separation of photonic and thermal effects is essential for interpreting photo-enhanced behavior, as kinetic factors can cause potential plateau shifts that significantly affect the outcome. In this regard, the voltage-dependent nature of redox kinetics plays a central role in interpreting CA results, especially under non-illuminated conditions.

In summary, the enhanced electrochemical response of LMO under illumination arises from a synergistic interplay between photonic and thermal effects. Disentangling these contributions provides not only a deeper understanding of the underlying mechanisms but also clear guidance for the design of photo-active cathodes. Future work should explore wavelength dependence, long-term stability under cyclic illumination, and interface engineering to optimize and utilize these photo-accelerated phenomena in battery applications.

5 Hybrid Organic Inorganic Perovskite Anode Material

Hybrid organic–inorganic perovskites (HOIPs) have emerged as promising materials for a wide range of optoelectronic and energy-related applications due to their tunable crystal structures, ease of synthesis, and favorable charge transport properties [215]. This chapter presents their potential as active materials for electrochemical energy storage, with a focus on their function as anode materials. To provide the reader with a concise overview of the current research landscape regarding HOIPs as potential LIB materials, the state of the art is presented in Section 5.1. This is followed by a detailed description of the synthesis procedures employed for the HOIPs studied in this work, as outlined in Section 5.2. The structural integrity and phase purity of the materials are confirmed by X-ray diffraction (XRD) analysis in Section 5.3. Subsequent electrochemical characterization is conducted to investigate lithium storage mechanisms, cycling behavior, and the influence of various material and device configurations. The following experimental variations are explored to systematically evaluate the electrochemical performance of HOIP anode materials:

1. **$MAPbBr_3$ reaction mechanism:** Full voltage window scans were performed in two different electrolytes to analyze redox behavior, revealing three distinct reaction mechanisms (Section 5.4.1).

2. **Isolated reaction pathway studies:** Electrochemical cycling within limited voltage windows was employed to target specific redox reactions (Section 5.4.2).

3. **Electrolyte optimization:** Eight different electrolytes were tested to enhance cycling stability and performance (Section 5.4.3).

4. **Comparison of different HOIP systems:** In addition to $MAPbBr_3$, three other HOIPs were examined, 1D-$EBAPbI_3$, the lead-free $CsMnBr_3$, and $EBA_4Bi_2Br_{10}$, to assess structural and compositional influences on performance (Section 5.4.4).

5. **Photothermal and photo-assisted charging studies:** The impact of photothermal effects and photo-accelerated charging was investigated, particularly in the presence of a hole-blocking additive.

5.1 Hybrid Organic Inorganic Battery Material: State of the Art

In recent years, hybrid organic–inorganic hybrid perovskites (HOIPs) have gained attention in optoelectronics due to their high photovoltaic efficiency, broad absorption range, compositional flexibility, and low-cost fabrication [216, 217]. Their solution-based synthesis is simple and efficient, enabling precise control over the material´s dimensionality, which influences key properties such as band gap, stability, and charge recombination [218]. These tunable characteristics make HOIPs highly suitable for applications in solar cells, LEDs, and photodetectors, further supported by their excellent defect tolerance [219–221]. In recent years, HOIPs have gained attention in the field of lithium-ion batteries due to their promising potential to improve electrode performance and enhance ionic conductivity.

5.1.1 Hybrid Organic Inorganic Perovskites

The fundamental structure of a HOIP, follows the general formula ABX_3, as illustrated in Figure 5.1. In this configuration, the A-site is occupied by a monovalent cation such as methylammonium (MA, $CH_3NH_3^+$), α-ethylbenzylamine (EBA, $C_6H_5CH(C_2H_5)NH_2$), or cesium (Cs^+). The B-site typically hosts a divalent cation like lead (Pb^{2+}) or manganese (Mn^{2+}). And the X-site comprises halide ions such as chloride (Cl^-), bromide (Br^-), iodide (I^-), or their mixtures. The material forms a three-dimensional perovskite structure due to its extended network of corner-sharing BX_6^- octahedra. The bandgap of these materials can be finely tuned by altering the A, B, or X-site ions or their combinations. Over time, the traditional ABX_3 definition has evolved with the development of related material families, including low-dimensional 2D perovskites like the Ruddlesden–Popper [99] and Dion–Jacobson phases [222], double perovskites [223], anti-perovskites [224], and lead-free alternatives aimed at reducing environmental impact [225].

Studies have explored how lithium ions interact with halide perovskites, showing that lithium (Li^+) doping can enhance the electronic properties of these materials without altering their crystal structure. Doping with Li^+ or Na^+ results in n-type behavior and improved conductivity, light absorption, and photocurrent, particularly in $CsPbBr_3$ crystals [227].

Vicente et al. [228] propose a three-stage discharge (lithium storage) mechanism in halide perovskite electrodes, using $MAPbBr_3$ as a representative material (Figure 5.2). This

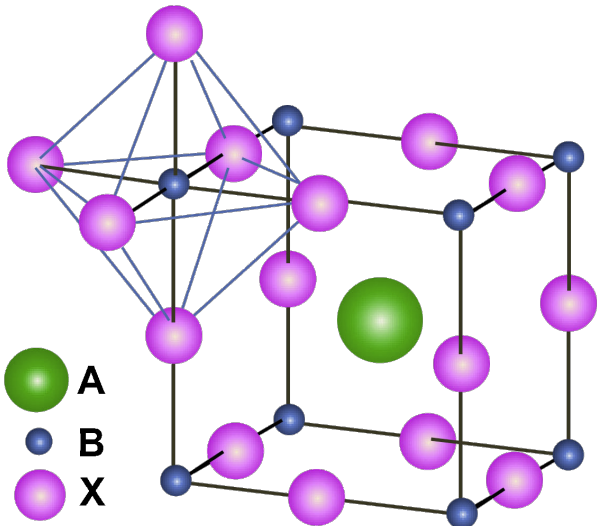


Figure 5.1: Schematic representation of the crystal structure of a hybrid organic–inorganic perovskite (HOIP) with the general formula ABX_3. Adapted from [226].

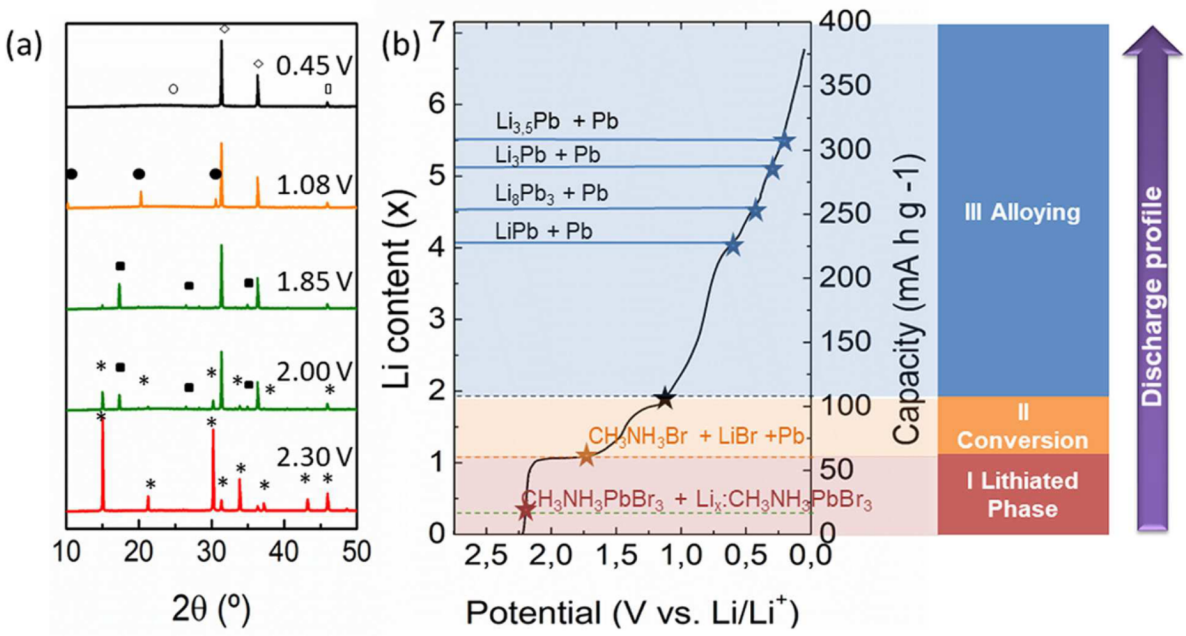


Figure 5.2: Proposed three-stage lithium storage mechanism in $MAPbBr_3$, adapted from Vicente et al. [228]. **a)** X-ray diffraction (XRD) patterns of $MAPbBr_3$ at different discharge potentials, illustrating structural evolution with increasing lithium content. **b)** Schematic representation of the three-step storage mechanism (I) lithiation (red), (II) conversion (yellow), and (III) alloying (blue), corresponding to distinct plateaus in the galvanostatic charge–discharge profile.

mechanism can likely be generalized to other metal halide perovskites and proceeds as follows:

1. **Lithiation (2.5 – 1.85 V):** Between open-circuit voltage (OCV) and 1.85 V vs Li/Li^+, the perovskite undergoes lithium intercalation to form $Li_xMAPbBr_3$, where $0.00 < x < 1.10$. This process can be expressed by the general reaction [229]:

$$xLi + CH_3NH_3PbX_3 \rightarrow Li_xCH_3NH_3PbX_3 \tag{5.1}$$

   Li^+ can intercalate into different crystal sites (tetrahedral, octahedral), although the intercalation was initially assumed to be limited to $x \approx 1$, significantly higher specific capacities observed in experiments suggest additional reaction mechanisms must occur.

2. **Conversion (1.85 – 1.08 V):** Between 1.85 V and 1.08 V vs Li/Li^+, conversion reactions dominate, resulting in the decomposition of the perovskite structure into MABr, LiBr, and metallic lead (Pb^0). These irreversible reactions are described by the following equations:

$$Li + CH_3NH_3PbX_3 \rightarrow CH_3NH_3X + LiPbX_2 \tag{5.2}$$

$$2Li + CH_3NH_3PbX_3 \rightarrow CH_3NH_3X + 2LiX + Pb \tag{5.3}$$

   These reactions indicate the collapse of the perovskite framework and the formation of new crystalline and amorphous products, including metallic Pb.

3. **Alloying (1.08 – 0.01 V):** Below 1.08 V, the metallic Pb formed in the previous stage reacts with additional lithium through multi-step alloying reactions. These alloying steps are responsible for the majority of the reversible capacity observed in later cycles and involve the formation of various Li-Pb phases, as detailed in the following equation and Table 5.1:

$$Pb + x\,Li \rightarrow Li_xPb \quad \text{(e.g.: LiPb, } Li_8Pb_3\text{, } Li_3Pb\text{, } Li_{3.5}Pb\text{)} \tag{5.4}$$

This three-stage mechanism highlights two critical observations. First, the potential window for reversible lithium intercalation into the perovskite phase is relatively narrow and contributes modestly to the overall capacity. Second, the majority of the specific capacity arises from irreversible conversion reactions during the first discharge and subsequent reversible alloying reactions between Li and metallic Pb. These structural transformations,

Alloy Phase	Li Content (x)	Potential Range (V vs. Li/Li$^+$)	Specific Capacity ($\mathrm{mA\,h\,g^{-1}}$)
Pb	$1.90 < x < 4.10$	1.08 – 0.60	225
Pb LiPb	$4.10 < x < 4.50$	0.60	225
Pb Li_8Pb_3	$4.50 < x < 5.15$	0.60 – 0.45	255
Pb Li_3Pb	$5.15 < x < 5.50$	0.45 – 0.37	285
Pb $Li_{3.5}Pb$	$x > 5.50$	0.37 – 0.29	315

Table 5.1: Multi-stage Pb-Li alloying reactions responsible for the reversible capacity observed at low potentials in Pb-based perovskite electrodes. Data adapted from [228, 230].

including the breakdown of the perovskite framework and the formation of alloy phases, explain the rapid capacity fading observed during cycling.

The DFT-based study by Dawson et al. [231] further supports this mechanism by showing that although Li^+ intercalation is thermodynamically plausible within the perovskite structure, conversion reactions are energetically more favorable. Theoretical calculations also reveal preferential Li insertion sites and compositional effects on the stability of lithiated structures, dependent on the halide (X = Br, I, Cl).

Challenges and Limitations

The issues limiting the practical application of halide perovskites as anode materials in lithium-ion batteries can be summarized as follows:

1. **Electrolyte Stability:** The use of conventional aprotic organic electrolytes in LIBs could lead to the dissolution of the perovskite material, rendering it unsuitable for stable cycling [232]. As discussed in Section 5.4.3, the use of solid-state electrolytes or electrolytes with high salt concentrations represents a promising strategy to address this challenge, as proposed by Mathieson et al. [99, 233].

2. **Irreversible Structural Degradation:** Although conversion reactions contribute substantially to the initial discharge capacity, they are irreversible and result in the permanent loss of the perovskite phase. Reversibility can only be preserved if the potential window is carefully controlled to avoid the conversion regime, an approach discussed in Chapter 5.

3. **Mechanical Instability:** The large volume changes associated with Li-Pb alloy formation lead to structural instability, pulverization of the electrode material, and degradation of cycle life.

To overcome these issues, current research is focused on designing more robust materials, including 2D layered and lead-free perovskites, with improved electrochemical stability and reversibility. Understanding the complex interplay of intercalation, conversion, and alloying through combined experimental and theoretical approaches is essential for advancing hybrid perovskite-based energy storage systems.

$MAPbBr_3$

Methylammonium lead bromide ($MAPbBr_3$), a hybrid organic-inorganic halide perovskite, has emerged as a promising anode material for lithium-ion batteries (LIBs) due to its favorable structural and electrochemical properties. First introduced as an anode in 2015 by Xia et al. [229], $MAPbBr_3$ demonstrated a high initial capacity of $332\,mA\,h\,g^{-1}$ and retained $121\,mA\,h\,g^{-1}$ after 200 cycles, corresponding to a capacity retention of 76.9 % at a current density of $200\,mA\,g^{-1}$. This performance notably surpasses that of its iodide counterpart, $MAPbI_3$, under similar conditions. These two perovskites, $CH_3NH_3PbI_3$ and $CH_3NH_3PbBr_3$, were synthesized as active materials using a hydrothermal method [229]. Morphology and crystal size significantly influence $MAPbBr_3$'s electrochemical performance [234]. Smaller crystals, which provide a higher surface area and more active sites, exhibit improved charge transfer and higher capacity. Efforts to enhance performance have also included the incorporation of carbon-based conductive additives such as carbon nanotubes (CNTs), which synergistically improve electrical conductivity and stabilize the perovskite framework during cycling [222]. Despite its promising electrochemical behavior, challenges remain regarding the long-term stability and toxicity of lead-based perovskites [235]. Nonetheless, $MAPbBr_3$ serves as an important model system for understanding lithium-ion interactions with hybrid perovskites and highlights the potential of halide perovskites as next-generation LIB electrode materials.

$EBAPbI_3$

α-ethylbenzylamine lead iodide ($EBAPbI_3$) is a hybrid perovskite incorporating the larger organic cation (α-ethylbenzylamine, EBA^+) in place of the commonly used methylammonium (MA^+). The substitution of MA^+ with EBA^+ results in a modified crystal structure and electronic environment, potentially enhancing the structural stability and electrochemical properties of the perovskite during charge–discharge cycles [236]. $EBAPbI_3$ exhibits a quasi-1D to 2D structure under ambient conditions, which can promote favorable ion transport pathways and improved tolerance to volume changes during lithiation and delithiation [237]. Although research on $EBAPbI_3$ for energy storage is less mature than

on MAPb-based systems, its larger organic spacer is expected to provide improved resistance to structural degradation, which is critical for the reversibility and cyclability of LIBs [238]. While direct studies on lithium-ion intercalation in $EBAPbI_3$ are limited, analogous behavior observed in structurally similar perovskites like $MAPbI_3$ suggests that $EBAPbI_3$ may also support reversible Li^+ storage with minimal structural degradation at low intercalation levels [231, 239]. However, as with other lead halide perovskites, full lithiation may induce phase transformations and decomposition, leading to the formation of metallic Pb and Li through conversion reactions, particularly under deep discharge conditions [230]. Despite its potential, the use of $EBAPbI_3$ in LIBs remains in the early stages, with limited experimental data available. Further investigation is needed to evaluate its long-term cycling performance, optimize synthesis methods for improved phase purity, and explore its compatibility with different electrolytes. Importantly, any development of $EBAPbI_3$-based electrodes must also address the inherent toxicity concerns of lead, reinforcing the parallel need for lead-free analogs

$CsMnBr_3$

To adress the issue of lead toxicity, lead-free halide perovskites such as cesium manganese bromide ($CsMnBr_3$) are gaining attention as potential anode materials in lithium-ion batteries (LIBs) [240]. $CsMnBr_3$ belongs to a class of perovskite-inspired materials with tunable optoelectronic and electrochemical properties, making it a viable candidate for sustainable energy storage. $CsMnBr_3$ single crystals (SCs) were synthesized via a slow evaporation method by dissolving CsBr and $MnBr_2$ in a water–hydrobromic acid mixture, followed by storage at 40 °C for 5 days [241]. The inherent rigidity of the Mn–Br framework could contribute to better cycling stability compared to traditional organic-inorganic perovskites [242]. Preliminary studies have indicated that Mn-based halide perovskites like $CsMnBr_3$ can exhibit both intercalation and conversion-type behavior, potentially enabling high specific capacities [243, 244]. The redox activity of the Mn^{2+}/Mn_0 couple could be significant for reversible lithium storage [50, 245, 246]. While detailed mechanistic insights into $CsMnBr_3$ remain under active investigation, its performance can be enhanced by nanoengineering, surface modification, or composite formation with conductive additives, similar to other perovskite systems [222]. However, challenges such as moisture sensitivity, moderate electrical conductivity, and structural degradation upon deep lithiation must still be addressed [235, 238].

$EBA_4Bi_2Br_{10}$

The bismuth-based, low-dimensional halide perovskite-inspired compound $EBA_4Bi_2Br_{10}$ is of interest for lithium-ion battery (LIB) applications due to its lead-free composition, structural anisotropy, and potential redox-active centers. This compound features a quasi-two-dimensional layered structure, built from $[Bi_2Br_{10}]^{-4}$ polyanions separated by bulky α-ethylbenzylamine cations. Such a configuration could theoretically allow for interlayer lithium-ion diffusion with limited lattice disruption, a structural motif previously shown to benefit intercalation behavior in layered materials [237]. While $EBA_4Bi_2Br_{10}$ has not yet been explicitly studied as an anode material, insights can be inferred from related bismuth-containing perovskite and oxide systems. For example, Bi-based perovskite oxides such as $Na_{0.5}Bi_{0.5}TiO_3$ (NBT) have demonstrated reversible lithium storage behavior, where Bi^{3+} undergoes conversion to metallic Bi^0 during lithiation, followed by alloying with Li to form Li–Bi phases [247]. Similarly, bismuth halides have been explored in other energy storage applications, showing that the Bi^{3+}/Bi^0 redox couple is capable of supporting high theoretical capacities and contributes to structural robustness during cycling [248]. However, challenges such as the inherently low electronic conductivity of halide perovskites and potential volume expansion during Bi redox transitions must be addressed. Composite strategies, such as the inclusion of carbonaceous matrices (e.g., carbon nanotubes or graphene), and particle downsizing to the nanoscale have proven effective in related systems to enhance conductivity and mitigate mechanical degradation [222]. Although experimental validation is needed, the structural features and bismuth chemistry of $EBA_4Bi_2Br_{10}$ indicate that it may be a viable lead-free perovskite-based anode material for future LIB research.

5.2 Synthesis of Hybrid Organic–Inorganic Perovskites

All hybrid organic–inorganic perovskite (HOIP) materials used in this study were synthesized by Dr. Shangpu Liu from the research group of Prof. Felix Deschler[1]. The following subsections summarize the synthesis procedures for each compound. For comprehensive experimental details, the recipient is referred to Liu et al. [236].

[1]Institute for Physical Chemistry, Heidelberg University

5.2.1 $MAPbBr_3$

Single crystals of $MAPbBr_3$ were synthesized via a hydrothermal method. Methylammonium bromide (MABr, 1 mmol) and lead(II) bromide ($PbBr_2$, 1 mmol) were dissolved in 4 mL of hydrobromic acid (HBr) under continuous stirring at 80 °C for approximately 30 min. The resulting solution was transferred into a 20 mL autoclave and reacted at 80 °C for 12 h. Upon slow cooling of the autoclave to room temperature at a rate of 1 °C h^{-1}, large single crystals were obtained. In contrast, natural cooling led to the formation of powder samples. All products were washed and subsequently stored in an inert N_2 atmosphere glovebox.

5.2.2 $EBAPbI_3$

Chiral perovskite single crystals of $EBAPbI_3$ were synthesized hydrothermally. Lead(II) oxide (PbO, 200 mg) and α-ethylbenzylamine (EBA, 200 µL) were separately dissolved in 6 mL of hydroiodic acid (HI) at 95 °C. The two solutions were then combined and transferred into 25 mL autoclaves, which were maintained at 95 °C for 24 h. After slow cooling to room temperature at a rate of 1 °C h^{-1}, needle-shaped single crystals formed at the bottom of the autoclaves. The crystals were washed three times with diethyl ether, dried under vacuum, and stored in a N_2-filled glovebox.

5.2.3 $CsMnBr_3$

Single crystals of $CsMnBr_3$ were prepared using a hydrothermal approach. Cesium bromide (CsBr, 0.5 mmol) and manganese(II) bromide ($MnBr_2$, 0.5 mmol) were dissolved in 2 mL of HBr and stirred at 40 °C for approximately 5 days. The solution was subsequently transferred to a 20 mL autoclave and maintained at 95 °C for 12 h. Upon controlled cooling to room temperature at a rate of 1 °C h^{-1}, large single crystals were obtained. Natural cooling resulted in powder formation. All samples were washed and stored in a glovebox under inert atmosphere.

5.2.4 $EBA_4Bi_2Br_{10}$

Lead-free perovskite derivative crystals of $EBA_4Bi_2Br_{10}$ were synthesized hydrothermally. Bismuth(III) oxide (Bi_2O_3, 0.25 mmol) and excess α-ethylbenzylamine (EBA, 1.5 mmol) were dissolved in 6 mL of aqueous HBr (48 wt%) under stirring at 100 °C for approximately 30 min. The resulting solution was transferred into a 20 mL autoclave and reacted at 120 °C

for 12 h. Large single crystals were obtained after slow cooling to room temperature (25 °C) at 1 °C h^{-1}, while natural cooling led to powder formation. All crystals were washed and stored in a N_2-filled glovebox.

5.3 Physical Characterization

To confirm the structural integrity and phase purity of the synthesized hybrid organic–inorganic perovskite materials, powder X-ray diffraction (PXRD) analysis was carried out. This technique was primarily applied to $MAPbBr_3$ to verify their crystalline phase formation and compare experimental data with established reference patterns.

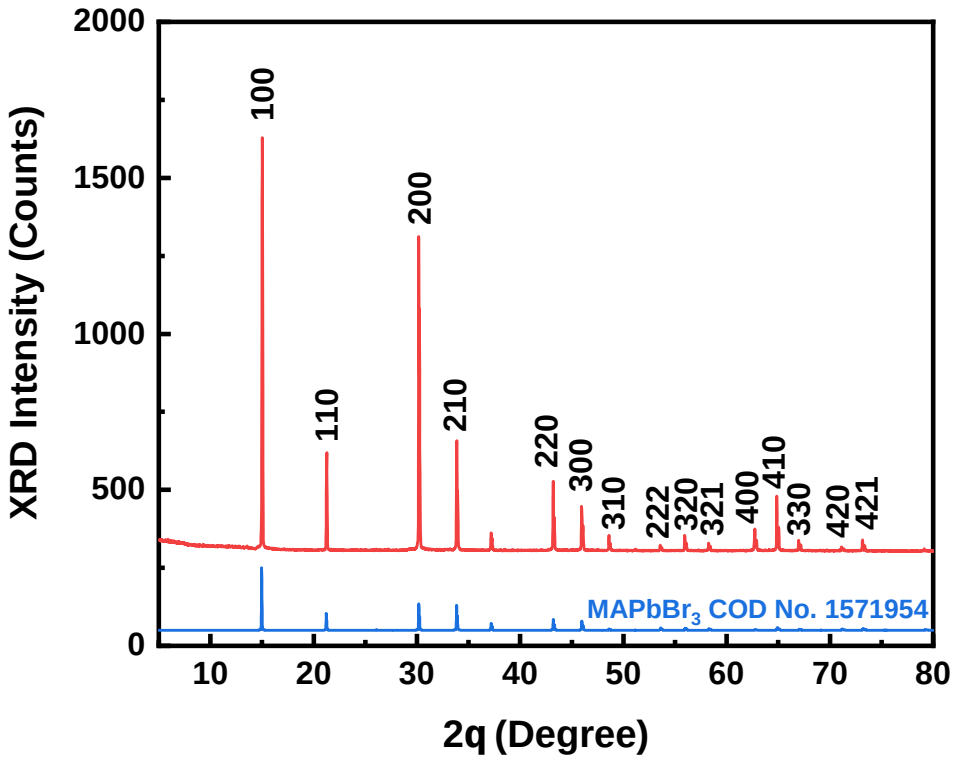


Figure 5.3: X-ray diffraction patterns of polycrystalline $MAPbBr_3$ sample. It exhibit characteristic peaks consistent with the perovskite structure, indicating phase purity. The absence of impurity peaks confirms the effectiveness of the selected synthesis conditions.

For $MAPbBr_3$, PXRD measurements were performed by Ilse Glas (see Section 2.3.1 for experimental details). As shown in Figure 5.3, the red curve represents the measured diffraction pattern of the synthesized sample. It is in good agreement with the reference pattern from the Crystallography Open Database (COD No. 1571954), displayed in blue. Additionally, peak positions and indices labeled in black were assigned based on comparison to the reference by Xia et al. [229]. The diffraction pattern exhibits sharp

and well-defined peaks, characteristic of a crystalline $MAPbBr_3$ phase. The absence of secondary or impurity peaks further confirms the high phase purity of the sample.

For $EBAPbI_3$, Liu et al. (2025) reported structural characterization indicating the formation of a chiral, low-dimensional perovskite phase. The material crystallizes in a non-centrosymmetric space group, which was verified through single-crystal and powder XRD analysis. The anisotropic crystal growth leads to needle-shaped single crystals, consistent with the observed morphology. Since the exact same material batch synthesized by Liu et al. was used in this work, the structural properties are assumed to be identical and are not remeasured here.

5.4 Electrochemical Characterization

To evaluate the potential of hybrid organic–inorganic perovskites as anode materials for lithium-ion storage, a comprehensive electrochemical analysis was conducted. The focus of this section lies on $MAPbBr_3$, chosen as a representative system due to its well-defined crystallinity. Initially, full voltage scans were performed to investigate its redox behavior and to identify the underlying reaction mechanisms, including lithiation, conversion, and alloying. Subsequently, the voltage range was selectively narrowed to isolate and stabilize individual electrochemical processes, and the lithiation breakdown voltage was determined to gain deeper insight into the lithiation mechanism. Variations in electrolyte composition and material morphology were systematically explored to assess their influence on electrochemical performance and stability. Finally, the role of external factors such as illumination and the incorporation of TiO_2 as a hole-blocking component were investigated to understand their impact on charge transport while illumination[2].

5.4.1 Reaction Mechanisms in $MAPbBr_3$

Before investigating the detailed electrochemical behavior of $MAPbBr_3$, it is essential to identify a suitable electrolyte system. HOIPs have demonstrated sensitivity and instability in conventional aprotic organic electrolytes, often leading to decomposition or suppressed electrochemical activity, as discussed in Section 5.1.1. As a result, recent studies have explored a wide range of electrolyte formulations to improve the compatibility and stability of HOIPs in lithium-ion battery environments [95]. In this context, our investigation began

[2]Electrochemical data in this work are subject to an estimated uncertainty of 5 – 10 %, primarily due to manual electrode preparation (weighing accuracy, slurry homogeneity, and mass loading), as explained in Section 2.4.1.

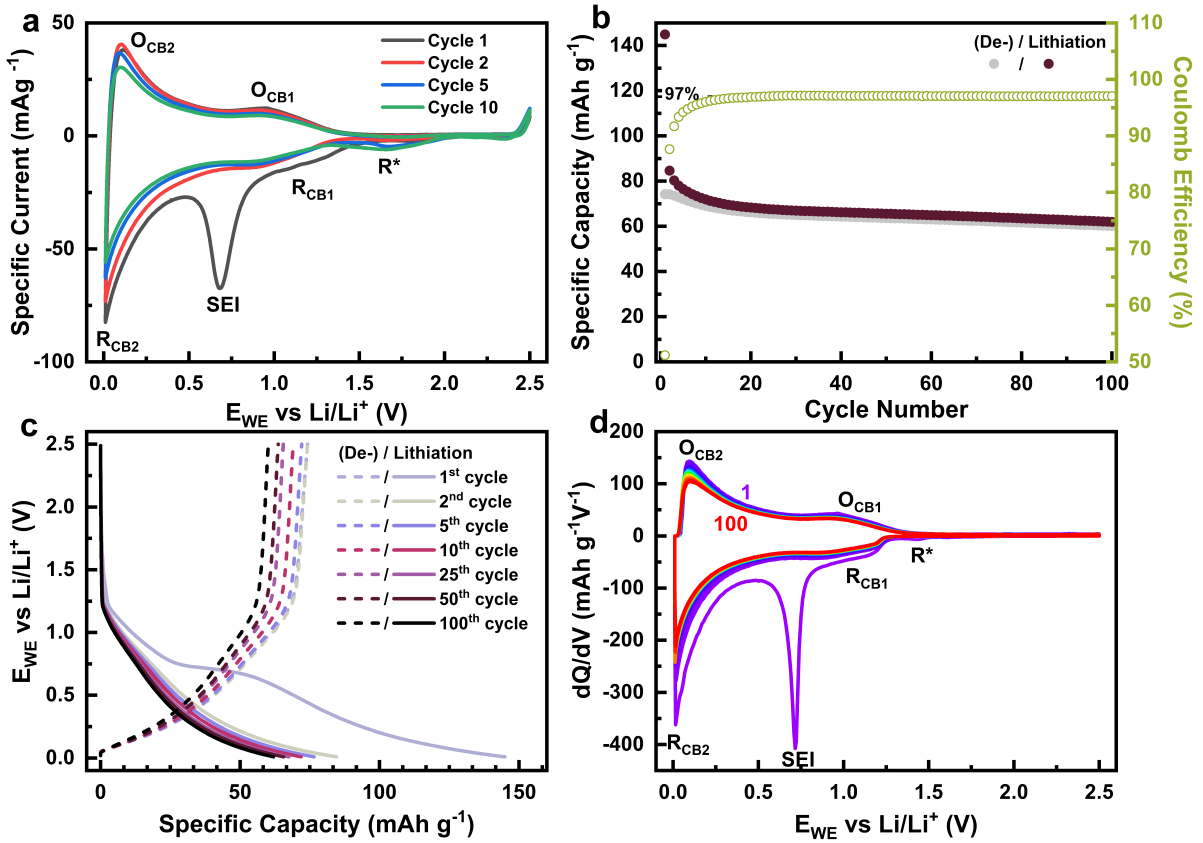


Figure 5.4: Electrochemical characterization of $MAPbBr_3$ in $LiPF_6$/EC:DMC. **a)** Cyclic voltammogram (CV) showing only the characteristic redox activity of CB (O/R_{CBi}) and a reductive feature corresponding to solid electrolyte interphase (SEI) formation (R_{SEI}), with no observable redox activity attributable to $MAPbBr_3$. **b)** Long-term GCPL cycling confirming the electrochemical inactivity of $MAPbBr_3$ under these conditions. **c)** Galvanostatic charge/discharge cycling (GCPL) profile at a current density of $100\,mA\,g^{-1}$, showing negligible capacity beyond that contributed by CB. **d)** Differential capacity plots (dQ/dV) highlighting the absence of additional redox peaks, supporting the conclusion that $MAPbBr_3$ remains electrochemically inactive in carbonate-based electrolyte.

with a comparative assessment of different electrolytes to determine which system enables reliable and reversible lithiation behavior in $MAPbBr_3$.

$LiPF_6$ — Inactive Electrochemical Behavior

To evaluate the electrochemical activity of $MAPbBr_3$ as a potential anode material for lithium-ion batteries, initial experiments were conducted using a conventional electrolyte system comprising 1 M $LiPF_6$ dissolved in a 1:1 (v/v) mixture of ethylene carbonate (EC) and dimethyl carbonate (DMC). This carbonate-based electrolyte represents a widely established standard in commercial LIBs and serves here as a reference to benchmark the electrochemical response of $MAPbBr_3$.

Figure 5.4 a) presents the cyclic voltammogram (CV) of a $MAPbBr_3$ electrode. The recorded signal shows only two distinct features: (i) the characteristic redox couples O/R_{CB} attributed to carbon black (CB), and (ii) a reduction peak associated with solid electrolyte interphase (SEI) formation, labeled R_{SEI} (cf. Section 2.4.5). Notably, no additional redox activity is observed that could be associated with the perovskite phase, indicating its electrochemical inactivity in this environment. This observation is supported by long-term galvanostatic charge/discharge cycling (GCPL), shown in Figure 5.4 b) and c. Here, the specific capacity is normalized to the total mass of materials expected to contribute electrochemically within the applied voltage range, namely, 60 % $MAPbBr_3$ and 30 % CB. The obtained capacity closely matches the measured contribution of CB alone under this normalization (see discussion in Section 2.4.5), further supporting the conclusion that $MAPbBr_3$ does not participate in the redox process under these conditions. To further analyze the charge/discharge behavior, differential capacity plots (dQ/dV) are shown in Figure 5.4 d). The absence of additional peaks beyond those associated with CB and SEI supports the CV and GCPL results, confirming the electrochemical passivity of the $MAPbBr_3$.

One possible explanation of these results could be due to dissolution of the active material $MAPbBr_3$ into the carbonate-based solvents of the used electrolyte. Similar results are shown for various HOIPs [238, 249–251]. However in other works $MAPbBr_3$ electrode show partly electrochemical activation in $LiPF_6$ but almost only with the addition of Ethyl methyl carbonate (EMC) resulting in 1 M $LiPF_6$ in EC:DMC:EMC (1:1:1) [228, 229, 252].

These results highlight the critical role of electrolyte selection in enabling redox activity in hybrid organic-inorganic perovskite materials. As such, the system was further investigated using an ether-based electrolyte composed of LiTFSI in DOL:DME, which, as detailed in the following section, enables lithiation, conversion, and alloying reactions consistent with electrochemically active behavior of $MAPbBr_3$.

LiTFSI — Observable Lithiation/Conversion/Alloying

To investigate the electrochemical activity of $MAPbBr_3$ under different electrolyte conditions, we employed an ether-based electrolyte consisting of 1 M LiTFSI in a 1:1 mixture of 1,3-dioxolane (DOL) and dimethoxyethane (DME).

Figure 5.5 displays CV curves of $MAPbBr_3$ electrodes recorded at a scan rate of 0.1 $mV\,s^{-1}$ for cycles 1, 2, 5, and 10. In the first cycle, a sharp and prominent reduction peak is

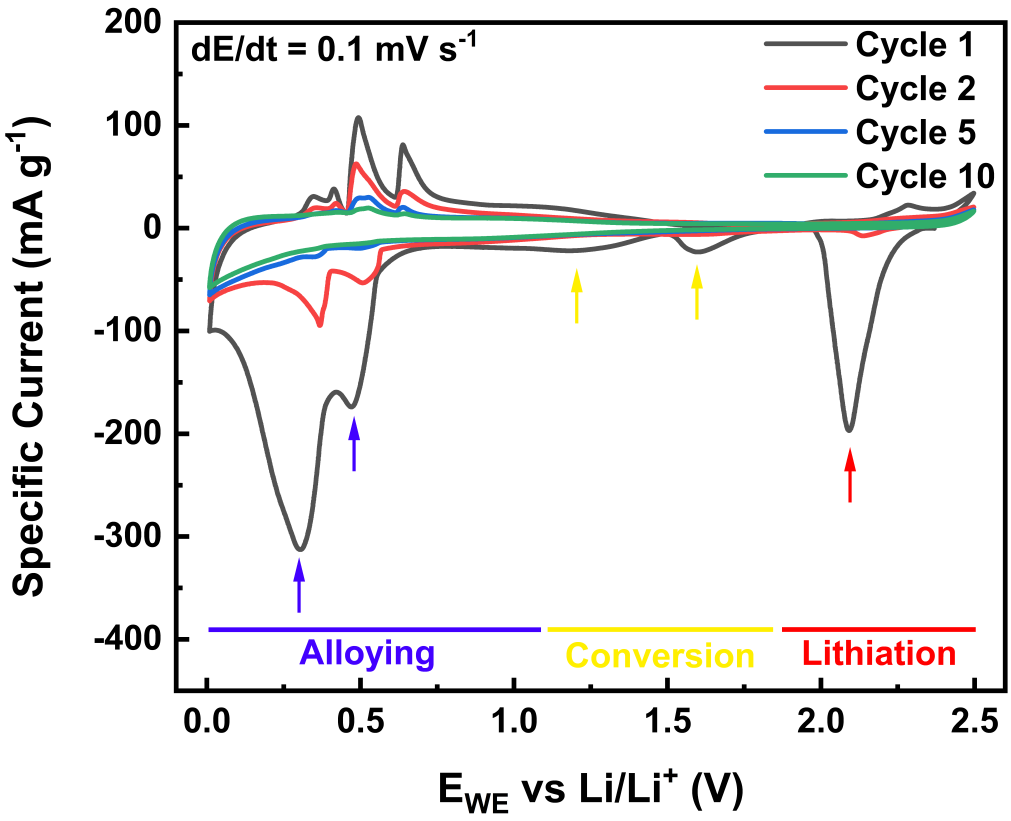


Figure 5.5: Cyclic voltammetry of $MAPbBr_3$ in 1 M LiTFSI/DOL:DME at a scan rate of 0.1 mV s^{-1} for cycles 1, 2, 5, and 10. Reduction and oxidation features are color-coded by mechanism: Lithiation (sharp peak at 2.09 V), Conversion (broad peaks at 1.61 V and 1.12 V), and Alloying (features at 0.47 V and 0.30 V). Corresponding dealloying and oxidation peaks diminish with continued cycling, indicating partial irreversibility of the processes.

observed at 2.09 V, which disappears in subsequent cycles. This feature is attributed to an initial lithiation process of $MAPbBr_3$, consistent with the behavior reported by Vicente et al. [230]. The lithiation is highlighted in red in the CV plot. Additional broad and irreversible reduction features are evident at 1.61 V and 1.12 V during the first cycle. These are assigned to sequential conversion reactions of the perovskite structure, leading to the formation of lithium halide and elemental lead species. These processes, also observed by Vicente et al., are indicated in yellow. At lower potentials, a strong reduction peak centered at 0.30 V, accompanied by a shoulder at 0.47 V, emerges during the initial cycles. These features diminish after the fifth cycle and are associated with alloying reactions between lithium and metallic lead, producing lithium–lead intermetallic compounds. These processes are marked in blue. The corresponding oxidation behavior exhibits several weak peaks between 0.35 V and 0.64 V, consistent with dealloying of Li_xPb phases. However, these features progressively fade and are no longer detectable after the

tenth cycle. A weak and broad oxidation peak appears at 1.20 V, likely related to partial oxidation of conversion products, but no further oxidation is observed in the lithiation region except for a small irreversible signal at 2.28 V, which vanishes after the first cycle. Overall, the electrochemical profile confirms the occurrence of the expected lithiation, conversion, and alloying reactions in $MAPbBr_3$, in agreement with the literature. The respective reaction pathways are summarized in Section 5.1.1.

The electrochemical signatures observed in the CV measurements clearly indicate the presence of distinct lithiation, conversion, and alloying processes in $MAPbBr_3$ when using a LiTFSI-based ether electrolyte.

Electrochemical Performance in Full Range

To complement the insights gained from cyclic voltammetry, galvanostatic cycling was employed to evaluate the electrochemical behavior of $MAPbBr_3$ across the full voltage window and over extended cycling. This allows a more comprehensive understanding of capacity contributions from lithiation, conversion, and alloying processes, as well as their stability.

Figure 5.6 a) shows the first-cycle GCPL profile of $MAPbBr_3$, benchmarked against literature data from Vicente et al. [230]. The lithiation region around 2.23 V delivers approximately a specific capacity of $65\,\mathrm{mA\,h\,g^{-1}}$, followed by distinct conversion features from 1.49 V to 0.61 V, contributing roughly $135\,\mathrm{mA\,h\,g^{-1}}$. Alloying reactions emerge below 0.56 V, yielding approximately $160\,\mathrm{mA\,h\,g^{-1}}$ and $100\,\mathrm{mA\,h\,g^{-1}}$ at 0.56 V and 0.40 V, respectively. A broad alloying shoulder below 0.40 V contributes further, resulting in a total first-cycle capacity of $561\,\mathrm{mA\,h\,g^{-1}}$. Compared to the literature, similar lithiation behavior is observed, with Vicente et al. [230] reporting a lithiation peak at 2.21 V contributing $50\,\mathrm{mA\,h\,g^{-1}}$. Their conversion and alloying contributions are significantly lower, resulting in a total capacity of only $381\,\mathrm{mA\,h\,g^{-1}}$. These differences may arise from synthesis conditions, particle size distribution, or electrode formulation. The long-term GCPL performance and coulomb efficiency are shown in Figure 5.6 b). A rapid capacity fading is observed, with specific capacity dropping from $561\,\mathrm{mA\,h\,g^{-1}}$ to $109\,\mathrm{mA\,h\,g^{-1}}$ within the first 20 cycles, followed by a gradual decay to $48\,\mathrm{mA\,h\,g^{-1}}$ after 100 cycles, indicative of full degradation of $MAPbBr_3$ activity, leaving only the CB contribution. Superimposed oscillations with a periodicity of $\approx 24\,\mathrm{h}$ suggest temperature fluctuations (e.g., diurnal variation) affecting reaction kinetics due to insufficient cooling during testing. Coulomb efficiency increases from $\approx 50\,\%$ to $95\,\%$ within the first 30 cycles, then gradually stabilizes at $\approx 99\,\%$, reflecting the predominance of reversible intercalation of lithium into

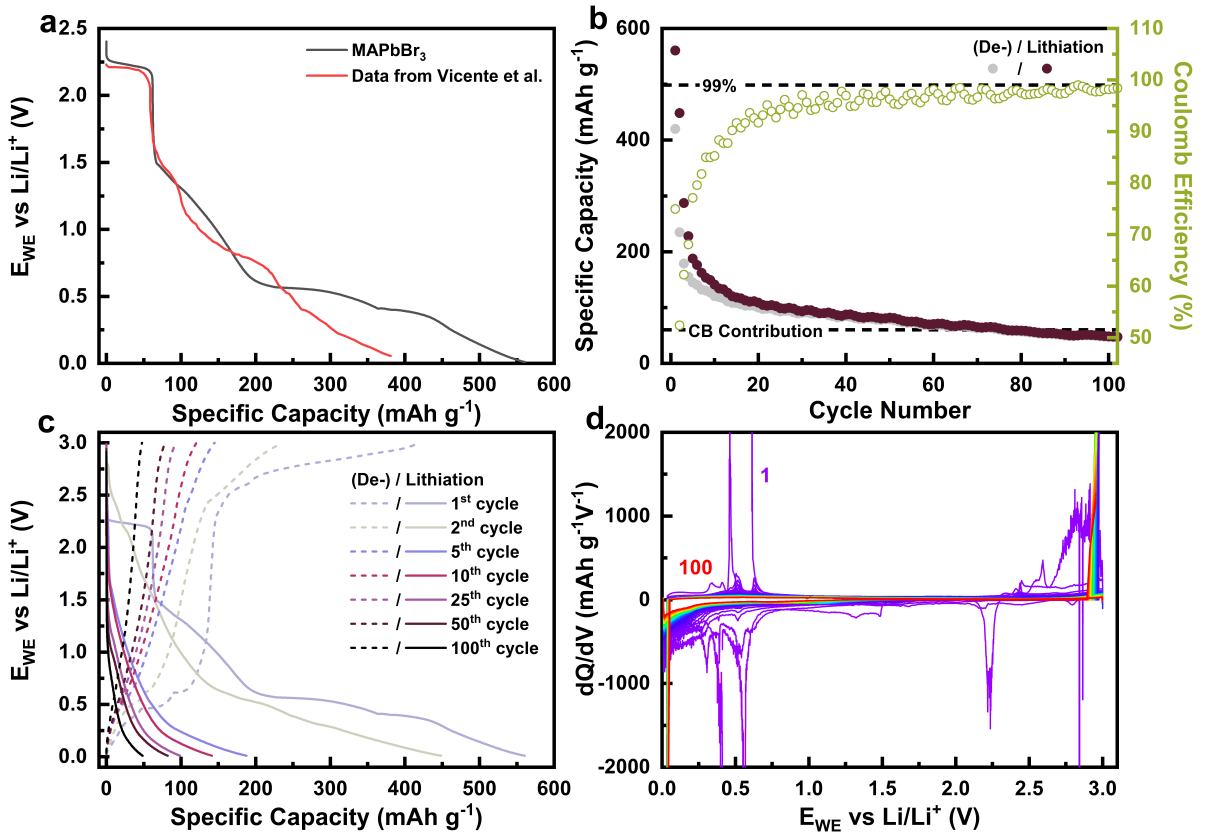


Figure 5.6: Electrochemical performance of $MAPbBr_3$ in LiTFSI/DOL:DME. **a)** First-cycle GCPL profile compared to data adapted from Vicente et al. [230], highlighting individual reaction contributions. **b)** Long-term cycling performance and coulomb efficiency over 100 cycles. **c)** Full potential profiles of 100 cycles. **d)** Differential capacity (dQ/dV) evolution from cycle 1 (magenta) to cycle 100 (red), indicating fading of active processes.

carbon at later stages. Figure 5.6 c) presents full potential profiles for 100 cycles. In the first upsweep dealloying between 0 and 1 V provides a capacity of $\approx 130\,\mathrm{mA\,h\,g^{-1}}$, corresponding to a retention of $\approx 72\,\%$ compared to the initial alloying capacity. Delithiation at 2.59 V yields $\approx 50\,\mathrm{mA\,h\,g^{-1}}$, while an irreversible plateau from 2.62 V to 3.00 V consumes $\approx 200\,\mathrm{mA\,h\,g^{-1}}$, likely linked to irreversible structural changes. The evolution of differential capacity (dQ/dV) from cycle 1 to 100 is illustrated in Figure 5.6 d). Initially distinct lithiation, conversion, and alloying features gradually vanish, with only minor contributions from carbon black persisting beyond 100 cycles.

Taken together, these results confirm the rapid fading of $MAPbBr_3$ activity under full voltage cycling. The observed degradation aligns with the CV trends (Figure 5.5), and highlights the need to stabilize individual processes by restricting the voltage window. In the following section, we explore isolated reaction studies aimed at decoupling alloying and lithiation to improve long-term performance.

5.4.2 Limited Voltage Range Studies

The goal of this section is twofold: (1) to assess whether electrochemical degradation can be mitigated by isolating alloying and lithiation reactions, and (2) to determine the origins of the irreversible breakdown observed during cycling, particularly whether conversion reactions are responsible for this instability.

Alloying — Stability and Degradation during Cycling

The first approach involves isolating the alloying process by applying a restricted voltage window of 0 – 1.2 V, which targets only the low-potential alloying reactions. The goal is to investigate whether this separation improves cycling stability and reversibility of the redox features.

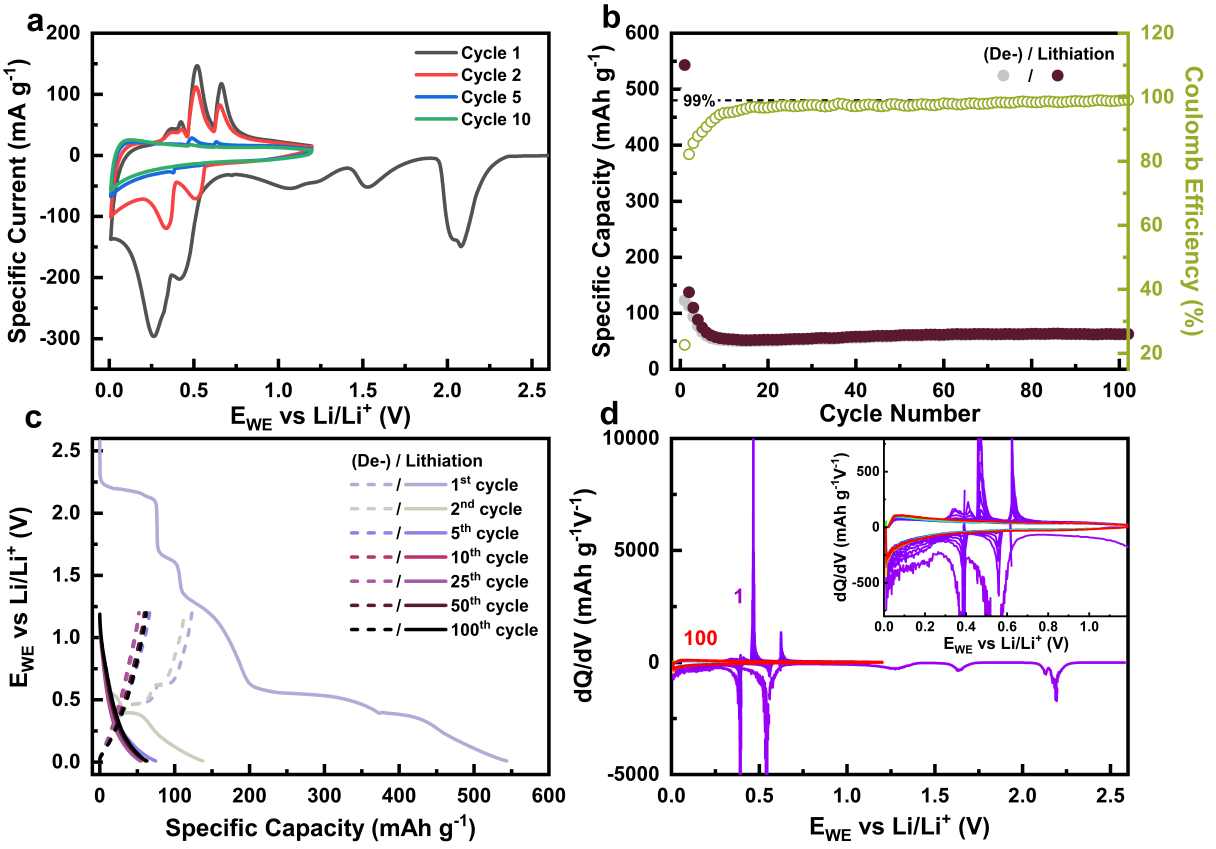


Figure 5.7: Electrochemical characterization of $MAPbBr_3$ in the alloying regime (0 – 1.2 V). **a)** CV scans for cycles 1, 2, 5, and 10. **b)** Long-term GCPL cycling and coulomb efficiency over 100 cycles. **c)** GCPL potential profiles over 100 cycles. **d)** Differential capacity plots (dQ/dV) from cycle 1 (magenta) to cycle 100 (red).

Figure 5.7 a) displays CV scans for selected cycles (1, 2, 5, and 10) within the alloying window. Despite the voltage limitation, the downsweep from the open-circuit voltage of

2.6 V still includes lithiation at 2.19 V and conversion reductions at 1.56 V and 1.12 V, which appear slightly shifted compared to previous CVs (see Figure 5.5). The alloying reduction manifests as a dominant peak at 0.27 V with a shoulder at 0.43 V. Four corresponding oxidation peaks are observed at 0.36 V, 0.42 V, 0.52 V, and 0.67 V. Notably, all redox activity fades by cycle five, closely resembling the behavior observed under unrestricted cycling conditions. To evaluate long-term performance, GCPL cycling within the alloying window was conducted for 100 cycles (Figure 5.7 b). The first cycle yields a high specific capacity of 544 mA h g^{-1}, which rapidly drops to 55 mA h g^{-1} by cycle 10. A slight recovery occurs, stabilizing around 63 mA h g^{-1} by cycle 90, possibly due to gradual electrolyte wetting of the electrode surface [253]. However, the sustained specific capacity is attributed primarily to the CB additive, not active material redox activity. This is corroborated by the coulomb efficiency (CE), which starts at 23 % due to asymmetric charge/discharge profiles, increases sharply within the first 10 cycles, and stabilizes around 99 % by cycle 80, typical for inert conductive additives (see section 2.4.5). Figure 5.7 c) shows potential profiles for 100 cycles. On the downsweep, lithiation occurs at 2.18 V ($\approx$ 70 mA h g^{-1}), followed by conversion at 1.64 V and 1.31 V ($\approx$ 30 and 100 mA h g^{-1}, respectively), and finally alloying at 0.55 V and 0.39 V, each contributing $\approx$ 175 mA h g^{-1}. This results in a total specific capacity of 544 mA h g^{-1}. On the upsweep, broad alloying features persist up to 0.45 V, with two oxidation peaks at 0.47 V and 0.63 V, contributing $\approx$ 40 and 50 mA h g^{-1}, respectively. However, this reversibility degrades quickly and is no longer visible after five cycles. To monitor peak evolution and identify redox plateaus, differential capacity plots (dQ/dV) are presented in Figure 5.7 d) from cycle 1 (magenta) to cycle 100 (red). Initially, lithiation, conversion, and alloying signatures are visible. The main alloying redox couples remain distinct but fade rapidly, vanishing completely after cycle 9. From cycle 20 onward, only broad features attributable to carbon black remain, consistent with the CE and capacity trends. This strongly suggests that the alloying reactions are not inherently stabilized by isolation and that degradation arises from the dissolution of the active perovskite material into the electrolyte.

In summary, restricting the voltage to isolate alloying does not improve the electrochemical stability of $MAPbBr_3$. Redox features decay rapidly, and capacity retention is limited beyond a few cycles. The findings suggest that the degradation of the alloying processes are not only caused by interference from lithiation or conversion reactions, but rather by dissolution of the perovskite material into the electrolyte, a mechanism that aligns with degradation processes proposed by Büttner et al. [232]. To test whether lithiation suffers from similar instability, the next section examines the behavior of $MAPbBr_3$ under isolated lithiation.

Lithiation - Stabilization via Voltage Window Optimization

To better understand and separate the lithiation process in $MAPbBr_3$, the voltage range was restricted to 1.8 – 2.8 V and the current density was set to 10 mA g^{-1}. This approach was motivated by two key goals: (1) to examine whether the lithiation step alone can exhibit stable electrochemical behavior when decoupled from conversion and alloying reactions, and (2) to determine whether the degradation observed in the full voltage range is intrinsic to lithiation or caused by other side reactions.

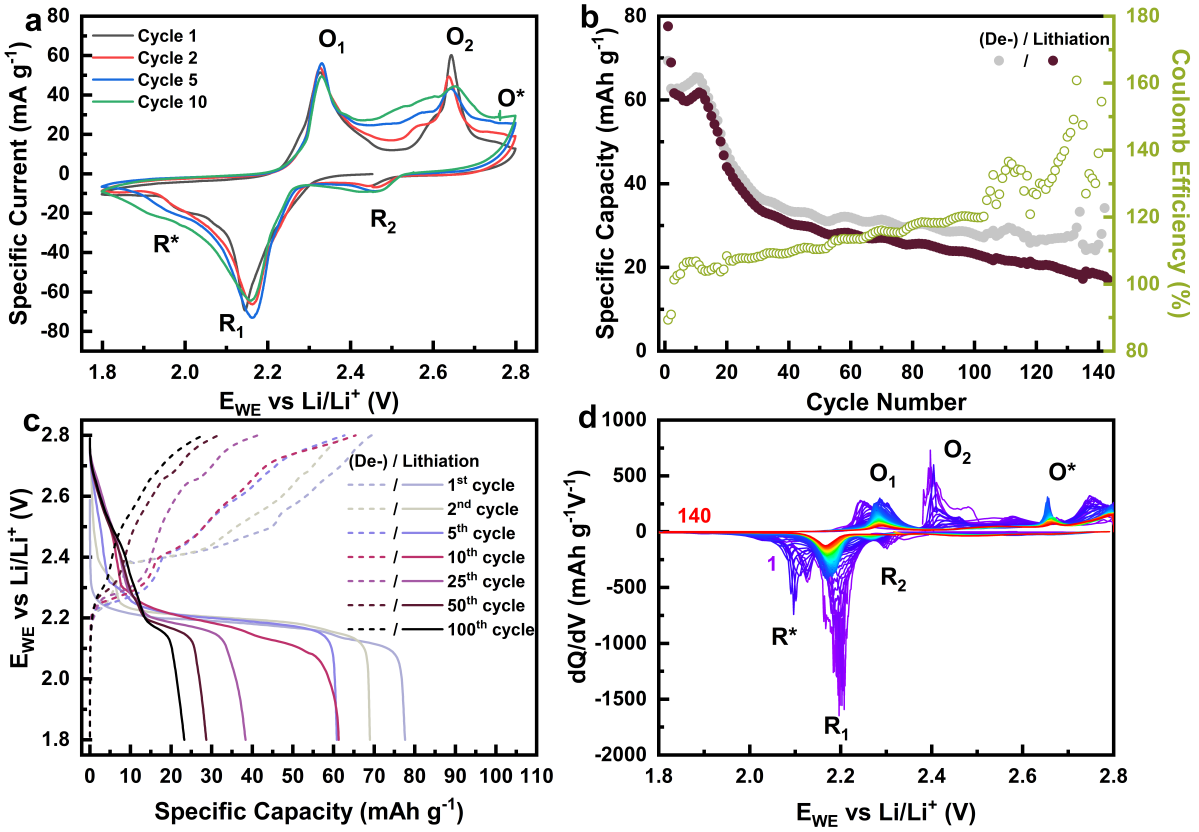


Figure 5.8: Electrochemical characterization of the isolated lithiation regime in $MAPbBr_3$ between 1.8 and 2.8 V. **a)** CV measurements for cycles 1, 2, 5, and 10 showing reversible lithiation/delithiation peaks. **b)** Long-term GCPL cycling over 145 cycles indicating gradual capacity fading with increasing coulomb inefficiency. **c)** First-cycle GCPL potential profile with defined lithiation and delithiation plateaus with current densities of 10 mA g^{-1}. **d)** Differential capacity plots (dQ/dV) over 140 cycles illustrating the evolution and disappearance of reaction features.

Figure 5.8 a) depicts CV studies in the lithiation voltage region for cycles 1, 2, 5, and 10. The downsweep from OCV at 2.5 V shows a distinct lithiation peak R_1 at 2.15 V, along with a shoulder-like feature R* at 1.98 V. The peak height is approximately 75 mA g^{-1}, about half of that observed in previous measurements with unrestricted voltage, which may be due to hindered kinetics or insufficient electrolyte wetting. On the upsweep,

two delithiation peaks O_1 and O_2 appear at 2.32 V and 2.68 V, respectively. A third, shoulder-like oxidation feature O* emerges at 2.80 V. The previously unseen splitting of the oxidation peak suggests more defined processes due to the restricted window. Additionally, a small reduction peak R_2 at 2.50 V appears, the origin of which remains unclear. In subsequent cycles 2, 5, and 10, the R_1/O_1 couple shows minimal change, indicating good reversibility. However, O_2 broadens and decreases over time, potentially reflecting ongoing structural changes. Figure 5.8 b) shows Long-term GCPL cycling limited to the lithiation window over 145 cycles. The first cycle delivers a specific capacity of 78 mA h g^{-1}, in agreement with the CV data. This drops to 62 mA h g^{-1} by the third cycle, forming a plateau that persists until cycle 12. A gradual decay follows, reaching 34 mA h g^{-1} at cycle 30 and declining further to 17 mA h g^{-1} at cycle 145. Notably, delithiation capacity is consistent slightly higher than lithiation capacity throughout cycling, especially in the plateau and long-term regions. This suggests that the material undergoes irreversible structural changes, possibly indicating the slow degradation of the perovskite structure. A similar trend is visible in the coulomb efficiency, which steadily increases from 100 % to 120 % over 100 cycles, again highlighting partial irreversibility. Still, these results represent significantly improved stability compared to the full voltage range. Figure 5.8 c) shows GCPL potential profiles of the 145 cycles. During the downsweep, the R_1 plateau at 2.20 V and the R* shoulder at 2.16 V contribute approximately 60 and 15 mA h g^{-1}, respectively, resulting in 78 mA h g^{-1} total specific capacity. On the upsweep, the O_1 and O_2 plateaus at 2.24 V and 2.40 V yield around 10 and 35 mA h g^{-1}, respectively, while the broad oxidation feature O* between 2.5 and 2.8 V contributes an additional 25 mA h g^{-1}, resulting in 69 mA h g^{-1}. Figure 5.8 d) depicts a differential capacity (dQ/dV) plot showing the evolution of the lithiation process over 140 cycles. Cycle 1 is shown in magenta, fading to red by cycle 140. R_1 and R* appear to merge by cycle 3. Interestingly, R* reappears at cycle 7 but fades entirely by cycle 20. O_1 shifts from 2.23 V in cycle 1 to 2.29 V by cycle 20. The O_2 peak at 2.40 V broadens and vanishes after cycle 15. Two new oxidation features, O*, emerge at 2.66 V and 2.75 V, which were not clearly distinguishable in the CV.

Restricting the voltage range to isolate the lithiation regime improves the cycling stability of $MAPbBr_3$ drastically, though capacity fading and rising coulomb inefficiencies persist. This suggests that the degradation of the delithiation and lithiation process in $MAPbBr_3$ is probably mainly caused by structural changes during conversion or alloying reactions. Rather, interactions with the electrolyte, possibly involving dissolution of active material, may still play a significant role. In the next subsection, a stepwise expansion of the voltage window in CV measurements will be carried out to pinpoint the specific voltage range

in which irreversible structural changes and therefore degradation of the (de-)/lithiation process occurs.

Identifying the Breakdown Voltage of Lithiation

By reducing the lower cut-off voltage in small increments from 2.0 to 0.2 V in steps of 0.1 V, it becomes possible to observe which reaction mechanisms contribute to the progressive degradation of the lithiation process.

Figure 5.9 a) shows a sequence of CV measurements in which the lower voltage limit was decreased from 2.0 to 0.2 V in steps of 0.1 V, with each step applied for three cycles. The smallest voltage window (2.0 – 2.5 V) is represented in red (cycle 1 – 3), and the color scale shifts gradually to magenta for the broadest window (0.2 – 2.5 V, cycle 55 – 57). Initially, distinct lithiation (R_1) and delithiation (O_1) peaks are observed at 2.09 V and 2.29 V, respectively. Over the first few cycles, the lithiation peak height decreases slightly from 149 to 123 mA g^{-1}, which corresponds to behavior previously seen under isolated lithiation conditions (cf. Figure 5.8). This early capacity decay is thus not attributed to the changing voltage window. However, around cycle 20 (yellow region), a more pronounced and continuous decline of the lithiation peak emerges. This correlates with the onset of the conversion reaction, likely leading to structural alterations that impair the reversibility of lithiation. The subsequent introduction of alloying processes below 0.6 V, occurring after approximately 40 cycles, further accelerates the degradation. Figure 5.9 b) provides a magnified view of the lithiation region. A small positive shift of the lithiation peak is observed between the first and third cycle (from 2.09 to 2.16 V) and again after cycle nine (to 2.14 V). Beyond this point, the lithiation peak position remains largely constant, suggesting that the observed electrochemical degradation is not linked to voltage drift, but rather to irreversible structural changes introduced by lower voltage reactions.

In summary, this stepwise approach reveals that the breakdown of the lithiation process is primarily initiated by the irreversible conversion reaction. The structural changes triggered by this reaction likely inhibit lithium insertion/extraction, even in otherwise stable voltage regimes.

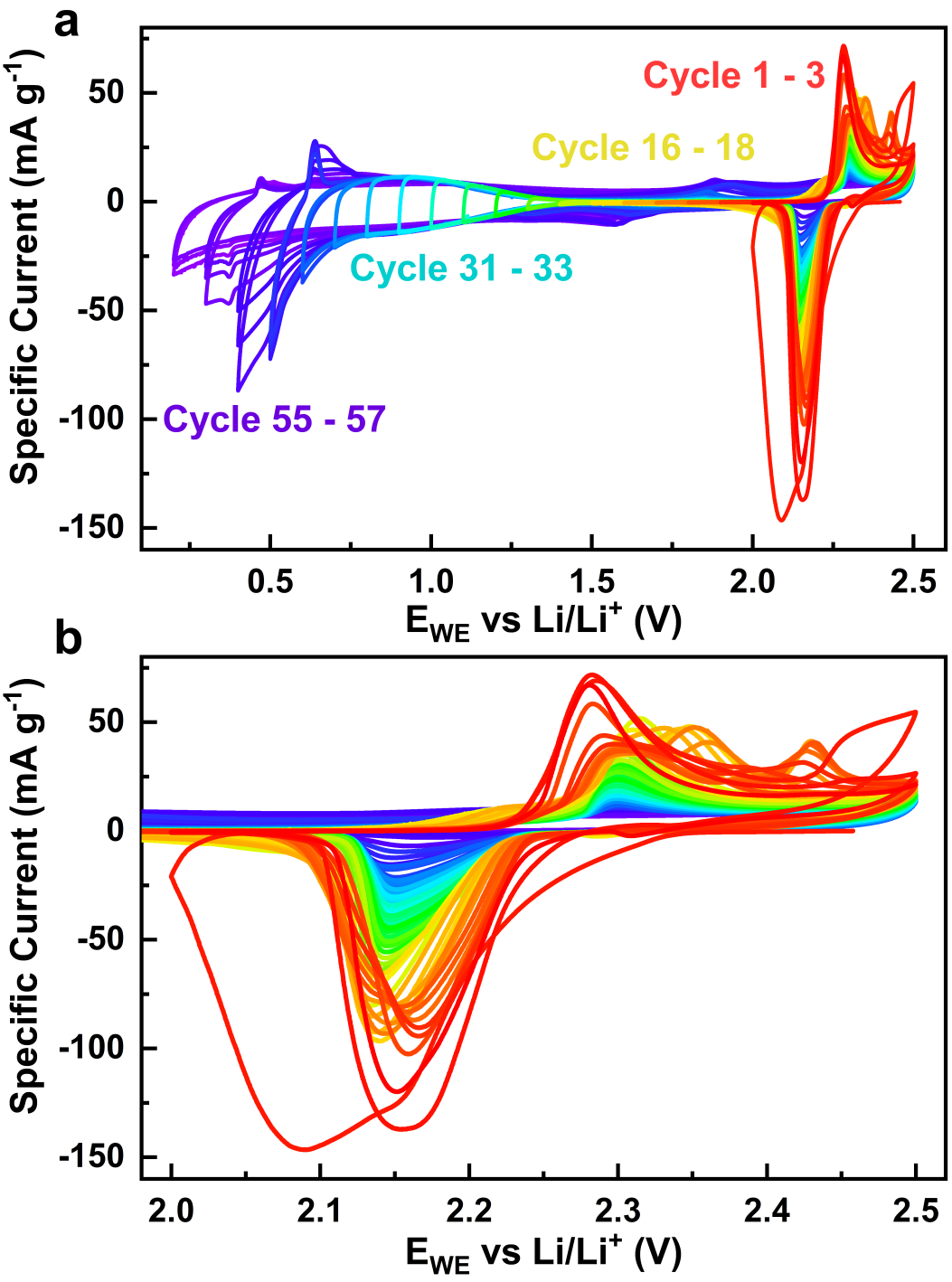


Figure 5.9: Stepwise cyclic voltammetry to identify the breakdown voltage of lithiation. **a)** Full CV scans with the lower cut-off voltage gradually decreased from 2.0 to 0.2 V in steps of 0.1 V every three cycles. Color gradient from red (cycle 1 – 3) to magenta (cycle 55 – 57). **b)** Zoom into the lithiation region (1.95 V $<$ E_{WE} $<$ 2.5 V) to observe shifts and degradation of the lithiation peak.

5.4.3 Electrolyte Studies

Given the decisive role of the electrolyte in the electrochemical behavior of $MAPbBr_3$, as demonstrated in earlier sections, we systematically studied the impact of electrolyte composition. Variations included different lithium salts, salt concentrations, common additives, and the implementation of a solid polymer electrolyte. The aim was to gain a better understanding of the electrolyte–HOIP interactions and their effect on electrochemical stability. Details of the electrolyte systems used can be found in Section 2.4.3. The electrolyte strongly influences both the stability and reactivity of hybrid perovskites, as emphasized in recent literature [95]. In this study, we explored the electrochemical behavior of $MAPbBr_3$ in a range of electrolyte formulations and compared them to the standard 1 M $LiPF_6$ in EC:DMC (e)). The Table 5.2 presents a range of electrolyte formulations used for electrochemical testing of $MAPbBr_3$ and related hybrid perovskites. Most electrolytes are based on lithium salts such as LiTFSI, $LiPF_6$, or $LiClO_4$ dissolved in common organic solvents (e.g., DOL:DME, EC:DMC), with salt concentrations ranging from 1 M to 5 M. Several systems include additives like $LiNO_3$ or FEC to enhance interfacial stability or SEI formation. While the majority of the electrolytes are liquid-phase, one solid-state electrolyte based on LiTFSI in PEO is also included, enabling comparisons between liquid and solid systems.

	Salt Concentration	Salt	Solvent (1:1) by Volume	Additives	Electrolyte Type
a)	1 M	LiTFSI	DOL:DME	-	liquid
b)	1 M	LiTFSI	DOL:DME	1 % $LiNO_3$	liquid
c)	3.6 M	LiTFSI	DOL:DME	10 % FEC	liquid
d)	5 M	LiTFSI	EC:PC	-	liquid
e)	1 M	$LiPF_6$	EC:DMC	-	liquid
f)	1 M	$LiPF_6$	EC:DMC	10 % FEC	liquid
g)	1 M	$LiClO_4$	EC:DMC	-	liquid
h)	2.5 M	LiTFSI	PEO	-	solid

Table 5.2: Summary of electrolyte formulations used for electrochemical testing of $MAPbBr_3$ and related HOIPs. Each system is defined by salt type and concentration, solvent composition (1:1 by volume), additive presence, and electrolyte type.

Figure 5.10 presents the CV profiles for cycles 1, 2, 5, and 10 under identical conditions (scan rate 0.1 mV s^{-1}, voltage range 0 – 2.5 V, normalized to $MAPbBr_3$ and conductive carbon mass). In the following the changes of the electrochemical responses of the 8 different cases will be discussed individually with respect to the benchmark measurement b).

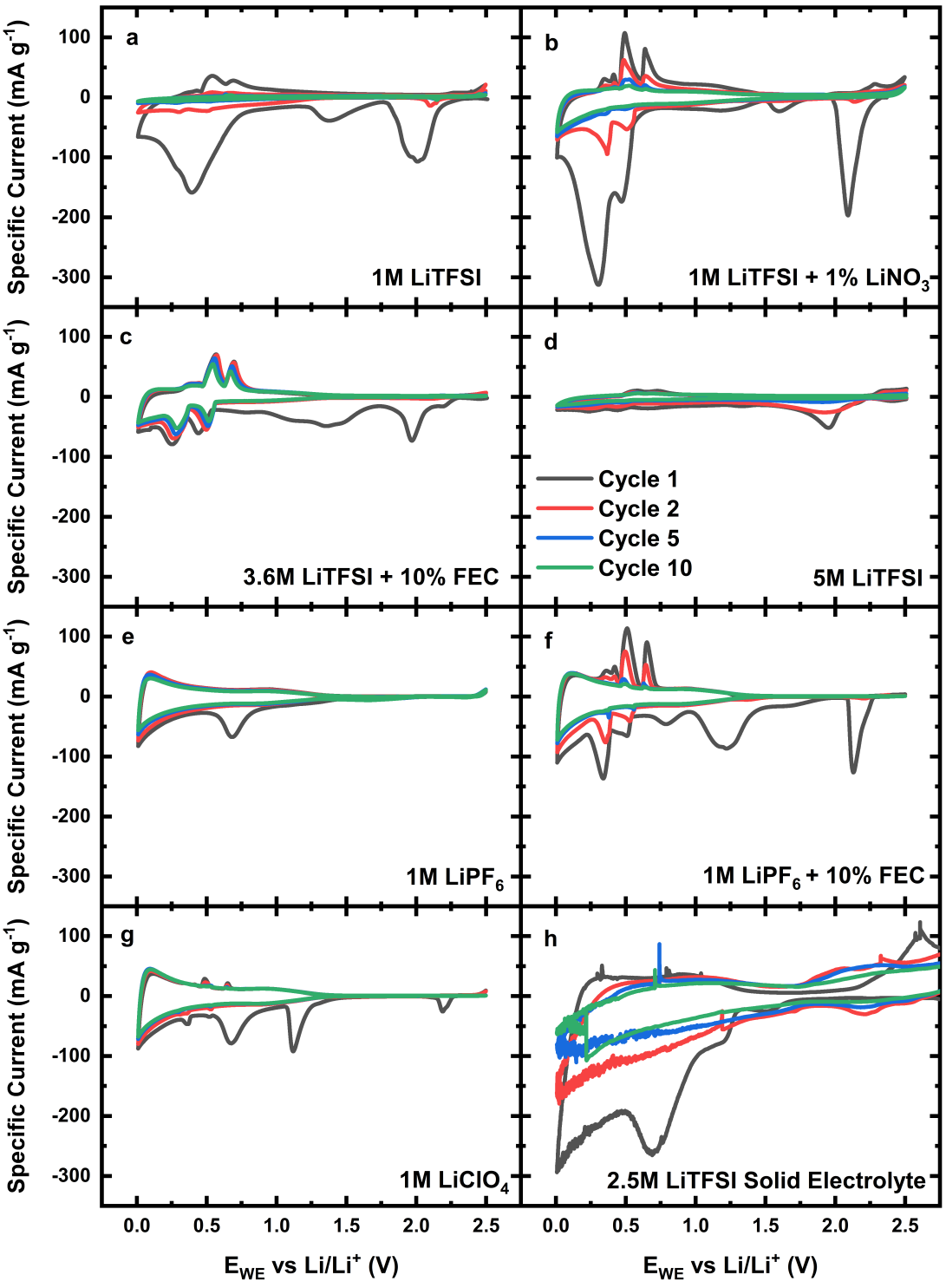


Figure 5.10: CV of $MAPbBr_3$ in various electrolytes over cycles 1, 2, 5, and 10. **a)** 1 M LiTFSI in DOL:DME, **b)** 1 M LiTFSI + 1 % $LiNO_3$ in DOL:DME, **c)** 3.6 M LiTFSI + 10 % FEC in DOL:DME, **d)** 5 M LiTFSI in EC:PC, **e)** 1 M $LiPF_6$ in EC:DMC, **f)** 1 M $LiPF_6$ + 10 % FEC in EC:DMC, **g)** 1 M $LiClO_4$ in EC:DMC, **h)** 2.5 M LiTFSI in PEO. The observed redox processes, including lithiation, conversion, alloying, and SEI formation, vary significantly with electrolyte composition.

a) 1 M LiTFSI in DOL:DME

The electrochemical response of $MAPbBr_3$ in a 1 M LiTFSI DOL:DME electrolyte is depicted in Figure 5.10 a). A lithiation reduction peak is observed at 2.00 V with a specific current of 105 mA g^{-1}, which vanishes completely by the second cycle. Irreversible conversion occurs at 1.37 V (40 mA g^{-1}), followed by broad alloying features at 0.38 V and 0.27 V. On the anodic sweep, oxidation peaks emerge at 0.54 V (36 mA g^{-1}) and 0.69 V (28 mA g^{-1}), along with a minor delithiation peak at 2.27 V (8 mA g^{-1}). All redox features vanish after two cycles, suggesting rapid degradation or passivation of the electrode surface.

b) 1 M LiTFSI + 1 % $LiNO_3$ in DOL:DME

As shown in Figure 5.10 b), the addition of 1 % $LiNO_3$ significantly enhances the lithiation peak to 2.09 V with a current of 200 mA g^{-1}. The alloying reactions occur at 0.30 V and 0.47 V, with specific currents of 312 and 170 mA g^{-1}, respectively, and persist up to the fifth cycle. On the anodic side, alloying oxidation occurs at 0.49 V (107 mA g^{-1}) and 0.64 V (81 mA g^{-1}). A minor delithiation feature appears at 2.28 V (22 mA g^{-1}). While reactions persist longer than in the additive-free system, they are still fully suppressed by cycle five, suggesting intermediate stability enhancement.

c) 3.6 M LiTFSI + 10 % FEC in DOL:DME

Electrochemical features under a highly concentrated 3.6 M LiTFSI electrolyte with 10 % FEC are presented in Figure 5.10 c). The initial lithiation (1.97 V, 73 mA g^{-1}) and conversion (1.39 V, 48 mA g^{-1}) reactions fade quickly, but the alloying reductions at 0.44 V and 0.25 V remain stable through 10 cycles. Corresponding oxidation peaks at 0.55 V (65 mA g^{-1}) and 0.70 V (56 mA g^{-1}) also remain consistent. The long-term presence of these peaks suggests the formation of a stable interphase, possibly mediated by FEC decomposition products.

d) 5 M LiTFSI in EC:PC

Figure 5.10 d) illustrates that increasing salt concentration to 5 M LiTFSI reduces redox activity overall. Lithiation occurs at 1.95 V (52 mA g^{-1}), followed by conversion at 1.36 V and alloying at 0.44 V and 0.24 V. Anodic alloying oxidation peaks are seen at 0.57 V and 0.74 V, both with specific currents of 10 mA g^{-1}. A minor delithiation signal at 2.34 V (10 mA g^{-1}) is also detected. All signals are suppressed after two cycles, suggesting that overly concentrated electrolytes may negatively impact interfacial dynamics [254].

e) 1 M $LiPF_6$ in EC:DMC

In the 1 M $LiPF_6$ EC:DMC system (Figure 5.10 e), no reversible redox peaks are detected. The only feature is an irreversible SEI formation process at 0.67 V (10 mA g^{-1}). This is consistent with previous observations in Subsection 5.4.1, and confirms that $MAPbBr_3$ is electrochemically inactive in this conventional lithium-ion electrolyte formulation.

f) 1 M $LiPF_6$ + 10 % FEC in EC:DMC

The CV data in Figure 5.10 f) reveal that adding 10 % FEC activates redox behavior. Lithiation is seen at 2.13 V (126 mA g^{-1}), with alloying reductions at 0.51 V and 0.33 V. Oxidation peaks are centered at 0.51 V (114 mA g^{-1}) and 0.65 V (91 mA g^{-1}). An SEI formation step is also noted at 0.75 V. While initial activity is high, all peaks diminish by cycle 10, indicating poor long-term performance.

g) 1 M $LiClO_4$ in EC:DMC

Cyclic voltammograms in Figure 5.10 g) show moderate lithiation at 2.19 V (25 mA g^{-1}), followed by conversion at 1.12 V and alloying at 0.52 V and 0.37 V. Oxidation reactions occur at 0.48 V (29 mA g^{-1}) and 0.65 V (21 mA g^{-1}). All redox activity fades by the second cycle, despite the electrolyte's acceptable initial compatibility.

h) 2.5 M LiTFSI in PEO (solid polymer electrolyte)

Figure 5.10 h) presents electrochemical behavior in a solid-state 2.5 M LiTFSI PEO-based electrolyte. A broad lithiation peak is detected at 2.21 V (30 mA g^{-1}) and conversion at 1.15 V (81 mA g^{-1}). A large reduction peak at 0.69 V (266 mA g^{-1}) is recognizable possibly assigned to formation of SEI. However, distinct alloying and oxidation peaks are hard to discernible, likely due to low ionic conductivity or poor electrode-electrolyte contact. This is also supported by the width of the reductions peaks. The absence of further redox features highlights the kinetic limitations associated with solid polymer systems.

Summary

Electrochemical behavior of $MAPbBr_3$ is highly sensitive to the electrolyte composition. While standard carbonate-based electrolytes (e.g., $LiPF_6$ in EC:DMC) offer poor compatibility, ether-based systems with LiTFSI or $LiNO_3$ additives exhibit enhanced, albeit transient, redox activity (see Figure 5.10 b)). Concentrated electrolytes and additives like FEC can extend the lifetime of alloying reactions but do not fundamentally prevent degradation (see Figure 5.10 f)). Solid polymer electrolytes show largely broadened redoxpeaks, potentially due to suppressed solvent–perovskite interactions or low ionic conductivity.

Overall, these results highlight the critical role of electrolyte engineering for stabilizing HOIP-based anodes in lithium-ion systems.

To further evaluate the electrochemical behavior of $MAPbBr_3$ in lithium-ion batteries, galvanostatic cycling was conducted using a range of liquid and solid-state electrolytes. Figure 5.11 illustrates the specific capacity of $MAPbBr_3$ electrodes over 100 cycles at a constant current density of $100\,mA\,g^{-1}$. Eight different electrolyte formulations were investigated, including conventional carbonate-based electrolytes (e.g., $LiPF_6$ in EC:DMC), ether-based systems (e.g., LiTFSI in DOL:DME), and a solid polymer electrolyte (PEO-based with LiTFSI).

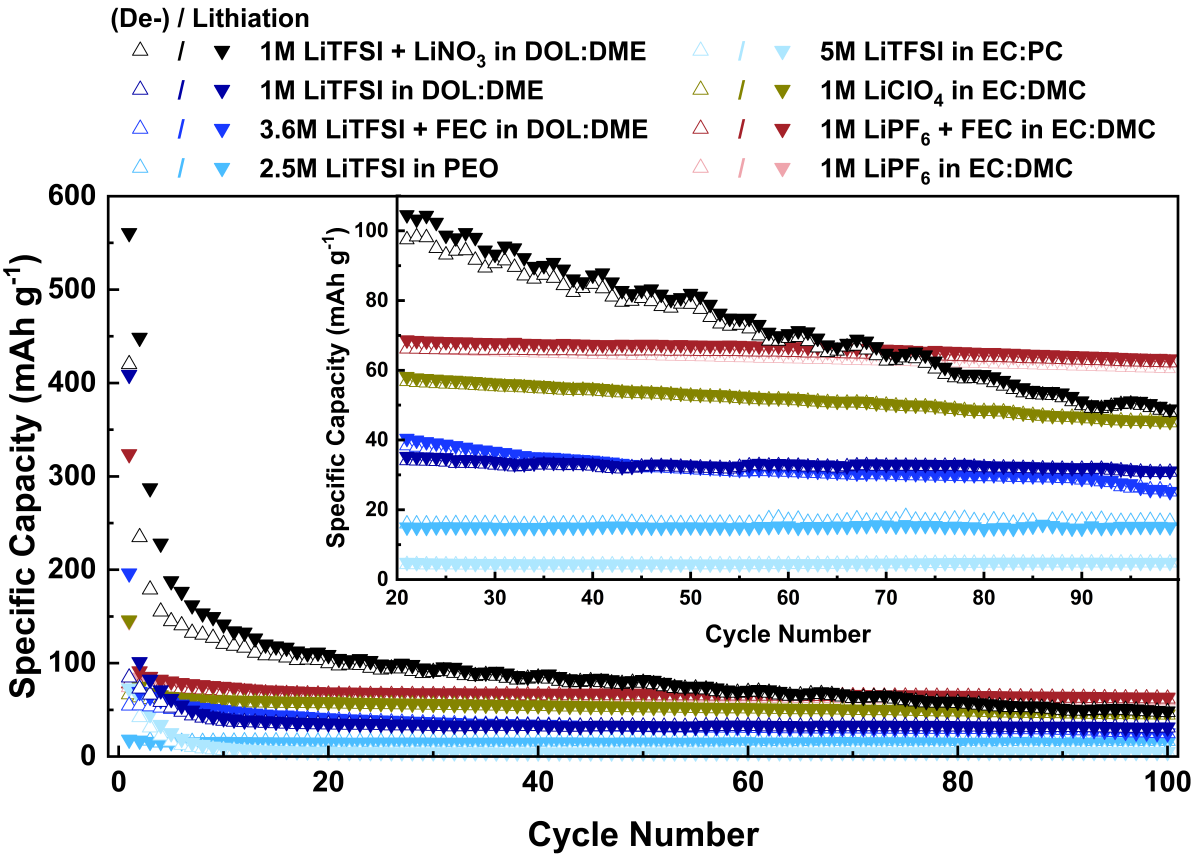


Figure 5.11: Galvanostatic cycling performance of $MAPbBr_3$ anodes in various electrolyte formulations over 100 cycles. Main panel shows the full cycle range; inset shows magnified view of cycles 20 - 100. Electrolyte compositions include liquid (LiTFSI, $LiPF_6$, $LiClO_4$) and solid-state (PEO-based) systems, with and without additives ($LiNO_3$, FEC).

Among all electrolytes, 1 M LiTFSI with 1 % $LiNO_3$ in DOL:DME (black) delivers the highest initial specific capacity of $561\,mA\,h\,g^{-1}$. A pronounced exponential decay occurs within the first 20 cycles, reducing the capacity to $105\,mA\,h\,g^{-1}$, followed by a more gradual linear fading to $49\,mA\,h\,g^{-1}$ at cycle 100. Small oscillations in capacity throughout the measurement are attributed to thermal fluctuations in the laboratory, as discussed

previously. The same electrolyte without $LiNO_3$ (1 M LiTFSI in DOL:DME) reaches a lower initial specific capacity of 409 mA h g^{-1}, with a sharp decay to 38 mA h g^{-1} after just 10 cycles. It then stabilizes at approximately 32.30 mA h g^{-1} by cycle 30. This emphasizes a possible beneficial effect of $LiNO_3$ in suppressing rapid degradation and promoting more stable cycling [255]. A variation in molarity and additive type specifically, 3.6 M LiTFSI with 10 % FEC in DOL:DME results in a much lower initial specific capacity of 106 mA h g^{-1}, with a rapid initial drop to 69 mA h g^{-1} and a stabilization around 30 mA h g^{-1} by cycle 40. Interestingly, a secondary decay sets in after cycle 90, indicating long-term instability potentially linked to FEC-induced side reactions or electrolyte degradation. When the solvent is changed to EC:PC (5 M LiTFSI in EC:PC), a relatively low initial specific capacity of 73 mA h g^{-1} is observed. Within the first 10 cycles, the specific capacity drops to nearly zero, pointing to complete dissolution of the active material and loss of electrochemical functionality. The standard electrolyte, 1 M $LiPF_6$ in EC:DMC, does not support reversible lithiation/delithiation of $MAPbBr_3$. The initial capacity of 145 mA h g^{-1} decreases to 85 mA h g^{-1}, and stabilizes at roughly 65 mA h g^{-1}. This plateau corresponds to the specific capacity of conductive carbon black (CB) alone, indicating that $MAPbBr_3$ is electrochemically inactive in this system. Normalizing to the CB content yields a value of approximately 200 mA h g^{-1}, consistent with the CB-only reference experiment (see Section 2.4.5), further confirming the inertness of the perovskite in this electrolyte. In contrast, the addition of 10 % FEC to the standard electrolyte (1 M $LiPF_6$ + 10 % FEC in EC:DMC) leads to a significantly higher initial capacity of 324 mA h g^{-1}. However, a rapid decline occurs after the first cycle, with capacity stabilizing at 68 mA h g^{-1}. This suggests that $MAPbBr_3$ may initially contribute to the capacity, but is quickly rendered inactive, similar to the behavior observed in the CV response shown in Figure 5.10. A comparable trend is observed for 1 M $LiClO_4$ in EC:DMC, which starts at 146 mA h g^{-1}, decreases to 75 mA h g^{-1}, and then gradually fades to 45 mA h g^{-1} at cycle 100. This steady decline suggests a modest and progressively degrading contribution from the $MAPbBr_3$ and/or SEI formation. The solid polymer electrolyte (2.5 M LiTFSI in PEO) exhibits the lowest overall performance, with a specific capacity of only 18 mA h g^{-1} that remains nearly constant over 100 cycles. This limited activity is likely due to poor ionic conductivity or insufficient electrode/electrolyte interfacial contact in the solid-state setup [256].

The comparative analysis of electrolyte formulations (Table 5.3) highlights the critical role of solvent type, salt concentration, and additives in determining the electrochemical performance of $MAPbBr_3$ anodes. Ether-based electrolytes, particularly 1 M LiTFSI with 1 % $LiNO_3$ in DOL:DME, exhibited the highest initial capacity and retained measurable

activity even after 100 cycles, suggesting partial reversibility and SEI stabilization. In contrast, similar formulations without $LiNO_3$ or with high salt concentrations and FEC additives showed more rapid capacity fading and reduced long-term stability. Carbonate-based electrolytes such as 1 M $LiPF_6$ in EC:DMC served as inert systems for $MAPbBr_3$, with cycling behavior dominated by the carbon black additive. The transient capacity increase upon FEC addition suggests some initial reactivity of $MAPbBr_3$, but this is quickly lost after the first cycle. The severe capacity drop in EC:PC-based electrolytes points toward complete perovskite dissolution, whereas solid-state PEO-based systems demonstrated poor ionic transport and interfacial limitations, resulting in minimal activity [256]. Taken together, these results demonstrate that ether-based systems with SEI-stabilizing additives are performing better than without additives and are therefore more suitable for promoting reversible lithiation behavior in hybrid perovskites, although long-term stability remains a significant challenge.

Electrolyte	**Redoxpotential (V)**			**Initial Capacity** ($mA\,h\,g^{-1}$)	**Capacity @ 100** ($mA\,h\,g^{-1}$)	**Degradation Pattern**
	Lithiation	Conversion	Alloying			
1 M LiTFSI in DOL:DME	2.00 / 2.27	1.37 / –	0.27 / 0.54 0.38 / 0.69	561	49	Rapid decay to 20 cycles, then linear
1 M LiTFSI + 1% $LiNO_3$ in DOL:DME	2.09 / 2.28	–	0.47 / 0.49 0.30 / 0.64	409	32	Sharp drop, stable after 30 cycles
3.6 M LiTFSI + 10% FEC in DOL:DME	1.97 / –	1.39 / –	0.25 / 0.55 0.44 / 0.70	106	30	Quick drop, second decay after cycle 90
5 M LiTFSI in EC:PC	1.95 / 2.34	1.36 / –	0.24 / 0.57 0.44 / 0.74	73	0	Immediate drop to near-zero
1 M $LiPF_6$ in EC:DMC	– / –	– / –	– / –	145	65	Initial loss, then stable (CB-only)
1 M $LiPF_6$ + 10% FEC in EC:DMC	2.13 / –	– / –	0.33 / 0.51 0.51 / 0.65	324	68	Sharp drop after 1st cycle
1 M $LiClO_4$ in EC:DMC	2.19 / –	1.12 / –	0.37 / 0.48 0.52 / 0.65	324	68	Sharp drop after 1st cycle
2.5 M LiTFSI in PEO (solid)	2.21 / –	1.15 / –	– / –	18	18	Constant low capacity

Table 5.3: Summary of electrochemical performance of $MAPbBr_3$ in various electrolytes. The table lists observed redox potentials (lithiation, conversion, and alloying), initial specific capacities, capacities after 100 cycles, and qualitative degradation behavior. Redox potentials are given as pairs of lithiation/delithiation voltages where applicable. Electrolyte compositions include both liquid and solid-state systems, with additives such as $LiNO_3$ and FEC evaluated for their stabilizing effects.

5.4.4 Perovskite Variations

To further investigate structure–property relationships and enhance the electrochemical performance of perovskite-based anode materials, a series of structurally and chemically distinct perovskite compounds were studied. The motivation behind exploring different perovskite chemistries lies in the intrinsic tunability of their structure, dimensionality, and elemental composition, which can drastically influence both stability and electrochemical behavior [217]. The one-dimensional (1D) hybrid organic-inorganic perovskite $EBAPbI_3$ was selected based on the hypothesis that lowering the dimensionality of the perovskite framework may enhance structural robustness during lithiation/delithiation cycles. This idea is inspired by recent work, such as [99], which demonstrated increased battery performance in low-dimensional $(BA)_2(MA)_3Pb_4Br_{11}$. In contrast to the hybrid nature of $EBAPbI_3$, the fully inorganic perovskite $CsMnBr_3$ was investigated to assess the effect of removing volatile organic components and to probe the stability of purely inorganic lattices during electrochemical cycling. An additional advantage of $CsMnBr_3$ is its environmental benignity, as it entirely avoids the use of toxic lead (Pb), which remains a major concern in conventional hybrid perovskites. The incorporation of Mn^{2+} instead of a heavier transition metal such as Pb^{2+} also introduces potential redox activity from the B-site cation, which may open alternative lithium storage pathways. Additionally, $EBA_4Bi_2Br_{10}$ was selected as a representative of more complex HOIP featuring lower-dimensional layered structures and non-toxic Bi^{3+} in place of lead. This compound serves to explore how chemical complexity and alternative cation chemistry influence electrochemical properties, particularly with respect to safety, environmental impact, and reversibility of electrochemical processes. By systematically comparing these three materials, 1D $EBAPbI_3$, all-inorganic $CsMnBr_3$, and complex HOIP $EBA_4Bi_2Br_{10}$, this study aims to provide a broader understanding of the interplay between composition, dimensionality, and lithium storage capability in perovskite-based anode materials.

Electrochemical Behavior of 1D Hybrid Perovskite $EBAPbI_3$

Reducing the dimensionality of hybrid perovskites has been proposed as a strategy to improve structural stability, suppress ion migration, and enhance resistance to environmental degradation. In this context, 1D α-ethylbenzylamine lead iodide ($EBAPbI_3$) represents a promising candidate due to its quasi-one-dimensional crystal structure, where lead iodide chains are separated by organic cations. To explore its suitability as an anode material in LIBs, we investigated the electrochemical behavior of $EBAPbI_3$ in standard carbonate-based electrolyte using CV, galvanostatic cycling, and differential capacity analysis.

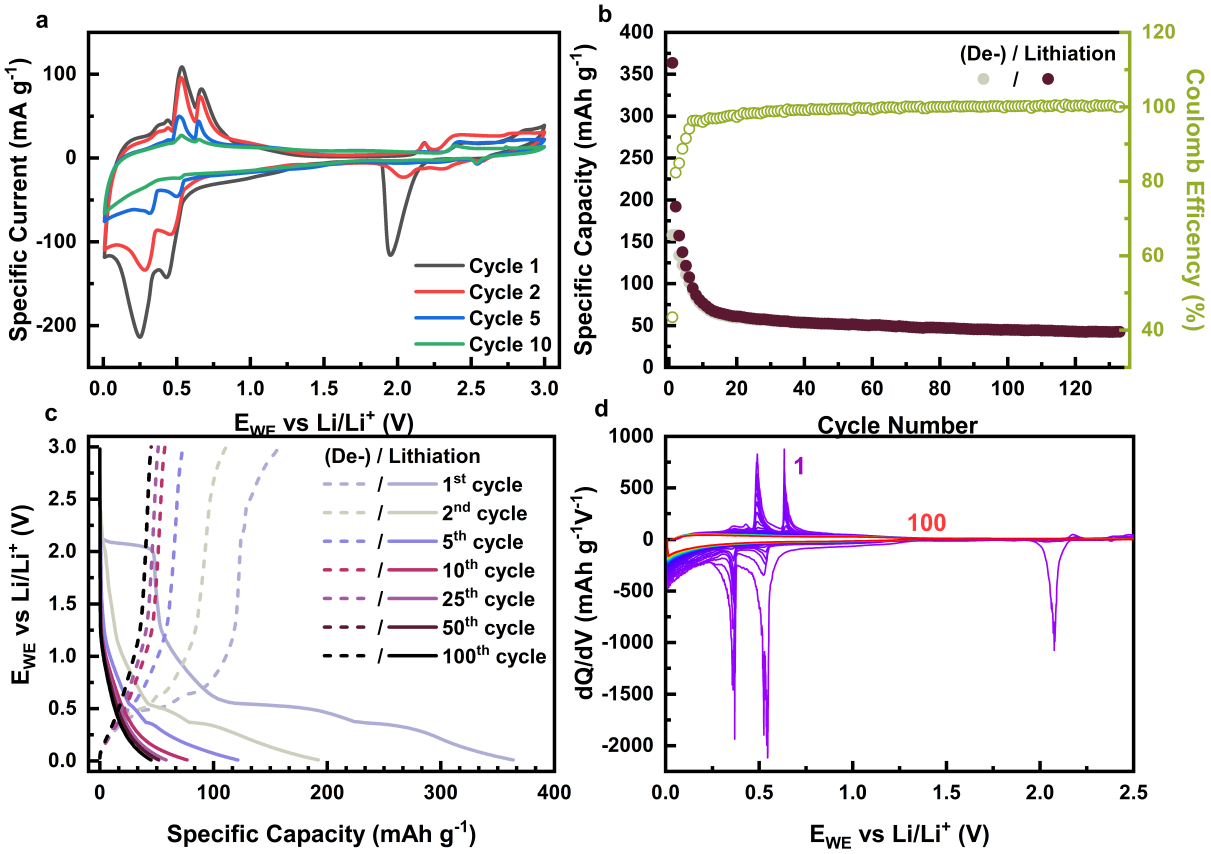


Figure 5.12: Electrochemical characterization of 1D EBAPbI$_3$. **a)** Cyclic voltammetry at a scan rate of 0.1 mV s^{-1} for cycles 1, 2, 5, and 10. **b)** Galvanostatic cycling performance and Coulombic efficiency over 130 cycles. **c)** Selected voltage profiles during lithiation and delithiation. **d)** Differential capacity (dQ/dV) plot showing evolution from cycle 1 to cycle 100.

Figure 5.12 a) displays the cyclic voltammetry curves of EBAPbI$_3$ over the voltage range 0 – 3 V (vs. Li/Li$^+$) for cycles 1, 2, 5, and 10. In the first cycle, a large defined lithiation peak appears at 1.95 V with a current of 116 mA g^{-1}. A broad and poorly defined peak can be seen between 1.5 - 0.9 V, suggesting a conversion-type reaction of limited reversibility. Two distinct alloying peaks are observed at lower potentials: a first reduction at 0.43 V (143 mA g^{-1}) and a second at 0.24 V (214 mA g^{-1}). Corresponding oxidation peaks occur at 0.53 V (109 mA g^{-1}) and 0.87 V (82 mA g^{-1}), indicating partial reversibility of the alloying process. A small delithiation feature at 2.18 V (18 mA g^{-1}) is also present but disappears rapidly. From cycle 2 onward, both lithiation and delithiation features fade completely, and by cycle 10, the alloying reactions also vanish, suggesting rapid decomposition and passivation of the active material similar to MAPbBr$_3$. The galvanostatic cycling data in Figure 5.12 b) further supports this observation. The electrode initially delivers a specific capacity of 364 mA h g^{-1}, which decays steeply to 59 mA h g^{-1} within the

first 20 cycles. Beyond this point, the capacity gradually declines and stabilizes around 43 mA h g^{-1} after 130 cycles, values consistent with the contribution from carbon black alone. Coulombic efficiency improves from 45 % to 96 % within the first 10 cycles, in line with the disappearance of irreversible lithiation/alloying. A stable efficiency near 99% is reached after 40 cycles, further confirming the inactivity of $EBAPbI_3$ after a few cycles and the dominance of background intercalation into conductive carbon. The GCPL voltage curves shown in Figure 5.12 c) offer additional insight into the mechanisms. A initial plateau is seen at 2.06 V, corresponding to the aforementioned lithiation process, contributing approximately 50 mA h g^{-1}. A second broader conversion plateau from 1.5 V to 0.9 V delivers around 25 mA h g^{-1}, followed by two sharper alloying plateaus at 0.54 V and 0.35 V, which yield 125 mA h g^{-1} and 100 mA h g^{-1}, respectively. Upon delithiation, the recovery is incomplete: only partial dealloying is seen between 0 V and 1 V (110 mA h g^{-1}), representing a 50 % retention compared to the alloying capacity. No reconversion or delithiation features at higher voltages are observed, confirming the irreversibility of the initial conversion process. The dQ/dV plot in Figure 5.12 d) presents the evolution of the redox activity across 100 cycles. The first cycle (magenta) exhibits clear lithiation and alloying features, which progressively fade within the first 7 cycles. From cycle 10 onward, no active redox features remain, and the signal resembles the differential capacity of carbon black alone. This further underscores the lack of durable lithium storage pathways in 1D $EBAPbI_3$ under these conditions.

Overall, $EBAPbI_3$ exhibits similar degradation behavior to 3D $MAPbBr_3$, with rapid fading of lithiation, conversion and alloying reactions. Despite its lower dimensionality and presumed enhanced structural stability, $EBAPbI_3$ fails to maintain electrochemical activity over extended cycling. This suggests that intrinsic decomposition and interface instability are dominant failure mechanisms in both materials. As a next step, we investigate whether mechanical processing, such as solid-state grinding, can improve the performance by enhancing particle connectivity and increasing surface area.

Impact of Mechanical Grinding on 1D $EBAPbI_3$ Anodes

To further investigate the influence of morphology and particle size on the electrochemical behavior of 1D $EBAPbI_3$, the material was mechanically ground using a mortar for 60 minutes by hand. This process was intended to reduce the crystalline flake-like structures into finer particles and enhance the contact surface area, potentially improving lithium-ion accessibility and overall electrochemical activity. Figure 5.13 compares the morphology and electrochemical performance of the pristine and ground 1D $EBAPbI_3$ samples.

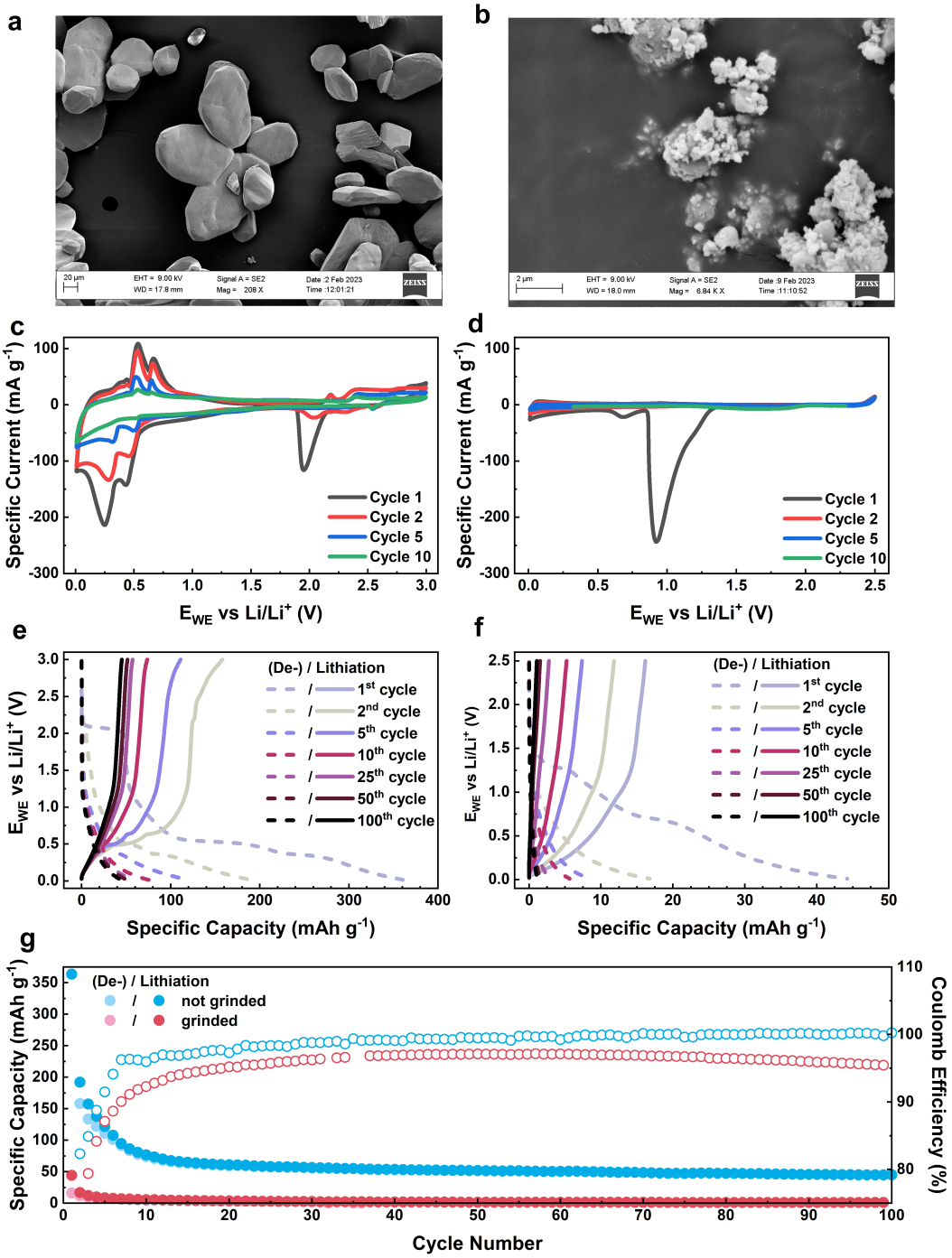


Figure 5.13: Comparison of pristine and ground 1D $EBAPbI_3$ anode materials. **a)** SEM image of pristine 1D $EBAPbI_3$ with particle sizes ranging from 30 - 150 µm. **b)** SEM image of ground 1D $EBAPbI_3$ showing sub-100 nm 100 nm particles. **c)** CV curves of pristine $EBAPbI_3$ over 10 cycles, showing initial lithiation, conversion, and alloying reactions that fade rapidly. **d)** CV curves of ground $EBAPbI_3$ indicating significant suppression of redox activity. **e)** GCPL potential profiles of pristine sample showing partial dealloying but no reconversion or delithiation. **f)** GCPL profiles of ground sample, showing minimal and irreversible lithiation activity. **g)** Long-term cycling performance comparing pristine (blue) and ground (red) $EBAPbI_3$, showing a dramatic capacity loss and instability in the ground sample.

Figures 5.13 a) and b show the surface morphology of the pristine and ground $EBAPbI_3$, respectively. The pristine sample exhibits anisotropic flakes with particle sizes between 30 - 150 µm, while the ground sample displays a significantly reduced and more homogeneous particle distribution below 100 nm. Figure 5.13 c) presents the CV of pristine $EBAPbI_3$. The initial lithiation peak at 1.96 V (110 mA g^{-1}) and small, broad conversion process between 1.4 - 0.9 V are characteristic of a partially reversible electrochemical mechanism. The distinct alloying/dealloying redox couples between 0.44 V/0.26 V (reduction) and 0.50 V/0.81 V (oxidation) rapidly diminish after the first few cycles, confirming the previously observed fading behavior. In contrast, the CV of the ground $EBAPbI_3$ in Figure 5.13 d) shows a complete absence of lithiation and alloying reactions. Instead, a strong irreversible reduction peak emerges at 0.92 V (243 mA g^{-1}), accompanied by a weaker signal at 0.67 V. No identifiable reactions persist beyond cycle 1, suggesting that mechanical grinding significantly alters or destroys the electrochemical activity, likely due to increased dissolution into the electrolyte or disruption of the 1D crystal structure. The GCPL curves of the pristine sample in Figure 5.13 e) confirm the partial reversibility of alloying reactions. Initial plateaus at 2.05 V (lithiation), 1.4 – 0.8 V (conversion), and sharp alloying steps at 0.51 V and 0.32 V provide a combined capacity of approximately 375 mA h g^{-1}. However, only around 40 % of the specific capacity is recovered during upsweep, and no reconversion or high-voltage delithiation is observed. In the ground sample (Figure 5.13 f)), only faint reduction plateaus at 1.29 V and 0.72 V are detectable, contributing a total initial capacity of only 44 mA h g^{-1}. These features vanish entirely after the first cycle, indicating electrochemical irreversibility and supporting the hypothesis of structural degradation. Finally, Figure 5.13 g) compares the long-term GCPL cycling behavior of both samples. The pristine material (blue) shows an initial capacity of 364 mA h g^{-1}, which decays exponentially to 77 mA h g^{-1} by cycle 10, stabilizing at around 50 mA h g^{-1}. In contrast, the ground sample (red) begins with a significantly lower capacity (44 mA h g^{-1}) and drops to 17 mA h g^{-1} after the first cycle, stabilizing at only 1.25 mA h g^{-1} thereafter. Coulombic efficiency analysis supports this loss in electrochemical activity, showing poor stability for the ground material.

The electrochemical analysis of 1D $EBAPbI_3$ highlights a complex and partially reversible reactions involving lithiation, conversion, and alloying mechanisms. However, these processes exhibit rapid fading, with most redox activity vanishing by the 10th cycle. Mechanical grinding, while successful in reducing particle size, significantly compromises the structural integrity and electrochemical functionality of $EBAPbI_3$. The resulting ground material shows no meaningful lithiation, conversion, or alloying activity and retains almost no capacity after initial cycling. These findings emphasize that while dimensional control

and morphological tuning are often considered beneficial strategies in battery research, excessive mechanical treatment of 1D hybrid perovskites can lead to structural degradation and a complete loss of active lithium storage mechanisms. Alternative approaches, such as mild post-synthetic treatments, surface coating, or composite formation, may be more promising routes for enhancing the stability and performance of such materials.

All-Inorganic $CsMnBr_3$ as Potential Anode Material

The investigation of alternative perovskite compositions for lithium-ion battery anodes is driven by the need to improve structural and electrochemical stability, as well as to eliminate toxic heavy metals. $CsMnBr_3$ represents a lead-free, all-inorganic perovskite, offering potential environmental advantages over hybrid organic-inorganic analogues. In this study, its electrochemical behavior as an anode material was evaluated using CV, GCPL profiles, and differential capacity (dQ/dV) analysis.

Figure 5.14 a) presents the cyclic voltammogram of $CsMnBr_3$ over the full potential range of 0 to 3 V (vs. Li/Li^+) at a scan rate of $0.1\,mV\,s^{-1}$ for cycles 1, 2, 5, and 10. The OCV is recorded at 2.22 V. No distinct lithiation peak is observed. A small irreversible conversion-related reduction peak appears at 1.64 V with a current response of $2.70\,mA\,g^{-1}$, and a more prominent irreversible peak at 0.67 V ($33\,mA\,g^{-1}$), likely associated with solid electrolyte interphase (SEI) formation. In the lower voltage range, only contributions from CB are apparent. During the anodic sweep, two small oxidation peaks are observed: one at 2.29 V ($5\,mA\,g^{-1}$) and a set of two-step redox processes post-2.5 V at 2.35/2.63 V and 2.73/2.93 V, which are hypothesized to represent a two-step high-voltage lithiation mechanism. These features do not align over consecutive cycles, indicating poor reversibility and instability. To further explore the stability of this reaction, a restricted voltage range was investigated. Figure 5.14 b) shows the CV in the restricted potential window of 2 to 3 V (vs. Li/Li^+). Here, the OCV is slightly lower at 1.98 V. Unlike the full-range CV, the two redox pairs are clearly stabilized and repeatable: R_1/O_1 at 2.36 V ($7\,mA\,g^{-1}$) and 2.64 V ($30\,mA\,g^{-1}$), and R_2/O_2 at 2.71 V ($22\,mA\,g^{-1}$) and 2.94 V ($71\,mA\,g^{-1}$), suggesting that the high-voltage lithiation process is more electrochemically stable within this limited regime. In Figure 5.14 c), GCPL voltage profiles are presented for selected cycles in the full voltage range with a constant current density of $100\,mA\,g^{-1}$. The OCV is measured at 2.23 V. A strong irreversible reduction plateau at 0.66 V, corresponding to SEI formation, delivers an initial capacity of approximately $30\,mA\,h\,g^{-1}$. Other reaction features are negligible in the low-voltage region. During the delithiation process, two minor steps are observed at 2.60 V and 2.93 V, contributing around $5\,mA\,h\,g^{-1}$ and $10\,mA\,h\,g^{-1}$, respectively. The

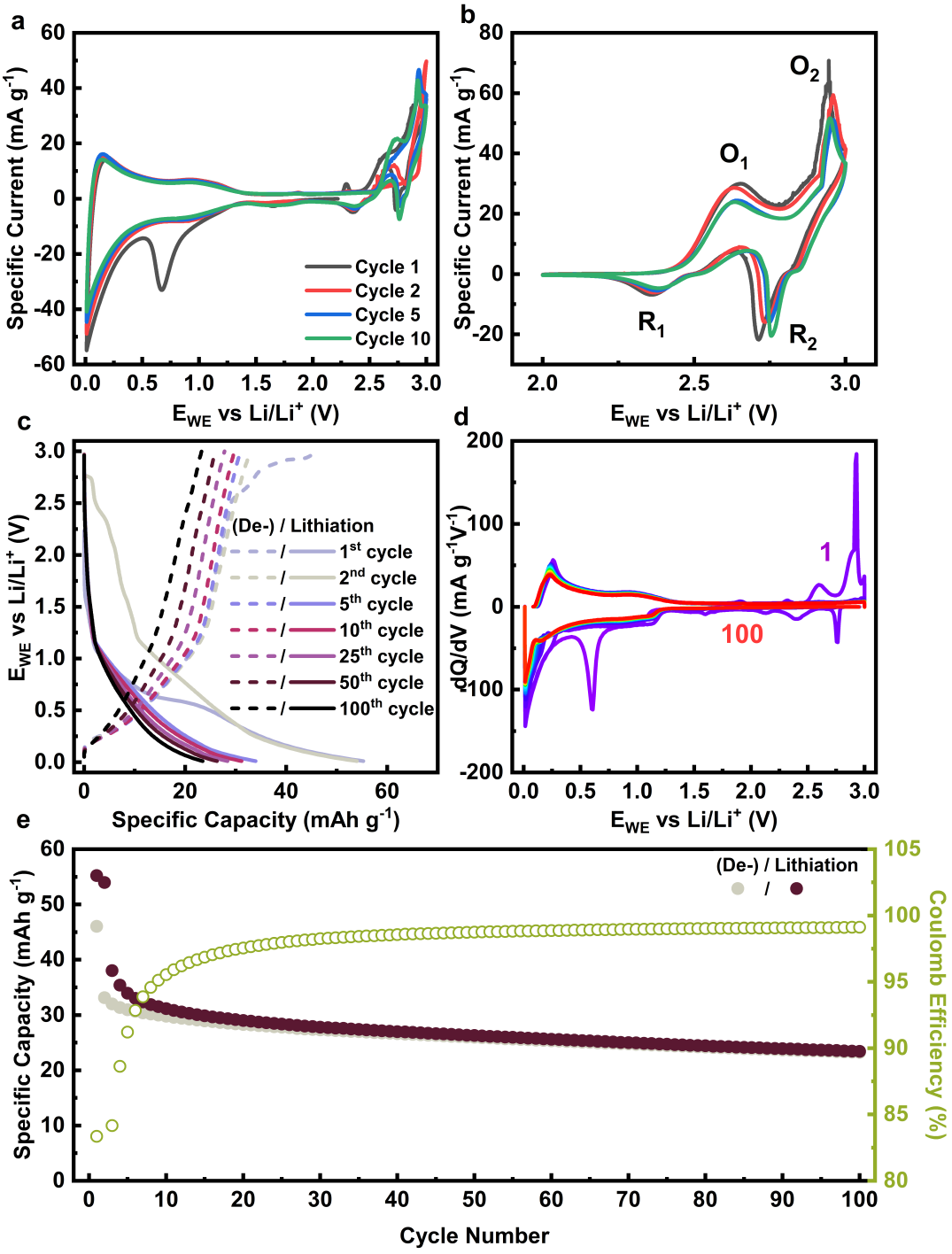


Figure 5.14: Electrochemical characterization of $CsMnBr_3$: **a)** Cyclic voltammogram in the full voltage range (0 - 3 V vs. Li/Li^+). **b)** CV in the limited high-voltage region (2 - 3 V). **c)** GCPL potential profiles for selected cycles. **d)** Differential capacity (dQ/dV) plots showing the evolution of reaction mechanisms. **e)** Long-term GCPL cycling performance and Coulombic efficiency.

lithiation process proceeds through two steps at 2.76 V and 2.38 V, contributing 2 mA h g^{-1} and 5 mA h g^{-1}, respectively. To more accurately track the evolution and disappearance of these reaction features, differential capacity plots (dQ/dV) were evaluated and are shown in Figure 5.14 d). The color-coded curves, from cycle 1 (magenta) to cycle 100 (red), confirm that the distinct redox peaks disappear rapidly after the second cycle, indicating poor long-term electrochemical stability and possible structural degradation of the active material. Figure 5.14 e) illustrates the long-term cycling behavior and CE. The initial specific capacity is 55 mA h g^{-1}, which declines to 38 mA h g^{-1} by cycle 3 and continues to decay gradually to 23 mA h g^{-1} by cycle 100. This continuous capacity fade is likely due to irreversible structural changes or dissolution of $CsMnBr_3$ into the electrolyte. The CE, however, improves from 83 % in the first cycle to over 99 % by cycle 50, suggesting that while the material becomes electrochemically inert, side reactions diminish with cycling.

The electrochemical investigation of all-inorganic, lead-free $CsMnBr_3$ reveals the absence of conventional lithiation, conversion, or alloying behavior. Only a two-step redox reaction is observed in the high-voltage region (2 - 3 V), which is electrochemically reversible under restricted conditions probably corresponding to lithiation. However, this mechanism deteriorates rapidly, indicating poor long-term stability in the full voltage range. The initial SEI formation is dominant in the low-voltage regime. The material exhibits only minimal reversible capacity, with the primary contributions attributed to carbon additives. Despite the environmental benefit of being lead-free, $CsMnBr_3$ in its current form does not show promise as a stable anode material.

Complex Hybrid Perovskite $EBA_4Bi_2Br_{10}$

The hybrid perovskite $EBA_4Bi_2Br_{10}$ represents a more chemically complex lead-free system, incorporating Bi^{3+} and demonstrating potential for varied electrochemical behavior due to its structural complexity. Its evaluation as a potential anode material for lithium-ion batteries is motivated by the exploration of diverse HOIP chemistries beyond Pb-based systems, targeting both functionality and environmental compatibility.

Figure 5.15 summarizes the electrochemical performance of $EBA_4Bi_2Br_{10}$ across multiple techniques. Figure 5.15 a) presents the CV profiles of $EBA_4Bi_2Br_{10}$ in the full voltage range (0 - 3 V). The OCV is observed at 2.36 V. The initial cathodic scan shows a broad conversion-related reduction peak centered at 1.12 V (32 mA g^{-1}). Multiple alloying reactions are identifiable at lower potentials: 0.76 V (107 mA g^{-1}), 0.68 V (227 mA g^{-1}), and 0.30 V (216 mA g^{-1}). On the anodic sweep, only a dominant dealloying peak is observed at 0.88 V (187 mA g^{-1}). At higher voltages, two reversible redox couples emerge:

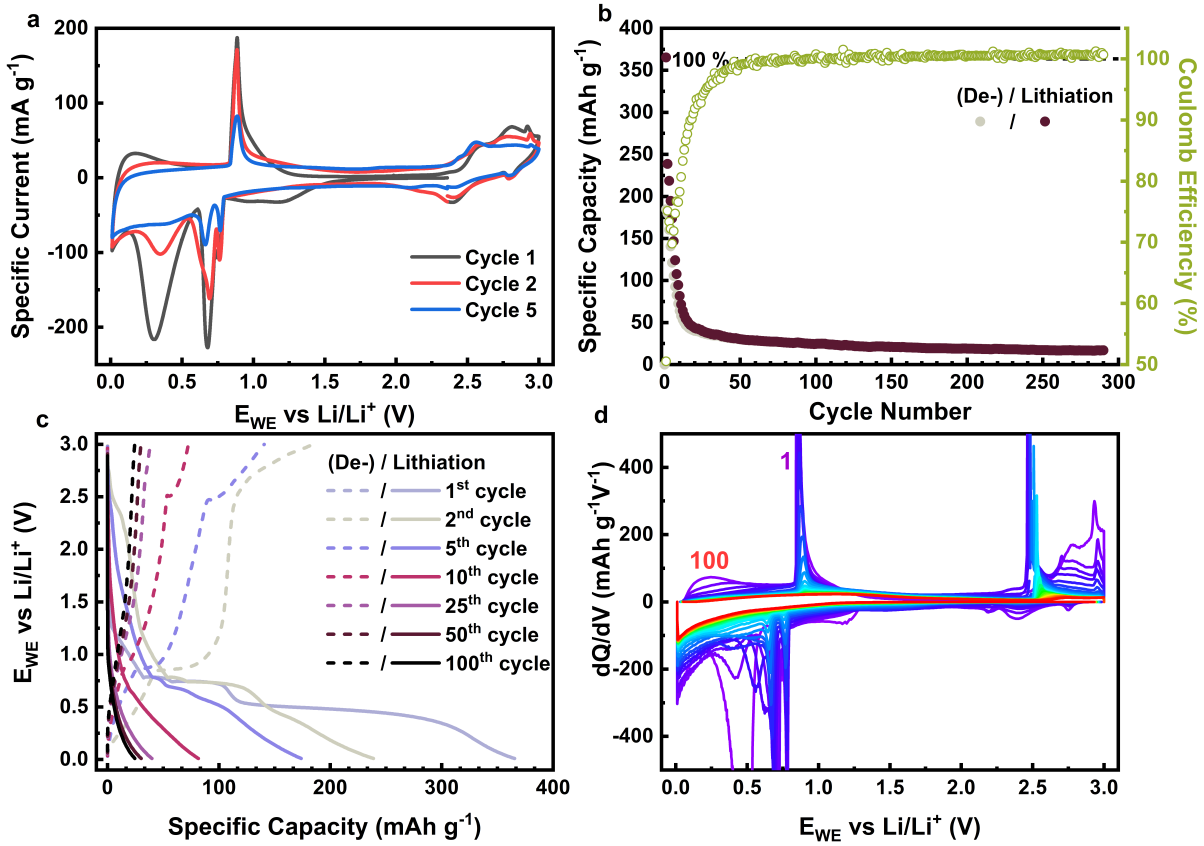


Figure 5.15: Electrochemical characterization of $EBA_4Bi_2Br_{10}$. **a)** CV in the full voltage range (0 - 3 V) at 0.1 mV s^{-1} for cycles 1, 2, and 5. **b)** Long-term GCPL and coulombic efficiency over 290 cycles at 100 mA g^{-1}. **c)** Selected GCPL potential profiles showing redox plateaus. **d)** Differential capacity plots (dQ/dV) showing evolution and fading of electrochemical features over 100 cycles.

2.39 V/2.55 V and 2.79 V/2.81 V, with currents of 33, 47, 2, and 68 mA g^{-1}, respectively. These redox pairs are analogous to the high-voltage 2-step mechanism seen in $CsMnBr_3$. However, all alloying and lithiation-related features fade significantly by the fifth cycle, indicating rapid degradation. Figure 5.15 b) shows the long-term GCPL cycling performance over 290 cycles at a current density of 100 mA g^{-1}. A steep decline in specific capacity is evident, dropping from an initial 365 mA h g^{-1} to 44 mA h g^{-1} within the first 20 cycles. Subsequently, a gradual decay leads to a final capacity of 17 mA h g^{-1}, consistent with only CB contribution. The Coulombic efficiency rises sharply from 50 % to 78 % in the first 10 cycles, stabilizing beyond 100 % after approximately 100 cycles, again pointing to non-faradaic CB-related charge/discharge contributions. Figure 5.15 c) displays representative GCPL voltage profiles. The lithiation plateau is absent, and a broad conversion region occurs between 1.5 V and 0.9 V, yielding approximately 30 mA h g^{-1}. Two alloying plateaus at 0.74 V and 0.49 V deliver 80 and 220 mA h g^{-1}, respectively. In the initial upsweep, par-

tial dealloying occurs between 0 and 1 V, resulting in about 100 mA h g^{-1}, amounting to a 30 % alloying capacity retention. A high-voltage delithiation plateau is observed at 2.83 V, contributing approximately 70 mA h g^{-1}. By cycle 25, all lithiation/conversion/alloying reactions vanish, leaving only capacitive CB contributions. Figure 5.15 d) provides the differential capacity plot (dQ/dV) from cycle 1 (magenta) to cycle 100 (red). The initial cycles clearly show lithiation, conversion, and alloying features. By cycle 25, however, all distinct peaks disappear, confirming the electrochemical inactivity of $EBA_4Bi_2Br_{10}$ beyond early cycling. This fading behavior is comparable to that of other HOIPs such as $MAPbBr_3$.

The $EBA_4Bi_2Br_{10}$ hybrid perovskite exhibits a combination of conversion and alloying reactions in early cycles, along with a reversible high-voltage lithiation mechanism. However, all electrochemical activity, including lithiation and alloying, rapidly diminishes within a few cycles. The material ultimately behaves like inert carbon black, indicating structural or chemical decomposition, possibly due to instability of the HOIP framework in the electrolyte environment. These findings suggest limited practical applicability of $EBA_4Bi_2Br_{10}$ as an anode material in its current form.

Comparison of Electrochemical Performance

To evaluate the cycling stability and capacity retention of the investigated HOIPs, GCPL were recorded over 100 cycles at a current density of 100 mA g^{-1} within a voltage window of 0 to 3 V. Figure 5.16 summarizes the long-term electrochemical performance, with an inset highlighting cycles 20 to 100 to facilitate comparison of the later-stage capacity retention behavior.

Among the materials tested, $MAPbBr_3$ (black curve) exhibited the highest initial specific capacity of 561 mA h g^{-1}. However, it experienced a rapid decrease to 141 mA h g^{-1} by cycle 10 and to 109 mA h g^{-1} at cycle 20. Beyond this point, the material demonstrated a more gradual decline, reaching 48 mA h g^{-1} by cycle 100. Small oscillations in capacity throughout the measurement are attributed to thermal fluctuations in the laboratory, as discussed previously. $EBAPbI_3$ (blue curve) showed a moderate initial specific capacity of 364 mA h g^{-1}, followed by a sharp reduction to 77 mA h g^{-1} at cycle 10 and 61 mA h g^{-1} at cycle 20. From cycle 20 onward, the capacity stabilized, showing minimal degradation and retaining 45 mA h g^{-1} at cycle 100. $CsMnBr_3$ (yellow curve) displayed the lowest electrochemical activity, with an initial specific capacity of merely 55 mA h g^{-1}. A significant drop to 38 mA h g^{-1} occurred by cycle 3, followed by a further decrease to 29 mA h g^{-1} at cycle 20. The capacity stabilized thereafter, maintaining 23 mA h g^{-1} at cycle 100.

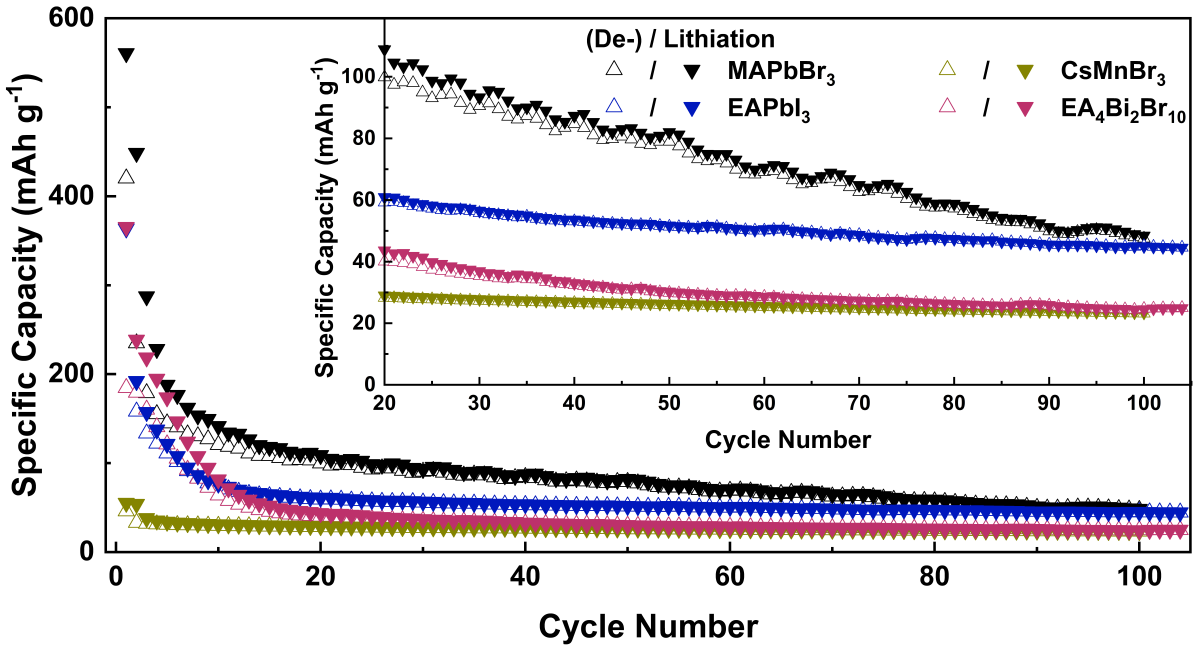


Figure 5.16: Long-term galvanostatic charge–discharge cycling performance of various HOIP materials at a current density of 100 mA g^{-1} within a voltage window of 0 to 3 V. $MAPbBr_3$ (black), $EBAPbI_3$ (blue), $CsMnBr_3$ (yellow), and $EBA_4Bi_2Br_{10}$ (red) are compared over 100 cycles. The inset zooms into cycles 20 to 100 to highlight the plateauing capacity behavior of each material.

$EBA_4Bi_2Br_{10}$ (red curve) also showed a relatively high initial capacity of 365 mA h g^{-1}, yet degraded rapidly to 82 mA h g^{-1} and 44 mA h g^{-1} by cycles 10 and 20, respectively. A gradual decline to a specific capacity of 25 mA h g^{-1} at cycle 100 is recognizable.

In summary, all HOIPs exhibited significant capacity fading during the initial 20 cycles, suggesting pronounced degradation or dissolution processes upon cycling [257, 258]. Beyond this early stage, the specific capacity plateaued for most materials, implying that the contribution of the active HOIP phases diminished significantly and that the observed specific capacities may predominantly arise from the carbon black (CB) additive (see Section 5.4.1). Notably, $MAPbBr_3$ retained the highest capacity throughout the entire cycling range, indicating a relatively improved stability among the tested HOIPs. Nevertheless, the continued decline across all samples supports the hypothesis that none of the HOIP materials remain electrochemically active after 100 cycles, likely due to their dissolution in the electrolyte, as discussed previously [257, 258].

While all HOIP-based electrodes exhibited notable capacity fading during prolonged cycling under dark conditions, recent studies have shown that external stimuli—particularly light irradiation—can positively influence the electrochemical behavior of semiconducting materials. To investigate this potential in the context of HOIPs, the following section ex-

plores photothermal and photoelectrochemical effects during cycling, with a focus on the role of a hole-blocking additive in facilitating charge separation and enhancing electrode performance under illumination.

5.4.5 External Effects

As HOIPs are semiconducting materials, they possess the intrinsic ability to generate electron–hole pairs under light irradiation. This opens up the possibility of using external stimuli, particularly light, as a means to enhance electrochemical performance by increasing charge carrier density and influencing redox kinetics. However, preliminary cycling experiments presented in the following section, conducted under both light and dark conditions, showed no significant difference in performance, suggesting that nonradiative recombination of photogenerated carriers is the dominant process. These findings suggest that light activation alone is insufficient to improve performance unless complemented by appropriate charge separation strategies. To address this, a hole-blocking additive composed of electrochemically inactive TiO_2 was incorporated into the electrode architecture. The following subsection investigates this approach and evaluates photothermal and photoelectrochemical effects during cycling through controlled illumination and temperature-dependent experiments.

Photothermal Effects During Cycling

To explore whether external light irradiation could enhance the electrochemical performance of hybrid perovskites, initial experiments were performed using $MAPbBr_3$ electrodes under light-on/light-off conditions. The concept follows similar findings reported for inorganic $LiMn_2O_4$ (LMO), where illumination has been shown to accelerate redox kinetics and increase charge carrier mobility, as discussed in Section 4. For this purpose, a windowed coin cell setup equipped with a xenon lamp similar to that used in Section 4 (see Sections 2.4.2 and 2.4.4) was used to isolate the photothermal contributions during battery cycling.

Figure 5.17 a) displays the chronoamperometric response of $MAPbBr_3$ when held at a constant potential of 1.8 V for 80 s. The light-on condition (cyan) and the dark reference with external heating to 30 °C (blue) exhibit nearly identical current transients. Both measurements begin with a specific current of approximately 11 $mA\,g^{-1}$ and increase slightly before decaying steadily to zero over the duration of the test. This similarity confirms two key observations: (1) no photo-induced enhancement in current response is detectable

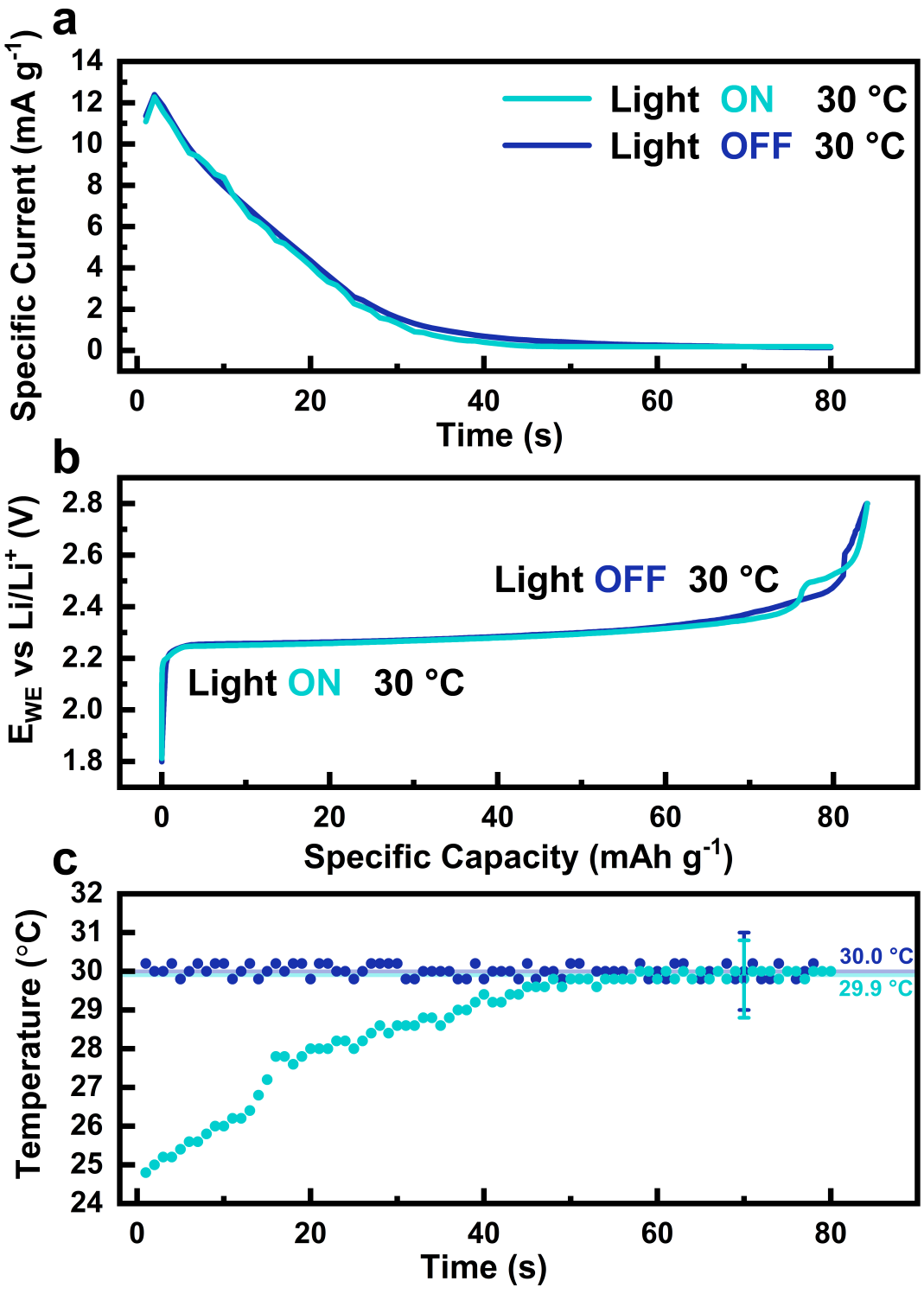


Figure 5.17: Electrochemical and thermal response of $MAPbBr_3$ under light and dark conditions. **a)** Chronoamperometry at a constant voltage of 1.8 V for 80 s under illumination (cyan) and dark conditions with external heating to 30 °C (blue). **b)** Galvanostatic discharge profiles at 10 mA g^{-1} immediately following the chronoamperometry. **c)** Surface temperature profile recorded during chronoamperometry using an IR thermometer.

under illumination, and (2) external heating to 30 °C successfully mimics the thermal load induced by light exposure, as confirmed by the surface temperature profile in Figure 5.17 c). There, the illuminated cell shows a gradual temperature rise from 25 °C to approximately 30 °C within the first 50 s, whereas the dark control remains at a stable 30 °C throughout. Following chronoamperometry, a galvanostatic discharge at 10 mA g^{-1} was performed over a voltage range of 1.8 to 2.8 V (Figure 5.17 b). Both light-on and dark conditions yielded identical capacity values of 84 mA h g^{-1}. A distinct plateau at approximately 2.26 V indicates delithiation processes in the $MAPbBr_3$ structure, as previously discussed in Section 5.4.2. No measurable deviation between the two conditions was observed across the entire voltage profile.

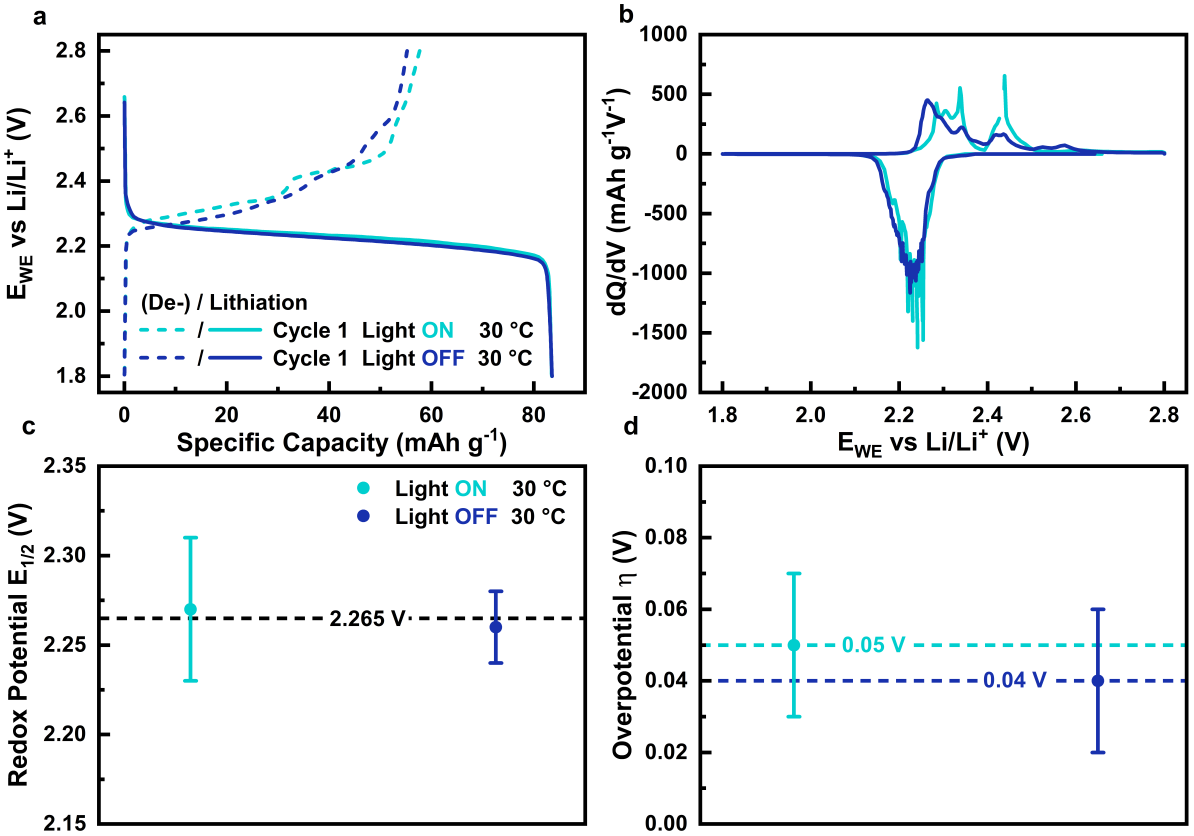


Figure 5.18: Comparison of first-cycle galvanostatic cycling of $MAPbBr_3$ under light-on and dark conditions at 30 °C.**a)** GCPL voltage profiles at 30 mA g^{-1} under illumination (cyan) and in the dark (blue). **b)** Corresponding differential capacity curves (dQ/dV) highlighting redox features. **c)** Redox potentials ($E_{1/2}$) extracted via Gaussian peak fitting of derivative curves. **d)** Calculated overpotentials (η) for oxidation and reduction reactions.

To further evaluate redox behavior, GCPL curves of the first cycle at 30 mA g^{-1} are presented in Figure 5.18 a). The charge/discharge profiles under both conditions are similar, with specific capacities of 84 mA h g^{-1}. Only minor deviations appear toward the end of

the oxidation plateau. But it should be noted that the specific capacity retained during the delithiation process is hindered, with specific capacities of $57\,\mathrm{mA\,h\,g^{-1}}$ (light-on) and $55\,\mathrm{mA\,h\,g^{-1}}$ (dark). In comparison to investigations on the lithiation regime of $MAPbBr_3$ in Subsection 5.4.2, the capacity retention is decreased. This is probably due to the enhanced current density during this measurement. To analyze this in more detail, the differential capacity curves shown in Figure 5.18 b) reveal comparable redox features in both measurements. Under illumination, the reduction peak appears at 2.22 V, while the dark reference shows it at 2.24 V. The main oxidation peak is located at 2.28 V (light-on) and 2.26 V (dark), both accompanied by a shoulder at 2.34 V and a secondary oxidation feature at 2.44 V (light) and 2.43 V (dark), respectively. The half-wave potentials ($E_{1/2}$) were obtained by identifying individual anodic or cathodic peaks in the derivative plot and applying Gaussian fitting to each peak. The center positions of the fitted Gaussians were taken as the $E_{1/2}$ values, which are summarized in Figure 5.18 c). The values remain statistically consistent between the two different experimental conditions: $E_{1/2} = 2.27 \pm 0.04\,\mathrm{V}$ for the illuminated case and $E_{1/2} = 2.26 \pm 0.02\,\mathrm{V}$ in the dark. Similarly, the overpotentials (η), defined as the potential difference between the oxidation and reduction processes, shown in Figure 5.18 d) reveal negligible variation between the two different experimental conditions, with $\eta_{\mathrm{light}} = 0.05 \pm 0.02\,\mathrm{V}$ and $\eta_{\mathrm{dark}} = 0.04 \pm 0.02\,\mathrm{V}$.

These findings indicate that illumination alone does not influence the electrochemical performance of $MAPbBr_3$. Unlike the photo-enhanced charge dynamics observed in LMO (cf. Fig. 4.4), no evidence of additional charge generation or photo-accelerated redox processes was found under light exposure. A plausible explanation is the rapid recombination of photogenerated electron–hole pairs within the perovskite structure, a behavior also reported by Boruah et al. [259]. Consequently, to effectively create light-induced charge generation, a charge-separation strategy is required. In the subsequent section, the incorporation of an electrochemically inactive TiO_2 hole-blocking additive is introduced and evaluated as a means to enable photogenerated charge transfer in $MAPbBr_3$ electrodes.

TiO_2 as Hole-Blocking Additive Enables Photoelectrochemical Response

Incorporating TiO_2 as a hole-blocking additive serves a dual function for the goal of light response enhancement: (i) it suppresses hole transport, thereby reducing recombination losses, and (ii) it facilitates selective electron transport, supporting efficient photocharging processes.

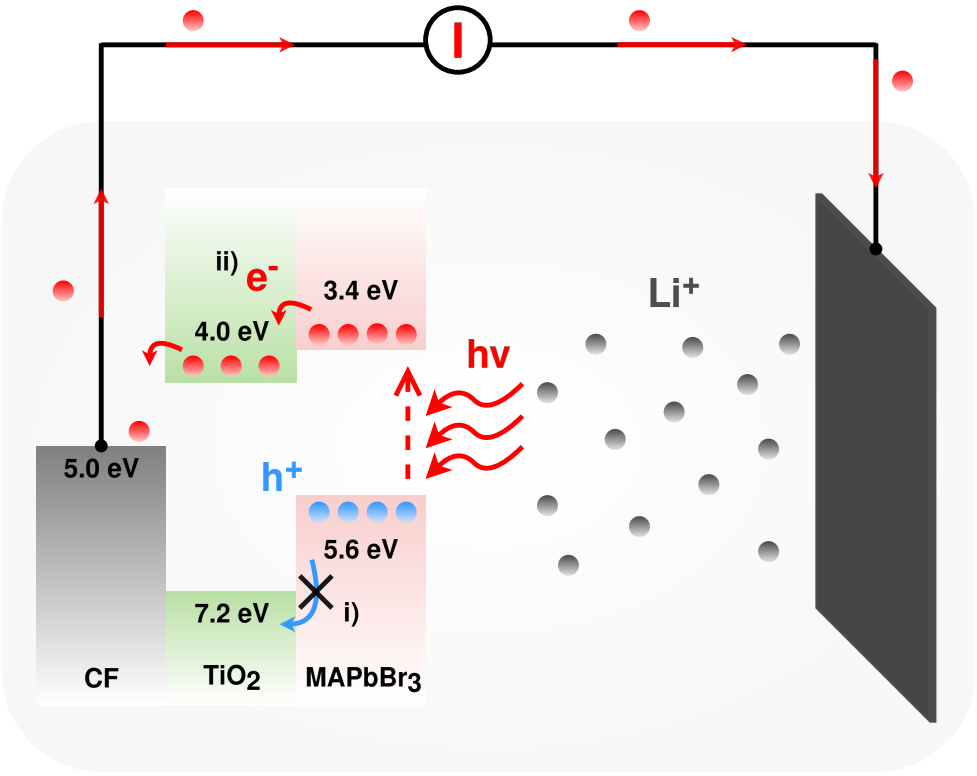


Figure 5.19: Schematic representation of the proposed photocharging mechanism of Photo-LIB. Adapted from [259]

To investigate the role of illumination and isolate photogenerated effects from thermal contributions, a combination of CA, GCPL, and surface temperature monitoring was performed.

Figure 5.20 a) presents the chronoamperometric response of the $MAPbBr_3 + TiO_2$ composite electrode at a constant bias of 1.8 V. Under illumination (cyan), the specific current initially registers at 11 mA g^{-1}, reaches a maximum of 14.6 mA g^{-1} after 4 s, and subsequently decays to 0.9 mA g^{-1} by 80 s. In comparison, the dark reference measurement (blue) shows a distinguishable but similar-in-shape temporal profile, peaking at 12.5 mA g^{-1} after 2 s, decaying to 1.2 mA g^{-1} after 80 s. The illuminated cell maintains a higher specific current than the dark reference until approximately 73 s, after which the curves intersect. This behavior indicates enhanced photoelectrochemical activity under illumination. The subsequent galvanostatic measurement (Figure 5.20 b), conducted at 10 mA g^{-1}, reveals

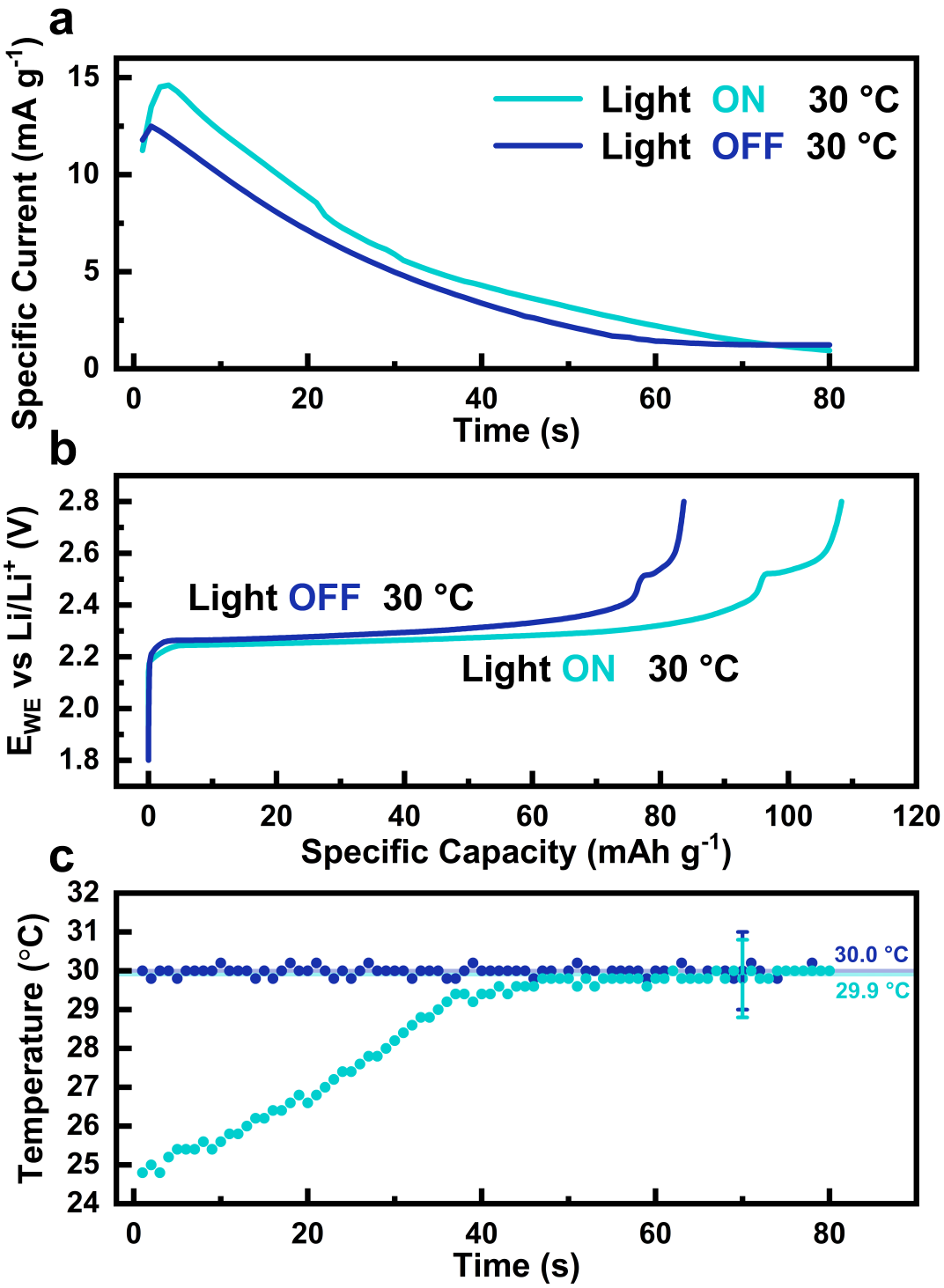


Figure 5.20: Electrochemical and thermal behavior of $MAPbBr_3 + TiO_2$ electrodes under illuminated and dark conditions. **a)** Chronoamperometry at 1.8 V for 80 s under light exposure (cyan) and dark with external heating to 30 °C (blue). **b)** GCPL discharge curves at 10 mA g^{-1} directly following the CA step. Both a) and b) indicate clear differences between the illuminated and dark experimental condition. **c)** Surface temperature profiles recorded during CA using infrared thermometry.

a sharper plateau at 2.25 V for the illuminated cell, followed by a secondary feature at 2.52 V, yielding a total capacity of 108 mA h g^{-1}. In contrast, the dark reference measurement shows similar redox features with a slightly lower total capacity of 84 mA h g^{-1}. These results are consistent with improved charge extraction under light exposure all while thermal effects can be ruled out as driver by the reference measurement. Figure 5.20 c) shows surface temperature measurements during the CA step. The illuminated sample heats up gradually from 25 °C to 30 °C, while the dark reference is externally maintained at a constant 30 °C. This confirms that the increased current response in the illuminated cell arises predominantly from photogenerated carriers, rather than thermal effects.

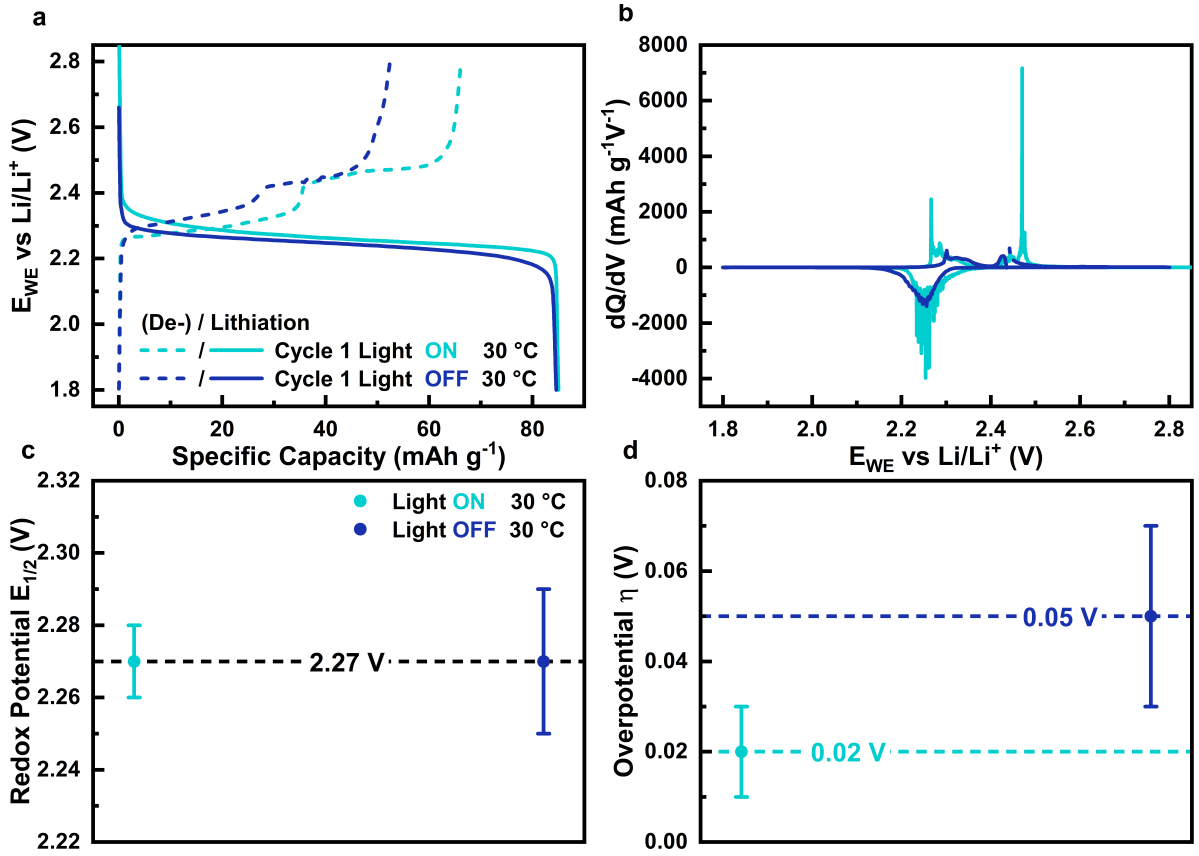


Figure 5.21: Electrochemical analysis of $MAPbBr_3 + TiO_2$ electrodes under light-on and dark conditions at 30 °C. **a)** GCPL voltage profiles during the first cycle at 30 mA g^{-1}. **b)** Corresponding differential capacity curves (dQ/dV). **c)** Redox potentials ($E_{1/2}$) determined from Gaussian peak fitting. **d)** Extracted overpotentials (η) for redox reactions.

To further assess redox kinetics, first-cycle GCPL curves at 30 mA g^{-1} are shown in Figure 5.21 a). Both light-on and dark conditions exhibit initial lithiation capacities of 85 mA h g^{-1} (cyan) and 85 mA h g^{-1} (blue), respectively. The primary lithiation plateau appears at 2.26 V for the illuminated case and at 2.25 V in the dark, with the slightly elevated plateau under illumination suggesting eventually enhanced lithium kinetics. No-

tably, the delithiation profile under illumination features a first plateau at 2.29 V and a second at 2.47 V, yielding a discharge capacity of 66 mA h g^{-1} (78 % capacity retention). The dark condition shows plateaus at 2.32 V and 2.44 V, resulting in a lower discharge capacity of 52 mA h g^{-1} (62 % retention). The differential capacity plots in Figure 5.21 b) highlight consistent redox behavior. Both cells show reduction peaks near 2.26 V, while oxidation features shift slightly: the illuminated cell shows peaks at 2.27 V and 2.44 V, whereas the dark cell peaks at 2.30 V and 2.47 V. Shoulder features further differentiate the two curves at 2.29 V (light-on) and 2.32 V (dark). Redox half-wave potentials ($E_{1/2}$), shown in Figure 5.21 c), remain statistically identical within error: $E_{1/2} = 2.27 \pm 0.01$ V (light-on) and 2.27 ± 0.02 V (dark). However, the overpotentials η (Figure 5.21 d) differ: under illumination, η_{light} is reduced to 0.02 ± 0.01 V, while the dark reference exhibits $\eta_{dark} = 0.05 \pm 0.02$ V, confirming an illumination-induced enhancement in redox kinetics.

It is important to note that reference measurements were carried out on TiO_2 electrodes to prove the electrochemical inactivity of TiO_2. This is essential, as otherwise it can be argued that the additional specific capacity produced in Figures 5.20 and 5.21 can be attributed to TiO_2. Figure 5.22 shows galvanostatic measurements on TiO_2-CB-PVDF electrodes over 1000 cycles. A current rate of 30 mA g^{-1} in a voltage range of 1.8 to 2.8 V was selected. Figure 5.22 a shows a stable specific capacity of 3.5 mA h g^{-1} over 1000 cycles revealing that TiO_2 content in $MAPbBr_3$ electrodes can be neglected for further measurements. The potential plateaus shown in Figure 5.22 b also confirm this statement.

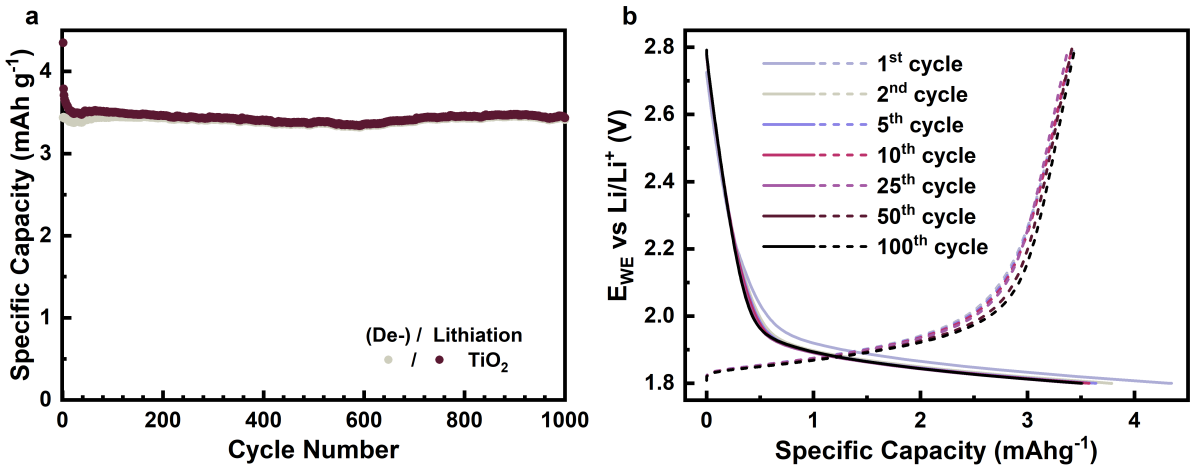


Figure 5.22: Electrochemical reference analysis of TiO_2 electrodes. **a)** GCPL measurements for 1000 cycles at 30 mA g^{-1} in a voltage range of 1.8 to 2.8 V. **b)** Galvanostatic potential profiles.

This section investigated the influence of external factors, specifically light exposure and temperature, on the electrochemical behavior of $MAPbBr_3$-based composite electrodes. A key objective was to isolate potential photo-induced enhancements from thermal effects.

Chronoamperometric and galvanostatic measurements were performed under illumination and compared to reference experiments conducted in the dark but externally heated to match the illuminated surface temperature (30 °C). The resulting similarity in current response and capacity between both conditions confirms two critical observations: (1) no enhancement due to light exposure was detected, and (2) external heating to 30 °C successfully replicated the thermal load induced by illumination. Thus, the results demonstrate that $MAPbBr_3$ composite electrodes without additional charge-selective additives do not exhibit intrinsic photoelectrochemical activity. In contrast, incorporating TiO_2 seemed to successfully enable a measurable response to light. Under illumination, $MAPbBr_3 + TiO_2$ electrodes exhibited enhanced specific current, increased specific capacity, and reduced overpotentials. This is attributed to improved photogenerated charge separation facilitated by TiO_2, but has still to be proven from a theoratical perspective, which is not within the scope of this experimental thesis. This highlights the importance of composite engineering in activating light-induced electrochemical functionality.

5.5 Conclusions and Overview

This chapter presents a comprehensive investigation of the electrochemical behavior mainly of $MAPbBr_3$ and related hybrid organic–inorganic perovskites (HOIPs) as anode materials for lithium-ion batteries. A variety of experimental strategies were employed to assess and understand the redox activity, stability, and degradation mechanisms of these materials under different electrochemical conditions. While the long-term performance falls short of practical application requirements, the experiments themselves are successful and yield several key insights that may inform future research directions.

Systematic galvanostatic cycling and half-cell characterization demonstrate that the electrochemical response of $MAPbBr_3$ is highly dependent on the electrolyte environment. Specifically, carbonate-based electrolytes with $LiPF_6$ exhibit no detectable redox activity, likely due to adverse interactions between the solvent and the perovskite lattice. In contrast, ether-based electrolytes containing LiTFSI and SEI-modifying additives such as $LiNO_3$ support clear electrochemical signatures, including lithiation, conversion, and alloying processes, at least during the early stages of cycling.

Through careful voltage window segmentation and process isolation, distinct degradation pathways are resolved. Alloying reactions, although initially active, show rapid and irreversible capacity loss. Conversion reactions introduced significant structural changes that correlate with a sharp decline in reversibility. In contrast, lithiation reactions confined to

a narrow voltage window exhibit comparatively improved cycling stability and coulombic efficiency. This suggests that targeted voltage control may be a viable strategy to prolong activity in HOIP-based electrodes.

Additional experiments explore the influence of electrolyte composition, solvent polarity, and solid-state configurations. While no single formulation prevented long-term degradation, the study reveals consistent trends, such as accelerated dissolution in polar solvents and limited interfacial kinetics in polymer electrolytes. Comparative testing of related HOIP compositions indicates that $MAPbBr_3$ offers marginally better performance than analogs, though all suffered from notable capacity fading, especially within the first 20 cycles.

External stimuli such as light and temperature were also evaluated. No intrinsic photoelectrochemical activity is observed in $MAPbBr_3$ alone; however, the inclusion of TiO_2 as a composite additive enables a moderate and reproducible photo-response. Although the underlying mechanism remains uncertain, it may involve enhanced charge separation or interfacial effects. Importantly, thermal controls rules out simple photothermal contributions.

Taken together, these results show that while $MAPbBr_3$ and related HOIPs are not yet suitable for practical lithium-ion battery applications, the experiments conducted here establish a strong methodological foundation for further exploration. In particular, the identification of stable lithiation regimes and the potential role of light-responsive composites highlight promising avenues for material and device optimization.

The chapter thus contributes to a first experimental benchmark for HOIP anode behavior in lithium-ion systems. Although the simplest material configurations do not yield durable performance, the findings help clarify the key challenges, especially material dissolution and phase instability, and point toward more nuanced design strategies. Continued research integrating theoretical modeling, advanced characterization, and tailored composite engineering will be essential to fully understand and harness the electrochemical potential of these complex materials.

6 Summary and Conclusion

This dissertation reports the development and characterization of novel electrode materials for lithium-based batteries. The studied materials are systematically examined with respect to their physical and electrochemical properties to elucidate correlations between structural characteristics and electrochemical behavior. A comprehensive set of characterization techniques was employed to gain insight into the structural, chemical, and electrochemical properties of the investigated materials. From a physical characterization standpoint, methods such as powder X-ray diffraction (PXRD) and scanning electron microscopy (SEM) were used to determine the crystallinity, phase purity, and morphological features of the samples. Additional information was provided through collaborative measurements, including photoluminescence (PL), photoluminescence quantum yield (PLQY), compositional analysis, time-of-flight secondary ion mass spectrometry (ToF-SIMS), Raman and FT-IR spectroscopy, thermogravimetric analysis (TGA), and Brunauer–Emmett–Teller (BET) surface area analysis. These techniques offer detailed perspectives on the optical behavior, elemental composition, thermal stability, and porosity of the materials under investigation. Electrochemical performance was examined using complementary techniques such as cyclic voltammetry (CV), galvanostatic cycling with potential limitation (GCPL), and chronoamperometry (CA) to assess redox activity, specific capacity, coulombic efficiency, charge-transfer kinetics, and interfacial resistances across different material systems.

The first chapter examines the development and electrochemical performance of nitrogen-centered triphenylamine analogues (N-HTAs) for use in redox-active polymers, focusing on FTN-Pol and its structurally modified derivatives incorporating various functional groups. The results highlight the adjustable nature and inherent trade-offs involved in designing triphenylamine-based cathode materials. A wide range of physical characterization measurements were used to investigate the structure of triphenylamine-based cathode materials. The effect of polymerization on the PL properties of FTN-based systems is examined using emission spectroscopy, with comparative analysis conducted against the molecularly dissolved reference compound FTN. FTN displays a distinct emission maximum at 377 nm (3.29 eV), accompanied by a shoulder at 368 nm and a spectral tail extending to 500 nm.

In contrast, the polymeric analogue FTN-Pol, when dispersed in tetrahydrofuran (THF), exhibits a pronounced bathochromic shift with a broadened emission band centered at 490 nm (2.53 eV), extending up to 750 nm. Solvent-dependent PL measurements reveal broad dual-emission features (approximately 430 nm and 500 nm) across various solvent systems, with increasing solvent polarity inducing systematic red-shifts. PLQYs for FTN-Pol were measured in the range of 0.01 to 0.03, comparable to the value observed for FTN ($\Phi = 0.04$). A trend of reduced PLQY values with increasing solvent polarity is noted. Elemental analysis via combustion confirms the expected chemical composition for both FTN-Pol and FTN-H-Pol. ToF-SIMS analysis verifies the absence of residual nickel species. PXRD measurements demonstrate that both polymers are amorphous in nature. Spectroscopic characterization using Raman and FT-IR spectroscopy confirm the complete conversion of bromo-functionalized precursors, as indicated by the disappearance of C-Br stretching vibrations in the $1058-1060\ \mathrm{cm^{-1}}$ region and the presence of characteristic C-H vibrations from the fluorenyl units around $1019\ \mathrm{cm^{-1}}$, consistent with spectra from dehalogenated model compounds. TGA indicates high thermal stability, with decomposition onsets observed at approximately 500 °C for FTN-Pol and 700 °C for FTN-H-Pol. Minor mass losses below 400 °C are attributed to desorption of adsorbed moisture and gases, while mass loss between 400 and 600 °C is likely associated with the cleavage of tert-butyl side chains. SEM reveals that both materials form amorphous globular particles with coralloid surface morphologies, which assemble into larger agglomerates. Nitrogen adsorption-desorption isotherms measured at 77 K exhibit type I characteristics with hysteresis, indicative of microporous structures that undergo elastic deformation. BET surface area measurements yield high values of 690 and $682\ \mathrm{m^2\,g^{-1}}$ for FTN-Pol and FTN-H-Pol, respectively. Pore size distribution determined using non-local density functional theory (NL-DFT) reveals the presence of micropores (0.70 nm) in FTN-Pol, in addition to mesopores centered at 0.84 nm and 1.21 nm. In comparison, FTN-H-Pol exhibits a broader pore distribution ranging from 0.78 to 3.08 nm, which is attributed to the absence of bulky tert-butyl substituents in the monomer. These substituents enhance solubility, guide the polymerization process, and protect reactive positions on the N-HTA core. Due to the improved structural uniformity and synthetic reproducibility, subsequent electrochemical investigations focus exclusively on FTN-Pol.

Electrochemical analysis demonstrates in the base system, FTN-Pol, that N-HTAs serve as electrochemically stable and redox-active backbones within polymeric cathodes. The rigid spirocyclic framework leads to the formation of a defined microporous structure that enhances redox site accessibility while minimizing undesired side reactions. This behavior is supported by a high Coulombic efficiency of 99.6 % and stable cycling over extended

periods. Although the specific capacity is limited by the relatively high molecular weight of the redox unit, FTN-Pol achieves a utilization rate of 73 % of its theoretical capacity, thereby performing more efficiently than some conventional triphenylamine systems. These results support the concept that rigid, conjugated structures enhance charge transport and redox reversibility in organic cathode materials. Building upon this system, sulfur chains were incorporated into FTN-Pol as an approach to increase capacity by introducing additional redox-active moieties. The incorporation of sulfur leads to new redox processes, particularly within the voltage range of 2.0 – 2.4 V vs. Li/Li^+. However, the performance of these sulfur-functionalized polymers is strongly influenced by the electrolyte system. Ether-based electrolytes (1 M LiTFSI in DOL:DME) allow for more reversible sulfur redox activity, whereas carbonate-based electrolytes ($LiPF_6$ or $LiClO_4$ in EC:DMC) show rapid capacity degradation and reduced reversibility, likely due to polysulfide dissolution and shuttle effects. Even under the more favorable ether-based conditions, the contribution from sulfur redox activity diminishes significantly over time, with only approximately 3 – 10 % of the initial capacity retained after 400 cycles. These findings underscore the practical difficulties associated with integrating sulfur chemistry into redox polymers, particularly in terms of interfacial instability and insufficient confinement of reactive sulfur species. An alternative strategy involves the functionalization of FTN-Pol with terthiophene (3T) groups to enhance initial capacity via π-conjugated, sulfur-containing units. The FTN-Pol + 3T composite displays an increased initial capacity ($101\,mA\,h\,g^{-1}$), primarily due to additional faradaic activity at lower voltages. Nevertheless, this capacity gain is offset by significant fading during the first 50 cycles, which is attributed to irreversible oxidation processes involving the 3T moieties. Despite the observed decline in capacity, the system maintains a high long-term Coulombic efficiency of 99.7 %, suggesting that the redox activity eventually reverts to the more stable FTN backbone. These results point to a common limitation in the field: although capacity can be improved through functional group modifications, such changes often compromise long-term electrochemical stability due to irreversible reactions or degradation of the introduced functionalities.

In summary, the investigations described in this chapter illustrate the opportunities and limitations associated with the molecular engineering of triphenylamine-based cathode materials. FTN-Pol provides a stable platform with reliable redox activity, while the addition of sulfur chains or 3T units can enhance energy density but tends to reduce cycle life and reversibility. These findings underscore the need to carefully balance capacity, redox kinetics, and long-term durability through targeted molecular design. Future work in this area may benefit from approaches that stabilize additional redox-active components, particularly sulfur- and thiophene-based groups, through strategies such as covalent tethering,

encapsulation, or network formation. Electrolyte optimization, including the development of hybrid or solid-state systems, may also mitigate dissolution effects and improve redox selectivity. Moreover, expanding the use of nitrogen-centered redox units to other rigid, π-conjugated backbones may lead to novel design principles for organic cathodes with broader voltage ranges, higher energy densities, and improved cycling performance. Such developments would contribute to the ongoing advancement of sustainable and efficient organic lithium-ion batteries.

The second chapter presents the photo-enhanced electrochemical behavior of $LiMn_2O_4$ (LMO) cathodes, highlighting their potential to improve battery performance via light-induced effects. Chronoamperometric and galvanostatic methods were combined to evaluate the influence of illumination on reaction kinetics and capacity delivery. The data indicate that light exposure leads to measurable enhancements in electrochemical activity; however, the contributions of thermal effects due to localized heating must be considered when interpreting these observations. Through a series of controlled chronoamperometric and galvanostatic experiments, it is possible to differentiate between thermal and photonic influences. The results show that, even at comparable temperatures ($\approx 30\,^{\circ}C$), illuminated samples exhibit significantly higher charge extraction during fixed-voltage oxidation steps relative to non-illuminated controls. These findings suggest that light interacts with the electronic structure of LMO, potentially by enhancing charge carrier mobility or suppressing recombination, which results in lower interfacial resistances and faster redox reactions. Additionally, spatially resolved illumination studies reveal that the degree of enhancement is proportional to the illuminated area, indicating that the underlying mechanisms are at least partially surface-localized and dependent on photo-induced charge transport. Overall, the findings demonstrate that while thermal contributions are non-negligible, genuine photochemical effects are present when illumination is appropriately managed and aligned with the material's absorption characteristics. The electrochemical performance of LMO was also evaluated under repeated illuminated and non-illuminated conditions. CA and GCPL data show that brief light exposure (22 minutes) significantly accelerates the electrochemical response, achieving levels of charge transfer that otherwise require prolonged dark operation (70 minutes). Over time, longer dark measurements reach similar electrochemical endpoints, suggesting that illumination primarily serves to reduce the time required to attain a given electrochemical state. Thermal monitoring confirms consistent heating trends, reinforcing the importance of controlling and distinguishing photothermal and photochemical effects in these experiments.

In conclusion, the enhancement of LMO electrochemical activity under illumination results from a combined effect of thermal and photonic mechanisms. Disentangling these

contributions provides a more detailed understanding of the phenomena involved and offers insights for the design of photo-responsive electrode materials. Future studies could focus on wavelength-dependent behavior, cycling stability under intermittent illumination, and interfacial modifications aimed at enhancing or controlling these light-driven effects in practical battery configurations.

The third chapter examines the electrochemical properties of methylammonium lead bromide ($MAPbBr_3$) and related hybrid organic–inorganic perovskites (HOIPs) within lithium-ion battery systems. While the initial aim was to explore their viability as active electrode materials, the primary contribution of this study lies in establishing a first experimental benchmark and identifying both the limitations and the latent potential of these materials. Through systematic experimentation, including variation in electrolyte composition, voltage window control, and composite design, several important findings were uncovered. It is demonstrated that the electrochemical behavior of $MAPbBr_3$ is highly sensitive to the electrolyte environment. Carbonate-based systems containing $LiPF_6$ show no detectable activity, likely due to instability of the HOIP structure in polar solvents. This confirms previous reports and underscores the importance of solvent–material compatibility. In contrast, ether-based electrolytes incorporating LiTFSI and additives such as $LiNO_3$ enable the detection of distinct lithiation, conversion, and alloying processes. While these processes are largely confined to the initial stages of cycling, they provide clear evidence that redox activity is possible under optimized conditions. Notably, the lithiation process within a narrow voltage range emerges as the most stable, suggesting a direction for future work that focuses on controlled and limited redox regimes. The stepwise separation of electrochemical processes reveals that conversion reactions contribute significantly to material degradation, including capacity fading and loss of reversibility. Lithiation alone, when isolated, performs comparatively better, though not without inefficiencies. These mechanistic insights are critical, as they point to specific electrochemical pathways that must be either optimized or avoided in future designs. The study also addresses material and interfacial stability challenges, particularly those arising from electrolyte composition. While certain formulations yield improved early-cycle performance, none succeed in halting degradation over extended cycling. Perovskite dissolution and poor interface formation are recurring issues. Among the HOIP variants tested, $MAPbBr_3$ consistently delivers the best relative performance, yet capacity fading remains substantial. Importantly, external stimuli such as light and temperature were explored as potential modifiers of electrochemical behavior. No intrinsic photoelectrochemical activity is observed in $MAPbBr_3$ alone. However, composite electrodes incorporating TiO_2 display a moderate and reproducible enhancement in response under illumination. Although the mechanism remains specula-

tive, the effect may relate to improved charge separation or interfacial dynamics, a finding that opens the door for photoactive composite architectures.

Taken together, this work demonstrates that while $MAPbBr_3$ is currently not suitable for long-term battery applications, it exhibits measurable and tunable electrochemical behavior under well-defined conditions. These results represent a successful and necessary first step in understanding the complex interactions that govern HOIP-based electrodes. The insights gained here, particularly regarding electrolyte compatibility, process stability, and photo-induced effects, provide a solid foundation for further targeted research. Future studies may build on this benchmark by exploring strategies to suppress material degradation, such as structural stabilization or dissolution prevention. In parallel, a more detailed theoretical understanding of redox mechanisms in HOIPs could enable the rational design of more robust and functional electrode architectures. As such, the work presented in this thesis not only identifies the current limitations but also outlines the essential questions and directions for advancing HOIP materials in the field of electrochemical energy storage.

Across the three systems studied, organic triphenylamine-based polymers, photo-responsive $LiMn_2O_4$ spinels, and hybrid perovskite materials, unifying principles emerge. Among these the interfacial stability and charge transport seem to play a central role in long-term electrochemical performance. Whether through molecular design, illumination, or electrolyte tuning, each system aimed to enhance electron and ion mobility while mitigating parasitic reactions at the electrode–electrolyte interface. These findings suggest that future advances in lithium battery materials will depend not only on the intrinsic properties of active materials but also on the holistic optimization of the material–electrolyte system and operational environment. Common challenges also became apparent. Across all systems, attempts to introduce additional redox-active components or leverage external stimuli (such as light) often come at the cost of decreased stability or increased complexity. Sulfur functionalities in polymers and alloying, conversion pathways in HOIPs all lead to capacity fading, side reactions, or interface degradation over time. These outcomes underscore a persistent trade-off between increasing energy density and maintaining long-term reversibility. Moving forward, the design of lithium-ion battery materials may benefit from strategies that integrate multiple functionalities while minimizing their destabilizing effects. This could include covalent confinement of reactive groups in organic systems, or solid-state electrolyte integration.

Bibliography

[1] Energy-Institute, "In collaboration with statistical review of world energy", 2024, ISSN: 2976-7857. [Online]. Available: https://www.energyinst.org/statistical-review.

[2] J. Cook, N. Oreskes, P. T. Doran, W. R. Anderegg, B. Verheggen, E. W. Maibach, J. S. Carlton, S. Lewandowsky, A. G. Skuce, S. A. Green, D. Nuccitelli, P. Jacobs, M. Richardson, B. Winkler, R. Painting, and K. Rice, "Consensus on consensus: A synthesis of consensus estimates on human-caused global warming", *Environmental Research Letters*, vol. 11, p. 048 002, 4 Apr. 2016, ISSN: 1748-9326. DOI: 10.1088/1748-9326/11/4/048002. [Online]. Available: https://iopscience.iop.org/article/10.1088/1748-9326/11/4/048002.

[3] C. D. Keeling, R. B. Bacastow, A. E. Bainbridge, C. A. E. Jr, P. R. Guenther, L. S. Waterman, J. F. S. Chin, B. D. C. Keeling, C. A. Ekdahl, and L. E. E. S. Waterman, "Atmospheric carbon dioxide variations at mauna loa observatory, hawaii", *Tellus*, vol. 28, pp. 538–551, 6 1976, ISSN: 00402826. DOI: 10.3402/TELLUSA.V28I6.11322. [Online]. Available: https://www.tandfonline.com/doi/abs/10.3402/tellusa.v28i6.11322.

[4] U. S. Diego and S. I. for Oceanography, *The keeling curve*, 2025. [Online]. Available: https://keelingcurve.ucsd.edu/.

[5] IPCC, "Climate change 2023 synthesis report a report of the intergovernmental panel on climate change", pp. 22–23, 2023. DOI: 10.59327/IPCC/AR6-9789291691647.

[6] J. F. Mitchell, "The "greenhouse" effect and climate change", *Reviews of Geophysics*, vol. 27, pp. 115–139, 1 Feb. 1989, ISSN: 1944-9208. DOI: 10.1029/RG027I001P00115. [Online]. Available: https://onlinelibrary.wiley.com/doi/full/10.1029/RG027i001p00115.

[7] S. H. Schneider, "The greenhouse effect: Science and policy", *Science*, vol. 243, pp. 771–781, 4892 Feb. 1989, ISSN: 00368075. DOI: 10.1126/SCIENCE.243.4892.771. [Online]. Available: https://www.science.org/doi/10.1126/science.243.4892.771.

[8] S. C. Doney, V. J. Fabry, R. A. Feely, and J. A. Kleypas, "Ocean acidification: The other co2 problem", *Annual Review of Marine Science*, vol. 1, pp. 169–192, Volume 1, 2009 Jan. 2009, ISSN: 19411405. DOI: 10.1146/ANNUREV.MARINE.010908.163834. [Online]. Available: https://www.annualreviews.org/content/journals/10.1146/annurev.marine.010908.163834.

[9] L. Cheng, J. Abraham, K. E. Trenberth, J. Fasullo, T. Boyer, M. E. Mann, J. Zhu, F. Wang, R. Locarnini, Y. Li, B. Zhang, F. Yu, L. Wan, X. Chen, L. Feng, X. Song, Y. Liu, F. Reseghetti, S. Simoncelli, V. Gouretski, G. Chen, A. Mishonov, J. Reagan, and G. Li, "Another year of record heat for the oceans", *Advances in Atmospheric Sciences*, vol. 40, pp. 963–974, 6 Jun. 2023, ISSN: 18619533. DOI: 10.1007/S00376-023-2385-2.

[10] T. Jacob, J. Wahr, W. T. Pfeffer, and S. Swenson, "Recent contributions of glaciers and ice caps to sea level rise", *Nature 2012 482:7386*, vol. 482, pp. 514–518, 7386 Feb. 2012, ISSN: 1476-4687. DOI: 10.1038/nature10847. [Online]. Available: https://www.nature.com/articles/nature10847.

[11] A. Cazenave and W. Llovel, "Contemporary sea level rise", *Annual Review of Marine Science*, vol. 2, pp. 145–173, 1 Jan. 2010, ISSN: 19411405. DOI: 10.1146/ANNUREV-MARINE-120308-081105. [Online]. Available: https://www.annualrevie%5C%5Cws.org/content/journals/10.1146/annurev-marine-120308-081105.

[12] P. Stott, "How climate change affects extreme weather events", *Science*, vol. 352, pp. 1517–1518, 6293 Jun. 2016, ISSN: 10959203. DOI: 10.1126/SCIENCE.AAF7271. [Online]. Available: https://www.science.org/doi/10.1126/science.aaf7271.

[13] A. E. Cahill, M. E. Aiello-Lammens, M. C. Fisher-Reid, X. Hua, C. J. Karanewsky, H. Y. Ryu, G. C. Sbeglia, F. Spagnolo, J. B. Waldron, O. Warsi, and J. J. Wiens, "How does climate change cause extinction?", *Proceedings of the Royal Society B: Biological Sciences*, vol. 280, 1750 2013, ISSN: 14712954. DOI: 10.1098/RSPB.2012.1890. [Online]. Available: https://royalsocietypublishing.org/doi/10.1098/rspb.2012.1890.

[14] C. D. Thomas, A. Cameron, R. E. Green, M. Bakkenes, L. J. Beaumont, Y. C. Collingham, B. F. Erasmus, M. F. D. Siqueira, A. Grainger, L. Hannah, L. Hughes, B. Huntley, A. S. V. Jaarsveld, G. F. Midgley, L. Miles, M. A. Ortega-Huerta, A. T. Peterson, O. L. Phillips, and S. E. Williams, "Extinction risk from climate change", *Nature 2003 427:6970*, vol. 427, pp. 145–148, 6970 Jan. 2004, ISSN: 1476-4687. DOI: 10.1038/nature02121. [Online]. Available: https://www.nature.com/articles/nature02121.

[15] A. Baldwin, "Climate change, migration, and the crisis of humanism", *Wiley Interdisciplinary Reviews: Climate Change*, vol. 8, e460, 3 May 2017, ISSN: 1757-7799. DOI: 10.1002/WCC.460. [Online]. Available: https://onlinelibrary.wiley.com/doi/full/10.1002/wcc.460.

[16] Q. Hassan, P. Viktor, T. J. Al-Musawi, B. M. Ali, S. Algburi, H. M. Alzoubi, A. K. Al-Jiboory, A. Z. Sameen, H. M. Salman, and M. Jaszczur, "The renewable energy role in the global energy transformations", *Renewable Energy Focus*, vol. 48, p. 100 545, Mar. 2024, ISSN: 1755-0084. DOI: 10.1016/J.REF.2024.100545.

[17] M. H. Nehrir, C. Wang, K. Strunz, H. Aki, R. Ramakumar, J. Bing, Z. Miao, and Z. Salameh, "A review of hybrid renewable/alternative energy systems for electric power generation: Configurations, control, and applications", *IEEE Transactions on Sustainable Energy*, vol. 2, pp. 392–403, 4 Oct. 2011, ISSN: 19493029. DOI: 10.1109/TSTE.2011.2157540.

[18] D. Gielen, F. Boshell, D. Saygin, M. D. Bazilian, N. Wagner, and R. Gorini, "The role of renewable energy in the global energy transformation", *Energy Strategy Reviews*, vol. 24, pp. 38–50, Apr. 2019, ISSN: 2211-467X. DOI: 10.1016/J.ESR.2019.01.006.

[19] N. Mahmud and A. Zahedi, "Review of control strategies for voltage regulation of the smart distribution network with high penetration of renewable distributed generation", *Renewable and Sustainable Energy Reviews*, vol. 64, pp. 582–595, Oct. 2016, ISSN: 1364-0321. DOI: 10.1016/J.RSER.2016.06.030.

[20] P. Denholm, M. O'Connell, G. Brinkman, and J. Jorgenson, "Overgeneration from solar energy in california. a field guide to the duck chart", Nov. 2015. DOI: 10.2172/1226167. [Online]. Available: http://www.osti.gov/servlets/purl/1226167/.

[21] T. M. Phan, T. T. Nguyen, M. Q. Duong, and T. T. Nguyen, "Optimal design and operation of battery energy storage systems in renewable power plants to reach maximum total electric sale revenues", *Neural Computing and Applications*, vol. 36, pp. 12 061–12 082, 20 Jul. 2024, ISSN: 14333058. DOI: 10.1007/S00521-024-09769-w. [Online]. Available: https://link.springer.com/article/10.1007/s00521-024-09769-w.

[22] F. Yang, D. Wang, Y. Zhao, K. L. Tsui, and S. J. Bae, "A study of the relationship between coulombic efficiency and capacity degradation of commercial lithium-ion batteries", *Energy*, vol. 145, pp. 486–495, Feb. 2018, ISSN: 0360-5442. DOI: 10.1016/J.ENERGY.2017.12.144.

[23] I. Dincer, "Renewable energy and sustainable development: A crucial review", *Renewable and Sustainable Energy Reviews*, vol. 4, pp. 157–175, 2 Jun. 2000, ISSN: 1364-0321. DOI: 10.1016/S1364-0321(99)00011-8.

[24] A. Volta, "Xvii. on the electricity excited by the mere contact of conducting substances of different kinds. in a letter from mr. alexander volta, f. r. s. professor of natural philosophy in the university of pavia, to the rt. hon. sir joseph banks, bart. k.b. p. r. s", *Philosophical Transactions of the Royal Society of London*, vol. 90, pp. 403–431, Dec. 1800, ISSN: 0261-0523. DOI: 10.1098/RSTL.1800.0018. [Online]. Available: https://royalsocietypublishing.org/doi/10.1098/rstl.1800.0018.

[25] W. B. Jensen, *The leclanché cell : Notes from the oesper collections, no. 24, january/february 2014*, Dec. 2013. [Online]. Available: http://hdl.handle.net/2374.UC/731246.

[26] B. Scrosati, "History of lithium batteries", *Journal of Solid State Electrochemistry*, vol. 15, pp. 1623–1630, 7-8 Jul. 2011, ISSN: 14328488. DOI: 10.1007/S10008-011-1386-8. [Online]. Available: https://link.springer.com/article/10.1007/s10008-011-1386-8.

[27] S. M. Selis, J. P. Wondowski, and R. F. Justus, "A high-rate, high-energy thermal battery system", *Journal of The Electrochemical Society*, vol. 111, p. 6, 1 Jan. 1964, ISSN: 00134651. DOI: 10.1149/1.2426065. [Online]. Available: https://iopscience.iop.org/article/10.1149/1.2426065.

[28] E. J. Casey, A. R. Dubois, P. E. Lake, and W. J. Moroz, "Effects of foreign ions on nickel hydroxide and cadmium electrodes", *Journal of The Electrochemical Society*, vol. 112, p. 371, 4 Apr. 1965, ISSN: 00134651. DOI: 10.1149/1.2423552. [Online]. Available: https://iopscience.iop.org/article/10.1149/1.2423552.

[29] M. S. Whittingham, "Chemistry of intercalation compounds: Metal guests in chalcogenide hosts", *Progress in Solid State Chemistry*, vol. 12, pp. 41–99, 1 Jan. 1978, ISSN: 0079-6786. DOI: 10.1016/0079-6786(78)90003-1.

[30] J. M. Tarascon and M. Armand, "Issues and challenges facing rechargeable lithium batteries", *Nature 2001 414:6861*, vol. 414, pp. 359–367, 6861 Nov. 2001, ISSN: 1476-4687. DOI: 10.1038/35104644. [Online]. Available: https://www.nature.com/articles/35104644.

[31] F. Xu, X. Chen, Z. Tang, D. Wu, R. Fu, and D. Jiang, "Redox-active conjugated microporous polymers: A new organic platform for highly efficient energy storage", *Chemical Communications*, vol. 50, pp. 4788–4790, 37 Apr. 2014, ISSN: 1364-548X.

DOI: 10.1039/C4CC01002G. [Online]. Available: https://pubs.rsc.org/en/content/articlehtml/2014/cc/c4cc01002g.

[32] N. Ding, A. Sumboja, X. Yin, Y. Zheng, D. W. H. Fam, and Y. Zong, "Reversible lithium electroplating for high-energy rechargeable batteries", *Journal of The Electrochemical Society*, vol. 170, p. 010 540, 1 Jan. 2023, ISSN: 1945-7111. DOI: 10.1149/1945-7111/ACB400. [Online]. Available: https://iopscience.iop.org/article/10.1149/1945-7111/acb400.

[33] K. Mizushima, P. C. Jones, P. J. Wiseman, and J. B. Goodenough, "Lixcoo2 (0<x<-1): A new cathode material for batteries of high energy density", *Materials Research Bulletin*, vol. 15, pp. 783–789, 6 Jun. 1980, ISSN: 0025-5408. DOI: 10.1016/0025-5408(80)90012-4.

[34] J. O. Besenhard, E. Theodoridou, H. Möhwald, and J. J. Nickl, "Electrochemical applications of graphite intercalation compounds", *Synth. Met.; (Switzerland)*, vol. 4:3, pp. 211–223, 3 1982, ISSN: 03796779. DOI: 10.1016/0379-6779(82)90014-5.

[35] R. Yazami and P. Touzain, "A reversible graphite-lithium negative electrode for electrochemical generators", *Journal of Power Sources*, vol. 9, pp. 365–371, 3 Jan. 1983, ISSN: 0378-7753. DOI: 10.1016/0378-7753(83)87040-2.

[36] A. Yoshino, "The birth of the lithium-ion battery", *Angewandte Chemie International Edition*, vol. 51, pp. 5798–5800, 24 Jun. 2012, ISSN: 1521-3773. DOI: 10.1002/ANIE.201105006. [Online]. Available: https://onlinelibrary.wiley.com/doi/full/10.1002/anie.201105006.

[37] N. Nitta, F. Wu, J. T. Lee, and G. Yushin, "Li-ion battery materials: Present and future", *Materials Today*, vol. 18, pp. 252–264, 5 Jun. 2015, ISSN: 1369-7021. DOI: 10.1016/J.MATTOD.2014.10.040.

[38] S. Hideki, H. A. J., and M. A. G., *The nobel prize in chemistry 2000 - popular information - nobelprize.org*, 2000. [Online]. Available: https://www.nobelprize.org/prizes/chemistry/2000/popular-information/.

[39] G. J. B., W. M. Stanley, and Y. Akira, *The nobel prize in chemistry 2019 - popular information - nobelprize.org*, 2019. [Online]. Available: https://www.nobelprize.org/prizes/chemistry/2019/popular-information/.

[40] M. Armand and J.-M. Tarascon, "Building better batteries", *Nature 2008 451:7179*, vol. 451, pp. 652–657, 7179 Feb. 2008, ISSN: 1476-4687. DOI: 10.1038/451652a. [Online]. Available: https://www.nature.com/articles/451652a.

[41] J. B. Goodenough and Y. Kim, "Challenges for rechargeable li batteries", *Chemistry of Materials*, vol. 22, pp. 587–603, 3 Feb. 2010, ISSN: 08974756. DOI: 10.1021/CM901452Z. [Online]. Available: https://pubs.acs.org/doi/full/10.1021/cm901452z.

[42] S. Muench, A. Wild, C. Friebe, B. Häupler, T. Janoschka, and U. S. Schubert, "Polymer-based organic batteries", *Chemical Reviews*, vol. 116, pp. 9438–9484, 16 Aug. 2016, ISSN: 15206890. DOI: 10.1021/acs.chemrev.6b00070. [Online]. Available: https://pubs.acs.org/doi/full/10.1021/acs.chemrev.6b00070.

[43] H. Zhang, Y. Yang, D. Ren, L. Wang, and X. He, "Graphite as anode materials: Fundamental mechanism, recent progress and advances", *Energy Storage Materials*, vol. 36, pp. 147–170, Apr. 2021, ISSN: 2405-8297. DOI: 10.1016/J.ENSM.2020.12.027.

[44] G. G. Amatucci and N. Pereira, "Fluoride based electrode materials for advanced energy storage devices", *Journal of Fluorine Chemistry*, vol. 128, pp. 243–262, 4 Apr. 2007, ISSN: 0022-1139. DOI: 10.1016/J.JFLUCHEM.2006.11.016.

[45] J. Lu, Z. Chen, F. Pan, Y. Cui, and K. Amine, "High-performance anode materials for rechargeable lithium-ion batteries", *Electrochemical Energy Reviews*, vol. 1, pp. 35–53, 1 Mar. 2018, ISSN: 25208136. DOI: 10.1007/S41918-018-0001-4. [Online]. Available: https://link.springer.com/article/10.1007/s41918-018-0001-4.

[46] C. M. Park, J. H. Kim, H. Kim, and H. J. Sohn, "Li-alloy based anode materials for li secondary batteries", *Chemical Society Reviews*, vol. 39, pp. 3115–3141, 8 Jul. 2010, ISSN: 1460-4744. DOI: 10.1039/B919877F. [Online]. Available: https://pubs.rsc.org/en/content/articlehtml/2010/cs/b919877f.

[47] W. J. Zhang, "A review of the electrochemical performance of alloy anodes for lithium-ion batteries", *Journal of Power Sources*, vol. 196, pp. 13–24, 1 Jan. 2011, ISSN: 0378-7753. DOI: 10.1016/J.JPOWSOUR.2010.07.020.

[48] M. N. Obrovac and V. L. Chevrier, "Alloy negative electrodes for li-ion batteries", *Chemical Reviews*, vol. 114, pp. 11 444–11 502, 23 Dec. 2014, ISSN: 15206890. DOI: 10.1021/CR500207G. [Online]. Available: https://pubs.acs.org/doi/full/10.1021/cr500207g.

[49] R. C. Massé, C. Liu, Y. Li, L. Mai, and G. Cao, "Energy storage through intercalation reactions: Electrodes for rechargeable batteries", *National Science Review*, vol. 4, pp. 26–53, 1 Jan. 2017, ISSN: 2095-5138. DOI: 10.1093/NSR/NWW093. [Online]. Available: https://dx.doi.org/10.1093/nsr/nww093.

[50] P. Poizot, S. Laruelle, S. Grugeon, L. Dupont, and J. M. Tarascon, "Nano-sized transition-metal oxides as negative-electrode materials for lithium-ion batteries", *Nature 2000 407:6803*, vol. 407, pp. 496–499, 6803 Sep. 2000, ISSN: 1476-4687. DOI: 10.1038/35035045. [Online]. Available: https://www.nature.com/articles/35035045.

[51] N. Loeffler, D. Bresser, S. Passerini, and M. Copley, "Secondary lithium-ion battery anodes: From first commercial batteries to recent research activities", *Johnson Matthey Technology Review*, vol. 59, pp. 34–44, 1 Jan. 2015, ISSN: 20565135. DOI: 10.1595/205651314X685824.

[52] ICSD, *Inorganic crystal structure database (icsd)*, 2025. [Online]. Available: https://icsd.fiz-karlsruhe.de/index.xhtml;jsessionid=0449898459AC53582799-274E607AE11A.

[53] M. Tiwari, G. Chawla, and A. K. Bansal, "Quantification of olanzapine polymorphs using powder x-ray diffraction technique", *Journal of Pharmaceutical and Biomedical Analysis*, vol. 43, pp. 865–872, 2007. DOI: 10.1016/j.jpba.2006.08.030.

[54] S. Alam, S. Patel, and A. K. Bansal, "Effect of sample preparation method on quantification of polymorphs using pxrd", *Pharmaceutical Development and Technology*, vol. 15, pp. 452–459, 5 Oct. 2010, ISSN: 10837450. DOI: 10.3109/10837450903286511. [Online]. Available: https://www.tandfonline.com/doi/abs/10.3109/10837450-903286511.

[55] H. Khan, A. S. Yerramilli, A. D'Oliveira, T. L. Alford, D. C. Boffito, and G. S. Patience, "Experimental methods in chemical engineering: X-ray diffraction spectroscopy—xrd", *The Canadian Journal of Chemical Engineering*, vol. 98, pp. 1255–1266, 6 Jun. 2020, ISSN: 1939-019X. DOI: 10.1002/CJCE.23747. [Online]. Available: https://onlinelibrary.wiley.com/doi/full/10.1002/cjce.23747.

[56] A. Weibel, R. Bouchet, F. Boulch, and P. Knauth, "The big problem of small particles: A comparison of methods for determination of particle size in nanocrystalline anatase powders", *Chemistry of Materials*, vol. 17, pp. 2378–2385, 9 May 2005, ISSN: 08974756. DOI: 10.1021/CM0403762.

[57] K. O'Connell and J. R. Regalbuto, "High sensitivity silicon slit detectors for 1 nm powder xrd size detection limit", *Catalysis Letters*, vol. 145, pp. 777–783, 3 Mar. 2015, ISSN: 1572879X. DOI: 10.1007/S10562-015-1479-6. [Online]. Available: https://link.springer.com/article/10.1007/s10562-015-1479-6.

[58] J. I. Goldstein, D. E. Newbury, P. Echlin, D. C. Joy, C. E. Lyman, E. Lifshin, L. Sawyer, and J. R. Michael, "Special topics in scanning electron microscopy", *Scanning Electron Microscopy and X-ray Microanalysis*, pp. 195–270, 2003. DOI: 10.1007/978-1-4615-0215-9_5. [Online]. Available: https://link.springer.com/chapter/10.1007/978-1-4615-0215-9_5.

[59] K. Charles, "Introduction to solid state physics", vol. 8, p. 567, 2004. [Online]. Available: https://www.wiley.com/en-us/Introduction+to+Solid+State+Physics%2C+8th+Edition-p-9780471415268.

[60] R. F. Egerton, "Physical principles of electron microscopy: An introduction to tem, sem, and aem", *Physical Principles of Electron Microscopy: An Introduction to TEM, SEM, and AEM*, pp. 1–202, 2005. DOI: 10.1007/B136495/COVER.

[61] L. Reimer, "Scanning electron microscopy: Physics of image formation and microanalysis, second edition", *Measurement Science and Technology*, vol. 11, p. 1826, 12 Dec. 2000, ISSN: 0957-0233. DOI: 10.1088/0957-0233/11/12/703. [Online]. Available: https://iopscience.iop.org/article/10.1088/0957-0233/11/12/703.

[62] O. C. Wells, "Penetration effect at sharp edges in the scanning electron microscope", *Scanning*, vol. 1, pp. 58–60, 1 Jan. 1978, ISSN: 1932-8745. DOI: 10.1002/SCA.4950010106. [Online]. Available: https://onlinelibrary.wiley.com/doi/full/10.1002/sca.4950010106.

[63] A. J. Bard, L. R. Faulkner, and H. S. White, "Electrochemical methods: Fundamentals and applications, 3rd edition", *Transition Metal Chemistry*, vol. 48, pp. 433–436, 6 Dec. 2001, ISSN: 0340-4285. DOI: 10.1007/S11243-023-00555-6.

[64] W. Schmickler and E. Santos, "Interfacial electrochemistry", 2010. DOI: 10.1007/978-3-642-04937-8. [Online]. Available: https://link.springer.com/book/10.1007/978-3-642-04937-8.

[65] J. B. Goodenough and K. S. Park, "The li-ion rechargeable battery: A perspective", *Journal of the American Chemical Society*, vol. 135, pp. 1167–1176, 4 Jan. 2013, ISSN: 00027863. DOI: 10.1021/JA3091438. [Online]. Available: https://pubs.acs.org/doi/abs/10.1021/ja3091438.

[66] R. Compton and C. Banks, "Understanding voltammetry", 2007. [Online]. Available: https://www.worldscientific.com/doi/abs/10.1142/9781800615984_0005.

[67] F. Harnisch and S. Freguia, "A basic tutorial on cyclic voltammetry for the investigation of electroactive microbial biofilms", *Chemistry – An Asian Journal*, vol. 7, pp. 466–475, 3 Mar. 2012, ISSN: 1861-471X. DOI: 10.1002/ASIA.201100740. [Online]. Available: https://onlinelibrary.wiley.com/doi/full/10.1002/asia.201100740.

[68] N. Elgrishi, K. J. Rountree, B. D. McCarthy, E. S. Rountree, T. T. Eisenhart, and J. L. Dempsey, "A practical beginner's guide to cyclic voltammetry", *Journal of Chemical Education*, vol. 95, pp. 197–206, 2 Feb. 2018, ISSN: 19381328. DOI: 10.1021/ACS.JCHEMED.7B00361. [Online]. Available: https://pubs.acs.org/doi/full/10.1021/acs.jchemed.7b00361.

[69] E. Laviron, "General expression of the linear potential sweep voltammogram in the case of diffusionless electrochemical systems", *Journal of Electroanalytical Chemistry and Interfacial Electrochemistry*, vol. 101, pp. 19–28, 1 Jul. 1979, ISSN: 0022-0728. DOI: 10.1016/S0022-0728(79)80075-3.

[70] K. Ariyoshi and S. Hiroshima, "Chronoamperometric analyses of lithium insertion/extraction kinetics of lithium nickel manganese oxide using the diluted electrode method", *Electrochimica Acta*, vol. 487, p. 144 192, May 2024, ISSN: 0013-4686. DOI: 10.1016/J.ELECTACTA.2024.144192.

[71] F. G. Cottrell, "Der reststrom bei galvanischer polarisation, betrachtet als ein diffusionsproblem", *Zeitschrift für Physikalische Chemie*, vol. 42U, pp. 385–431, 1 Oct. 1903, ISSN: 2196-7156. DOI: 10.1515/ZPCH-1903-4229. [Online]. Available: https://www.degruyterbrill.com/document/doi/10.1515/zpch-1903-4229/html.

[72] J. Xiao, Q. Li, Y. Bi, M. Cai, B. Dunn, T. Glossmann, J. Liu, T. Osaka, R. Sugiura, B. Wu, J. Yang, J. G. Zhang, and M. S. Whittingham, "Understanding and applying coulombic efficiency in lithium metal batteries", *Nature Energy 2020 5:8*, vol. 5, pp. 561–568, 8 Jun. 2020, ISSN: 2058-7546. DOI: 10.1038/s41560-020-0648-z. [Online]. Available: https://www.nature.com/articles/s41560-020-0648-z.

[73] X. Liu, Y. Li, X. Jiang, and K. Xu, "Lifespan prediction of li-ion batteries in electrical vehicles by applying coulombic efficiency: From anode material to battery cell to vehicle application", *Sustainable Energy & Fuels*, vol. 8, pp. 621–630, 3 Jan. 2024, ISSN: 2398-4902. DOI: 10.1039/D3SE01455J. [Online]. Available: https://pubs.rsc.org/en/content/articlehtml/2024/se/d3se01455j.

[74] N. Meddings, M. Heinrich, F. Overney, J. S. Lee, V. Ruiz, E. Napolitano, S. Seitz, G. Hinds, R. Raccichini, M. Gaberšček, and J. Park, "Application of electrochemical impedance spectroscopy to commercial li-ion cells: A review", *Journal of*

Power Sources, vol. 480, p. 228 742, Dec. 2020, ISSN: 0378-7753. DOI: 10.1016/J.JPOWSOUR.2020.228742.

[75] S. Wang, J. Zhang, O. Gharbi, V. Vivier, M. Gao, and M. E. Orazem, "Electrochemical impedance spectroscopy", *Nature Reviews Methods Primers 2021 1:1*, vol. 1, pp. 1–21, 1 Jun. 2022, ISSN: 2662-8449. DOI: 10.1038/s43586-021-00039-w. [Online]. Available: https://www.nature.com/articles/s43586-021-00039-w.

[76] E. Barsoukov and J. R. Macdonald, *Impedance Spectroscopy: Theory, Experiment, and Applications*. American Chemical Society, Sep. 2005, vol. 127, pp. 12 431–12 431. DOI: 10.1021/JA0597420. [Online]. Available: https://pubs.acs.org/doi/abs/10.1021/ja059742o.

[77] B. EIS, *Why use electrochemical impedance spectroscopy (eis) for battery research? - biologic learning center*, 2025. [Online]. Available: https://www.biologic.net/topics/why-use-electrochemical-impedance-spectroscopy-for-battery-research/.

[78] W. Choi, H. C. Shin, J. M. Kim, J. Y. Choi, and W. S. Yoon, "Modeling and applications of electrochemical impedance spectroscopy (eis) for lithium-ion batteries", *Journal of Electrochemical Science and Technology*, vol. 11, pp. 1–13, 1 Feb. 2020, ISSN: 22889221. DOI: 10.33961/JECST.2019.00528.

[79] B. VMPPotentiostat, *Biologic - vmp-3e multichannel potentiostat*, 2025. [Online]. Available: https://www.biologic.net/products/vmp-3e-potentiostat/.

[80] B. VSPPotentiostat, *Biologic - vsp potentiostat*, 2025. [Online]. Available: https://www.biologic.net/products/vsp-potentiostat/.

[81] B. BatteryCyclers, *Biologic - discover battery cyclers*, 2025. [Online]. Available: https://www.biologic.net/discover-battery-cyclers/.

[82] B. EC-LabSoftware, *Biologic - ec-lab® software*, 2025. [Online]. Available: https://www.biologic.net/softwares/ec-lab-software/.

[83] T. Elisa, "Präparation und elektrochemische charakterisierung von neuartigen elektrodenmaterialien für lithium-ionen-batterien", Ph.D. dissertation, Heidelberg Universität, 2014.

[84] E.-C. ECCOpto10, *El-cell ecc-opto-10*, 2025. [Online]. Available: https://www.el-cell.com/products/test-cells/optical-test-cells/ecc-opto-10/.

[85] K. GmbH, *Kit – campus transfer*, 2025. [Online]. Available: https://kit-campus-transfer.de/.

[86] E.-C. P. Cell, *Pat series test cells | el-cell*, 2024. [Online]. Available: https://www.el-cell.com/pat-series/pat-test-cells/.

[87] V. Murray, D. S. Hall, and J. R. Dahn, "A guide to full coin cell making for academic researchers", *Journal of The Electrochemical Society*, vol. 166, A329–A333, 2 Jan. 2019, ISSN: 0013-4651. DOI: 10.1149/2.1171902JES. [Online]. Available: https://iopscience.iop.org/article/10.1149/2.1171902jes.

[88] Z. Xue, D. Guan, J. Zeng, Y. Cao, Z. Peng, G. Hu, and K. Du, "Research on the assembly process of full coin cells: Key factors affecting data reliability", *Ionics*, vol. 29, pp. 5285–5293, 12 Dec. 2023, ISSN: 18620760. DOI: 10.1007/S11581-023-05225-2. [Online]. Available: https://link.springer.com/article/10.1007/s11581-023-05225-2.

[89] S. Klink, E. Madej, E. Ventosa, A. Lindner, W. Schuhmann, and F. L. Mantia, "The importance of cell geometry for electrochemical impedance spectroscopy in three-electrode lithium ion battery test cells", *Electrochemistry Communications*, vol. 22, pp. 120–123, 1 Aug. 2012, ISSN: 1388-2481. DOI: 10.1016/J.ELECOM.2012.06.010.

[90] E.-C. P. core, "Pat-core insulation sleeve with built-in separator and optional reference electrode and current collectors", Tech. Rep., 2024. [Online]. Available: https://www.el-cell.com/pat-series/the-pat-core-concept/.

[91] K. Xu, "Nonaqueous liquid electrolytes for lithium-based rechargeable batteries", *Chemical Reviews*, vol. 104, pp. 4303–4417, 10 Oct. 2004, ISSN: 00092665. DOI: 10.1021/CR030203G. [Online]. Available: https://pubs.acs.org/doi/abs/10.1021/cr030203g.

[92] D. Aurbach, "Review of selected electrode–solution interactions which determine the performance of li and li ion batteries", *Journal of Power Sources*, vol. 89, pp. 206–218, 2 Aug. 2000, ISSN: 0378-7753. DOI: 10.1016/S0378-7753(00)00431-6.

[93] M. Dahbi, F. Ghamouss, F. Tran-Van, D. Lemordant, and M. Anouti, "Comparative study of ec/dmc litfsi and lipf6 electrolytes for electrochemical storage", *Journal of Power Sources*, vol. 196, pp. 9743–9750, 22 Nov. 2011, ISSN: 0378-7753. DOI: 10.1016/J.JPOWSOUR.2011.07.071.

[94] L. Péter and J. Arai, "Anodic dissolution of aluminium in organic electrolytes containing perfluoroalkylsulfonyl imides", *Journal of Applied Electrochemistry*, vol. 29, pp. 1053–1061, 9 1999, ISSN: 0021891X. DOI: 10.1023/A:1003573430989. [Online]. Available: https://link.springer.com/article/10.1023/A:1003573430989.

[95] B. Han, J. Zhao, Z. Luo, F. Cai, Z. Yuan, and H. Zeng, "Energy storage research of metal halide perovskites for rechargeable batteries", *Nano Energy*, vol. 115, p. 108 646, Oct. 2023, ISSN: 2211-2855. DOI: 10.1016/J.NANOEN.2023.108646.

[96] H. Liang, X. Zuo, L. Zhang, W. Huang, Q. Chen, T. Zhu, J. Liu, and J. Nan, "Nonflammable litfsi-ethylene carbonate/1,2-dimethoxyethane electrolyte for high-safety li-ion batteries", *Journal of The Electrochemical Society*, vol. 167, p. 090 520, 9 Apr. 2020, ISSN: 1945-7111. DOI: 10.1149/1945-7111/AB8803. [Online]. Available: https://iopscience.iop.org/article/10.1149/1945-7111/ab8803.

[97] X. Yao, N. Huang, F. Han, Q. Zhang, H. Wan, J. P. Mwizerwa, C. Wang, and X. Xu, "High-performance all-solid-state lithium–sulfur batteries enabled by amorphous sulfur-coated reduced graphene oxide cathodes", *Advanced Energy Materials*, vol. 7, p. 1 602 923, 17 Sep. 2017, ISSN: 1614-6840. DOI: 10.1002/AENM.201602923. [Online]. Available: https://onlinelibrary.wiley.com/doi/full/10.1002/aenm.201602923.

[98] E. Peled, "The electrochemical behavior of alkali and alkaline earth metals in nonaqueous battery systems—the solid electrolyte interphase model", *Journal of The Electrochemical Society*, vol. 126, pp. 2047–2051, 12 Dec. 1979, ISSN: 0013-4651. DOI: 10.1149/1.2128859. [Online]. Available: https://iopscience.iop.org/article/10.1149/1.2128859.

[99] A. Mathieson, M. Rahil, Y. Zhang, W. M. Dose, J. T. Lee, F. Deschler, S. Ahmad, and M. D. Volder, "Ruddlesden popper 2d perovskites as li-ion battery electrodes", *Materials Advances*, vol. 2, pp. 3370–3377, 10 May 2021, ISSN: 2633-5409. DOI: 10.1039/D1MA00020A. [Online]. Available: https://pubs.rsc.org/en/content/articlehtml/2021/ma/d1ma00020a.

[100] D. T. Hallinan and N. P. Balsara, "Polymer electrolytes", *Annual Review of Materials Research*, vol. 43, pp. 503–525, Volume 43, 2013 Jul. 2013, ISSN: 15317331. DOI: 10.1146/annurev-matsci-071312-121705. [Online]. Available: https://www.annualreviews.org/content/journals/10.1146/annurev-matsci-071312-121705.

[101] FlukeGmbH, *Mini-infrarotthermometer | ir-thermometer fluke 62 max | fluke*, 2025. [Online]. Available: https://www.fluke.com/de-de/produkt/temperaturmessung/ir-thermometer/fluke-62-max.

[102] X. Lu, G. J. Lian, J. Parker, R. Ge, M. K. Sadan, R. M. Smith, and D. Cumming, "Effect of carbon blacks on electrical conduction and conductive binder do-

main of next-generation lithium-ion batteries", *Journal of Power Sources*, vol. 592, p. 233 916, Feb. 2024, ISSN: 0378-7753. DOI: 10.1016/J.JPOWSOUR.2023.233916.

[103] P. M. Attia, S. Das, S. J. Harris, M. Z. Bazant, and W. C. Chueh, "Electrochemical kinetics of sei growth on carbon black: Part i. experiments", *Journal of The Electrochemical Society*, vol. 166, E97–E106, 4 Feb. 2019, ISSN: 0013-4651. DOI: 10.1149/2.0231904JES. [Online]. Available: https://iopscience.iop.org/article/10.1149/2.0231904jes.

[104] M. P. Bondarde, R. Jain, J. S. Sohn, K. D. Lokhande, M. A. Bhakare, P. S. Dhumal, and S. Some, "Carbon-based anode materials for lithium-ion batteries", *Lithium-Sulfur Batteries: Materials, Challenges and Applications*, pp. 521–545, Jan. 2022. DOI: 10.1016/B978-0-323-91934-0.00004-1.

[105] J. R. Dahn, T. Zheng, Y. Liu, and J. S. Xue, "Mechanisms for lithium insertion in carbonaceous materials", *Science*, vol. 270, pp. 590–593, 5236 Oct. 1995, ISSN: 0036-8075. DOI: 10.1126/SCIENCE.270.5236.590. [Online]. Available: https://www.science.org/doi/10.1126/science.270.5236.590.

[106] M. Endo, C. Kim, K. Nishimura, T. Fujino, and K. Miyashita, "Recent development of carbon materials for li ion batteries", *Carbon*, vol. 38, pp. 183–197, 2 Jan. 2000, ISSN: 0008-6223. DOI: 10.1016/S0008-6223(99)00141-4.

[107] J. Y. Zhang, L. B. Kong, L. Z. Zhan, J. Tang, H. Zhan, Y. H. Zhou, and C. M. Zhan, "Sulfides organic polymer: Novel cathode active material for rechargeable lithium batteries", *Journal of Power Sources*, vol. 168, pp. 278–281, 1 May 2007, ISSN: 0378-7753. DOI: 10.1016/J.JPOWSOUR.2007.02.043.

[108] T. Janoschka, M. D. Hager, and U. S. Schubert, "Powering up the future: Radical polymers for battery applications", *Advanced Materials*, vol. 24, pp. 6397–6409, 48 Dec. 2012, ISSN: 1521-4095. DOI: 10.1002/ADMA.201203119. [Online]. Available: https://onlinelibrary.wiley.com/doi/full/10.1002/adma.201203119.

[109] H. Nishide and K. Oyaizu, "Toward flexible batteries", *Science*, vol. 319, pp. 737–738, 5864 Feb. 2008, ISSN: 00368075. DOI: 10.1126/SCIENCE.1151831. [Online]. Available: https://www.science.org/doi/10.1126/science.1151831.

[110] A. Gandini and T. M. Lacerda, "From monomers to polymers from renewable resources: Recent advances", *Progress in Polymer Science*, vol. 48, pp. 1–39, Sep. 2015, ISSN: 0079-6700. DOI: 10.1016/J.PROGPOLYMSCI.2014.11.002.

[111] H. Shirakawa, E. J. Louis, A. G. MacDiarmid, C. K. Chiang, and A. J. Heeger, "Synthesis of electrically conducting organic polymers: Halogen derivatives of polyacetylene, (ch) x", *Journal of the Chemical Society, Chemical Communications*, vol. 0, pp. 578–580, 16 Jan. 1977, ISSN: 00224936. DOI: 10.1039/C39770000578. [Online]. Available: https://pubs.rsc.org/en/content/articlelanding/1977/c3/c39770000578.

[112] P. Novák, K. Müller, K. S. Santhanam, and O. Haas, "Electrochemically active polymers for rechargeable batteries", *Chemical Reviews*, vol. 97, pp. 207–281, 1 1997, ISSN: 00092665. DOI: 10.1021/CR9411810. [Online]. Available: https://pubs.acs.org/doi/full/10.1021/cr941181o.

[113] H.-K. Song, G. Tayhas, R. Palmore, and G. T. R. Palmore, "Redox-active polypyrrole: Toward polymer-based batteries", *research.brown.eduHK Song, GTR Palmore-Advanced Materials, 2006•research.brown.edu*, vol. 18, pp. 1764–1768, 13 Jul. 2006. DOI: 10.1002/adma.200600375. [Online]. Available: https://research.brown.edu/publications/1138722377.pdf.

[114] A. Moliton and R. C. Hiorns, "Review of electronic and optical properties of semiconducting π-conjugated polymers: Applications in optoelectronics", *Polymer International*, vol. 53, pp. 1397–1412, 10 Oct. 2004, ISSN: 1097-0126. DOI: 10.1002/PI.1587. [Online]. Available: https://onlinelibrary.wiley.com/doi/full/10.1002/pi.1587.

[115] J. Heinze, B. A. Frontana-Uribe, and S. Ludwigs, "Electrochemistry of conducting polymers-persistent models and new concepts", *Chemical Reviews*, vol. 110, pp. 4724–4771, 8 Aug. 2010, ISSN: 00092665. DOI: 10.1021/CR900226K. [Online]. Available: https://pubs.acs.org/doi/full/10.1021/cr900226k.

[116] M. D. Levi and D. Aurbach, "A short review on the strategy towards development of π-conjugated polymers with highly reversible p- and n-doping", *Journal of Power Sources*, vol. 180, pp. 902–908, 2 Jun. 2008, ISSN: 0378-7753. DOI: 10.1016/J.JPOWSOUR.2007.08.080.

[117] G. Nyström, A. Razaq, M. Strømme, L. Nyholm, and A. Mihranyan, "Ultrafast all-polymer paper-based batteries", *Nano Letters*, vol. 9, pp. 3635–3639, 10 Oct. 2009, ISSN: 15306984. DOI: 10.1021/NL901852H. [Online]. Available: https://pubs.acs.org/doi/full/10.1021/nl901852h.

[118] A. Mohammadi, O. Inganäs, and I. Lundström, "Properties of polypyrrole-electrolyte-polypyrrole cells", *Journal of The Electrochemical Society*, vol. 133, pp. 947–949,

5 May 1986, ISSN: 0013-4651. DOI: 10.1149/1.2108770/XML. [Online]. Available: https://iopscience.iop.org/article/10.1149/1.2108770.

[119] H. Manjunatha, G. S. Suresh, and T. V. Venkatesha, "Electrode materials for aqueous rechargeable lithium batteries", *Journal of Solid State Electrochemistry*, vol. 15, pp. 431–445, 3 Mar. 2011, ISSN: 14328488. DOI: 10.1007/S10008-010-1117-6. [Online]. Available: https://link.springer.com/article/10.1007/s10008-010-1117-6.

[120] G. J. Wang, L. C. Yang, Q. T. Qu, B. Wang, Y. P. Wu, and R. Holze, "An aqueous rechargeable lithium battery based on doping and intercalation mechanisms", *Journal of Solid State Electrochemistry*, vol. 14, pp. 865–869, 5 May 2009, ISSN: 14328488. DOI: 10.1007/S10008-009-0869-3. [Online]. Available: https://link.springer.com/article/10.1007/s10008-009-0869-3.

[121] M. Zhou, J. Qian, X. Ai, and H. Yang, "Redox-active fe(cn){sub 6}{sup 4-}-doped conducting polymers with greatly enhanced capacity as cathode materials for li-ion batteries", *Advanced Materials (Weinheim)*, vol. 23, pp. 4913–4917, 42 Nov. 2011, ISSN: 09359648. DOI: 10.1002/ADMA.201102867.

[122] K. S. Park, S. B. Schougaard, and J. B. Goodenough, "Conducting-polymer/iron-redox- couple composite cathodes for lithium secondary batteries", *Advanced Materials*, vol. 19, pp. 848–851, 6 Mar. 2007, ISSN: 1521-4095. DOI: 10.1002/ADMA.200600369. [Online]. Available: https://onlinelibrary.wiley.com/doi/full/10.1002/adma.200600369.

[123] K. Kaneto, K. Yoshino, and Y. Inuishi, "Characteristics of polythiophene battery.", *Japanese Journal of Applied Physics, Part 2: Letters*, vol. 22, pp. 567–568, 9 Sep. 1983, ISSN: 0021-4922. DOI: 10.1143/JJAP.22.L567. [Online]. Available: https://iopscience.iop.org/article/10.1143/JJAP.22.L567.

[124] C. Y. Wang, G. Tsekouras, P. Wagner, S. Gambhir, C. O. Too, D. Officer, and G. G. Wallace, "Functionalised polyterthiophenes as anode materials in polymer/polymer batteries", *Synthetic Metals*, vol. 160, pp. 76–82, 1-2 Jan. 2010, ISSN: 0379-6779. DOI: 10.1016/J.SYNTHMET.2009.10.001.

[125] J. Tang, L. Kong, J. Zhang, L. Zhan, H. Zhan, Y. Zhou, and C. Zhan, "Solvent-free, oxidatively prepared polythiophene: High specific capacity as a cathode active material for lithium batteries", *Reactive and Functional Polymers*, vol. 68, pp. 1408–1413, 9 Sep. 2008, ISSN: 1381-5148. DOI: 10.1016/J.REACTFUNCTPOLYM.2008.07.001.

[126] T. K. Kunz and M. O. Wolf, "Electrodeposition and properties of tempo functionalized polythiophene thin films", *Polymer Chemistry*, vol. 2, pp. 640–644, 3 Feb. 2011, ISSN: 17599954. DOI: 10.1039/C0PY00308E. [Online]. Available: https://pubs.rsc.org/en/content/articlehtml/2011/py/c0py00308e.

[127] S. N. Patel, A. E. Javier, G. M. Stone, S. A. Mullin, and N. P. Balsara, "Simultaneous conduction of electronic charge and lithium ions in block copolymers", *ACS Nano*, vol. 6, pp. 1589–1600, 2 Feb. 2012, ISSN: 19360851. DOI: 10.1021/NN2045664.

[128] R. D. Surville, M. Jozefowicz, L. T. Yu, J. Pepichon, and R. Buvet, "Electrochemical chains using protolytic organic semiconductors", *Electrochimica Acta*, vol. 13, pp. 1451–1458, 6 Jun. 1968, ISSN: 0013-4686. DOI: 10.1016/0013-4686(68)80071-4.

[129] A. Vlad, K. Arnould, B. Ernould, L. Sieuw, J. Rolland, and J. F. Gohy, "Exploring the potential of polymer battery cathodes with electrically conductive molecular backbone", *Journal of Materials Chemistry A*, vol. 3, pp. 11 189–11 193, 21 May 2015, ISSN: 2050-7496. DOI: 10.1039/C5TA01500F. [Online]. Available: https://pubs.rsc.org/en/content/articlehtml/2015/ta/c5ta01500f.

[130] S. C. Zhang, L. Zhang, W. K. Wang, and W. J. Xue, "A novel cathode material based on polyaniline used for lithium/sulfur secondary battery", *Synthetic Metals*, vol. 160, pp. 2041–2044, 17-18 Sep. 2010, ISSN: 0379-6779. DOI: 10.1016/J.SYNTHMET.2010.07.029.

[131] L. Li, Y. Sun, H. Bao, X. Li, and G. Wang, "Synthesis and characterization of a poly(aniline-based disulfide)/diisocyanate-modified graphite oxide hybrid by a grafting technique", *European Polymer Journal*, vol. 47, pp. 1630–1635, 8 Aug. 2011, ISSN: 0014-3057. DOI: 10.1016/J.EURPOLYMJ.2011.05.014.

[132] C. Su, L. Ji, L. Xu, X. Zhu, H. He, Y. Lv, M. Ouyang, and C. Zhang, "A novel ferrocene-containing aniline copolymer: Its synthesis and electrochemical performance", *RSC Advances*, vol. 5, pp. 14 053–14 060, 18 Jan. 2015, ISSN: 2046-2069. DOI: 10.1039/C4RA12476F. [Online]. Available: https://pubs.rsc.org/en/content/articlehtml/2015/ra/c4ra12476f%20https://pubs.rsc.org/en/content/articlelanding/2015/ra/c4ra12476f.

[133] L. Huo and J. Hou, "Benzo[1,2-b:4,5-b]dithiophene -based conjugated polymers : Band gap and energy level control and their application in polymer solar cells", *Polymer Chemistry*, vol. 2, pp. 2453–2461, 11 Oct. 2011, ISSN: 17599962. DOI: 10.1039/C1PY00197C. [Online]. Available: https://pubs.rsc.org/en/content/articlehtml/2011/py/c1py00197c.

[134] L. Li, E. Liu, Y. Yang, H. Shen, Z. Huang, and X. Xiang, "Nitrogen-containing carbons prepared from polyaniline as anode materials for lithium secondary batteries", *Materials Letters*, vol. 64, pp. 2115–2117, 19 Oct. 2010, ISSN: 0167-577X. DOI: 10.1016/J.MATLET.2010.06.057.

[135] Z. Song, H. Zhan, and Y. Zhou, "Anthraquinone based polymer as high performance cathode material for rechargeable lithium batteries", *Chemical Communications*, pp. 448–450, 4 Jan. 2009, ISSN: 1364-548X. DOI: 10.1039/B814515F. [Online]. Available: https://pubs.rsc.org/en/content/articlehtml/2009/cc/b814515f.

[136] A. Li, Z. Rong, B. Yuan, F. Cheng, and W. Zhang, "Crosslinked polyimides as cathodes for lithium-ion batteries", *ACS Applied Energy Materials*, vol. 6, pp. 1862–1870, 3 Feb. 2023, ISSN: 25740962. DOI: 10.1021/ACSAEM.2C03758. [Online]. Available: https://pubs.acs.org/doi/full/10.1021/acsaem.2c03758.

[137] T. L. Gall, K. H. Reiman, M. C. Grossel, and J. R. Owen, "Poly(2,5-dihydroxy-1,4-benzoquinone-3,6-methylene): A new organic polymer as positive electrode material for rechargeable lithium batteries", *Journal of Power Sources*, vol. 119-121, pp. 316–320, Jun. 2003, ISSN: 0378-7753. DOI: 10.1016/S0378-7753(03)00167-8.

[138] Z. Song, T. Xu, M. L. Gordin, Y. B. Jiang, I. T. Bae, Q. Xiao, H. Zhan, J. Liu, and D. Wang, "Polymer-graphene nanocomposites as ultrafast-charge and -discharge cathodes for rechargeable lithium batteries", *Nano Letters*, vol. 12, pp. 2205–2211, 5 May 2012, ISSN: 15306984. DOI: 10.1021/NL2039666. [Online]. Available: https://pubs.acs.org/doi/full/10.1021/nl2039666.

[139] J. G. Wagenfeld, K. Al-Ali, S. Almheiri, A. F. Slavens, and N. Calvet, "Sustainable applications utilizing sulfur, a by-product from oil and gas industry: A state-of-the-art review", *Waste Management*, vol. 95, pp. 78–89, Jul. 2019, ISSN: 0956-053X. DOI: 10.1016/J.WASMAN.2019.06.002.

[140] F. Dong, C. Peng, H. Xu, Y. Zheng, H. Yao, J. Yang, and S. Zheng, "Lithiated sulfur-incorporated, polymeric cathode for durable lithium-sulfur batteries with promoted redox kinetics", *ACS nano*, vol. 15, pp. 20 287–20 299, 12 Dec. 2021, ISSN: 1936-086X. DOI: 10.1021/ACSNANO.1C08449. [Online]. Available: https://pubmed.ncbi.nlm.nih.gov/34817165/.

[141] S. Jia, R. Wang, F. Liu, H. Huo, J. Zhou, and L. Li, "One action, two benefits: Improving the performance of lithium–sulfur batteries with a poly(ionic liquid)", *Materials Advances*, vol. 5, pp. 3696–3705, 9 May 2024, ISSN: 26335409. DOI: 10.1039/D4MA00115J. [Online]. Available: https://pubs.rsc.org/en/content/articlehtml/2024/ma/d4ma00115j.

[142] G. G. Rodríguez-Calero, M. A. Lowe, S. E. Burkhardt, and H. D. Abruña, "Electrocatalysis of 2,5-dimercapto-1,3,5-thiadiazole by 3,4-ethylenedioxy-substituted conducting polymers", *Langmuir*, vol. 27, pp. 13 904–13 909, 22 Nov. 2011, ISSN: 07437463. DOI: 10.1021/LA202706S. [Online]. Available: https://pubs.acs.org/doi/full/10.1021/la202706s.

[143] Y. Kiya, O. Hatozaki, N. Oyama, and H. D. Abruña, "Kinetic studies for the electrocatalytic reduction of bis(2-mercapto-1,3,4- thiadiazoyl)-5,5-disulfide at a poly(3,4-ethylenedioxythiophene) film-modified electrode via rotating-disk electrode voltammetry", *Journal of Physical Chemistry C*, vol. 111, pp. 13 129–13 136, 35 Sep. 2007, ISSN: 19327447. DOI: 10.1021/JP073486F. [Online]. Available: https://pubs.acs.org/doi/full/10.1021/jp073486f.

[144] J. K. Feng, Y. L. Cao, X. P. Ai, and H. X. Yang, "Polytriphenylamine: A high power and high capacity cathode material for rechargeable lithium batteries", *Journal of Power Sources*, vol. 177, pp. 199–204, 1 Feb. 2008, ISSN: 0378-7753. DOI: 10.1016/J.JPOWSOUR.2007.10.086.

[145] C. Su, F. Yang, Y. Ye, L. Xu, L. Wang, and C. Zhang, "Poly[tris(thienylphenyl)-amine] derivatives as a performance-improved cathode material for lithium ion batteries", *Journal of The Electrochemical Society*, vol. 160, A2021–A2026, 11 Sep. 2013, ISSN: 0013-4651. DOI: 10.1149/2.043311JES. [Online]. Available: https://iopscience.iop.org/article/10.1149/2.043311jes.

[146] L. Zhu and X. Cao, "P-dopable poly(4-cyano)triphenylamine: A high voltage organic cathode for lithium ion batteries", *Materials Letters*, vol. 150, pp. 16–19, Jul. 2015, ISSN: 0167-577X. DOI: 10.1016/J.MATLET.2015.02.129.

[147] C. Steiner, J. Gebhardt, M. Ammon, Z. Yang, A. Heidenreich, N. Hammer, A. Görling, M. Kivala, and S. Maier, "Hierarchical on-surface synthesis and electronic structure of carbonyl-functionalized one- and two-dimensional covalent nanoarchitectures", *Nature Communications 2017 8:1*, vol. 8, pp. 1–11, 1 Mar. 2017, ISSN: 2041-1723. DOI: 10.1038/ncomms14765. [Online]. Available: https://www.nature.com/articles/ncomms14765.

[148] M. Bieri, S. Blankenburg, M. Kivala, C. A. Pignedoli, P. Ruffieux, K. Müllen, and R. Fasel, "Surface-supported 2d heterotriangulene polymers", *Chemical Communications*, vol. 47, pp. 10 239–10 241, 37 Sep. 2011, ISSN: 1364-548X. DOI: 10.1039/C1CC12490K. [Online]. Available: https://pubs.rsc.org/en/content/articlehtml/2011/cc/c1cc12490k.

[149] X. Wang, X. Zheng, X. Wang, Y. Qiu, Y. Li, C. Zhou, Y. Sui, Y. Li, and J. Ma, "One-electron oxidation of an organic molecule by b(c6f 5)3; isolation and structures of stable non- para -substituted triarylamine cation radical and bis(triarylamine) dication diradicaloid", *Journal of the American Chemical Society*, vol. 135, pp. 14 912–14 915, 40 Oct. 2013, ISSN: 15205126. DOI: 10.1021/JA407318H. [Online]. Available: https://pubs.acs.org/doi/abs/10.1021/ja407318h.

[150] M. Hirai, N. Tanaka, M. Sakai, and S. Yamaguchi, "Structurally constrained boron-, nitrogen-, silicon-, and phosphorus-centered polycyclic π-conjugated systems", *Chemical Reviews*, vol. 119, pp. 8291–8331, 14 Jul. 2019, ISSN: 15206890. DOI: 10.1021/ACS.CHEMREV.8B00637. [Online]. Available: https://pubs.acs.org/doi/abs/10.1021/acs.chemrev.8b00637.

[151] Y. Wang, T. Zhang, R. Duan, Y. Zhao, D. Su, Z. Liu, and C. Li, "A novel conjugated heterotriangulene polymer for high performance organic lithium-ion battery", *Dyes and Pigments*, vol. 191, p. 109 352, Jul. 2021, ISSN: 0143-7208. DOI: 10.1016/J.DYEPIG.2021.109352.

[152] K. Schmoltner, F. Schlütter, M. Kivala, M. Baumgarten, S. Winkler, R. Trattnig, N. Koch, A. Klug, E. J. List, and K. Müllen, "A heterotriangulene polymer for air-stable organic field-effect transistors", *Polymer Chemistry*, vol. 4, pp. 5337–5344, 20 Sep. 2013, ISSN: 1759-9962. DOI: 10.1039/C3PY00089C. [Online]. Available: https://pubs.rsc.org/en/content/articlehtml/2013/py/c3py00089c.

[153] T. A. Schaub, T. Mekelburg, P. O. Dral, M. Miehlich, F. Hampel, K. Meyer, and M. Kivala, "A spherically shielded triphenylamine and its persistent radical cation", *Chemistry – A European Journal*, vol. 26, pp. 3264–3269, 15 Mar. 2020, ISSN: 1521-3765. DOI: 10.1002/CHEM.202000355. [Online]. Available: https://onlinelibrary.wiley.com/doi/full/10.1002/chem.202000355.

[154] M. Krug, M. Wagner, T. A. Schaub, W. S. Zhang, C. M. Schüßlbauer, J. D. Ascherl, P. W. Münich, R. R. Schröder, F. Gröhn, P. O. Dral, M. Barbatti, D. M. Guldi, and M. Kivala, "The impact of aggregation on the photophysics of spiro-bridged heterotriangulenes", *Angewandte Chemie International Edition*, vol. 59, pp. 16 233–16 240, 37 Sep. 2020, ISSN: 1521-3773. DOI: 10.1002/ANIE.202003504. [Online]. Available: https://onlinelibrary.wiley.com/doi/full/10.1002/anie.202003504.

[155] A. Jocic, T. Wickenhäuser, S. Lindenthal, W. S. Zhang, J. Zaumseil, R. Schröder, R. Klingeler, and M. Kivala, "Redox-active, photoluminescent porous polymers based on spirofluorene-bridged n -heterotriangulenes and their feasibility as organic

cathode materials", *Chemical Science*, vol. 15, pp. 19 094–19 103, 45 Nov. 2024, ISSN: 20416539. DOI: 10.1039/D4SC04276J. [Online]. Available: https://pubs.rsc.org/en/content/articlehtml/2024/sc/d4sc04276j.

[156] A. Manthiram, S. H. Chung, and C. Zu, "Lithium–sulfur batteries: Progress and prospects", *Advanced Materials*, vol. 27, pp. 1980–2006, 12 Mar. 2015, ISSN: 1521-4095. DOI: 10.1002/ADMA.201405115. [Online]. Available: https://onlinelibrary.wiley.com/doi/full/10.1002/adma.201405115.

[157] R. V. Noorden, "The rechargeable revolution: A better battery", *Nature*, vol. 507, pp. 26–28, 7490 2014, ISSN: 14764687. DOI: 10.1038/507026A.

[158] X. Ji, K. T. Lee, and L. F. Nazar, "A highly ordered nanostructured carbon–sulphur cathode for lithium–sulphur batteries", *Nature Materials 2009 8:6*, vol. 8, pp. 500–506, 6 May 2009, ISSN: 1476-4660. DOI: 10.1038/nmat2460. [Online]. Available: https://www.nature.com/articles/nmat2460.

[159] G. He, X. Ji, and L. Nazar, "High c rate li-s cathodes: Sulfur imbibed bimodal porous carbons", *Energy & Environmental Science*, vol. 4, pp. 2878–2883, 8 Aug. 2011, ISSN: 1754-5706. DOI: 10.1039/C1EE01219C. [Online]. Available: https://pubs.rsc.org/en/content/articlehtml/2011/ee/c1ee01219c.

[160] P. G. Bruce, S. A. Freunberger, L. J. Hardwick, and J. M. Tarascon, "Li-o2 and li-s batteries with high energy storage", *Nature Materials 2011 11:1*, vol. 11, pp. 19–29, 1 Dec. 2011, ISSN: 1476-4660. DOI: 10.1038/nmat3191. [Online]. Available: https://www.nature.com/articles/nmat3191.

[161] D. Luo, M. Li, Q. Ma, G. Wen, H. Dou, B. Ren, Y. Liu, X. Wang, L. Shui, and Z. Chen, "Porous organic polymers for li-chemistry-based batteries: Functionalities and characterization studies", *Chemical Society Reviews*, vol. 51, pp. 2917–2938, 8 Apr. 2022, ISSN: 1460-4744. DOI: 10.1039/D1CS01014J. [Online]. Available: https://pubs.rsc.org/en/content/articlehtml/2022/cs/d1cs01014j.

[162] H. Yang, S. Zhang, L. Han, Z. Zhang, Z. Xue, J. Gao, Y. Li, C. Huang, Y. Yi, H. Liu, and Y. Li, "High conductive two-dimensional covalent organic framework for lithium storage with large capacity", *ACS Applied Materials and Interfaces*, vol. 8, pp. 5366–5375, 8 Mar. 2016, ISSN: 19448252. DOI: 10.1021/ACSAMI.5B12370. [Online]. Available: https://pubs.acs.org/doi/abs/10.1021/acsami.5b12370.

[163] L. Huang, Z. Yu, L. Wang, B. Qin, F. Cai, Z. Yuan, and Z. Luo, "Spiro-based triphenylamine molecule with steric structure as a cathode material for high-stable all organic lithium dual-ion batteries", *Journal of Energy Chemistry*, vol. 83, pp. 24–31, Aug. 2023, ISSN: 2095-4956. DOI: 10.1016/J.JECHEM.2023.04.018.

[164] W. Huang, T. Jia, G. Zhou, S. Chen, Q. Hou, Y. Wang, S. Luo, G. Shi, and B. Xu, "A triphenylamine-based polymer with anthraquinone side chain as cathode material in lithium ion batteries", *Electrochimica Acta*, vol. 283, pp. 1284–1290, Sep. 2018, ISSN: 0013-4686. DOI: 10.1016/J.ELECTACTA.2018.07.062.

[165] C. Zhang, X. Yang, W. Ren, Y. Wang, F. Su, and J. X. Jiang, "Microporous organic polymer-based lithium ion batteries with improved rate performance and energy density", *Journal of Power Sources*, vol. 317, pp. 49–56, Jun. 2016, ISSN: 0378-7753. DOI: 10.1016/J.JPOWSOUR.2016.03.080.

[166] C. Su, B. Han, J. Ma, and L. Xu, "A novel anthraquinone-containing poly(triphenylamine) derivative: Preparation and electrochemical performance as cathode for lithium-ion batteries", *ChemElectroChem*, vol. 7, pp. 4101–4107, 19 Oct. 2020, ISSN: 2196-0216. DOI: 10.1002/CELC.202001084. [Online]. Available: https://onlinelibrary.wiley.com/doi/full/10.1002/celc.202001084.

[167] Z. Chen, C. Su, X. Zhu, R. Xu, L. Xu, and C. Zhang, "Micro-/mesoporous conjugated polymer based on star-shaped triazine-functional triphenylamine framework as the performance-improved cathode of li-organic battery", *Journal of Polymer Science Part A: Polymer Chemistry*, vol. 56, pp. 2574–2583, 22 Nov. 2018, ISSN: 1099-0518. DOI: 10.1002/POLA.29239. [Online]. Available: https://onlinelibrary.wiley.com/doi/full/10.1002/pola.29239.

[168] S. Zhang, K. Ueno, K. Dokko, and M. Watanabe, "Recent advances in electrolytes for lithium–sulfur batteries", *Advanced Energy Materials*, vol. 5, p. 1 500 117, 16 Aug. 2015, ISSN: 1614-6840. DOI: 10.1002/AENM.201500117. [Online]. Available: https://onlinelibrary.wiley.com/doi/full/10.1002/aenm.201500117.

[169] F. Wu, Q. Zhu, R. Chen, N. Chen, Y. Chen, Y. Ye, J. Qian, and L. Li, "Ionic liquid-based electrolyte with binary lithium salts for high performance lithium–sulfur batteries", *Journal of Power Sources*, vol. 296, pp. 10–17, Nov. 2015, ISSN: 0378-7753. DOI: 10.1016/J.JPOWSOUR.2015.07.033.

[170] A. Gupta, A. Bhargav, and A. Manthiram, "Highly solvating electrolytes for lithium-sulfur batteries", *Advanced Energy Materials*, vol. 9, p. 1 803 096, 6 Feb. 2019, ISSN: 1614-6840. DOI: 10.1002/AENM.201803096. [Online]. Available: https://onlinelibrary.wiley.com/doi/full/10.1002/aenm.201803096.

[171] Y. He, S. Bi, C. Jiang, and J. Song, "Recent progress of sulfur cathodes and other components for flexible lithium–sulfur batteries", *Materials Today Sustainability*, vol. 19, p. 100 181, Nov. 2022, ISSN: 2589-2347. DOI: 10.1016/J.MTSUST.2022.100181.

[172] B. N. Olana, S. D. Lin, and B. J. Hwang, "In situ diffuse reflectance infrared fourier-transformed spectroscopy study of solid electrolyte interphase formation from lithium bis(trifluoromethanesulfonyl)imide in 1,2-dimethoxyethane and 1,3-dioxolane with and without lithium nitrate additive over lithium and copper metal anodes", *Electrochimica Acta*, vol. 416, p. 140 266, Jun. 2022, ISSN: 0013-4686. DOI: 10.1016/J.ELECTACTA.2022.140266.

[173] J. Kappler, S. V. Klostermann, P. L. Lange, M. Dyballa, L. Veith, T. Schleid, T. Weil, J. Kästner, and M. R. Buchmeiser, "Sulfur-composites derived from poly(acrylonitrile) and poly(vinylacetylene) – a comparative study on the role of pyridinic and thioamidic nitrogen", *Batteries & Supercaps*, vol. 6, e202200522, 3 Mar. 2023, ISSN: 2566-6223. DOI: 10.1002/BATT.202200522. [Online]. Available: https://onlinelibrary.wiley.com/doi/full/10.1002/batt.202200522.

[174] G. D. Donato, T. Ates, H. Adenusi, A. Varzi, M. A. Navarra, and S. Passerini, "Electrolyte measures to prevent polysulfide shuttle in lithium-sulfur batteries", *Batteries & Supercaps*, vol. 5, e202200097, 7 Jul. 2022, ISSN: 2566-6223. DOI: 10.1002/BATT.202200097. [Online]. Available: https://onlinelibrary.wiley.com/doi/full/10.1002/batt.202200097.

[175] M. Burgess, K. Hernández-Burgos, K. J. Cheng, J. S. Moore, and J. Rodríguez-López, "Impact of electrolyte composition on the reactivity of a redox active polymer studied through surface interrogation and ion-sensitive scanning electrochemical microscopy", *Analyst*, vol. 141, pp. 3842–3850, 12 Jun. 2016, ISSN: 1364-5528. DOI: 10.1039/C6AN00203J. [Online]. Available: https://pubs.rsc.org/en/content/articlehtml/2016/an/c6an00203j.

[176] A. Lee, M. Vörös, W. M. Dose, J. Niklas, O. Poluektov, R. D. Schaller, H. Iddir, V. A. Maroni, E. Lee, B. Ingram, L. A. Curtiss, and C. S. Johnson, "Photo-accelerated fast charging of lithium-ion batteries", *Nature Communications 2019 10:1*, vol. 10, pp. 1–7, 1 Oct. 2019, ISSN: 2041-1723. DOI: 10.1038/s41467-019-12863-6. [Online]. Available: https://www.nature.com/articles/s41467-019-12863-6.

[177] N. Mohamed and N. K. Allam, "Recent advances in the design of cathode materials for li-ion batteries", *RSC Advances*, vol. 10, pp. 21 662–21 685, 37 Jun. 2020, ISSN: 20462069. DOI: 10.1039/D0RA03314F. [Online]. Available: https://pubs.rsc.org/en/content/articlehtml/2020/ra/d0ra03314f.

[178] L. D. Dyer, B. S. Borie, and G. P. Smith, "Alkali metal-nickel oxides of the type mnio2", *Journal of the American Chemical Society*, vol. 76, pp. 1499–1503, 6 1954,

ISSN: 15205126. DOI: 10.1021/JA01635A012. [Online]. Available: https://pubs.acs.org/doi/pdf/10.1021/ja01635a012.

[179] D. D. MacNeil and J. R. Dahn, "The reaction of charged cathodes with nonaqueous solvents and electrolytes: I. li0.5coo2", *Journal of The Electrochemical Society*, vol. 148, A1205, 11 Sep. 2001, ISSN: 00134651. DOI: 10.1149/1.1407245. [Online]. Available: https://iopscience.iop.org/article/10.1149/1.1407245.

[180] J. R. Dahn, U. von Sacken, and C. A. Michal, "Structure and electrochemistry of li1±ynio2 and a new li2nio2 phase with the ni (oh)2 structure", *Solid State Ionics*, vol. 44, pp. 87–97, 1-2 Dec. 1990, ISSN: 0167-2738. DOI: 10.1016/0167-2738(90)90049-W.

[181] T. Ohzuku, A. Ueda, and M. Nagayama, "Electrochemistry and structural chemistry of linio2 (r3m) for 4 volt secondary lithium cells", *Journal of The Electrochemical Society*, vol. 140, pp. 1862–1870, 7 Jul. 1993, ISSN: 0013-4651. DOI: 10.1149/1.2220730. [Online]. Available: https://iopscience.iop.org/article/10.1149/1.2220730.

[182] X. Wu, Z. Zou, S. Li, and Q. Yang, "Solvothermal preparation of al/fe-doped v6o13 as cathode materials for lithium-ion batteries with enhanced electrochemical performance", *Journal of Electroanalytical Chemistry*, vol. 829, pp. 20–26, Nov. 2018, ISSN: 1572-6657. DOI: 10.1016/J.JELECHEM.2018.09.055.

[183] T. ting Lv, Z. guang Zou, Y. wei Li, S. yu Li, and Y. jiao Zhang, "Hydrothermal synthesis of high specific capacity al/na co-doped v6o13 cathode material for lithium-ion battery", *Journal of Electroanalytical Chemistry*, vol. 829, pp. 42–50, Nov. 2018, ISSN: 1572-6657. DOI: 10.1016/J.JELECHEM.2018.09.057.

[184] H. Jiang, H. Chen, Y. Wei, J. Zeng, H. Liu, Y. Zhang, and H. Wu, "Biotemplate-mediated structural engineering of rod-like v2o5 cathode materials for lithium-ion batteries", *Journal of Alloys and Compounds*, vol. 787, pp. 625–630, May 2019, ISSN: 0925-8388. DOI: 10.1016/J.JALLCOM.2019.02.118.

[185] H. Zhang, Y. Rong, W. Jia, H. Chai, and Y. Cao, "Simple solvent-free synthesis of rod-like cu-doped v2o5 for high storage capacity cathode materials of lithium ion batteries", *Journal of Alloys and Compounds*, vol. 802, pp. 139–145, Sep. 2019, ISSN: 0925-8388. DOI: 10.1016/J.JALLCOM.2019.06.192.

[186] J. Zeng, J. Huang, J. Liu, T. Xie, C. Peng, Y. Lu, P. Lu, R. Zhang, and J. Min, "Self-assembly of single layer v2o5 nanoribbon/graphene heterostructures as ultrahigh-performance cathode materials for lithium-ion batteries", *Carbon*, vol. 154, pp. 24–32, Dec. 2019, ISSN: 0008-6223. DOI: 10.1016/J.CARBON.2019.07.046.

[187] L. Zhu, P. Ge, L. Xie, Y. Miao, and X. Cao, "Doped-li1+xv3o8 as cathode materials for lithium-ion batteries: A mini review", *Electrochemistry Communications*, vol. 115, p. 106 722, Jun. 2020, ISSN: 1388-2481. DOI: 10.1016/J.ELECOM.2020.106722.

[188] L. Xiong, M. Sun, Y. Xu, X. Du, and X. Xiao, "Synthesis of carbon coated li2mno3 cathode material with enhanced rate capability for lithium-ion batteries", *Solid State Ionics*, vol. 325, pp. 170–175, Nov. 2018, ISSN: 0167-2738. DOI: 10.1016/J.SSI.2018.08.008.

[189] K. Zhang, L. Zhang, J. Liu, X. Wu, C. Zhou, W. Yan, C. Zhou, L. Fu, and Y. Wu, "Hollow microspherical layered xli2mno3·(1-x)linio2 (x=0.3–0.7) as cathode material for lithium–ion batteries", *Journal of Alloys and Compounds*, vol. 790, pp. 1034–1042, Jun. 2018, ISSN: 0925-8388. DOI: 10.1016/J.JALLCOM.2019.03.005.

[190] Q. Chang, A. Wei, W. Li, X. Bai, L. Zhang, R. He, and Z. Liu, "Structural and electrochemical characteristics of al2o3-modified lini0.5mn1.5o4 cathode materials for lithium-ion batteries", *Ceramics International*, vol. 45, pp. 5100–5110, 4 Mar. 2019, ISSN: 0272-8842. DOI: 10.1016/J.CERAMINT.2018.11.213.

[191] Z. Peng, K. Mu, Y. Cao, L. Xu, K. Du, and G. Hu, "Enhanced electrochemical performance of layered li-rich cathode materials for lithium ion batteries via aluminum and boron dual-doping", *Ceramics International*, vol. 45, pp. 4184–4192, 4 Mar. 2019, ISSN: 0272-8842. DOI: 10.1016/J.CERAMINT.2018.11.087.

[192] N. Rapulenyane, E. Ferg, and H. Luo, "High-performance li1.2mn0.6ni0.2o2 cathode materials prepared through a facile one-pot co-precipitation process for lithium ion batteries", *Journal of Alloys and Compounds*, vol. 762, pp. 272–281, Sep. 2018, ISSN: 0925-8388. DOI: 10.1016/J.JALLCOM.2018.05.207.

[193] W. Sun, Y. Li, K. Xie, S. Luo, G. Bai, X. Tan, and C. Zheng, "Constructing hierarchical urchin-like lini0.5mn1.5o4 hollow spheres with exposed {111} facets as advanced cathode material for lithium-ion batteries", *Nano Energy*, vol. 54, pp. 175–183, Dec. 2018, ISSN: 2211-2855. DOI: 10.1016/J.NANOEN.2018.10.006.

[194] F. A. Vasquez, J. E. Thomas, A. Visintin, and J. A. Calderón, "Limn1.8ni0.2o4 nanorods obtained from a novel route using a-mnooh precursor as cathode material for lithium-ion batteries", *Solid State Ionics*, vol. 320, pp. 339–346, Jul. 2018, ISSN: 0167-2738. DOI: 10.1016/J.SSI.2018.03.013.

[195] D. Huang, Y. Shi, A. P. Tornheim, J. Bareño, Z. Chen, Z. Zhang, A. Burrell, and H. Luo, "Nanoscale lini0.5co0.2mn0.3o2 cathode materials for lithium ion batteries via a polymer-assisted chemical solution method", *Applied Materials Today*, vol. 16, pp. 342–350, Sep. 2019, ISSN: 2352-9407. DOI: 10.1016/J.APMT.2019.06.008.

[196] M. M. Thackeray, A. de Kock, M. H. Rossouw, D. Liles, R. Bittihn, and D. Hoge, "Spinel electrodes from the li-mn-o system for rechargeable lithium battery applications", *Journal of The Electrochemical Society*, vol. 139, pp. 363–366, 2 Feb. 1992, ISSN: 0013-4651. DOI: 10.1149/1.2069222. [Online]. Available: https://iopscience.iop.org/article/10.1149/1.2069222.

[197] M. M. Thackeray, "Structural considerations of layered and spinel lithiated oxides for lithium ion batteries", *Journal of The Electrochemical Society*, vol. 142, pp. 2558–2563, 8 Aug. 1995, ISSN: 0013-4651. DOI: 10.1149/1.2050053. [Online]. Available: https://iopscience.iop.org/article/10.1149/1.2050053.

[198] M. O. Filsø, M. J. Turner, G. V. Gibbs, S. Adams, M. A. Spackman, and B. B. Iversen, "Visualizing lithium-ion migration pathways in battery materials", *Chemistry – A European Journal*, vol. 19, pp. 15 535–15 544, 46 Nov. 2013, ISSN: 1521-3765. DOI: 10.1002/CHEM.201301504. [Online]. Available: https://onlinelibrary.wiley.com/doi/full/10.1002/chem.201301504.

[199] K. Mukai, T. Uyama, and I. Yamada, "Structural and electrochemical analyses on the transformation of cafe 2 o 4 -type limn 2 o 4 from spinel-type limn 2 o 4", *ACS Omega*, vol. 4, pp. 6459–6467, 4 Apr. 2019, ISSN: 24701343. DOI: 10.1021/ACSOMEGA.9B00588. [Online]. Available: https://pubs.acs.org/doi/full/10.1021/acsomega.9b00588.

[200] A. M. Hashem, S. M. Abbas, X. Hou, A. E. Eid, and A. E. Abdel-Ghany, "Facile one step synthesis method of spinel limn2o4 cathode material for lithium batteries", *Heliyon*, vol. 5, 7 Jul. 2019, ISSN: 24058440. DOI: 10.1016/J.HELIYON.2019.E02027. [Online]. Available: https://www.cell.com/action/showFullText?pii=S2405844019356877.

[201] Z. Cai, Y. Ma, X. Huang, X. Yan, Z. Yu, S. Zhang, G. Song, Y. Xu, C. Wen, and W. Yang, "High electrochemical stability al-doped spinel limn2o4 cathode material for li-ion batteries", *Journal of Energy Storage*, vol. 27, p. 101 036, Feb. 2020, ISSN: 2352-152X. DOI: 10.1016/J.EST.2019.101036.

[202] D. Ahn and M. Song, "Variations of the electrochemical properties of limn[sub 2]o[sub 4] with synthesis conditions", *Journal of The Electrochemical Society*, vol. 147,

p. 874, 3 Mar. 2000, ISSN: 00134651. DOI: 10.1149/1.1393285. [Online]. Available: https://iopscience.iop.org/article/10.1149/1.1393285.

[203] X. Zhou, M. Chen, M. Xiang, H. Bai, and J. Guo, "Solid-state combustion synthesis of spinel limn2o4 using glucose as a fuel", *Ceramics International*, vol. 39, pp. 4783–4789, 5 Jul. 2013, ISSN: 0272-8842. DOI: 10.1016/J.CERAMINT.2012.11.068.

[204] X. Zhou, M. Chen, H. Bai, C. Su, L. Feng, and J. Guo, "Preparation and electrochemical properties of spinel limn2o4 prepared by solid-state combustion synthesis", *Vacuum*, vol. 99, pp. 49–55, Jan. 2014, ISSN: 0042-207X. DOI: 10.1016/J.VACUUM.2013.04.011.

[205] N. Yuan, "High-pressure single crystal growth and magnetization studies on correlated electron systems", 2024. DOI: 10.11588/HEIDOK.00035097.

[206] D. K. Kim, P. Muralidharan, H. W. Lee, R. Ruffo, Y. Yang, C. K. Chan, H. Peng, R. A. Huggins, and Y. Cui, "Spinel limn2o4 nanorods as lithium ion battery cathodes", *Nano Letters*, vol. 8, pp. 3948–3952, 11 Nov. 2008, ISSN: 15306984. DOI: 10.1021/NL8024328. [Online]. Available: https://pubs.acs.org/doi/full/10.1021/nl8024328.

[207] H. Xia, Z. Luo, and J. Xie, "Nanostructured limn2o4 and their composites as high-performance cathodes for lithium-ion batteries", *Progress in Natural Science: Materials International*, vol. 22, pp. 572–584, 6 Dec. 2012, ISSN: 1002-0071. DOI: 10.1016/J.PNSC.2012.11.014.

[208] A. Jossen, "Fundamentals of battery dynamics", *Journal of Power Sources*, vol. 154, pp. 530–538, 2 Mar. 2006, ISSN: 0378-7753. DOI: 10.1016/J.JPOWSOUR.2005.10.041.

[209] A. V. Kosov, O. V. Grishenkova, O. L. Semerikova, V. A. Isaev, and Y. P. Zaikov, "On the theory of cyclic voltammetry for multiple nucleation and growth: Scan rate influence", *Journal of Electroanalytical Chemistry*, vol. 883, p. 115 056, Feb. 2021, ISSN: 1572-6657. DOI: 10.1016/J.JELECHEM.2021.115056.

[210] M. M. Thackeray, W. I. David, P. G. Bruce, and J. B. Goodenough, "Lithium insertion into manganese spinels", *Materials Research Bulletin*, vol. 18, pp. 461–472, 4 Apr. 1983, ISSN: 0025-5408. DOI: 10.1016/0025-5408(83)90138-1.

[211] K. Amine, H. Tukamoto, H. Yasuda, and Y. Fujita, "Preparation and electrochemical investigation of limn2 - xmexo4 (me: Ni, fe, and x = 0.5, 1) cathode materials for secondary lithium batteries", *Journal of Power Sources*, vol. 68, pp. 604–608, 2 Oct. 1997, ISSN: 0378-7753. DOI: 10.1016/S0378-7753(96)02590-6.

[212] K. J. Laidler, "The development of the arrhenius equation", *Journal of Chemical Education*, vol. 61, pp. 494–498, 6 1984, ISSN: 00219584. DOI: 10.1021/ED061P494.

[213] S. S. Zhang, K. Xu, and T. R. Jow, "The low temperature performance of li-ion batteries", *Journal of Power Sources*, vol. 115, pp. 137–140, 1 Mar. 2003, ISSN: 0378-7753. DOI: 10.1016/S0378-7753(02)00618-3.

[214] J. Vetter, P. Novák, M. R. Wagner, C. Veit, K. C. Möller, J. O. Besenhard, M. Winter, M. Wohlfahrt-Mehrens, C. Vogler, and A. Hammouche, "Ageing mechanisms in lithium-ion batteries", *Journal of Power Sources*, vol. 147, pp. 269–281, 1-2 Sep. 2005, ISSN: 0378-7753. DOI: 10.1016/J.JPOWSOUR.2005.01.006.

[215] J. Berry, T. Buonassisi, D. A. Egger, G. Hodes, L. Kronik, Y.-L. Loo, I. Lubomirsky, S. R. Marder, Y. Mastai, J. S. Miller, D. B. Mitzi, Y. Paz, A. M. Rappe, I. Riess, B. Rybtchinski, O. Stafsudd, V. Stevanovic, M. F. Toney, D. Zitoun, A. Kahn, D. Ginley, and D. Cahen, "Hybrid organic–inorganic perovskites (hoips): Opportunities and challenges", *sas.upenn.eduJ Berry, T Buonassisi, DA Egger, G Hodes, L Kronik, YL Loo, I Lubomirsky, SR MarderAdvanced Materials, 2015•sas.upenn.edu*, 2015. DOI: 10.1002/adma.201502294. [Online]. Available: https://www.sas.upenn.edu/rappegroup/publications/Papers/Berry15p5102.pdf.

[216] A. K. Jena, A. Kulkarni, and T. Miyasaka, "Halide perovskite photovoltaics: Background, status, and future prospects", *Chemical Reviews*, vol. 119, pp. 3036–3103, 5 Mar. 2019, ISSN: 15206890. DOI: 10.1021/ACS.CHEMREV.8B00539. [Online]. Available: https://pubs.acs.org/doi/abs/10.1021/acs.chemrev.8b00539.

[217] W. Li, Z. Wang, F. Deschler, S. Gao, R. H. Friend, and A. K. Cheetham, "Chemically diverse and multifunctional hybrid organic–inorganic perovskites", *Nature Reviews Materials 2017 2:3*, vol. 2, pp. 1–18, 3 Feb. 2017, ISSN: 2058-8437. DOI: 10.1038/natrevmats.2016.99. [Online]. Available: https://www.nature.com/articles/natrevmats201699.

[218] M. Green, E. Dunlop, J. Hohl-Ebinger, M. Yoshita, N. Kopidakis, and X. Hao, "Solar cell efficiency tables (version 57)", *Progress in Photovoltaics: Research and Applications*, vol. 29, pp. 3–15, 1 Jan. 2021, ISSN: 1099-159X. DOI: 10.1002/PIP.3371. [Online]. Available: https://onlinelibrary.wiley.com/doi/full/10.1002/pip.3371.

[219] J. Y. Kim, J. W. Lee, H. S. Jung, H. Shin, and N. G. Park, "High-efficiency perovskite solar cells", *Chemical Reviews*, vol. 120, pp. 7867–7918, 15 Aug. 2020, ISSN: 15206890. DOI: 10.1021/ACS.CHEMREV.0C00107. [Online]. Available: https://pubs.acs.org/doi/abs/10.1021/acs.chemrev.0c00107.

[220] S. A. Veldhuis, P. P. Boix, N. Yantara, M. Li, T. C. Sum, N. Mathews, and S. G. Mhaisalkar, "Perovskite materials for light-emitting diodes and lasers", *Advanced Materials*, vol. 28, pp. 6804–6834, 32 Aug. 2016, ISSN: 1521-4095. DOI: 10.1002/ADMA.201600669. [Online]. Available: https://onlinelibrary.wiley.com/doi/full/10.1002/adma.201600669.

[221] W. J. Yin, T. Shi, and Y. Yan, "Unique properties of halide perovskites as possible origins of the superior solar cell performance.", *Advanced Materials (Deerfield Beach, Fla.)*, vol. 26, pp. 4653–4658, 27 May 2014, ISSN: 0935-9648. DOI: 10.1002/ADMA.201306281. [Online]. Available: https://europepmc.org/article/med/24827122.

[222] Y. Liu, L. K. Ono, G. Tong, H. Zhang, and Y. Qi, "Two-dimensional dion-jacobson structure perovskites for efficient sky-blue light-emitting diodes", *ACS Energy Letters*, vol. 6, pp. 908–914, 3 Mar. 2021, ISSN: 23808195. DOI: 10.1021/ACSENERGYLETT.1C00129. [Online]. Available: https://pubs.acs.org/doi/full/10.1021/acsenergylett.1c00129.

[223] Z. Ma, Q. Li, J. Luo, S. Li, L. Sui, D. Zhao, K. Yuan, G. Xiao, J. Tang, Z. Quan, and B. Zou, "Pressure-driven reverse intersystem crossing: New path toward bright deep-blue emission of lead-free halide double perovskites", *Journal of the American Chemical Society*, vol. 143, pp. 15 176–15 184, 37 Sep. 2021, ISSN: 15205126. DOI: 10.1021/JACS.1C06207. [Online]. Available: https://pubs.acs.org/doi/abs/10.1021/jacs.1c06207.

[224] S. Yan, K. Tang, Y. Lin, Y. Ren, W. Tian, H. Chen, T. Lin, L. Qiu, X. Pan, and W. Wang, "Light-emitting diodes with manganese halide tetrahedron embedded in anti-perovskites", *ACS Energy Letters*, vol. 6, pp. 1901–1911, 5 May 2021, ISSN: 23808195. DOI: 10.1021/ACSENERGYLETT.1C00250. [Online]. Available: https://pubs.acs.org/doi/abs/10.1021/acsenergylett.1c00250.

[225] F. Zhang, Z. Zhao, B. Chen, H. Zheng, L. Huang, Y. Liu, Y. Wang, and A. L. Rogach, "Strongly emissive lead-free 0d cs3cu2i5 perovskites synthesized by a room temperature solvent evaporation crystallization for down-conversion light-emitting devices and fluorescent inks", *Advanced Optical Materials*, vol. 8, p. 1 901 723, 8 Apr. 2020, ISSN: 2195-1071. DOI: 10.1002/ADOM.201901723. [Online]. Available: https://onlinelibrary.wiley.com/doi/full/10.1002/adom.201901723.

[226] N. G. Park, "Perovskite solar cells: An emerging photovoltaic technology", *Materials Today*, vol. 18, pp. 65–72, 2 Mar. 2015, ISSN: 1369-7021. DOI: 10.1016/J.MATTOD.2014.07.007.

[227] Q. Jiang, M. Chen, J. Li, M. Wang, X. Zeng, T. Besara, J. Lu, Y. Xin, X. Shan, B. Pan, C. Wang, S. Lin, T. Siegrist, Q. Xiao, and Z. Yu, "Electrochemical doping of halide perovskites with ion intercalation", *ACS Nano*, vol. 11, pp. 1073–1079, 1 Jan. 2017, ISSN: 1936086X. DOI: 10.1021/ACSNANO.6B08004. [Online]. Available: https://pubs.acs.org/doi/abs/10.1021/acsnano.6b08004.

[228] N. Vicente and G. Garcia-Belmonte, "Methylammonium lead bromide perovskite battery anodes reversibly host high li-ion concentrations", *Journal of Physical Chemistry Letters*, vol. 8, pp. 1371–1374, 7 Apr. 2017, ISSN: 19487185. DOI: 10.1021/ACS.JPCLETT.7B00189. [Online]. Available: https://pubs.acs.org/doi/abs/10.1021/acs.jpclett.7b00189.

[229] H. R. Xia, W. T. Sun, and L. M. Peng, "Hydrothermal synthesis of organometal halide perovskites for li-ion batteries", *Chemical Communications*, vol. 51, pp. 13 787–13 790, 72 Aug. 2015, ISSN: 1364-548X. DOI: 10.1039/C5CC05053G. [Online]. Available: https://pubs.rsc.org/en/content/articlehtml/2015/cc/c5cc05053g.

[230] N. Vicente, D. Bresser, S. Passerini, and G. Garcia-Belmonte, "Probing the 3-step lithium storage mechanism in ch3nh3pbbr3 perovskite electrode by operando-xrd analysis", *ChemElectroChem*, vol. 6, pp. 456–460, 2 Jan. 2019, ISSN: 2196-0216. DOI: 10.1002/CELC.201801291. [Online]. Available: https://onlinelibrary.wiley.com/doi/full/10.1002/celc.201801291.

[231] J. A. Dawson, A. J. Naylor, C. Eames, M. Roberts, W. Zhang, H. J. Snaith, P. G. Bruce, and M. S. Islam, "Mechanisms of lithium intercalation and conversion processes in organic-inorganic halide perovskites", *ACS Energy Letters*, vol. 2, pp. 1818–1824, 8 Aug. 2017, ISSN: 23808195. DOI: 10.1021/ACSENERGYLETT.7B00437. [Online]. Available: https://pubs.acs.org/doi/full/10.1021/acsenergylett.7b00437.

[232] J. Büttner, T. Berestok, S. Burger, M. Schmitt, M. Daub, H. Hillebrecht, I. Krossing, and A. Fischer, "Are halide-perovskites suitable materials for battery and solar-battery applications–fundamental reconsiderations on solubility, lithium intercalation, and photo-corrosion", *Advanced Functional Materials*, vol. 32, p. 2 206 958, 49 Dec. 2022, ISSN: 1616-3028. DOI: 10.1002/ADFM.202206958. [Online]. Available: https://onlinelibrary.wiley.com/doi/full/10.1002/adfm.202206958.

[233] A. Mathieson, S. Feldmann, and M. D. Volder, "Solid-state lithium-ion batteries as a method for doping halide perovskites with an in situ optical readout of dopant concentration", *JACS Au*, vol. 2, pp. 1313–1317, 6 Jun. 2022, ISSN: 26913704. DOI:

10.1021/JACSAU.2C00212. [Online]. Available: https://pubs.acs.org/doi/full/10.1021/jacsau.2c00212.

[234] Q. Wang, T. Yang, H. Wang, J. Zhang, X. Guo, Z. Yang, S. Lu, and W. Qin, "Morphological and chemical tuning of lead halide perovskite mesocrystals as long-life anode materials in lithium-ion batteries", *CrystEngComm*, vol. 21, pp. 1048–1059, 6 Feb. 2019, ISSN: 14668033. DOI: 10.1039/C8CE01779D. [Online]. Available: https://pubs.rsc.org/en/content/articlehtml/2019/ce/c8ce01779d.

[235] S. Narayanan, N. Parikh, M. M. Tavakoli, M. Pandey, M. Kumar, A. Kalam, S. Trivedi, D. Prochowicz, and P. Yadav, "Metal halide perovskites for energy storage applications", *European Journal of Inorganic Chemistry*, vol. 2021, pp. 1201–1212, 13 Apr. 2021, ISSN: 1099-0682. DOI: 10.1002/EJIC.202100015. [Online]. Available: https://onlinelibrary.wiley.com/doi/full/10.1002/ejic.202100015.

[236] S. Liu, J. Zerhoch, M. W. Heindl, C. Zhang, T. Kodalle, K. Sun, A. Shcherbakov, S. Bodnar, M. Miah, M. Gholipoor, C. Jandl, A. Pöthig, J. Ballmann, I. D. Sharp, P. M. Ller-Buschbaum, C. M. Sutter-Fella, U. W. Paetzold, and F. Deschler, "Orientation-driven chirality funnels in chiral low-dimensional lead-halide perovskite heterostructures", *Cite This: J. Am. Chem. Soc*, vol. 147, pp. 16 681–16 693, 2025. DOI: 10.1021/jacs.5c05172. [Online]. Available: https://doi.org/10.1021/jacs.5c05172.

[237] M. Tathavadekar, S. Krishnamurthy, A. Banerjee, S. Nagane, Y. Gawli, A. Suryawanshi, S. Bhat, D. Puthusseri, A. D. Mohite, and S. Ogale, "Low-dimensional hybrid perovskites as high performance anodes for alkali-ion batteries", *Journal of Materials Chemistry A*, vol. 5, pp. 18 634–18 642, 35 Sep. 2017, ISSN: 20507496. DOI: 10.1039/C7TA04529H. [Online]. Available: https://pubs.rsc.org/en/content/articlehtml/2017/ta/c7ta04529h.

[238] N. Tewari, D. Lam, C. H. A. Li, and J. E. Halpert, "Recent advancements in batteries and photo-batteries using metal halide perovskites", *APL Materials*, vol. 10, p. 40 905, 4 Apr. 2022, ISSN: 2166532X. DOI: 10.1063/5.0086599. [Online]. Available: https://pubs.aip.org/aip/apm/article/10/4/040905/2834935/Recent-advancements-in-batteries-and-photo.

[239] S. G. Choi and J. W. Lee, "Irreversible phase back conversion of α-fapbi3 driven by lithium-ion migration in perovskite solar cells", *EcoMat*, vol. 5, e12398, 10 Oct. 2023, ISSN: 2567-3173. DOI: 10.1002/EOM2.12398. [Online]. Available: https://onlinelibrary.wiley.com/doi/full/10.1002/eom2.12398.

[240] A. Gaurav, A. Das, A. Paul, A. Jain, B. D. Boruah, and M. A. Jalebi, "Could halide perovskites revolutionalise batteries and supercapacitors: A leap in energy storage", *Journal of Energy Storage*, vol. 88, p. 111 468, May 2024, ISSN: 2352-152X. DOI: 10.1016/J.EST.2024.111468.

[241] Y. Xu, J. Li, F. Zhao, Y. Gao, R. Chen, and T. He, "Optical properties of a csmnbr3 single crystal", *ACS Omega*, vol. 7, pp. 29 415–29 419, 33 Aug. 2022, ISSN: 24701343. DOI: 10.1021/ACSOMEGA.2C03661/ASSET/IMAGES/LARGE/AO2C03661_0006.JPEG. [Online]. Available: https://pubs.acs.org/doi/full/10.1021/acsomega.2c03661.

[242] W. Jia, J. Bao, H. Zhang, M. Wu, J. Qiu, H. Wu, and Y. Zhang, "Effect of mn-ion reconstructed lattice on lead-free halide perovskite cs3bi2-xmnxcl9 anode in li-ion batteries", *Journal of Environmental Sciences*, Apr. 2025, ISSN: 1001-0742. DOI: 10.1016/J.JES.2025.04.030. [Online]. Available: https://linkinghub.elsevier.com/retrieve/pii/S1001074225002190.

[243] C. Zhang, Y. Zhang, Z. Nie, C. Wu, T. Gao, N. Yang, Y. Yu, Y. Cui, Y. Gao, and W. Liu, "Double perovskite la2mnnio6 as a high-performance anode for lithium-ion batteries", *Advanced Science*, vol. 10, p. 2 300 506, 18 Jun. 2023, ISSN: 21983844. DOI: 10.1002/ADVS.202300506. [Online]. Available: https://pmc.ncbi.nlm.nih.gov/articles/PMC10288226/.

[244] Y. Deng, L. Wan, Y. Xie, X. Qin, and G. Chen, "Recent advances in mn-based oxides as anode materials for lithium ion batteries", *RSC Advances*, vol. 4, pp. 23 914–23 935, 45 Jun. 2014, ISSN: 2046-2069. DOI: 10.1039/C4RA02686A. [Online]. Available: https://pubs.rsc.org/en/content/articlehtml/2014/ra/c4ra02686a.

[245] M. M. Butala, K. R. Danks, M. A. Lumley, S. Zhou, B. C. Melot, and R. Seshadri, "Mno conversion in li-ion batteries: In situ studies and the role of mesostructuring", *ACS Applied Materials and Interfaces*, vol. 8, pp. 6496–6503, 10 Mar. 2016, ISSN: 19448252. DOI: 10.1021/ACSAMI.5B12840. [Online]. Available: https://pubs.acs.org/doi/full/10.1021/acsami.5b12840.

[246] Y. Zhao, C. Xie, Y. Song, and P. Yang, "Emission of mn2+ ions in mn:cspbx3 (x = cl, br, i) nanocrystals adjusted with halogen ion ratios", *Journal of Nanoparticle Research*, vol. 22, pp. 1–11, 6 Jun. 2020, ISSN: 1572896X. DOI: 10.1007/S11051-020-04884-W. [Online]. Available: https://link.springer.com/article/10.1007/s11051-020-04884-w.

[247] S. Chintha, S. Atif, A. Chaupatnaik, A. Golubnichiy, A. M. Abakumov, and P. Barpanda, "Na0.5bi0.5tio3 perovskite anode for lithium-ion batteries", *Sustainable Energy & Fuels*, vol. 8, pp. 5058–5064, 21 Oct. 2024, ISSN: 2398-4902. DOI: 10.1039/D4SE00935E. [Online]. Available: https://pubs.rsc.org/en/content/articlehtml/2024/se/d4se00935e.

[248] H. Wu, J. Pi, Q. Liu, Q. Liang, J. Qiu, J. Guo, Z. Long, D. Zhou, and Q. Wang, "All-inorganic lead free double perovskite li-battery anode material hosting high li+ion concentrations", *Journal of Physical Chemistry Letters*, vol. 12, pp. 4125–4129, 17 May 2021, ISSN: 19487185. DOI: 10.1021/ACS.JPCLETT.1C00041. [Online]. Available: https://pubs.acs.org/doi/full/10.1021/acs.jpclett.1c00041.

[249] S. M. Wood, C. H. Pham, A. Heller, and C. B. Mullins, "Communication—stages in the dynamic electrochemical lithiation of lead", *Journal of The Electrochemical Society*, vol. 163, A1027–A1029, 6 Mar. 2016, ISSN: 0013-4651. DOI: 10.1149/2.1251606JES. [Online]. Available: https://iopscience.iop.org/article/10.1149/2.1251606jes.

[250] H. D. Asfaw, A. Kotronia, N. Garcia-Araez, K. Edström, and D. Brandell, "Charting the course to solid-state dual-ion batteries", *Carbon Energy*, vol. 6, e425, 3 Mar. 2024, ISSN: 2637-9368. DOI: 10.1002/CEY2.425. [Online]. Available: https://onlinelibrary.wiley.com/doi/full/10.1002/cey2.425.

[251] O. V. Yarmolenko, G. R. Baymuratova, K. G. Khatmullina, G. Z. Tulibayeva, A. V. Yudina, T. A. Savinykh, I. K. Yakushchenko, P. A. Troshin, and A. F. Shestakov, "Influence of the lithium cation desolvation process at the electrolyte/electrode interface on the performance of lithium batteries", *Inorganics*, vol. 10, p. 176, 11 Nov. 2022, ISSN: 23046740. DOI: 10.3390/inorganics10110176. [Online]. Available: https://www.mdpi.com/2304-6740/10/11/176.

[252] N. Vicente and G. Garcia-Belmonte, "Organohalide perovskites are fast ionic conductors", *Advanced Energy Materials*, vol. 7, p. 1 700 710, 19 Oct. 2018, ISSN: 1614-6840. DOI: 10.1002/AENM.201700710. [Online]. Available: https://onlinelibrary.wiley.com/doi/full/10.1002/aenm.201700710.

[253] D. H. Jeon, "Wettability in electrodes and its impact on the performance of lithium-ion batteries", *Energy Storage Materials*, vol. 18, pp. 139–147, Mar. 2019, ISSN: 2405-8297. DOI: 10.1016/J.ENSM.2019.01.002.

[254] L. Faro, S. Krämer, D. Weintz, M. Winter, I. Cekic-Laskovic, and M. Grünebaum, "Importance of high-concentration electrolytes for lithium-based batteries", *Encyclopedia 2025, Vol. 5, Page 20*, vol. 5, p. 20, 1 Feb. 2025, ISSN: 2673-8392. DOI:

10.3390/encyclopedia5010020. [Online]. Available: https://www.mdpi.com/2673-8392/5/1/20.

[255] T. Jaumann, J. Balach, M. Klose, S. Oswald, J. Eckert, and L. Giebeler, "Role of 1,3-dioxolane and lino 3 addition on the long term stability of nanostructured silicon/carbon anodes for rechargeable lithium batteries", *Journal of The Electrochemical Society*, vol. 163, A557–A564, 3 Jan. 2016, ISSN: 0013-4651. DOI: 10.1149/2.1011603JES. [Online]. Available: https://iopscience.iop.org/article/10.1149/2.1011603jes.

[256] S. Ai, X. Wu, J. Wang, X. Li, X. Hao, and Y. Meng, "Research progress on solid-state electrolytes in solid-state lithium batteries: Classification, ionic conductive mechanism, interfacial challenges", *Nanomaterials 2024, Vol. 14, Page 1773*, vol. 14, p. 1773, 22 Nov. 2024, ISSN: 2079-4991. DOI: 10.3390/NANO14221773. [Online]. Available: https://www.mdpi.com/2079-4991/14/22/1773.

[257] N. Ahn and M. Choi, "Towards long-term stable perovskite solar cells: Degradation mechanisms and stabilization techniques", *Advanced Science*, vol. 11, p. 2 306 110, 4 Jan. 2024, ISSN: 2198-3844. DOI: 10.1002/ADVS.202306110. [Online]. Available: https://onlinelibrary.wiley.com/doi/full/10.1002/advs.202306110.

[258] J. P. Pender, G. Jha, D. H. Youn, J. M. Ziegler, I. Andoni, E. J. Choi, A. Heller, B. S. Dunn, P. S. Weiss, R. M. Penner, and C. B. Mullins, "Electrode degradation in lithium-ion batteries", *ACS Nano*, vol. 14, pp. 1243–1295, 2 Feb. 2020, ISSN: 1936086X. DOI: 10.1021/ACSNANO.9B04365. [Online]. Available: https://pubs.acs.org/doi/full/10.1021/acsnano.9b04365.

[259] B. D. Boruah, B. Wen, and M. D. Volder, "Light rechargeable lithium-ion batteries using v2o5cathodes", *Nano Letters*, vol. 21, pp. 3527–3532, 8 Apr. 2021, ISSN: 15306992. DOI: 10.1021/ACS.NANOLETT.1C00298. [Online]. Available: https://pubs.acs.org/doi/full/10.1021/acs.nanolett.1c00298.

Acknowledgement

I would like to take this opportunity to express my heartfelt gratitude to all those who have supported me during the preparation of this thesis and throughout my academic journey.

First and foremost, I am deeply grateful to Prof. Rüdiger Klingeler for making this work possible. His continuous support, valuable discussions, and guidance have been essential to the completion of this thesis.

I would also like to sincerely thank Prof. Joachim Spatz for kindly and spontaneously agreeing to serve as the second examiner.

My appreciation extends to all of my collaboration partners, both within Heidelberg University and beyond. Your contributions and insights were indispensable for the progress of this work.

I am also indebted to the many dedicated people at KIP who ensure the institute runs smoothly. In particular, I wish to thank the administration, the machine shop, the electronics workshop, and the IT department for their reliable assistance.

A very special thanks goes to all current and former members of the F25 research group at KIP. The stimulating conversations, constructive discussions, and friendly atmosphere made our collaboration both productive and enjoyable. I truly valued the spirit of teamwork and the many memorable moments we shared, with Jan, Lukas, Tobias, Luca, Birte, and Erik being just a few among many.

Finally, I would like to give special thanks to Lennart Singer, whose excellent training, patience in answering countless questions, and collegial spirit made working together an absolute pleasure. Sharing an office with you was not only instructive but also a lot of fun.

Many thanks to Alex, Kim, Marvin, Paul, and Vale for proofreading my thesis and for their kind support during our many conversations about my topic.

Last but not least, I would like to thank Louisa above all for her moral support. She has always been there for me through countless ups and downs.

heuslwdgu.

Declaration

I hereby confirm that I have written this thesis independently and have not used any sources or aids other than those specified.

Heidelberg, September 24, 2025